



Supramolecular Hydrogels and Discrete Structures based on Metal Coordination and Hydrogen Bonding

Lamia L. G. Al-mahamad

A thesis submitted for the degree of
Doctor of Philosophy

Newcastle University
School of Chemistry
Newcastle Upon Tyne, UK

2017

Declaration

I hereby declare that this thesis is my own work and has not been submitted to another University or Institute for the award of any other degree.

Lamia Al-mahamad

Dedication

To my Parents with my deepest gratitude.

Lamia Al-mahamad

2017

Acknowledgments

First, all thanks to *Allah* (my God) for the great help to achieve this work.

I would like to express my thanks to my supervisor Dr Benjamin R Horrocks for his valuable guidance, advice, and helpful comments through all the stages of this work. I also would like to thank my second supervisor Prof. Andrew Houlton.

I would like to thank Dr Osama El-Zubir at Chemical Nanoscience Laboratory and Dr Paul Waddell from Newcastle Chemical Crystallography Service for their help in this work.

I would also like to thank all colleagues in the Synthesis Lab of Chemical Nanoscience group especially Samantha Lunn, Rachel Little, and Liam Mistry for their help and moral support.

My sincere thanks also go to the School of Chemistry and Newcastle University for their help and services during my study.

I should also thank my sisters, Dr Sajida Al-mahamad and Programmer Linda Al-mahamad, who always help me to install different software and solve any problems.

Also, I must express my deeply gratitude to my family (my parents, sisters, and brothers) for their big support and prayers throughout all my life.

Finally, my thanks to the Iraqi Ministry of Higher Education and Scientific Research for the financial support.

Abstract

Supramolecular Hydrogels and Discrete Structures based on Metal Coordination and Hydrogen Bonding

The complexation of thiolated nucleosides and nucleobases with a range of group 11 metal ions (Au(I), Ag(I), Cu(I/II)), was observed to lead to the formation of hydrogels by simple inversion tests. Atomic force and electron microscopy of the xerogels showed, in many cases, the presence of fibres with lengths in the micrometre range and above; this provided evidence for the formation of coordination polymers. This thesis is concerned with the preparation, characterisation and investigation of the physical properties, mainly photoluminescence and conductivity, of these coordination polymers.

2'-Deoxy-6-thioguanosine was successfully synthesised and characterized by UV, IR, Mass, ^1H -NMR, and ^{13}C -NMR spectroscopy. The formation of coordination polymers upon reaction of Au(I), Ag(I), and Cu(II) ions with 2'-deoxy-6-thioguanosine and 6-thioguanosine in aqueous media produced hydrogels with up to 97% water+methanol by mass. The Au-6-thioguanosine gel was studied in more detail because of the interest in gold thiolate polymers and the novel properties observed for Au(I)-6-thioguanosine. Fluorescence spectroscopy observed a strong yellow emission ($\lambda_{\text{max}} = 606 \text{ nm}$) which is not present in 6-thioguanosine nor in the Au(I) solutions. The optical absorption spectrum of the coordination polymer showed a band at ($\lambda_{\text{max}} = 360 \text{ nm}$) assigned to the HOMO-LUMO transition located mainly on the S-Au-S...chain of the polymer. An induced CD band associated with the Au-S chain and an enhancement of the CD signal at shorter wavelengths, for transitions associated with the ligand, suggested the polymer has a helical structure. Further evidence was provided by analysis of the X-ray scattering pattern of the xerogel and atomic force microscopy of single fibres deposited on silicon chips.

The observation of long Au(I)-6-thioguanosine fibres and strong photoluminescence suggests some delocalisation of the states associated with the Au-S chains and the possibility of electronic conductivity. This was demonstrated upon oxidative doping of Au(I)-6-thioguanosine xerogels coated over platinum microband electrodes. Treatment with iodine vapour or $([\text{Br}(\text{C}_6\text{H}_4)_3\text{N}]\text{SbCl}_6)$ in anhydrous acetonitrile were found to result in linear current-voltage characteristics. The temperature dependence of the conductance showed Arrhenius behaviour (over range of temperature 223 to 323 K) with an activation energy of 94 kJ mol^{-1} .

More complex structures based on Au(I)-6-thioguanosine polymers were observed upon synthesising the polymer in the presence of duplex DNA (from calf thymus). The templating of the polymer on DNA produces long, regular, and uniform fibres with a beads-on-a-string morphology. An unusual self-assembly of Au(I)-6-thioguanosine at flat Si surfaces upon simple drop-casting, with slow evaporation was also observed. AFM images of these films showed the formation of well-defined layers, but with each layer comprising long ribbons exceeding the maximum length of the AFM scan (~15 micrometres).

Ag(I)-containing hydrogels formed by reactions with 6-thioguanine, 6-mercaptopurine, and 2-thiocytosine were prepared and characterised by AFM, TEM, XPS, X-Ray, FTIR, UV-Vis, and fluorescent spectroscopy. Au(I) 2-thiocytosine was also prepared, but this produced a discrete complex rather than a gel. AFM of the Ag(I) xerogels showed the formation of very long fibres and this was confirmed by TEM images. FTIR and X-ray diffraction studies suggested the metal coordination occurred via S atoms in all three gels. The Au(I) 2-thiocytosine was found to have strong luminescence (λ_{max} 622 nm). A new Ag(I):6-thioethero nucleoside complex was prepared containing 6-methylmercaptopurine riboside (6-MMPR) which was shown by single crystal X-ray diffraction to unexpectedly feature coordination via N7 rather than the thioether sulfur atom. Cu(II) & Co(II):6-methylmercaptopurine(6-MMP) were also synthesised as new discrete complexes. The metals binding was studied by single crystal X-ray diffraction which showed that the binding sites were N3& N9 for Cu(II) ions, and N9 for Co(II) ion in the complexes.

Table of Contents

Acknowledgments	III
Abstract	IV
Table of Contents	VI
Chapter 1. Introduction	1
1.1 Nucleic acids and metal ions	1
1.2 Gel: definition and classification.....	3
1.3 Coordination polymers	5
1.4 Chemistry of copper	8
1.5 Chemistry of silver	9
1.6 Chemistry of gold.....	9
1.7 Gold (I) complexes in medicine	11
1.8 Silver(I) complexes in medicine.....	11
1.9 Copper (I) complexes in medicine	12
1.10 Nucleobase and nucleoside hydrogels with and without coinage metal ions.....	13
1.11 Metal-nucleobase and nucleoside discrete entities.....	24
1.12 Mechanism of fibre formation.....	25
1.13 Hydrogen bonding and supramolecular chemistry	25
1.14 Thesis overview.....	28
Chapter 2. Experimental Methods	43
2.1 Chemicals and Materials	43
2.2 Silicon Chips preparation for AFM, XPS, and FTIR	43
2.3 Characterization of gels.....	43
2.3.1 Fourier transform infrared (FTIR) spectroscopy	44
2.3.2 UV-Visible absorption spectroscopy.....	45
2.3.3 Fluorescence spectroscopy	46
2.3.4 Circular Dichroism spectroscopy (CD)	48
2.3.5 X-Ray Photoelectron Spectroscopy (XPS).....	49
2.3.6 Crystal and Powder X-Ray Diffraction (XRD)	49
2.4 Gel characterization with the scanning probe microscope (SPM)	51
2.4.1 Atomic force microscope (AFM)	51
2.4.2 Epifluorescence Microscope	52
2.4.3 Transmission electron microscope (TEM)	53
2.5 Electrical measurements.....	54
Chapter 3. Au (I):6-Thioguanosine Hydrogel	57
3.1 Introduction	57
3.2 Experimental	58

3.2.1 Synthesis of Gold:6-Thioguanosine (Au:6-TGR) gel with 10 mg /ml 6-TGR.....	58
3.2.2 Synthesis Gold:6-Thioguanosine (Au:6-TGR) solutions with concentration 1, 0.1, and 0.01 mg of 6-TGR	58
3.2.3 Electrical measurements.....	59
3.3.3 UV-Vis Absorption spectroscopy.....	60
3.3.4 Fluorescence spectroscopy characterization of Au:6-TGR	61
3.3.5 Circular dichroism (CD).....	62
3.3.6 Powder x-ray diffraction	63
3.3.7 X-ray photoelectron spectroscopy (XPS) of Au:6-TGR	64
3.4 Atomic force microscopy (AFM).....	67
3.5 Transmission electron microscopy (TEM).....	70
3.6 Fluorescence microscopic imaging	71
3.7 Conductivity of Au:6-TGR hydro gel	72
3.7.1 Two-terminal I–V characteristics and temperature dependence of the Au:6-TGR conductance	72
3.7.2 Calculation the activation energy from Arrhenius plot	74
3.8 Diluted solutions of 1:1 Au-6-TGR with con. 1, 0.1, and 0.01 mg/ml 6-TGR	77
3.9 Fluorescence spectra of Au:6-TGR solutions.....	77
3.10 Atomic force microscopy (AFM).....	78
3.11 Fluorescence microscopic imaging	82
3.12 Templating 6-thioguanosine polymer on DNA	83
3.12.1 Synthesis Au(I):6-TGR hydrogel in the presence of DNA	83
3.12.2 Atomic force microscopy studies	83
3.13 Synthesis of gold:6-thioguanosine (Au:6-TGR) gel with urea.....	85
3.13.1 Interaction Au:6-TGR gel with urea.....	85
3.13.2 AFM images of reformed gel with urea solution	86
3.13.3 Fluorescence microscopy	87
3.14 Conclusion.....	88
Chapter 4. Synthesis and Structural Study of Copper and Silver Complexes of 6-Thioguanosine	96
Abstract	96
4.1 Introduction	96
4.2 Experimental	97
4.2.1 Synthesis of copper:6-thioguanosine (Cu:6-TGR) hydrogel.....	97
4.2.2 Synthesis of silver: 6-thioguanosine (Ag:6-TGR) hydrogel.....	97
4.3 Results & Discussion.....	97
4.3.1 Copper:6-thioguanosine (Cu:6-TGR) hydrogel.....	97
4.3.2 Silver: 6-thioguanosine (Ag:6-TGR) hydrogel	104
4.3.3 Atomic force microscopy (AFM).....	108

4.3.4 Transmission electron microscopy (TEM)	111
4.4 Conclusion	113
Chapter 5. Complexation of Coinage Metal Ions with 2'-deoxy-6-Thioguanosine (d TGR)	119
Abstract	119
5.1 Introduction	119
5.2 2'-Deoxy-6-thioguanosine nucleoside metal ions complexation.....	119
5.2.1 Synthesis of 2'-deoxy-6-thioguanosine (d TGR).....	120
5.2.2 Mechanism of the reaction	120
5.3 2'-Deoxy-6-thioguanosine (d TGR) characterization.....	121
5.3.1 Mass spectroscopy characterization	121
5.3.2 NMR studies.....	122
5.3.3 UV-Vis absorption characterization	124
5.3.4 Fourier transform infrared (FTIR) Characterization	125
5.4 Synthesis of Au, Ag, and Cu:d TGR hydrogels	125
5.5 Results & Dissociation	125
5.5.1 Atomic force microscopy (AFM) characterization	126
5.5.2 Transmission electron microscope (TEM) characterization.....	129
5.6 Conclusion.....	131
Chapter 6. Synthesis and Characterisation of Supramolecular Hydrogels formed by Silver Thionucleobases	134
Abstract	134
6.1 Introduction	134
6.2 Experimental	136
6.2.1 Synthesis of Silver: 6-Thioguanine (Ag:6-TG) hydrogel.....	136
6.2.2 Synthesis of Silver: 6-Mercaptopurine (Ag:6-MP) gel	136
6.2.3 Synthesis of Silver: 2-Thiocyto sine (Ag:2-TC) gel.....	136
6.3 Results & Discussion.....	137
6.3.1 Silver: 6-Thioguanine (Ag:6-TG) hydrogel	137
6.3.2 Silver: 6-Mercaptopurine (Ag:6-MP) gel	140
6.3.3 Silver: 2-Thiocyto sine (Ag:2-TC) gel	144
6.3.3.5 Mass spectra characterization for pale Ag:2-TC	151
6.4 Atomic force microscopy (AFM).....	151
6.4.1 Atomic force microscopy (AFM) characterization of the Ag: 6-TG & 6-MP hydrogels...	151
6.4.2 Atomic force microscopy (AFM) of Ag:2-TC	153
6.5 Transmission electron microscopy (TEM) characterization	155
6.6 Fluorescence microscopic images	156
6.7 Conclusion.....	158

Chapter 7. Synthesis and Crystal Structure Determination Complexes of Silver, Copper, and Cobalt with Thioether Purines	165
Abstract	165
7.1 Introduction	165
7.2 Experimental	168
7.2.1 Synthesis silver (I):6-methylmercaptapurine riboside	168
7.2.2 Synthesis of copper(II):6-methylmercaptapurine nucleobase $C_{12}H_{12}N_8S_2Cl_4Cu_2$ (2) and $C_{12}H_{12}Cu_2N_8O_2S_2$ (3)	168
7.2.3 Synthesis of cobalt (II): 6-methylmercaptapurine $C_{12}H_{22}N_8S_2O_6Co$ (4)	169
7.3 Results & Dissociation	169
7.3.1 Silver:6-methylmercaptapurine riboside $C_{22}H_{28}AgN_9O_{13}S_2$ (1) (Ag:6-MMPR).....	169
7.3.2 Copper:6-methylmercaptapurine $C_{12}H_{12}N_8S_2Cl_4Cu_2$ (2).....	173
7.3.3 Copper:6-methylmercaptapurine $C_{12}H_{12}Cu_2N_8O_2S_2$ (3)	178
7.3.4 Cobalt:6-methylmercaptapurine $C_{12}H_{22}N_8S_2O_6Co$ (4)	181
7.4 Conclusion.....	186
Chapter 8. Synthesis and Properties of a Au(I): 2-Thiocytosine Complex.....	202
Abstract	202
8.1 Introduction	202
8.2 Experimental	206
8.2.1 Synthesis of Au(I) 2-thiocytosine complex	206
8.3 Results & Discussion.....	206
8.3.1 Proposed structure	206
8.3.2 Fourier transform infrared spectroscopy (FTIR) characterisation.....	207
8.3.3 UV-Vis Absorption spectroscopy.....	208
8.3.4 Fluorescence spectroscopy of Au:2-TC	209
8.3.5 Elemental analysis (C.H.N).....	210
8.3.6 Mass spectra	210
8.3.7 1H and ^{13}C NMR of Au(I):2-TC complex	211
8.3.8 Powder X-ray diffraction (XRD) of Au:2-TC.....	214
8.3.9 Conductivity of Au(I):2-thiocytosine	215
8.3.10 Morphology of solid Au(I):2-TC.....	216
8.4 Conclusion.....	218
Chapter 9. Conclusion.....	223
9.1 Silver 6-mercaptapurine riboside (Ag:6-MPR).....	223
9.1.1 Experimental	223
9.1.2 Results &Dissociation	223
9.2 Conclusions	228

Chapter 1. Introduction

1.1 Nucleic acids and metal ions

Nucleic acids are interesting compounds for metal ion coordination polymers because they possess many metal-ion binding sites, *e.g.* the nitrogen atoms¹⁻⁶ of the nucleobases and the oxygen atoms of the phosphate groups.⁷⁻¹⁰ Hud¹¹ referred to DNA as an ionophore where the monovalent and divalent cations are coordinated in specific sequences at the grooves of the DNA. He explained how the width of this groove and the order of the electronegative groups on the nitrogen bases are rationalized with the binding sites that are preferred by the cations. Metal ion coordination to nucleic acids plays a vital role in biochemistry¹², and DNA binding drugs based on platinum are well known anticancer treatments.¹³

Alkali metal ions can be found- in the intracellular space bound to both RNA and DNA. K^+ has the highest concentration but other counter cations include Mg^+ , Na^+ , and Ca^+ are less concentration. Other metal ions such as Cu, Zn, Fe are present as trace elements. Increasing the concentration of these elements over the normal level is related to some known diseases, *e.g.* Fe in hematochromatosis and Cu in Wilson disease's patients.¹¹

There are two types of interactions between metal ions and nucleic acid: first, the non-covalent which involves mainly electrostatic interactions. The second type is coordinate bonding (inner-sphere) which is a direct interaction between the metal ions and the donor binding site in the ligand.¹¹ These two types of coordination are sometimes distinguished as first (outer) and second (inner) sphere coordination.

Nucleobases are classified into purine and pyrimidines. The purines include adenine and guanine and are characterised by a higher heteroatom number which makes them good bridging ligands.¹⁴ In addition, N1 and N7 are the preferred binding sites in adenine along with O6 in guanine.¹⁵ Pyrimidines involve cytosine, uracil, and thymine and the favored binding site with metal ions is N3. The exocyclic amino group in nucleobases is not usually a good binding site because of delocalization of the lone pair of electrons at N in the aromatic ring.¹⁶ Fig.1.1 displays the common binding sites in the nucleobases in natural and preferred tautomeric structures.

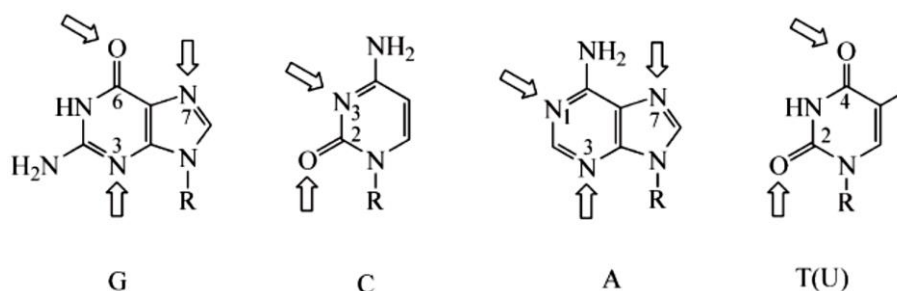


Figure 1.1. Common binding sites with metal ions in nucleobases guanine (G), cytosine (C), adenine (A), and thymine (T).¹¹

The complementary nucleobases pair via hydrogen bonding and dimers in DNA (A-T, G-C). They may also assemble into chains based on intermolecular hydrogen bonding interactions¹⁷ to give networks with the common Watson-Crick pairing and the Hoogsteen pairing, as shown in Fig. 1.2.

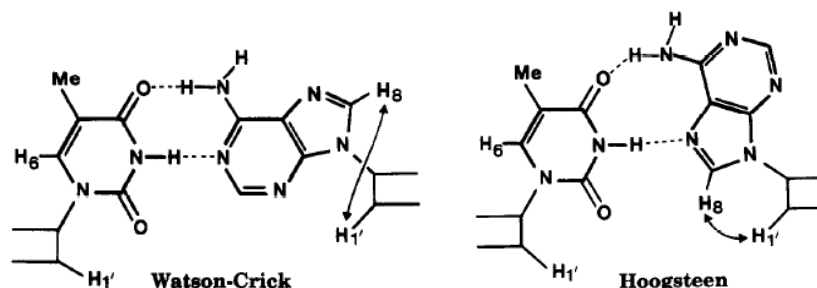
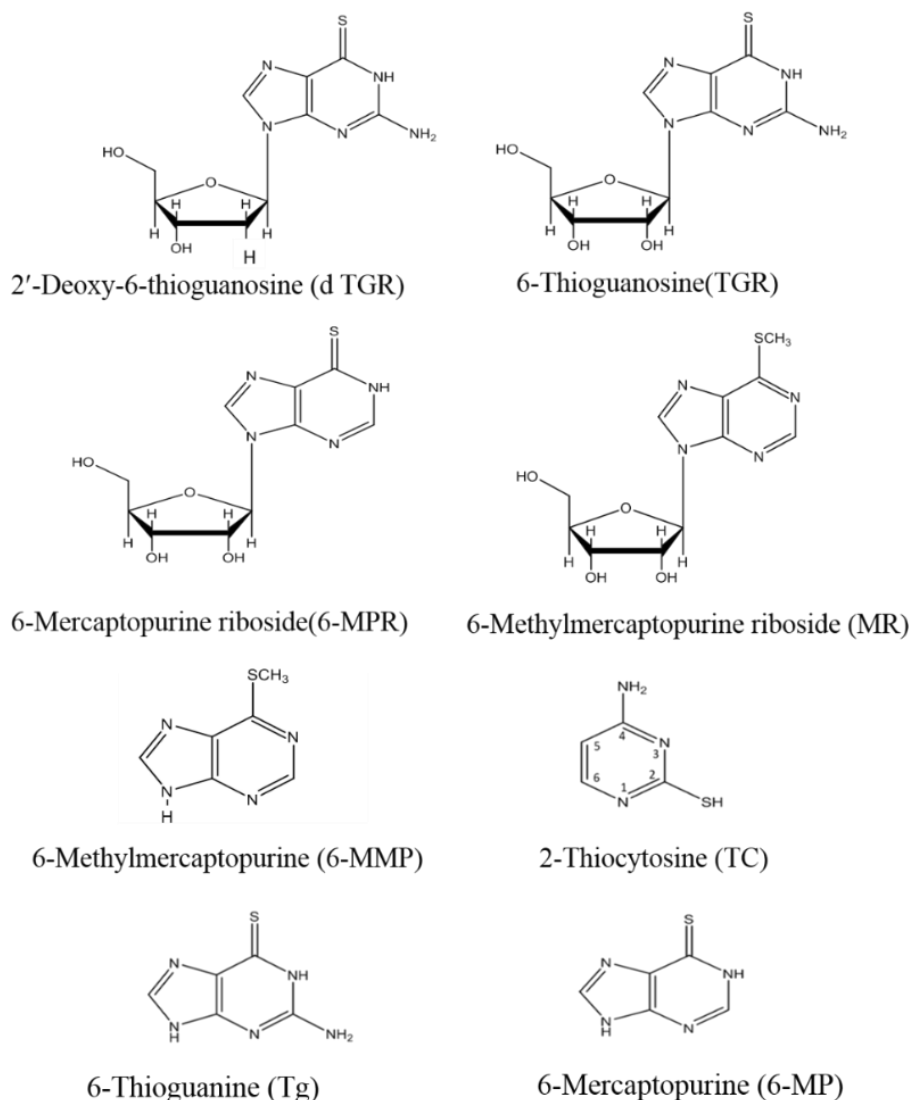


Figure 1.2. Shows adenine and thymine base pairs in Watson-Crick (left) and Hoogsteen pairing.¹⁸

The presence of additional binding sites in the nucleobases gives them a high tendency to self-assemble and form large structures such as fibres or ribbons.¹⁹ Nucleosides and deoxynucleosides have been demonstrated to combine with several metal ions to form gels from an aqueous medium, i.e., hydrogels.²⁰⁻²² Guanosine derivatives²³ are known to form hydrogels in the presence of alkali metal ions such as K^+ . Jean- Marie Lehn,²⁴ who had won Nobel prize in 1987 in supramolecular chemistry, demonstrated that in the presence of metal ions such as K^+ , Na^+ , and NH_4^+ , guanosine hydrazide forms stable gels. The natural nucleobases are O and N-donor atom ligands; in this thesis the interaction of metal ions with various thiolated nucleobases, which are expected to prefer softer metals (Au, Ag, Cu, *etc*) are investigated.

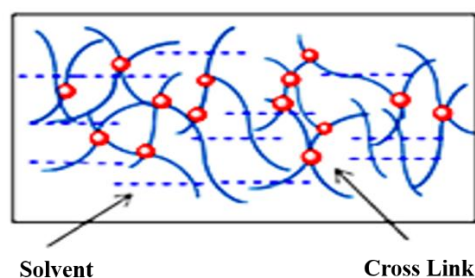
Scheme 1.1 presents the thio- nucleobases and thio -nucleosides that were used in this thesis.



Scheme1.1. Illustrates thio nucleobases and thio nucleosides that used in this work.

1.2 Gel: definition and classification

A gel has a crosslinked network in which there is a liquid phase, which is dominant in terms of volume, but the system which does not flow like liquid. Such a three-dimensional (3D) network may be formed by cross-linking polymer chains with either covalent or non-covalent bonds (*e.g.*, H-bonds), Scheme 1.2. In the absence of these cross-links the interactions of entangled polymer chains required to form an extended network does not occur and the sample rheology and viscosity are not that of a true gel. In particular, the sample will not retain its shape under an applied force. A gel is characterised as weak, non-covalent and reversible when it has physical cross-links, while strong, covalent, and irreversible properties can be found for chemically cross-linked gels.²⁵



Scheme. 1.2. Shows a gel with a network in three dimensions where the polymer chains (blue) are connected by cross links (red).

According to the solvent that is used to prepare the gel, a gel can be classified as hydrogel when the solvent is water and organogel when the solvent is an organic solvent. Another classification can be used depending on the state of the gel; drying the gel slowly at room temperature leads to a material called a xerogel.²⁶ These are characterized with high surface area ($150\text{-}900\text{ m}^2/\text{g}$), high porosity (25%), typical pore sizes in range 1-10 nm and have found applications in electronics.²⁷ A second kind is the aerogel, which is produced by drying the gel under supercritical conditions and this process leads to replace the liquid content by gas and in consequently a very low density solid is formed.²⁸

Gelation, the term that refers to the process of gel formation, occurs via physical or chemical cross linking.²⁸ The classic test for gel-formation is to invert the test tube, in that the gel is stable towards gravitational force when it is put upside down.

In general, the hydrophilic surface of a hydrogel makes it biocompatible with body fluids and proteins due to the low surface energy in such media, which reduces the tendency of macromolecules to adsorb.²⁸ Furthermore, because hydrogels are soft, they may cause less irritation. The high quantity of water (up to 99 %)²⁹ in their composition is similar to living tissue for these reasons hydrogels find numerous applications in the fields of pharmaceuticals and medical devices^{30,31} for example as lenses, artificial skin and heart, biosensor membranes, and devices for drug delivery. Steed³² used anion supramolecular gels as a new tool for controlling organic pharmaceutical crystal growth; bis (urea) with a variety of end groups were used as a crystallisation media. Gels can be obtained from various materials such as fatty acid, amino acid,³³⁻³⁵ steroids,³⁶ metal complexes,³⁷⁻³⁹ saccharides,⁴⁰⁻⁴³ and amides,⁴⁴⁻⁴⁷ in addition to bis (urea).⁴⁸⁻⁵⁶

1.3 Coordination polymers

The definition of coordination compound according to the IUPAC is a compound that has a coordinating entity, which can be defined as a metal ion or inorganic cluster to which is bound surrounding groups of atoms that form a ligand.⁵⁷

Coordination polymers (CPs) are hybrid compounds that are based on the reaction between metal ions and inorganic or organic compounds that connect by linkers to form structures of one, two, and three dimensions. This class of materials have attracted great attention due to the broad range of properties that found in these materials which make possible numerous applications e.g luminescence, electrical conductivity, porosity, and magnetism.⁵⁸

Building the blocks of coordination polymer by using the metal, which typically acts as a node, and the ligands, which are linkers, can be followed by self-assembly of these blocks to form different architectures of one, two, and three dimensions. The way that the components are joined with each other defines the architectures.⁵⁹ Fig. 1.3, 1.4, and 1.5 presents structural motifs of 1D, 2D, and 3D coordination polymers.⁶⁰

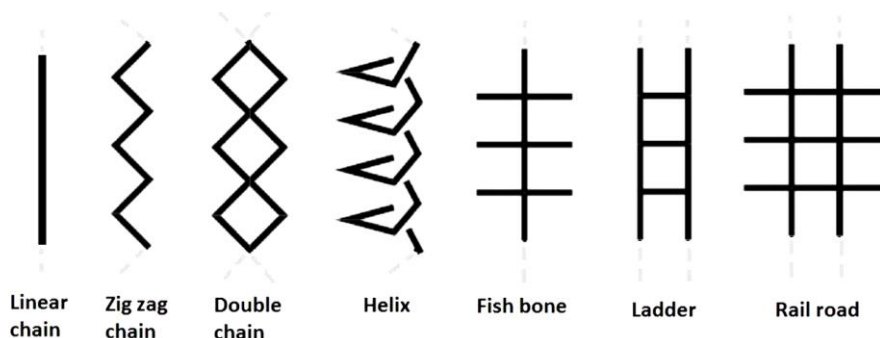


Figure 1.3. One-dimension coordination polymers.⁶⁰

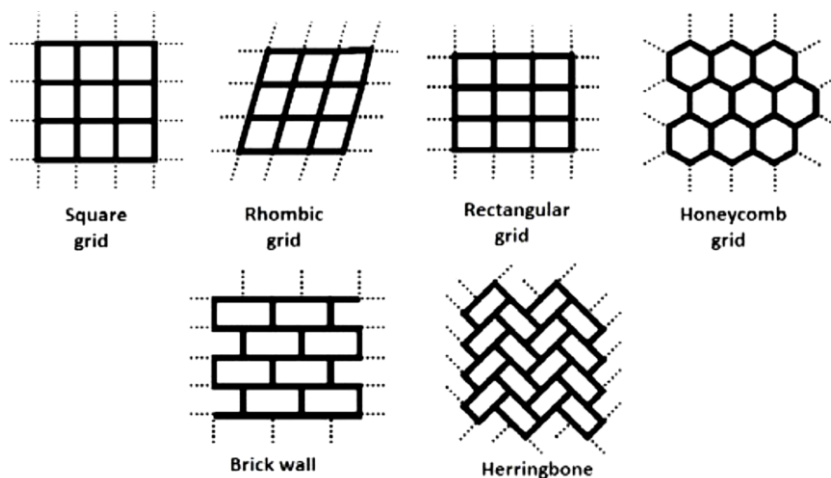


Figure 1.4. Two-dimension coordination polymers.⁶⁰

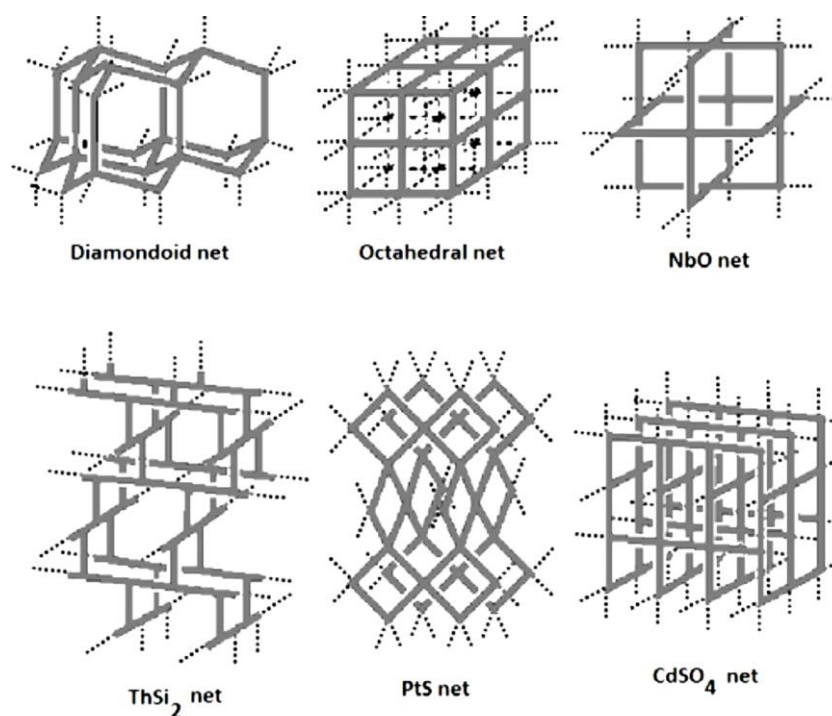
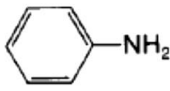
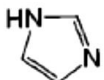


Figure 1.5. Three-dimension coordination polymers.⁶⁰

Metal ions usually bind to donor ligands with regard to the concept of hard-soft acids and bases. The term soft refers species which are large and polarizable, while hard refers to small species which are less polarizable.⁶¹ Metal ions are classified as Lewis acids, and the ligands as Lewis bases, and metal ions such as Au(I), Ag(I), Cu(I) can be classified as soft acids, while Co(III), Cr(III), Al(III), and Na(I) are hard acids. Some of them are classified as borderline, *e.g.* Cu(II), Co(II), Zn(II), and Fe(II). Table 1.1 shows some metal ions and ligands classified according to hard-soft acid-base theory.⁶¹ In general, soft acids prefer to combine with soft bases and hard acids with hard bases.

Table 1.1 Classification of metal ions and ligands according to hard-soft acid-base theory⁶¹.

Metals			Ligands		
Hard					
H ⁺	Mn ²⁺	Cr ³⁺	H ₂ O	CO ₃ ²⁻	NH ₃
Na ⁺	Al ³⁺	Co ³⁺	OH ⁻	NO ₃ ⁻	RNH ₂
K ⁺	Ga ³⁺	Fe ³⁺	CH ₃ CO ₂ ⁻	ROH	N ₂ H ₄
Mg ²⁺	Ca ²⁺	Tl ³⁺	PO ₄ ³⁻	R ₂ O	RO ⁻
			ROPO ₃ ²⁻	(RO) ₂ PO ₂ ⁻	Cl ⁻
Borderline					
Fe ²⁺	Ni ²⁺	Zn ²⁺	NO ₂ ⁻		
Co ²⁺	Cu ²⁺		N ₂		
			SO ₃ ²⁻		
			Br ⁻		
			N ₃ ⁻		
Soft					
Cu ⁺	Pt ²⁺	Pt ⁴⁺	R ₂ S	R ₃ P	
Au ⁺	Tl ⁺	Hg ²⁺	RS ⁻	CN ⁻	
Cd ²⁺	Pb ²⁺		RSH	RNC	
			(RS) ₂ PO ₂ ⁻	(RO) ₂ P(O)S ⁻	
			SCN ⁻	CO	
			H ⁻	R ⁻	

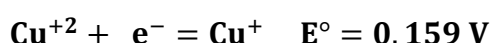
Coordination polymers that contain transition metal ions are attracting attention because they display various properties related to their geometry, and electronic functionality; which can make them useful as a means to introduce magnetism and redox properties into the final material.⁶² Different types of coordination geometries that may be seen with transition metals include linear, square planar, tetragonal, octahedral, *etc.*

Coordination polymers complexes are typically, insoluble, a few are soluble, and in some cases their solubility can cause decomposition, this feature can be exploited in nanotechnology.⁵⁹ These new applications are based upon organizing the CP on surfaces such as mica and graphite as materials for applications in nanoelectronics, nanosensing, and spintronics.⁶³ In the case of nanowires sonication of a suspension coordination polymers leads to cleavage the non-covalent bonds between single chains such as van der Waals and hydrogen bonds and the release of single CP chains which may be adsorbed on a smooth surface for study by probe microscopy. This strategy allows experimenters to obtain 1D CPs with controlled length such as the highly conductive wire of length 40 nm that was obtained from terpyridine and the metal ions, Co(II) & Fe(II).⁶⁴

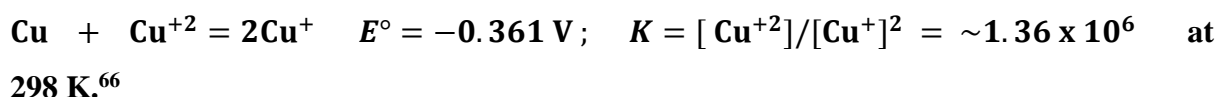
Using biomolecules as ligands can lead to the formation of a coordination polymer (CP) which has features that are compatible with the original ligand. Such ligands have multiple binding sites and that can increase the diversity of structures formed. The coordination of the metal ions is also affected by different conditions such as the oxidation state of the metal ion, the pH of the reaction, the mole ratio, etc. Nucleobases are ideal biomolecules to form different CPs with metal ions as they have different binding sites with lone pairs on atoms such as N, O, and S, and they have a hydrogen bonding system that helps to facilitate self-assembly of CPs. However, such spaces often do not form crystals and most of these compounds form amorphous material or particles.

1.4 Chemistry of copper

Copper ion exist in two common oxidation states Cu(I) and Cu(II). Cu(I) has the electronic configuration $3d^{10}$, and Cu(I) compounds are diamagnetic; the colour of these compounds is produced from charge transfer transitions or the anion. Cu(II) has the electronic configuration $3d^9$; the configuration d^9 makes Cu(II) complexes of both common geometries, octahedral and tetrahedral, subject to Jahn-Teller effect, and the compounds with this state are paramagnetic and blue in colour. In general, the blue or green colour of copper (II) complexes is produced by the absorption at 600-900 nm and this can be attributed to the $d-d$ transitions or ligand to metal transition. The reduction potential is used to indicate the stability of the two states⁶⁵ as the higher positive potential indicates a higher tendency for the complex to be reduced:



And

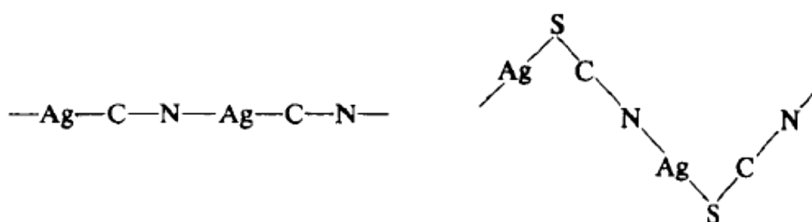


Where K is the equilibrium constant. In aqueous solutions, the stability of Cu(I) and Cu(II) compounds depend on different factors such as the anion, solvent, and other atoms in the crystal.⁶⁵ The only stable Cu(I) compounds in water are the simple compounds, for example CuCl and CuCN. The reason for the instability of Cu(I) complexes in water can be assigned to the solvation energies and the higher formation constants for complexes of Cu(II).⁶⁵ Cu(I) d^{10} has coordination number from 2 to 5 including linear, planar, tetrahedral, distorted planar, and

square planar geometries. Cu(II) adopts square planar, tetrahedral, octahedral, pentagonal, and disturbed octahedral geometries. In contrast to Cu(I), most Cu(II) salts are water soluble. The magnetic moment of Cu(II) complexes is in range of 1.75-2.2 BM.⁶⁵

1.5 Chemistry of silver

Silver possesses the highest electrical and thermal conductivity among all metals.⁶⁵ It has electronic configuration $4d^{10} 5s^1$. Ag(I), $4d^{10}$, is the most common oxidation state. In general, silver(I) d^{10} adopts coordination number in range of 2-6 involving linear, trigonal, tetrahedral and square planar, dist. pentagonal & pentagonal pyramidal, and octahedral geometries. The most common coordination geometry is linear as shown in Scheme 1.3. This can be assigned to the filled $4d^{10}$ and unfilled $5s$ which allows hybridization of the dz^2 and s orbitals. Silver complexes with linear geometry are normally formed with monodentate ligands, however, chelating ligands lead to polynuclear complexes. The coordination number depends on the type of the ligand and the anion and according to that, different kinds of structures are able to form as consequence of the ligand bonding and geometry. Many ligands which have donor atoms such as S, N, P, As, Se, *etc*, can form complexes with silver.



Scheme 1.3. Shows linear coordination for Ag(I) complexes.

Silver with oxidation state (II) d^9 , was formed with fluoride AgF_2 as a dark brown solid; other complexes with this state such as $[\text{Agpy}_4]^{+2}$, $[\text{Ag}(\text{dipy})_2]^{+2}$, and $[\text{Ag}(\text{phen})_2]^{+2}$ were also synthesized. Ag_2O_3 as black oxide was prepared for silver d^8 with oxidation state (III) but it was not purified compared to Ag_2O .⁶⁵ However, Ag(II) is a powerful oxidant and relatively unusual oxidation state.

1.6 Chemistry of gold

Gold has two common oxidation states (III) and (I), while the state (V) was found only with fluoro gold complexes. The coordination geometry for gold complexes with oxidation state (I) are linear, trigonal, and tetrahedral, and quadratic planar with oxidation state (III), while octahedral is the typical geometry for gold (V).^{65,67} No species were found for both bare Au(I)

and Au(III) in water because in aqueous solution both aurous and auric cations will be reduced to the metal by water.⁶⁸ The electronic configuration for Au(I) is $5d^{10}6s^06p^0$ and for Au(III) is $5d^86s^06p^0$. The closed shell $5d^{10}$ is not inert and can react with many elements. As a metal gold has high electric conductivity, thermal stability, and softness.⁶⁹ Gold (I) complexes are normally linearly coordinated and can be found as mononuclear complexes with forms $[\text{AuXL}]$, $[\text{AuL}_2]^+$ and $[\text{AuX}_2]^-$. In the solid state, these complexes are characterized with short intermolecular Au...Au distances. Au (I) complexes can be found with polydentate ligands such as diphosphines which form highly stable complexes with Au(I)⁶⁹. Au(III) complexes can be found with ligands that have, C, N, P, S, and O donor atoms.⁶⁹

Among the three metals of group 11 that involve Au, Ag, and Cu (coinage metal), silver seems to be the normal metal compare to Au and Cu, as Au has strong aurophilic interactions due to the relativistic effect, while Cu has abnormal features owing to the tight d shell orbital and the strong electron-electron repulsion that leads to the formation of Cu(II) and is responsible for the brown color of copper.⁷⁰ The massive Stokes shift of the luminescence in copper complexes can be assigned to the distorted excited state.⁷¹ Fig. 1.6 displays the main difference in the orbital energy between gold and silver which can be assigned to the relativistic effect.⁷²

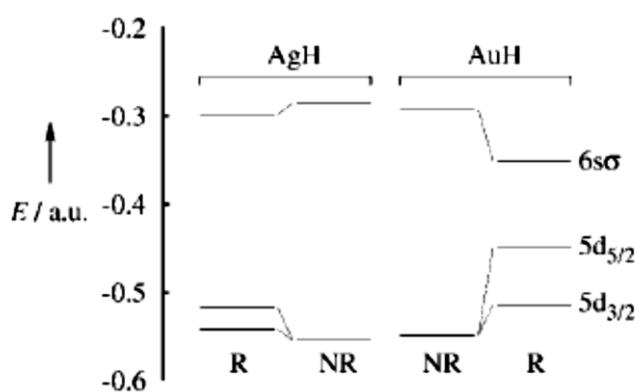


Figure 1.6. Comparison relativistic (R) and nonrelativistic (NR) energies in AgH and AuH showing the difference of orbital energy that is attributed to the relativistic effect.⁷²

For gold oligomer complexes, the Au-Au bonding is stronger in the first excited state and weaker in ground state and that can be assigned to the electronic configuration of closed shell ($5d^{10}$) in the ground state, compared to the excited state which has electronic configuration ($5d^96s^1$). Merging $6s$ and $6p$ with $5d$ orbitals, as a result of strong gold relativistic effects, can strengthen aurophilic bonding in the ground state.⁷³ Comparison between the complexes of Au and Ag (which do not have relativistic effects) found that the Au-Au bond is weaker in the first

excited state and stronger in the ground state as a consequence of relativistic effects which helps to merge $6s$, $6p$, and $5d$ orbitals rather than Ag-Ag bond and this can rationalise the large Stokes shift of the luminescence of gold complexes.

1.7 Gold (I) complexes in medicine

Among coinage metal ions, gold possesses special interest in pharmaceutical applications since ancient eras, because it was used by Arabic and Chinese people since 2500 BC to treat different diseases. More recently, it was used for rheumatoid arthritis treatment since 1930.⁷⁴ Complexes of Au(I) have a linear geometry while Au(III) complexes are often square planar. The linear arrangements of P-Au-S and Au-S-Au-S- systems showed significant bioactivity. Fig. 1.7 displays some of these compounds that are used for rheumatoid arthritis treatment such as myocrisin, auranofin, sanocrysin, solganol, and allocrysin.⁷⁵

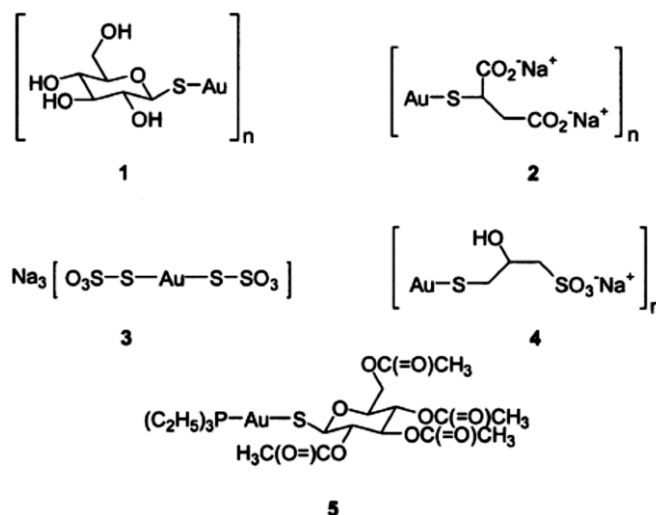


Figure 1.7. Chemical structures for some of gold thiolate compounds that are used for rheumatoid arthritis treatment:⁷⁵ 1) aurothioglucose (solganol), 2) aurothiomalate (myocrisin), 3) sanocrysin, 4) allocrysin, 5) and auranofin.

1.8 Silver(I) complexes in medicine

Silver has many applications; it has a long history of use as an antibiotic, for the purification of water, as an antiseptic in surgery, in wound treatment, and recently it found applications in bone prostheses and reconstructive orthopaedic surgery.⁷⁶ Silver sulfadiazine⁷⁷⁻⁷⁹ which is sold as a medicinal product under brands Silvadene and Flamazine, is the most common pharmaceutical product containing silver; it contains 1% silver, and is used for burns treatment in which it acts to prevent bacterial infection. Fig. 1.8 presents the chemical structure of silver sulfadiazine.

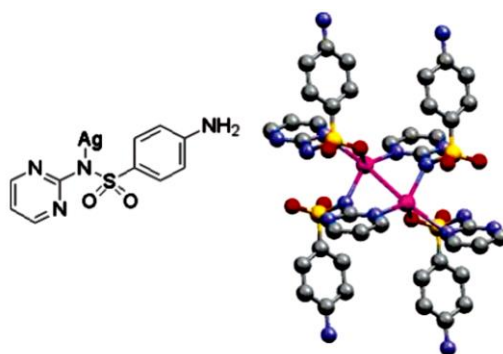


Figure 1.8. Silver sulfadiazine structure (left) and polymeric structure (right).⁷⁸

Other examples of bioactive silver (I) complexes include N-heterocyclic carbene complexes⁸⁰ which exhibit potential as antimicrobial agents. Fig. 1.9 displays the chemical structure of these complexes.

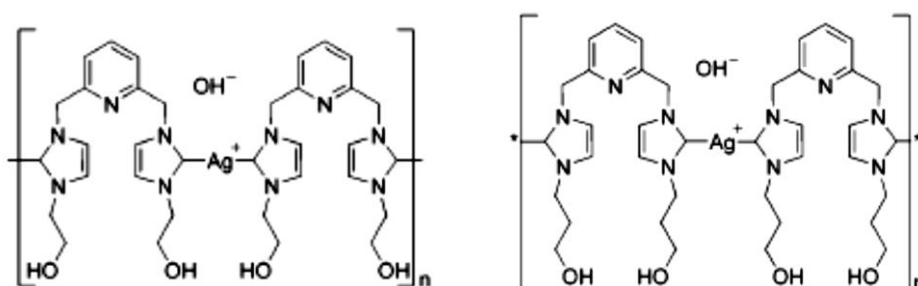


Figure 1.9. Silver(I)-2,6-bis(ethanolimidazolemethyl)pyridine hydroxide (left) and silver(I)-2,6-bis(propanolimidazolemethyl) pyridine hydroxide (right).⁸⁰

1.9 Copper (I) complexes in medicine

Copper plays important role in some non-enzymatic process in biological systems, such as angiogenesis and nerve myelination,⁸¹ and in oxidative enzymes; electron transfer is the common biochemical function of copper ions, in addition to energy capture.⁸² The best known diseases that related to disorders of copper homeostasis are Wilson's disease (autosomal recessive) and Menke's disease (inherited disorder). Wilson's disease involves an increase in the level of free copper and Menke's disease is related to copper deficiency.⁸³⁻⁸⁵ The interest in copper complexes has increased recently due to the potential of these complexes as antimicrobial, antiviral, anti-inflammatory, antitumor agents, *etc.*⁸⁵ Numerous Cu complexes were revealed to have potential of bioactivity.^{84,86-92} Some Cu complexes exhibit antibacterial activity such as the complex of Schiff bases derived from thio-benzoyldithiocarbamate and salicylaldehyde.⁹³ The Cu(II) complex of salicylaldehyde benzoylhydrazone (H₂sb) showed a dramatic increase in bioactivity compared to the bioactivity of the ligand. The Cu(II) complex

of salicylaldehyde acetylhydrazone (H₂as) also showed similar function.⁹⁴ Numerous Cu complexes were revealed to have potential of bioactivity.^{84,86-92}

1.10 Nucleobase and nucleoside hydrogels with and without coinage metal ions

The formation of gels has been widely reported, therefore this section will concentrate on metallogels. The incorporation of metals allows modification of the physical properties⁹⁵ of the gel such as optical, magnetic, and catalytic properties.⁹⁶⁻⁹⁸ On the other hand, the potential of using thio nucleobases in pharmaceutical application leads to more interest in these complexes.^{99,100} However the field of coinage metal/thionucleobase gels is relatively unexplored. There are a few examples of synthesis of some crystalline compounds, such as the derivative of gold ferrocenyl amide phosphine thiolate¹⁰¹ and amino phosphine gold(I) thiolate.¹⁰² Mann¹⁰³ synthesised a silver guanosine hydrogel and he assumed that the polymer is a dimer of two molecules of guanosine mono phosphate and Ag(I) ion was binding via O6 of one of the molecular and N7 of the other molecular, Fig. 1.10.

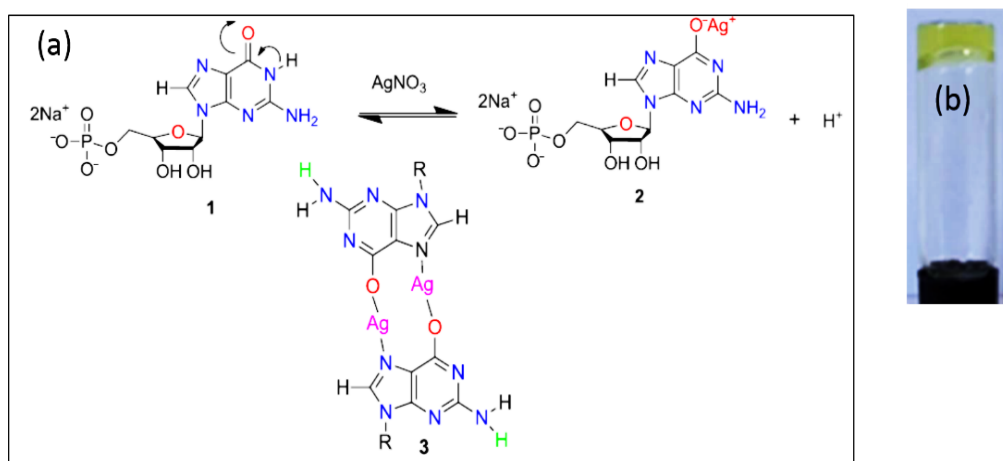


Figure 1.10. (a): The scheme of adding Ag(I) into GMP (1), (2) deprotonation of N1, and (3) dimer formation of Ag: GMP via N7 and O6. (b): Photograph of Ag: GMP hydrogel.¹⁰³

A coordination polymer of Ag(I) and guanine was prepared by Loo;¹⁰⁴ an increase in circular dichroism upon addition of Ag(I) to the guanine was observed and the author suggested that Ag(I) forms a dimer with guanine via N7 and O6, Fig.1.11.

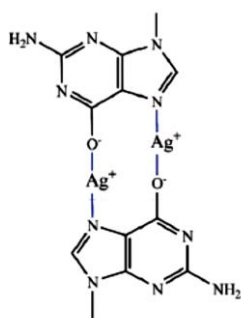


Figure 1.11. Dimer structure of Ag: guanine via N7 and O6.¹⁰⁴

The same complex of silver guanosine was synthesised by Matsuoka¹⁰⁵ and Orioli.¹⁰⁶ The former suggested that Ag(I) formed a dimer by replacing the enolic proton Ag(I) and also coordinated to N7 of another guanosine molecule, but the latter suggested that Ag(I) formed a chelate ring with the guanosine via N7 and O6. Studies of a series of monovalent cations including Ag(I), Au(I), Rb(I), K(I), Na(I), and Tl(I) ion on their ability to induce deoxy guanosine (dGs) and guanosine (Gs) purine to form hydrogel were performed by Adhikari,²⁰ Fig. 1.12.

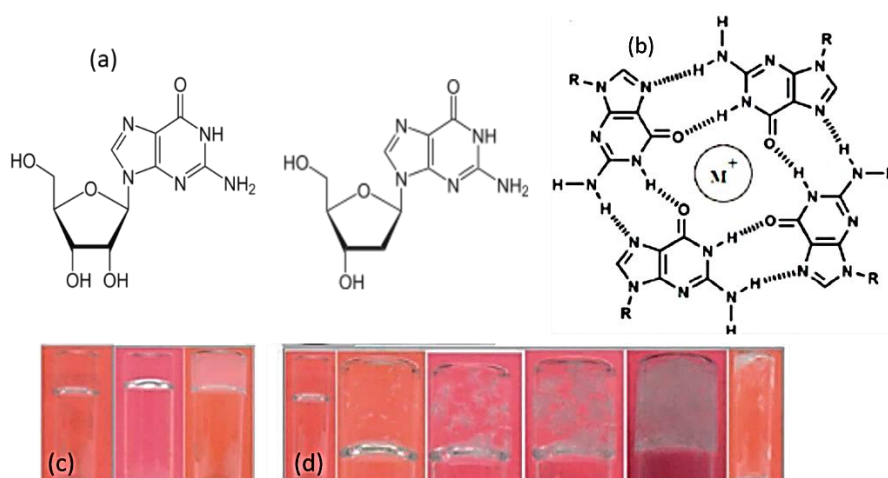


Figure 1.12. (a) Chemical structure of guanosine and deoxy guanosine, (b) G –quartet formation with metal ions, (c) Photo of hydrogels of Rb⁺, Ag⁺, and Tl⁺ with G from right to left respectively. (d) Photo of K⁺: G hydrogel display formation of crystal/ decomposition the gel from left to right with increasing time over several hours.²⁰

Coordination hydrogels of Ag(I) ion with adenine, thymine, cytosine, uracil, and guanine were synthesised recently by Sharma.¹⁰⁷ Single crystals of all the compounds were not obtained and it was assumed that the binding sites for coordinating Ag(I) with adenine, cytosine, uracil, and

thymine were via N9, N1, N3, and N3 ,respectively, while with guanine the binding site was via N7 and O6, Fig. 1.13 displays micrographs of the networks obtained.

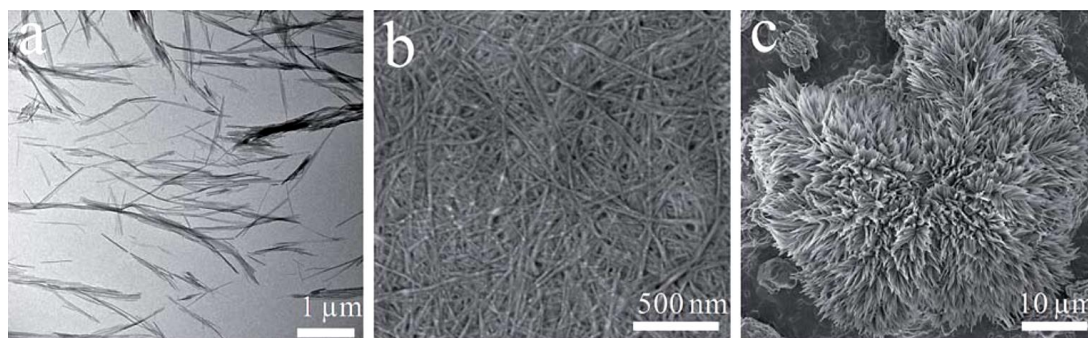


Figure 1.13. TEM (a) and SEM (b) images of Ag(I): adenine hydrogel, (c) SEM image of Ag(I): guanine precipitate that was prepared in basic medium.¹⁰⁷

The hydro-gels of guanosine derivatives were prepared by using binding modes via the sugar group, C8, and phosphate group. Peter¹⁰⁸ prepared a guanosine borate monoester hydrogel in the presence of $\text{KB}(\text{OH})_4$ and KOH , Fig. 1.14, it was found that using $\text{KB}(\text{OH})_4$ is more effective than $\text{LiB}(\text{OH})_4$ and this was assigned to the more effective stabilising role of K^+ than Li^+ in the formation of G-quartets.^{109,110}

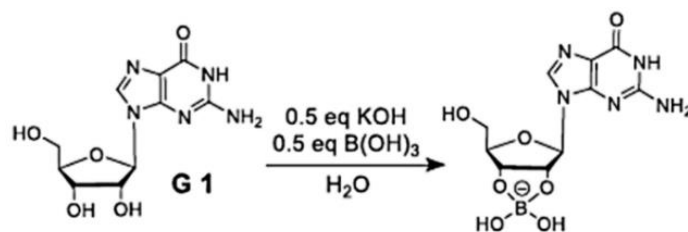


Figure 1.14. Synthesis of a guanosine borate monoester hydrogel in the presence of $\text{KB}(\text{OH})_4$ and KOH .¹⁰⁸

Using guanosine (G) and bromoguanosine (BrG), Das¹¹¹ prepared hydrogels by heating a mixture of G and BrG in the presence of K^+ to 100 °C. The gel was easily formed upon cooling the hot solution, Fig. 1.15.

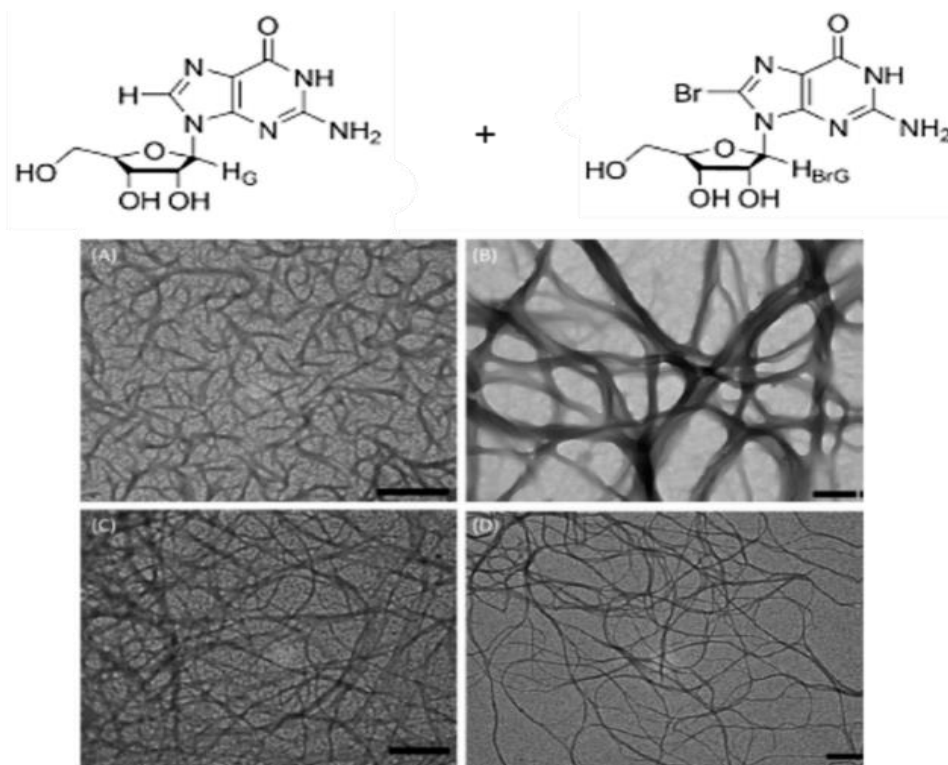


Figure 1.15. TEM images with scale bar 200 nm of: A) guanosine (G), B) bromoguanosine (BrG), C) 1:1 G:BrG, 2:1 G:BrG hydrogels.¹¹¹

Kwan¹⁰ observed that disodium 5'-thioguanosine-5'-monophosphate, $\text{Na}_2(5'\text{-GSMP})$ forms a gel in pH 8 (Fig. 1.16) but that disodium guanosine mono-5'-phosphate, $\text{Na}_2(5'\text{-GMP})$ does not. The author attributes the reason to the higher $\text{p}K_{\text{a}2}$ value (6.0) of $\text{Na}_2(5'\text{-GMP})$ compared to the lower value (5.1) for $\text{Na}_2(5'\text{-GSMP})$.

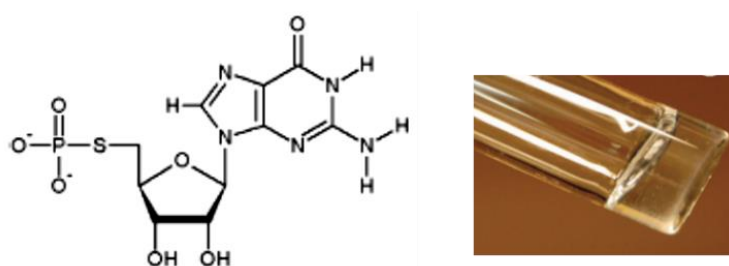


Figure 1.16. Photograph of the gel and the chemical structure of disodium 5'-thioguanosine-5'-monophosphate $\text{Na}_2(5'\text{-GSMP})$ at pH8.¹⁰

A stable gel of guanosine and guanosine (Gs)monophosphate(GMP) was prepared¹¹² at neutral pH, the binary mixture turned from liquid to gel upon heating. The high solubility of GMP at room temperature in water assists to solubilize Gs which is normally insoluble at the same conditions while the insolubility of Gs helps the formation of the gel, Fig. 1.17.



Figure 1.17. Binary mixture of guanosine (Gs) and guanosine monophosphate (GMP) from left to right, liquid, viscous fluid, and gel.¹¹²

A stable supramolecular hydrogel was synthesised based on the formation of G-quartets of a guanosine hydrazide derivative²⁴ in the presence of K^+ , Na^+ , and NH_4^+ , Fig. 1.18. The reaction of different aldehydes with hydrazide lead to form hydrogels of acylhydrazone.

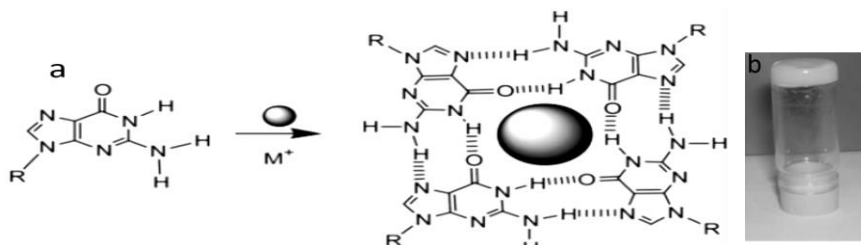


Figure 1.18. (a) Guanine derivatives self-assemble to G-quartets in the presence of metal ions. (b) photo image of the gel.²⁴

A stable supramolecular gel¹¹³ at neutral and basic pH was synthesised by coordination of Zn^{+2} with adenosine monophosphate (AMP), Fig. 1.19.

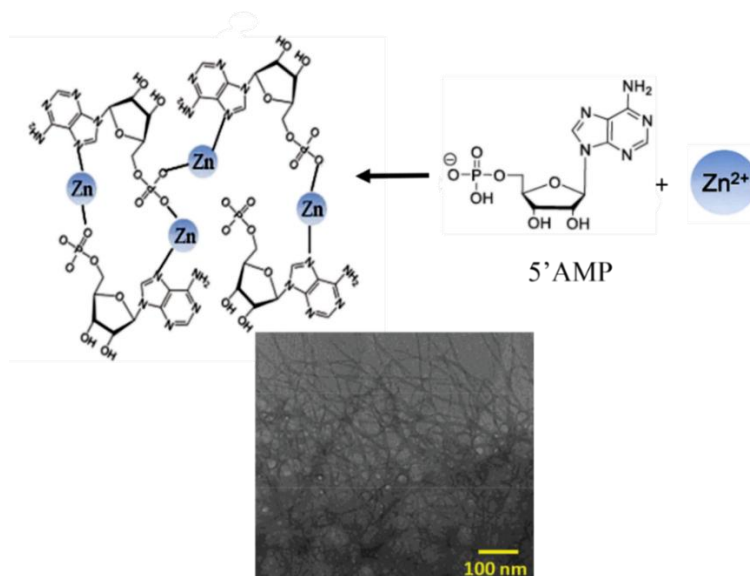


Figure 1.19. Coordination of Zn^{+2} to adenosine monophosphate (AMP) to form stable supramolecular gel at natural and basic pH via N7 and phosphate group.¹¹³ The TEM image shows the fibrous natural of the gel.

Under ultrasonic radiation, a 2'-deoxyadenosine derivative (Fig. 1.20) formed a hydrogel.¹¹⁴ The gelation was reversed by heating. Gelation was suggested to be driven by changes in the hydrophobic-hydrophilic nature of the compound upon oxidation of the 2'-deoxyadenosine derivative to a hydroxylated derivative, Fig.1.20 & Fig. 1.21.

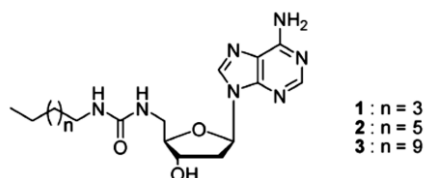


Figure 1.20. 2'-deoxyadenosine derivative with an octyl hydrocarbon tail and a urea linker.

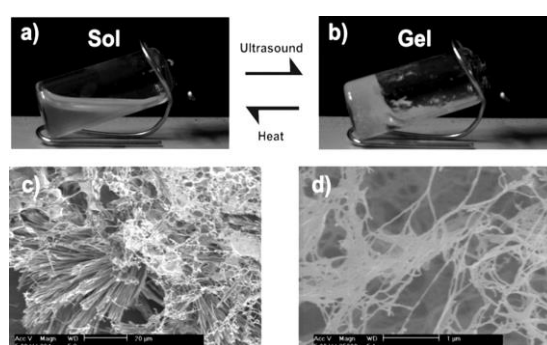


Figure 1.21. (a) & (c) Photo and SEM image of 2'-deoxyadenosine derivative (Fig. 1.20) before sonication, (b) & (d) after sonication.¹¹⁴

A solution mixture of cationic gemini surfactant and uracil monophosphate (2U5'MP) demonstrated gelling behaviour when added to adenosine monophosphate (2A5'MP),¹¹⁵ Fig. 1.22. The addition of guanosine showed formation of a precipitate while addition of cytidine formed a gel as result of forming non-complementary pairs by hydrogen bonding and base stacking.

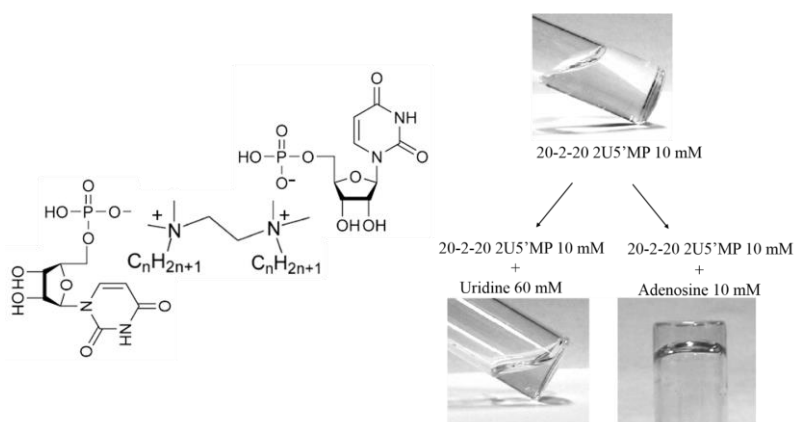


Figure 1.22. Gemini n-2- n - uracil 5'monophosphate (2U5'MP) solution demonstrated gelling behaviour upon addition of adenosine mono phosphate(2A5'MP).¹¹⁵

A superparamagnetic porous hydrogel was formed from 5'-adenosine monophosphate (5'-AMP) and β -iron oxyhydroxide (β -FeOOH) by Kumar.¹¹⁶ The morphology of the hydrogel was affected by the medium, pH, and temperature, Fig. 1.23. Also, the author observed that the morphology of the nanorods was altered to spherical nanoparticles upon addition of 5'-AMP into β -FeOOH and that lead to formation a porous hydrogel.

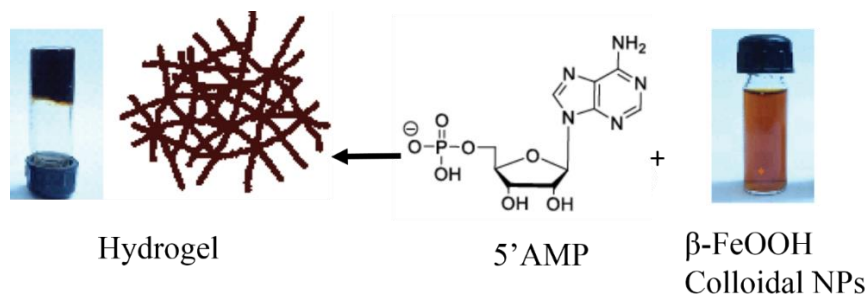


Figure 1.23. Pours superparamagnetic hydrogel of 5'AMP & β -FeOOH.¹¹⁶

No gel has been reported for coordination of gold ions with nucleobases or nucleosides to the best of my knowledge, but some researchers synthesised gold hydrogel with other compounds. The work by Odriozola,¹¹⁷ demonstrated the ability of Au(III) to form a transparent, thermally-stable hydrogel upon reaction with glutathione (GSH) in water. Fig. 1.24 shows the primary structure of the thiolate-gold polymer where the atoms of sulfur and gold are ordered in a 2D plane and the vertically chains of gold with thiol are lying to each side of the plane. The aurophilic interactions of Au-Au were estimated to contributed to the stability of the structure by 21-41.8 kJmol⁻¹. Self –assembly of the 2D sheets leads to the formation of a structure of 3D lamellar or multi bi layers via stacking of R groups.

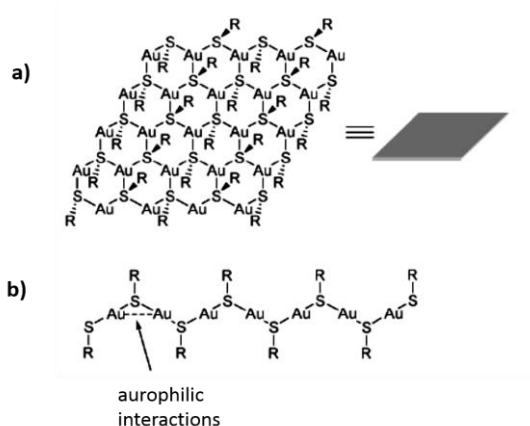


Figure 1.24. Gold (1) thiolate polymer structure, a) shows the 2D structure, b) showing the Au atoms are arranged to each other with a very small distance and stabilized by the effect of aurophilic.¹¹⁷

A few years later, the same researchers prepared a transparent hydrogel from gold (III) with the drug *N*-acetyl-L-cysteine (NAC), Fig. 1.25, using metallophilic attractions as a new system of drug delivery.³³ The gelation occurred via the self-assembly of the Au(I) thiolate polymer.

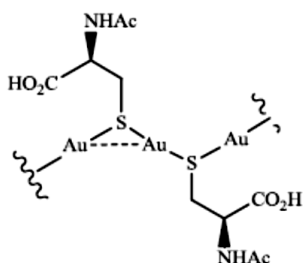


Figure 1.25. Au: *N*-acetyl-L-cysteine (NAC) hydrogel.³³

Recently, a luminescent hydrogel of the phosphine gold(I) alkynyl complex [Au(4-pyridylethynyl)(DAPTA)] was synthesised¹¹⁸ by reaction of 3,7-diacetyl-1,3,7-triaza-5-phosphabicyclo[3.3.1] nonane (DAPTA) with [Au(C≡C-C₅H₄N)_n], Fig.1.26. Aggregation of the complex in water led to formation of very long fibres, Fig. 1.27.

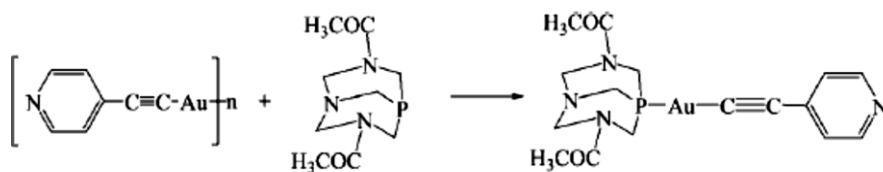


Figure 1.26. Synthesis [Au(C≡C-C₅H₄N)(DAPTA)] hydrogel.¹¹⁸

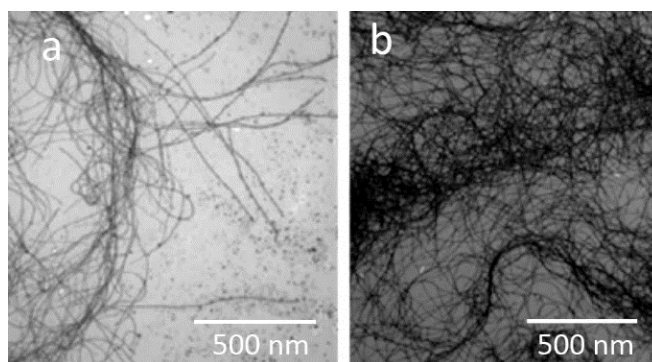


Figure 1.27. Optical microscopic image for [Au(C≡C-C₅H₄N)(DAPTA)] hydro gel fibres, a) after one day, b) after five days.¹¹⁸

Another water soluble luminescent [(PTA)Au(4-pyridylethynyl)] hydrogel was synthesised,¹¹⁹ Fig. 1.28, by reacting [Au(C≡C-C₅H₄N)_n] with phosphine 1,3,5-triaza-7-phosphaadamantane (PTA), Fig. 1.29. The insoluble water complex of analogous derivative with 2-pyridyl was

reported in a previous publication,¹²⁰ it was found that a small modification of the structure can cause a large change in the physical properties *e.g.* solubility in water.

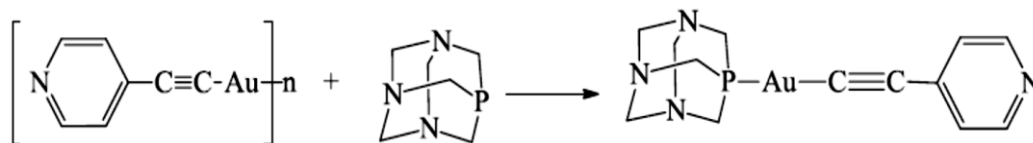


Figure 1.28. Synthesis [(PTA)Au(4-pyridylethynyl)] hydrogel.¹¹⁹

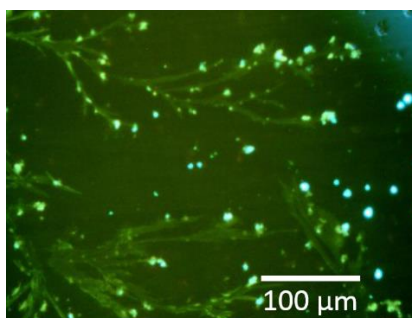


Figure 1.29. Fluorescence microscopy image of a [(PTA)Au(4-pyridylethynyl)] hydrogel.¹¹⁹

Rodriguez and co-workers¹²¹ reported the gelation of a phosphine-gold(I)-alkynyl- coumarin complex, [Au{7-(prop-2-ino-1-yloxy)-1-benzopyran-2-one}- (DAPTA)]. They explained the interesting role of aurophilic interactions in both the crystal structure of the gold complex in the aggregation process of this compound which affects the luminescence features of the gel. The other important impact of aurophilic interactions is on the stabilization of the structure; this was estimated to be in the range 29-50 kJ mol⁻¹, this is comparable to the free energy associated with confirmed with hydrogen bonding, Figs. 1.30 & 1.31 show fluorescence image of the gel and the chemical structure of DAPTA, respectively.

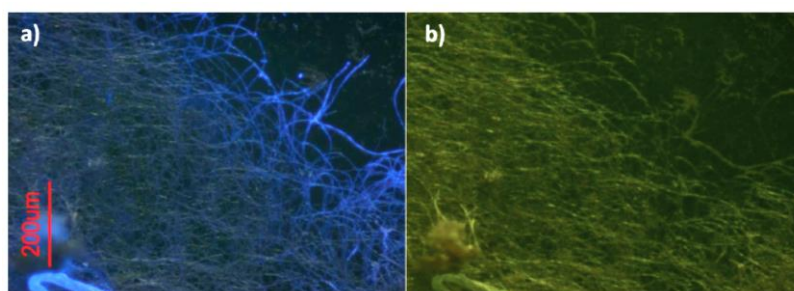


Figure 1.30. Fluorescence microscopy image of a dried solution of 1 mM (DAPTA) hydrogel using filters: 300-400 nm (a), and 450-490 nm (b).¹²¹

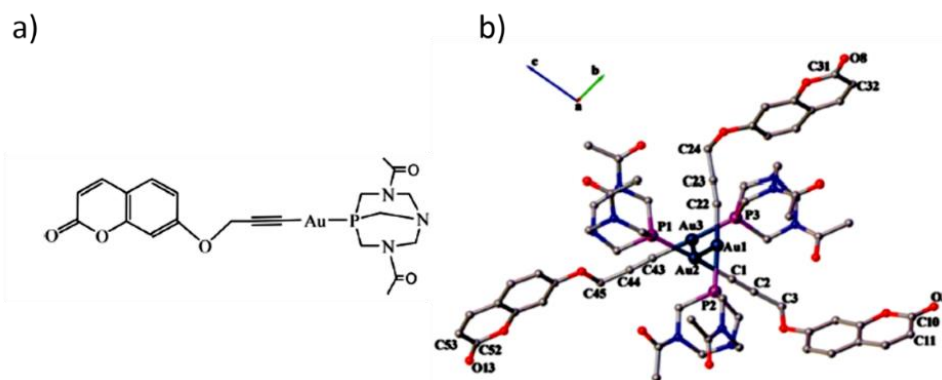


Figure 1.31. Shows the chemical structure (a), and crystal structure (b) of (DAPTA).¹²¹ The a-axis in (b) displays the aurophilic interactions.

Similar to gold, no gel was recorded for copper with any nucleobase or nucleoside before the work in this thesis. Copper metallogels are certainly known, such as the chiral coordination polymer gel of copper (II) that was prepared with L & D-aspartic acid (Asp),¹²² as shown in Fig. 1.32.

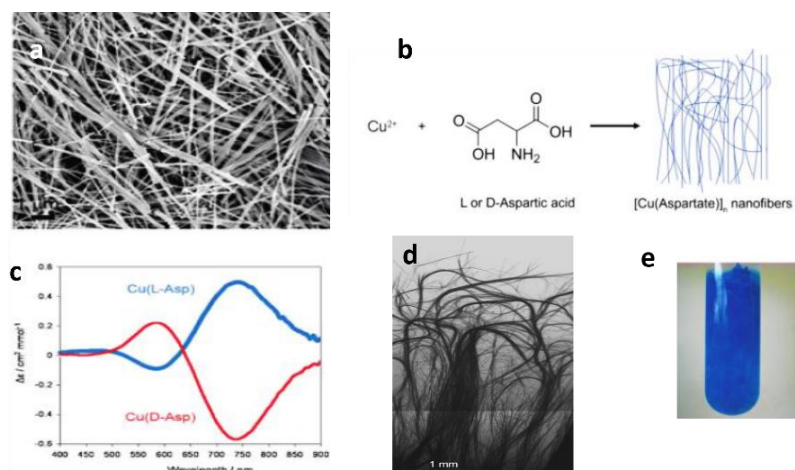


Figure 1.32. (a) SEM image of Cu-Asp nanofibers, (b) illustration Cu-Asp synthesis as nanofibers, (c) CD spectra of Cu-Asp-L (blue) & D(red), (d) optical image of Cu-(D-Asp) fibres, (e) photo image of Cu(II) gel.¹²²

A chiral coordination hydrogel of (D) and (L)-phenylalanine(Phe) with Cu(II) was synthesised by Shen.³⁴ The author found that the gelation formation process was increased upon increasing the percentage of enantiomeric excesses, Fig. 1.33.

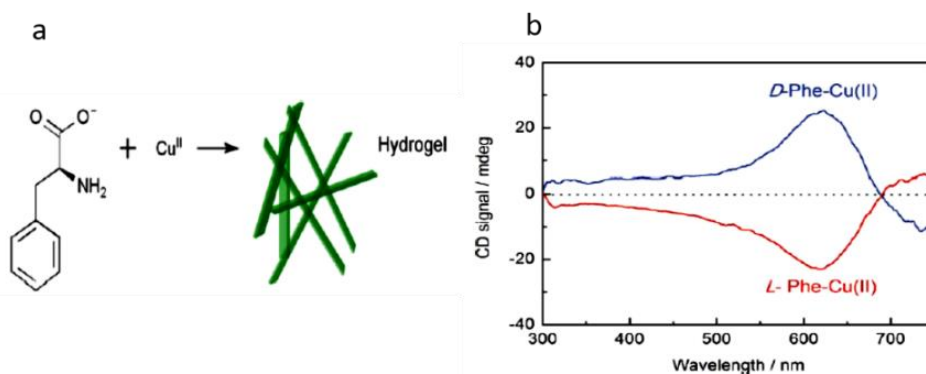


Figure 1.33. (a) Cu(II) phenylalanine(Phe) gel reaction. (b) CD spectra of Cu-(D-Phe, blue line) and (L-Phe, red line).³⁴

A photo-switchable hydrogel of 2′2-bipyridine was synthesised using a pincer-type Cu(II) terpyridine complex by Fang.¹²³ Upon UV irradiation at 320 nm the gel collapsed and reformed again when irradiated under visible light after 15 min, as shown in Fig. 1.34.

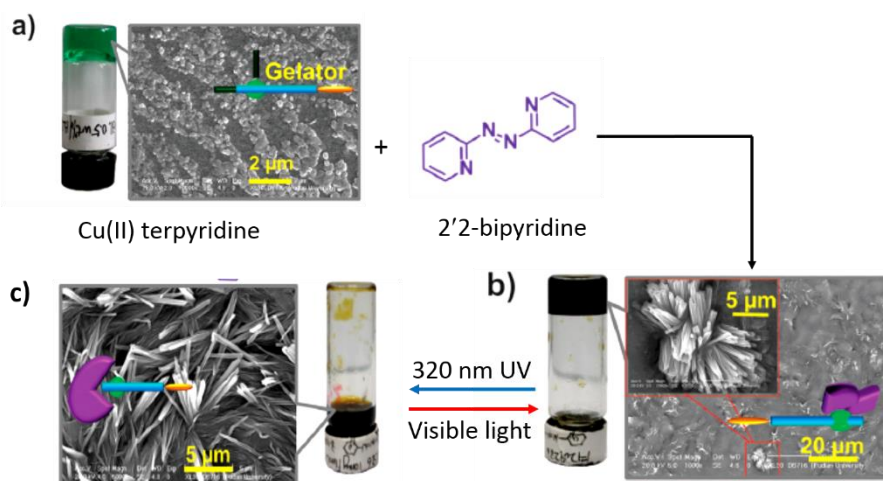


Figure 1.34. Synthesis of a hydrogel consist of 2′2-bipyridine and Cu(II) terpyridine(a) as pincer type. The gel was collapsed when irradiation under UV at 320 nm and reformed again when irradiation to visible light after 15 min.¹²³

A copper metallogel¹²⁴ was synthesised from copper chloride, 4-(1*H*-pyrazol-3-yl)pyridine(Hppy)₂ complex, and triethylamine in dimethylformamide (DMF), the gel revealed the ability to encapsulate an europium cluster to produce a luminescent gel, Fig. 1.35.

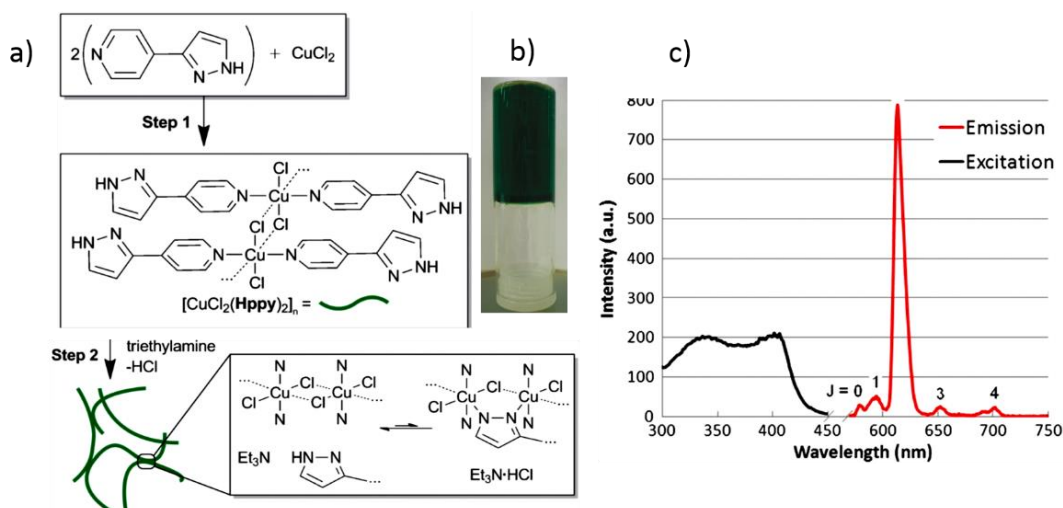


Figure 1.35. Synthesis of $\text{CuCl}_2(\text{Hppy})_2$ metallogel (a), photographic image of the gel (b), and emission spectrum of the xerogel encapsulated europium cluster with an excitation wavelength of 340 nm (c).¹²⁴

1.11 Metal-nucleobase and nucleoside discrete entities

Numerous compounds were reported concerning the formation of metal-nucleobases and metal nucleosides complexes. This class of compounds has a potential role in pharmaceuticals applications.⁵⁸ Pt(II) was studied intensively as consequence of the role of Cisplatin as an antitumor agent. Pioneering researchers who did intensive work in metal-nucleobase chemistry include Lippert,^{6,125-127} Zamora,^{58,128-133} Verma,¹³⁴⁻¹³⁷ Houlton,¹³⁸⁻¹⁴¹ etc., they synthesised numerous compounds biased on metal coordination with nitrogen bases of DNA and RNA and their derivatives. The reaction of metal ions with DNA and RNA bases usually forms amorphous¹⁴² or micro crystalline solids that are very difficult to characterize as a single crystal by using X-ray diffraction. Therefore, only a few metal-nucleobase compounds were successfully characterised in terms of their complete crystal structures by X-ray. Most of these compounds were derivatives of nucleobases.¹⁴³ Coordination of zinc with adenine and guanine compounds revealed that the complexation occurred via N7 and N9 respectively; the structure of these two complexes was successfully characterized by X-ray diffraction.¹⁴⁴ The work in this thesis is related to preparation of complexes of thio nucleobase derivatives because thio bases have not received much attention except the work of Zamora¹⁴⁵ and Dubler¹⁴⁶ who were able to synthesise crystalline compounds for Cu(I)/Cu(II) with 6-thioguanine and 6-mercaptopurine, respectively. In addition, the complexes of Co(II)/(III) were synthesised with 6-mercaptopurine riboside and its corresponding deoxy nucleoside by Zamora.¹³¹ Most other crystalline compounds that were synthesised with group 11 metals, for example, used non-thio

derivatives nucleobases such as Cu(II)- 9-methylguanine,¹⁴⁷ while some other compounds were not able to give any crystals such as Ag (I) and Au(I) complexes that were prepared by Cuin.¹⁴⁸

1.12 Mechanism of fibre formation

Intermolecular interactions such as hydrogen bonding, π - π stacking, electrical dipole interactions, and van der Waals forces are the factors implicated in the formation of fibrous structures.¹⁴⁹ Growth of the fibres can be assigned to the self-assembly of the chains of the polymer followed by bundling of these chains into fibres with assistance of intermolecular interactions.¹⁵⁰ The rate growth of most fibres increases with cooling, but some biological gels start to form upon heating.¹⁴⁹ The hierarchical structure of the fibres can be affected by the concentration, temperature, speed of drying, and other parameters, and thus, fibre topology can show different hierarchical structures such as linear, branched, spherical, stars, lattice, combs, etc. Studies of the transition of polymer chains from gas phase to solid bundles by a sublimation process showed an increase in the length of the polymer as a result of supramolecular of weak chain interactions.¹⁵⁰ The way that the chains of the polymer connected with each other can produce a diversity of structures which lead to different properties of the product in spite of the fact they consist of the same monomer. For example, the polymer of polyethylene can be found as a linear chain structure chains which is strong and hard or as a branched structure which is flexible, while combination more than one monomer can change the chemical properties and then different applications can be found.¹⁵¹

1.13 Hydrogen bonding and supramolecular chemistry

‘‘Supramolecular Chemistry’’ was described by Jean-Marie Lehn (who received Nobel Prize together with Pedersen and Cram in 1987 for Chemistry)¹⁵² as ‘‘Chemistry beyond the molecule’’. The elements of this subject include organic, inorganic, physical, coordination, and biochemistry. The essential kinds of bonds that connect atoms at the molecules are covalent, ionic, and metallic bonds, and the energy of these bonds is in the range 50-1000 kJmol⁻¹. Another kind of interaction which is the weakest among other interactions (0.5-5 kJmol⁻¹) is Van-der-Waals, but this may be crucial for the formation of aggregates such as micelles. In supramolecular chemistry, the important non-covalent interaction of hydrogen bonding forces has played a major role.¹⁵³ Hydrogen bonds can be defined as an attractive electrostatic interaction that occur in polar molecules in which an H atom is bound to an electronegative atom (N, F, S, O) and interacts with another electronegative atom. Numerous studies have been

made on H bonds in different fields such as chemistry, physics, and biology. The strength of hydrogen bonding is in range $4\text{--}120\text{ kJmol}^{-1}$, the variety of bonds strength depends on the electronegative atom at the acceptor group to which the H atom is attached and on the geometry of the structure that is formed.¹⁵⁴ Nucleobases, amino acids, and carbohydrates are examples of some natural materials that consider worth sources of donors and acceptors hydrogen bonds. The term donor (D) refers to the group that has an electronegative atom, such as O and N, to which H is attached and forms a dipole with a partial positive charge on H. The term acceptor (A) refers to the group that has withdrawing atoms to which the H atom that carrying positive charge can interact. For example, the $\text{O-H}\cdots\text{N}$ where the O-H is the donor and the N is the acceptor. This is illustrated in Fig. 1.36.

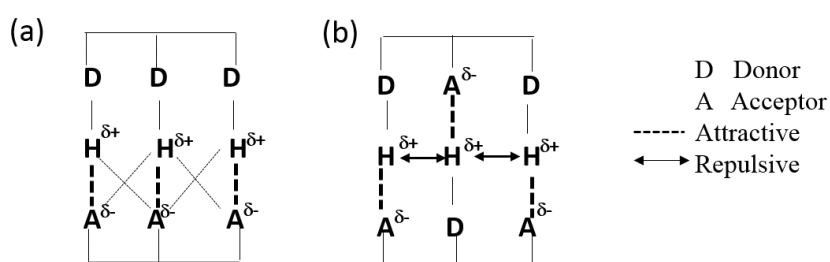


Figure 1.36. Showing the secondary interactions DDD and AAA array attractions (a), and repulsions DAD and ADA between neighbouring groups. The bold arrows in (b) refers to the primary interactions.¹⁵⁴

The direct interaction between donor and acceptor groups generates a *primary interaction*, Fig. 1.37, while interaction that occurred between neighbouring group called *secondary interaction*. Adenine and thymine binding is an example of double hydrogen bonding motif, this bond is not strong enough to form stable structures in solutions but it can help to drive the formation of ordered supramolecular structures in DNA.

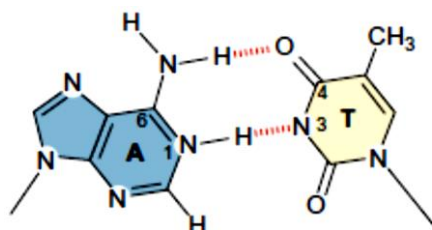


Figure 1.37. Primary interaction (red dots) between Adenine (A) and thymine (T) nucleobases.¹⁵⁵

Triple hydrogen bonding and quadruple hydrogen bonding are the systems that form secondary interaction. Triple hydrogen bonding can be found at purine and pyrimidine at DNA and RNA such as DDA-AAD triple hydrogen bonding that form between guanine and cytosine. It

includes three kinds of motifs, DAD-ADA, DDA-AAD, and DDD-AAA. The stability of the second kind is higher compare to the first kind, and the third one is higher than the second one and that can be assigned to the repulsions and attraction electrostatic that generated at these motifs accordingly to the theory of secondary interaction which is appeared for the three kinds as four repulsions, two repulsions, two attractions and four attractions, respectively.

The interaction between guanine and cytosine nucleobases, Fig. 1.38 is a good example that shows both the primary (three interactions) and secondary (two attractive and one repulsive) interactions.

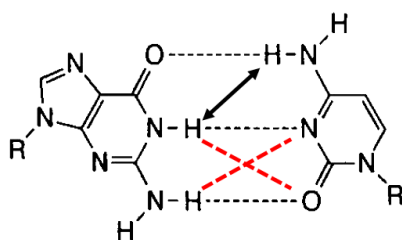


Figure 1.38. Displays the primary interactions (black dots) and secondary interactions including attractive (red dots) and repulsive (black arrow) between guanine and cytosine nucleobases, ADD facing DAA arrays, D is the donor and A is the acceptor

In quadruple hydrogen bonding, such as ADAD and AADD, the monomers can form homodimers while four different motifs of DAAD-ADDA, DDDA-AAAD, DDAD-AADA are formed heterodimeric system of quadruple hydrogen bonding, this system has found different application in supramolecular self-assembly.

Hydrogen bonding plays a major rule in the hierarchical structure process by arranging the molecules with high precision for example, the organization of the nucleotides molecules at the DNA.¹⁵⁶ The system of hydrogen bonding can be found as NH...N, NH...SH, HN...H, OH...O, HO...H, OH...NH, NH...O. The electronegativity of S atom is less than N or O atoms and that make hydrogen bonding systems that include S usually weak compared to other H-bonds.¹⁵⁷ SH is considered as a good donor and it is able to form different H-bonds systems, and it was found that the hydrogen bonding system of NH....S bond is stronger than NH...O.¹⁵⁸ The strength of hydrogen bonding correlates with the length of the bond^{159,160} between the donor and the acceptor; the shorter bonds are stronger than the longer bonds. The bond lengths are normally in range 3.5-2 Å. Programing the self-assembly of synthetic blocks building accompanying with the interactions of hydrogen bonding can lead to form more complicated structures.¹⁵⁶

1.14 Thesis overview

The structure of the thesis was organized as follows: Chapter 1 is an introduction, presents the importance of nucleic acids as ligands in coordination polymers with coinage metal ions. It also briefly discusses the definition, classification, and some applications of the gels, in addition, it gives a brief explanation about the chemistry of coinage metal ions, and discusses the mechanism of gel formation. Chapter 2, presents the techniques that were used to characterize the chemical structure and the morphology of the hydrogels and gives a brief description of the principles of these techniques. Chapter 3, concerns the synthesis and structural characterization of Au(I):6-thioguanosine hydrogel; the properties of this gel such as luminescence and conductivity are discussed. In addition, it shows the helical structures of the gel by CD spectrometry and AFM. Chapter 4, describes hydrogels formed with other coinage metal ions (Cu and Ag) but the same nucleoside (6-TGR), XPS characterization showed that Cu(II) was reduced by 6-TGR to Cu(I), chemical structures and morphology of the gels were studied in this chapter. Chapter 5, presents synthesis of 2'-deoxy-6-thioguanosine and displays the analytical techniques that were used to confirm the successful synthesis. This chapter also shows the ability of coinage metal ions to bind and form hydrogels in spite of the absence of 2'OH group from the sugar structure and the associated H bond capacity. This chapter also shows how the morphology of these hydrogels was affected by the absence of 2'OH group. Chapter 6, covers the synthesis of three kinds of silver gels with two purine nucleobases (6-MP & 6-Tg) and one pyrimidine nucleobase (2-TC), it shows the ability of these nucleobases to form hydrogels in spite of the absence sugar structures. Chapter 7, presents the synthesis and characterization crystalline coordination compounds between methyl thio purines and silver, copper, and cobalt ions. Chapter 8, concerns the synthesis and characterization crystal compound of gold thio pyrimidine. Chapter 9, provides the conclusion and summarized the major results of this work.

Table 1.2 New compounds synthesized in this work.

Name of Compound	Chemical formula	State	Code
Gold:6-thioguanosine	C ₁₀ H ₁₂ N ₅ O ₄ SAu	Gel	Au:6-TGR
Copper:6-thioguanosine	C ₁₀ H ₁₂ N ₅ O ₄ SCu	Gel	Cu:6-TGR
Silver:6-thioguanosine	C ₁₀ H ₁₂ N ₅ O ₄ SAg	Gel	Ag:6-TGR
Gold:2'-deoxy-6-thioguanosine	C ₁₀ H ₁₂ N ₅ O ₃ SAu	Gel	Au:d TGR
Copper :2'-deoxy-6-thioguanosine	C ₁₀ H ₁₂ N ₅ O ₃ SCu	Gel	Cu:d TGR
Silver:2'-deoxy-6-thioguanosine	C ₁₀ H ₁₂ N ₅ O ₃ SAg	Gel	Ag:d TGR
Silver:6-mercaptopurine	C ₅ H ₃ N ₄ SAg	Gel	Ag:6-MP
Silver:6-mercaptopurine riboside	C ₁₀ H ₁₂ N ₄ O ₄ SAg.NO ₃ ⁻	Gel	Ag:6-MPR
Silver:6-thioguanine	C ₅ H ₄ N ₅ SAg	Gel	Ag:6-TG
Silver:2-thiocytosine	C ₄ H ₄ N ₃ SAg	Gel	Ag:2-TC
Silver:6-methylmercaptopurine riboside	C ₂₂ H ₂₈ AgN ₉ O ₁₃ S ₂	Crystal	Ag:6-MMPR
Gold:2-thiocytosine	C ₈ H ₁₀ N ₆ S ₂ ClAu	Crystal	Au(I):2-TC
Copper:6-methylmercaptopurine	C ₁₂ H ₁₂ N ₈ S ₂ Cl ₄ Cu ₂	Crystal	Cu(II):6-MMP
Cobalt:6-methylmercaptopurine	C ₁₂ H ₂₂ N ₈ S ₂ O ₆ Co	Crystal	Co(II):6-MMP

References

1. Carrabine, J.A. & Sundaralingam, M. The Crystal Structure of a Copper-Cytoside Complex. *Chemical Communication*, 746 (1968).
2. Knobloch, B., Linert, W. & Sigel, H. Metal ion-binding properties of (N3)-deprotonated uridine, thymidine, and related pyrimidine nucleosides in aqueous solution. *Proceedings of the National Academy of Sciences (PNAS)*, **102**, 7459-7464 (2005).
3. Vetter, C. & Steinborn, D. Structural and Computational Studies of 1-Methyl-2-thiocytosine and its Coordination Mode in a Dinuclear Platinum(IV) Complex [(PtMe₃)₂(μ-1-MeSCy-1kN³,1:2k²S)₂][BF₄]₂. *Verlag der Zeitschrift für Naturforschung Tübingen*, 578-586 (2010).
4. Gao, Y.-G. & Wang, A.H. Crystallographic studies of metal ion - DNA interactions: different binding modes of cobalt(II), copper(II) and barium(II) to N⁷ of guanines in Z-DNA and a drug- DNA complex. *Nucleic Acids Research*, **21**, 4093 -4101 (1993).

5. Selvi, P.T. & Henkel, G. X-ray crystal structure of tetrakis(1-methylcytosine)copper(II) perchlorate dihydrate: effect of 1-methyl substitution on cytosine on the spectral and redox behaviour. . *Inorganica Chimica Acta*, **340**, 139-146 (2002).
6. Lippert, B. Multiplicity of metal ion binding patterns to nucleobases. *Coordination Chemistry Reviews*, **200-202**, 487-516 (2000).
7. Bertini, I., Gray, H.B., Lippard, S.J. & Valentine, J.S. Bioinorganic Chemistry. Barton, J. K. Chapter 8. Metal/Nucleic-Acid Interactions, .Division of Chemistry and Chemical Engineering.California Institute of Technology. University Science Books. USA., 455-503 (1994).
8. Brown, R.S. & Klug, A. Crystallographic and Biochemical Investigation of the Lead(II)-Catalyzed Hydrolysis of Yeast Phenylalanine tRNA. *Biochemistry*, **24**, 4785-4801 (1985).
9. Eichhorn, G.L. & Shin, Y.A. Interaction of Metal Ions with Polynucleotides and Related Compounds. XII. The Relative Effect of Various Metal. Ions on DNA Helicity. *Journal of the American Chemical Society*, **90**, 7323-7328 (1968).
10. Kwan, I.C., Delley, R.J., Hodgson, D.R. & Wu, G. Single atom modification leads to enhanced nucleotide self-assembly: the role of cation bridging. *Chemical Communication*, **47**, 3882-3884 (2011).
11. Hud, N.V. Nucleic Acid–Metal Ion Interactions. Lippert. B. Chapter 2, Coordinative Bond Formation Between Metal Ions and Nucleic Acid Bases. Royal Society of Chemistry. (2009).
12. Astrid Sigel, A., Helmut Sigel, H. & Sigel, R.K.O. Interrelations between Essential Metal Ions and Human Diseases. Springer Science+Business Media Dordrecht. **13**(2013).
13. Bonetti, A., Leone, R., Muggia, F.M. & Howell, S.B. Platinum and Other Heavy Metal Compounds in Cancer Chemotherapy. Molecular Mechanisms and Clinical Applications. Humana Press. (2009).
14. Beobide, G., Castillo, O., Luque, A. & Pérez-Yáñez, S. Porous materials based on metal–nucleobase systems sustained by coordination bonds and base pairing interactions. *CrystEngComm.*, **17**, 3051-3059 (2015).
15. Hud, N.V. Nucleic Acid–Metal Ion Interactions. Zhou, Z. and Dong, S.Chapter 12. DNA-Templated Metal Nanoclusters and Their Applications. Royal Society of Chemistry. (2009).

16. Sigel, A., Sigel, H. & Sigel, R.K.O. Interplay between Metal Ions and Nucleic Acids. Pechlaner, M and Sigel, R. K. O. Chapter 1. Characterization of Metal Ion-Nucleic Acid Interactions in Solution. Springer Science+Business Media B.V **10**(2012).
17. Bujnicki, J.M. Nucleic Acids and Molecular Biology. Volume 29. Kjems, J., Ferapontova, E., and Gothelf, K. V. Nucleic Acid Nanotechnology. Liu, L., Besenbacher, F., and Dong, MD. Chapter 1. Self-Assembly of DNA Bases via Hydrogen Bonding Studied by Scanning Tunneling Microscopy. Springer-Verlag Berlin Heidelberg. Poland. (2014).
18. Searle, M.S. & Wickham, G. Hoogsteen versus Watson-Crick A-T basepairing in DNA complexes of a new group of 'quinomycin-like' antibiotics. *Elsevier Science Publishers B. V. (Biomedical Division)*, **272**, 171-174 (1990).
19. Araki, K. & Yoshikawa, I. Nucleobase-containing gelators. *Topics in Current Chemistry*, **256**, 133-165 (2005).
20. Adhikari, B., Shah, A. & Kraatz, H.-B. Self-assembly of guanosine and deoxyguanosine into hydrogels: monovalent cation guided modulation of gelation, morphology and self-healing properties. *Journal of Materials Chemistry B*, **2**, 4802-4810 (2014).
21. Kumar, A. & Gupta, S.K. 5'-Guanosine monophosphate mediated biocompatible porous hydrogel of beta-FeOOH-viscoelastic behavior, loading, and release capabilities of freeze-dried gel. *The Journal of Physical Chemistry B*, **118**, 10543-10551 (2014).
22. Dash, J. & Saha, P. Functional architectures derived from guanine quartets. *Organic & Biomolecular Chemistry*, **14**, 2157-2163 (2016).
23. F, F. Low Molecular Mass Gelators: Design, Self-Assembly, Function. Topics in Current Chemistry 256. Araki, K and Yoshikawa, I. Nucleobase-Containing Gelators. Springer-Verlag Berlin Heidelberg. (2005).
24. Sreenivasachary, N. & Lehn, J.M. Gelation-driven component selection in the generation of constitutional dynamic hydrogels based on guanine-quartet formation. *Proceedings of the National Academy of Sciences (PNAS) USA*, **102**, 5938-5943 (2005).
25. Maity, G.C. Low Molecular Mass Gelators of Organic Liquids. *Journal of Physical Sciences*, **11**, 156-171 (2007).
26. Livage, J. & Sanchez, C. Sol-gel chemistry of transition metal oxides. *Progress in Solid State Chemistry*, **18**, 259-341 (1988).

27. Yang, D., Zhang, J.Z., Fu, S., Xue, Y. & Hu, J. Evolution process of polymethacrylate hydrogels investigated by rheological and dynamic light scattering techniques. *Colloids and Surfaces A: Physicochemical and Engineering Aspects* **353**, 197-203 (2010).
28. Gulrez, S.K.H. & Phillips, G.O. Hydrogels: Methods of Preparation, Characterisation and Applications, Progress in Molecular and Environmental Bioengineering-From Analysis and Modeling to Technology Applications, Prof. Angelo Carpi (Ed.), ISBN: 978-953-307-268-5, InTech, <http://www.intechopen.com>. (2011).
29. Kudela, V. Encyclopedia of Polymer Science and Engineering. Wiley, New York. (1987).
30. Peppas, N.A. & Ichikawa, H. Hydrogels in pharmaceutical formulations. *European Journal of Pharmaceutics and Biopharmaceutics*, **50**, 27-46 (2000).
31. Ratner, B.D. & Hoffman, A.S. Synthetic Hydrogels for Biomedical Applications. *Journal of the American Chemical Society*, **31**, 1-36 (1976).
32. Foster, J.A., Piepenbrock, M.O., Clarke, N. & Steed, J.W. Anion-switchable supramolecular gels for controlling pharmaceutical crystal growth. *Nature Chemistry*, **2**, 1037-1043 (2010).
33. Casuso, P., Carrasco, P., Loinaz, I., Grande, H.J. & Odriozola, I. Converting drugs into gelators: supramolecular hydrogels from N-acetyl-L-cysteine and coinage-metal salts. *Organic & Biomolecular Chemistry*, **8**, 5455-5458 (2010).
34. Shen, J.S., Mao, G.J., Zhou, Y.H., Jiang, Y.B. & Zhang, H.W. A ligand-chirality controlled supramolecular hydrogel. *Dalton Transactions*, **39**, 7054-7058 (2010).
35. Komarov, P. & Pakhomov, P. On Molecular Gelation Mechanism of L-Cysteine Based Hydrogel. *Nanoscience and Nanoengineering*, **1**, 23-35 (2013).
36. Boddu, S.H., Vaishya, R., Pal, D. & Mitra, A.K. Novel nanoparticulate gel formulations of steroids for the treatment of macular edema. *Journal of Ocular Pharmacology and Therapeutics*, **26**, 37-48 (2010).
37. Zhang, S., Yang, S., Lan, J., Yang, S. & You, J. Helical nonracemic tubular coordination polymer gelators from simple achiral molecules. *Chemical Communication*, 6170-6172 (2008).
38. Rowan, S.J. Stimuli-responsive metallo-supramolecular polymers. *Polymer Preprints*, **50**, 339-340 (2009).
39. Liu, K., Meng, L., Huang, C. & Yi, T. Colour change and luminescence enhancement in a cholesterol-based terpyridyl platinum metallogel via sonication. *Journal of Materials Chemistry C* **1**, 1753-1762 (2013).

40. Faoucher, E., Nativo, P., Bleloch, A.L. & Brust, M. In situ preparation of network forming gold nanoparticles in agarose hydrogels. *Chemical Communication*, , 6661-6663 (2009).
41. Amanokura, N. & Reinhoudt, D.N. New sugar-based gelators with an amino group, the gelation ability of which is remarkably reinforced by the hydrogen bond and the metal coordination. *Journal of the Chemical Society, Perkin Transactions*, **2**, 1995-2000 (1999).
42. Gronwald, O. & Seiji Shinkai, S. Sugar-Integrated Gelators of Organic Solvents *Chemistry A European Journal*, **7**, 4328-4334 (2001).
43. Serrero, A. & David, L. Polysaccharide Gels Based on Chitosan and Modified Starch: Structural Characterization and Linear Viscoelastic Behavior. *Biomacromolecules*, **11**, 1534–1543 (2010).
44. Leivo, K. *Thesis, University of Jyväskylä, Jyväskylä, Finland* (2011).
45. Lee, J.H., Lee, H., Lee, J.Y. & Jung, J.H. Fluorescence enhancement of a tetrazole-based pyridine coordination polymer hydrogel. *New Journal of Chemistry* **35**, 1054-1059 (2011).
46. Sato, H., Nogami, E., Yajima, T. & Yamagishi, A. Terminal effects on gelation by low molecular weight chiral gelators. *RSC Advances*. **4**, 1659-1665 (2014).
47. Cai, F., Shen, J.S., Zeng, E.M. & Jiang, Y.B. Hydrogelators of cyclotrimeratrylene derivatives. *Organic & Biomolecular Chemistry*, **10**, 1418-1423 (2012).
48. Meazza, L., Foster, J.A., Resnati, G. & Steed, J.W. Halogen-bonding-triggered supramolecular gel formation. *Nature Chemistry*, **5**, 42-47 (2013).
49. Dawn, A., Andrew, K.S., Jones, C.D., Aguilar, J.A. & Steed, J.W. Supramolecular Gel Control of Cisplatin Crystallization: Identification of a New Solvate Form Using a Cisplatin-Mimetic Gelator. *Crystal Growth & Design*, **15**, 4591-4599 (2015).
50. Pandurangan, K., Kitchen, J.A., Blasco, S., Paradisi, F. & Gunnlaugsson, T. Supramolecular pyridyl urea gels as soft matter with antibacterial properties against MRSA and/or E. coli. *Chemical Communication*, **50**, 10819-10822 (2014).
51. Byrne, P., Lloyd, G.O., Anderson, K.M., Clarke, N. & Steed, J.W. Metal-induced gelation in dipyridyl ureas. *New Journal of Chemistry*, **34**, 2261-2274 (2010).
52. Meazza, L., Foster, J.A., Resnati, G. & Steed, J.W. Halogen-bonding-triggered supramolecular gel formation. *Nature Chemistry*, **5**, 42-47 (2013).

53. Foster, J.A., Piepenbrock, M.O., Clarke, N. & Steed, J.W. Anion-switchable supramolecular gels for controlling pharmaceutical crystal growth. *Nature Chemistry*, **2**, 1037-1043 (2010).
54. Piepenbrock, M.O., Clarke, N., Foster, J.A. & Steed, J.W. Anion tuning and polymer templating in a simple low molecular weight organogelator. *Chemical Communication*, **47**, 2095-2097 (2011).
55. Liu, K. & Steed, J.W. Triggered formation of thixotropic hydrogels by balancing competitive supramolecular synthons. *Soft Matter*, **9**, 11699-11705 (2013).
56. Stanley, C.E., Clarke, N., Lenthall, J.T. & Steed, J.W. Anion binding inhibition of the formation of a helical organogel. *Chemical Communication*, 3199-3201 (2006).
57. Connelly, N.G. & Damhus, T. Nomenclature of Inorganic Chemistry I U P A C Recommendations *International Union of Pure and Applied Chemistry by The Royal Society of Chemistry, Biddles Ltd, King's Lynn, Norfolk, UK* (2005).
58. Amo-Ochoa, P. & Zamora, F. Coordination polymers with nucleobases: From structural aspects to potential applications. *Coordination Chemistry Reviews*, **276**, 34-58 (2014).
59. Gómez-Herrero, J. & Zamora, F. Coordination Polymers for Nanoelectronics. *Advanced Materials*, **23**, 5311-5317 (2011).
60. Dalai, S. Coordination Polymers. *Journal of Physical Sciences*, **15**, 223-230 (2011).
61. Lippard, S.J. & Berg, J.M. Principles of Bioinorganic Chemistry. Chapter 2: Principles of Coordination Chemistry Related to Bioinorganic Research. University Science Books, USA., 21 (1994).
62. Batten, S.R., Neville, S.M. & Turner, D.R. Coordination Polymers Design, Analysis and Application. Chapter 5. Transition Metal Coordination Polymers. The Royal Society of Chemistry, UK. (2009).
63. Mas-Balleste, R., Gomez-Herrero, J. & Zamora, F. One-dimensional coordination polymers on surfaces: towards single molecule devices. *Chemical Society Reviews*, **39**, 4220-4233 (2010).
64. Tuccitto, N., Ferri, V., Zhavnerko, G., Licciardello, A. & Rampi, M.A. Highly conductive approximately 40-nm-long molecular wires assembled by stepwise incorporation of metal centres. *Nature Materials*, **8**, 41-46 (2009).
65. Cotton, F.A. & Wilkinson, G. Advanced Inorganic Chemistry A Comprehensive Text. Fourth edition. John Wiley & Sons. USA. (1980).

66. Bard, A.J., Parsons, R. & Jordan, J. Standard Potentials in Aqueous Solutions. Marcel Dekker, New York. (1985).
67. Pyykkö, P. Theoretical Chemistry of Gold. *Angewandte Chemie International Edition* **43**, 4412-4456 (2004).
68. Stanley, G.G. The Extractive Metallurgy of Gold in South Africa. Nicol, M. J, Fleming, C. A, and Paul R. L. Chapter 15. The Chemistry of the Extraction of Gold. pp 831. National Book Printers, Goodwood, South Africa. **2**(1987).
69. Gimeno, M.C. The Chemistry of Gold. 1-63 (2008).
70. Pyykko, P. Strong Closed-Shell Interactions in Inorganic Chemistry. *Chemical Reviews*, **97**, 597-636 (1997).
71. Rasika Dias, H.V. & Omary, M.A. Bright Phosphorescence of a Trinuclear Copper(I) Complex: Luminescence Thermochromism, Solvatochromism, and "Concentration Luminochromism". *Journal of the American Chemical Society*, **125**, 12072-12073 (2003).
72. Desclaux, J.P. & Pyyhho, P. Dirac-fock one-centre calculations .The momolecules CuH, AgH and AuH including p-type symmetry functions. *Chemical Physics letters*, **39**, 300-303 (1976).
73. Rawashdeh-Omary, M.A. & Fackler, J.J.P. Excited-State Interactions for $[\text{Au}(\text{CN})_2^-]_n$ and $[\text{Ag}(\text{CN})_2^-]_n$ Oligomers in Solution. Formation of Luminescent Gold-Gold Bonded Excimers and Exciplexes. *Journal of the American Chemical Society*, **123**, 11237-11247 (2001).
74. Jones, C. & Thornback, J. Medicinal Applications of Coordination Chemistry, The Royal Society of Chemistry. (2007).
75. Tiekink, E.R. Gold derivatives for the treatment of cancer. *Critical Reviews in Oncology/Hematology* **42**, 225-248 (2002).
76. Lansdown, A.B. Silver in Health Care: Antimicrobial Effects and Safety in Use. *Curr Probl Dermatol. Basel, Karger*, **33**, 17-34 (2006).
77. Baenziger, N.C. & Struss, A.W. Crystal Structure of 2-Sulfanilamidopyrimidinesilver(I). *Inorganic Chemistry*, **15**, 1807-1809 (1976).
78. Garrison, J.C. & Youngs, W.J. Ag(I) N-heterocyclic carbene complexes: synthesis, structure, and application. *Chemical Reviews*, **105**, 3978-4008 (2005).
79. Fox, C.L. Silver sulfadiazine-a new topical therapy for pseudomonas in burns. *Archives of Surgery*, **96**, 184-188 (1968).

80. Melaiye, A. & Youngs, W.J. Formation of Water-Soluble Pincer Silver(I)-Carbene Complexes: A Novel Antimicrobial Agent. *Journal of Medicinal Chemistry*, **47**, 973-977 (2004).
81. Linder, M.C. The Biochemistry of Copper. Plenum Press, New York. (1991).
82. Zatta, P. & Frank, A. Copper deficiency and neurological disorders in man and animals. *Brain Research Reviews*, **54**, 19-33 (2007).
83. Brewer, G. Copper in medicine. *Current Opinion in Chemical Biology* **7**, 207-212 (2003).
84. Iakovidis, I., Delimaris, I. & Piperakis, S.M. Copper and its complexes in medicine: a biochemical approach. *Molecular Biology International*, **2011**, 594529 (2011).
85. Hordyjewska, A., Popiolek, L. & Kocot, J. The many "faces" of copper in medicine and treatment. *Biomaterials* **27**, 611-621 (2014).
86. Efthimiadou, E.K., Sanakis, Y., Katsaros, N. & Psomas, G. Neutral and cationic mononuclear copper(II) complexes with enrofloxacin: structure and biological activity. *Journal of Inorganic Biochemistry*, **100**, 1378-1388 (2006).
87. Psomas, G., Tarushi, A., Efthimiadou, E.K. & Katsaros, N. Synthesis, structure and biological activity of copper(II) complexes with oxolinic acid. *Journal of Inorganic Biochemistry*, **100**, 1764-1773 (2006).
88. Efthimiadou, E.K., Scorilas, A., Karaliota, A. & Psomas, G. Structure and biological properties of the copper(II) complex with the quinolone antibacterial drug N-propyl-norfloxacin and 2,2'-bipyridine. *Journal of Inorganic Biochemistry*, **101**, 64-73 (2007).
89. Efthimiadou, E.K., Katsarou, M.E., Karaliota, A. & Psomas, G. Copper(II) complexes with sparfloxacin and nitrogen-donor heterocyclic ligands: Structure-activity relationship. *Journal of Inorganic Biochemistry*, **102**, 910-920 (2008).
90. Chen, G.J., Liu, X. & Yan, S.P. Synthesis, DNA binding, photo-induced DNA cleavage, cytotoxicity and apoptosis studies of copper(II) complexes. *Journal of Inorganic Biochemistry*, **105**, 119-126 (2011).
91. Qiao, X., Zhang, Y.W., Chen, G.J. & Yan, S.P. Study on potential antitumor mechanism of a novel Schiff base copper(II) complex: synthesis, crystal structure, DNA binding, cytotoxicity and apoptosis induction activity. *Journal of Inorganic Biochemistry*, **105**, 728-737 (2011).
92. Katsarou, M.E. & Vourloumis, D. Novel Copper(II) Complex of N-Propyl-norfloxacin and 1,10-Phenanthroline with Enhanced Antileukemic and DNA Nuclease Activities. *Journal of Medicinal Chemistry*, **51**, 470-478 (2008).

93. Tarafder, M. & Crouse, K. Complexes of a tridentate ONS Schiff base. Synthesis and biological properties. *Transition Metal Chemistry*, **25**, 456-460 (2000).
94. Ainscough, E.W. & Waters, J.M. Antitumour copper(II) salicylaldehyde benzoylhydrazone (H₂sb) complexes: physicochemical properties and the single-crystal X-ray structures of [$\{\text{Cu}(\text{H}_2\text{sb})(\text{CCl}_3\text{CO}_2)_2\}_2$] and [$\{\text{Cu}(\text{Hsb})(\text{ClO}_4)(\text{C}_2\text{H}_5\text{OH})\}_2$] and the related salicylaldehyde acetylhydrazone (H₂sa) complex, $[\text{Cu}(\text{Hsa})\text{Cl}(\text{H}_2\text{O})]\cdot\text{H}_2\text{O}$. *Inorganica Chimica Acta*, **267**, 27-38 (1998).
95. Kung, P.-P. & Jones, R.A. One-Flask Syntheses of 6-Thioguanosine and 2'-Deoxy-6-Thioguanosine *Tetrahedron Letters*, **32**, 3919-3922 (1991).
96. Wang, X. & McHale, R. Metal-containing polymers: building blocks for functional (nano)materials. *Macromol Rapid Commun.*, **31**, 331-350 (2010).
97. Yan, Y., Zhang, J., Ren, L. & Tang, C. Metal-containing and related polymers for biomedical applications. *Chemical Society Reviews*, **45**, 5232-5263 (2016).
98. Zhang, J., Yan, J., Wang, Q. & Tang, C. Anion-Responsive Metallopolymer Hydrogels for Healthcare Applications. *Scientific Reports*, **5**, 11914-11923 (2015).
99. Jordheim, L.P., Durantel, D., Zoulim, F. & Dumontet, C. Advances in the development of nucleoside and nucleotide analogues for cancer and viral diseases. *Nature Reviews Drug Discovery*, **12**, 447-464 (2013).
100. Ford, L.T. & Berg, J.D. Thiopurine S-methyltransferase (TPMT) assessment prior to starting thiopurine drug treatment; a pharmacogenomic test whose time has come. *Journal of Clinical Pathology*, **63**, 288-295 (2010).
101. Goitia, H., Nieto, Y., Laguna, A. & Gimeno, M.C. Antitumoral Gold and Silver Complexes with Ferrocenyl-Amide Phosphines. *Organometallics*, **32**, 6069-6078 (2013).
102. Fillat, M.F., Ortego, L. & Villacampa, M.D. Synthesis, Structure and Bactericide Activity of (Aminophosphane)gold(I) Thiolate Complexes. *European Journal of Inorganic Chemistry*, **2011**, 1487-1495 (2011).
103. Dash, J., Patil, A.J., Das, R.N., Dowdall, F.L. & Mann, S. Supramolecular hydrogels derived from silver ion-mediated self-assembly of 5'-guanosine monophosphate. *Soft Matter*, **7**, 8120-8126 (2011).
104. Loo, K. & Petty, J.T. Ag⁺-Mediated Assembly of 5'-Guanosine Monophosphate. *The Journal of Physical Chemistry B*, **114**, 4320-4326 (2010).

105. Matsuoka, Y. & Norden, B. Nucleic Acid-Metal Interactions. 2. Complexes of Silver(I) with Guanosine and 7-Methylguanine from Studies of Isotropic and Dichroic Spectra. *The Journal of Physical Chemistry*, **88**, 971-976 (1984).
106. Orioli, P.L. & Cini, R. A Proton Magnetic Resonance Investigation on 1: 1 Cytidine and Guanosine Silver (I) Complexes. *Bioinorganic Chemistry*, **7**, 345-349 (1977).
107. Sharma, B., Mahata, A., Mandani, S., Sarma, T.K. & Pathak, B. Coordination polymer hydrogels through Ag(i)-mediated spontaneous self-assembly of unsubstituted nucleobases and their antimicrobial activity. *RSC Advances*, **6**, 62968-62973 (2016).
108. Peters, G.M. Guanosine -Borate Hydrogels- Form and Function. Thesis, University of Maryland, USA. (2015).
109. Wong, A. & Wu, G. Selective binding of monovalent cations to the stacking G-quartet structure formed by guanosine 5'-monophosphate: a solid-state NMR study. *Journal of The American Chemical Society*, **125**, 13895-13905 (2003).
110. Davis, J.T. G-quartets 40 years later: from 5'-GMP to molecular biology and supramolecular chemistry. *Angewandte Chemie International Edition*, **43**, 668-698 (2004).
111. Das, R.N., Kumar, Y.P., Pagoti, S., Patil, A.J. & Dash, J. Diffusion and birefringence of bioactive dyes in a supramolecular guanosine hydrogel. *Chemistry a European Journal*, **18**, 6008-6014 (2012).
112. Yu, Y. & McGown, L.B. Tunable Thermoassociation of Binary Guanosine Gels. *The Journal of Physical Chemistry B*, **112**, 1130-1134 (2008).
113. Liang, H., Zhang, Z., Yuan, Q. & Liu, J. Self-healing metal-coordinated hydrogels using nucleotide ligands. *Chemical Communication*, **51**, 15196-15199 (2015).
114. Park, S.M. & Kim, B.H. Ultrasound-triggered water gelation with a modified nucleoside. *Soft Matter*, **4**, 1995-1997 (2008).
115. Wang, Y., Desbat, B., Labrot, T. & Oda, R. Aggregation behaviors of gemini nucleotide at the air-water interface and in solutions induced by adenine-uracil interaction. *Journal of Colloid and Interface Science*, **283**, 555-564 (2005).
116. Kumar, A. & Gupta, S.K. Supramolecular-directed novel superparamagnetic 5'-adenosine monophosphate templated β -FeOOH hydrogel with enhanced multi-functional properties. *Green Chemistry*, **17**, 2524-2537 (2015).
117. Odriozola, I., Loinaz, I., Pomposo, J.A. & Grande, H.J. Gold-glutathione supramolecular hydrogels. *Journal of Materials Chemistry*, **17**, 4843-4845 (2007).

118. Aguiló, E., Gavara, R., Lima, J.C., Llorca, J. & Rodríguez, L. From Au(i) organometallic hydrogels to well-defined Au(0) nanoparticles. *Journal of Materials Chemistry C*, **1**, 5538-5547 (2013).
119. Gavara, R., Llorca, J., Lima, J.C. & Rodriguez, L. A luminescent hydrogel based on a new Au(I) complex. *Chemical Communication*, **49**, 72-74 (2013).
120. Vergara, E., *et al.* Antiproliferative Activity of Gold(I) Alkyne Complexes Containing Water-Soluble Phosphane Ligands. *Organometallics*, **29**, 2596-2603 (2010).
121. Moro, A.J., Rome, B., Lima, J.C. & Rodriguez, L. A coumarin based gold(I)-alkynyl complex: a new class of supramolecular hydrogelators. *Organic & Biomolecular Chemistry*, **13**, 2026-2033 (2015).
122. Imaz, I. & Maspoch, D. Amino Acid Based Metal-Organic Nanofiber. *Journal of the American Chemical Society*, **131**, 18222–18223 (2009).
123. Fang, W., Liu, X., Lu, Z. & Tu, T. Photoresponsive metallo-hydrogels based on visual discrimination of the positional isomers through selective thixotropic gel collapse. *Chemical Communication*, **50**, 3313-3316 (2014).
124. Gee, W.J. & Batten, S.R. Instantaneous gelation of a new copper(II) metallogel amenable to encapsulation of a luminescent lanthanide cluster. *Chemical Communication*, **48**, 4830-4832 (2012).
125. Zamora, F. & Lippert, B. Au^{III} binding to C5 of the model nucleobase 1,3-dimethyluracil (1,3-DimeU): Preparation and X-ray crystal structures of *trans*-K[Au(CN)₂ Cl(1,3-DimeU)] and of two derivatives. *Journal of Organometallic Chemistry*, **552**, 127-134 (1998).
126. Zamora, F. & Lippert, B. 5,5'-Diuracilyl Species from Uracil and [AuCl₄]⁻: Nucleobase Dimerization Brought about by a Metal. *Angewandte Chemie International Edition*, **38**, 2274-2275 (1999).
127. Roitzsch, M. & Lippert, B. Structural precursor of the hemideprotonated guanine pair. *Chemical Communication*, 5991-5993 (2005).
128. Zamora, F., Pilar Amo-Ochoa, M., Sanz Miguel, P.J. & Castillo, O. From metal-nucleobase chemistry towards molecular wires. *Inorganica Chimica Acta*, **362**, 691-706 (2009).
129. Mas-Ballesté, R., Olea, D., Gómez-Herrero, J. & Zamora, F. Towards Molecular Wires Based on Metal-Organic Frameworks. *European Journal of Inorganic Chemistry*, **2009**, 2885-2896 (2009).

130. Zamora, F. & Amo-Ochoa, P. Assembling of Dimeric Entities of Cd(II) with 6-Mercaptopurine to Afford One-Dimensional Coordination Polymers: Synthesis and Scanning Probe Microscopy Characterization. *Inorganic Chemistry*, **45**, 7642-7650 (2006).
131. Houlton, A., Amo-Ochoa, P., Hribesh, S., Pike, A.R. & Zamora, F. Coordination chemistry of 6-thioguanine derivatives with cobalt: toward formation of electrical conductive one-dimensional coordination polymers. *Inorganic chemistry*, **52**, 5290-5299 (2013).
132. Amo-Ochoa, P., Castillo, O., Welte, L., Gomez-Herrero, J. & Zamora, F. Synthesis of designed conductive one-dimensional coordination polymers of Ni(II) with 6-mercaptopurine and 6-thioguanine. *Inorganic chemistry*, **48**, 7931-7936 (2009).
133. Amo-Ochoa, P., Verma, S., Kumar, J. & Zamora, F. Semiconductive and magnetic one-dimensional coordination polymers of Cu(II) with modified nucleobases. *Inorganic chemistry*, **52**, 11428-11437 (2013).
134. Mishra, A.K. & Verma, S. Interconnected trimeric, pentameric, and hexameric metallacycles in a singular silver-adenine framework. *Inorganic chemistry*, **49**, 8012-8016 (2010).
135. Mishra, A.K. & Verma, S. *Indian Journal of chemistry*, **52**, 1041-1046 (2013).
136. Kumar, J., Purohit, C.S. & Verma, S. Directing spatial disposition of ferrocene around homoadenine tetrads. *Chemical Communication*, , 2526-2528 (2008).
137. Nagapradeep, N., Venkatesh, V., Tripathi, S.K. & Verma, S. Guanine-copper coordination polymers: crystal analysis and application as thin film precursors. *Dalton Transactions*, **43**, 1744-1752 (2014).
138. Galindo, M.A. & Houlton, A. Chelate-tethered nucleobases: New architectures and insights in metal ion–nucleobase chemistry. *Inorganica Chimica Acta*. **362**, 625-633 (2009).
139. Galindo, M.A., Clegg, W., Moreno Martinez, V. & Houlton, A. Reactions of Pd(II) with chelate-tethered 2,6-diaminopurine derivatives: N3-coordination and reaction of the purine system. *Inorganic Chemistry*, **48**, 11085-11091 (2009).
140. Galindo, M.A., Clegg, W., Harrington, R.W., Moreno Martinez, V. & Houlton, A. Probing metal-ion purine interactions at DNA minor-groove sites. *Inorganic chemistry*, **48**, 10295-10303 (2009).

141. Galindo, M.A., Clegg, W., Harrington, R.W. & Houlton, A. Self-assembly of a bis(adeninyl)-Cu(i) complex: a cationic nucleobase duplex mimic. *Chemical Communications*, 2833-2835 (2009).
142. LaChance-Galang, K.J. & Clarke, M.J. Disproportionation of [(py)(NH₃)₄Ru^{III}] at the N7 of Guanine Nucleosides: Severing the N-Glycosidic Bond. *Inorganic Chemistry*, **35**, 6021-6026 (1996).
143. Zhao, H., Guo, X., Chu, L., He, Y. & Chen, Q. Complex self-assembly of pyrimido[4,5-*d*]pyrimidine nucleoside supramolecular structures. *Nature Communications*, **5**, 3108-3018 (2014).
144. Srinivasan, L. & Taylor, M.R. X-Ray Crystal Structures of Zinc-Adenine and Zinc-Guanine Complexes. *Chemical communications* 1668-1669 (1970).
145. Amo-Ochoa, P., Castillo, O., Guijarro, A., Sanz Miguel, P.J. & Zamora, F. Supramolecular architectures based on 6-purinethione complexes. *Inorganica Chimica Acta*, **417**, 142-147 (2014).
146. Dubler, E. & Gyr, E. New Metal Complexes of the Antitumor Drug 6-Mercaptopurine. Syntheses and X-ray Structural Characterizations of Dichloro(6-mercaptopurinium)copper(I), Dichlorotetrakis(6-mercaptopurine)cadmium(II), and Bis (6-mercaptopurinato)cadmium (II) Dihydrate. *Inorganic chemistry*, **27**, 1466-1473 (1988).
147. Sletten, E. & Flogstad, N. Crystallographic Studies on Metal-Nucleotide Base Complexes. VII. Di-9-methylguaninetriaquocopper(II) Sulphate Trihydrate. *Acta Crystallographica*, **B32**, 461 (1976).
148. Cuin, A., Leite, C.Q., Heinrich, T.A. & Costa-Neto, C.M. 6-Mercaptopurine complexes with silver and gold ions: anti-tuberculosis and anti-cancer activities. *Biomedicine & Pharmacotherapy*, **65**, 334-338 (2011).
149. Douglas, J.F. Theoretical issues relating to thermally reversible gelation by supermolecular fiber formation. *Langmuir*, **25**, 8386-8391 (2009).
150. Huisman, B.A., Bolhuis, P.G. & Fasolino, A. Phase transition to bundles of flexible supramolecular polymers. *Physical Review Letters*, **100**, 188301-188304 (2008).
151. Matyjaszewski, K. Architecturally Complex Polymers with Controlled Heterogeneity. *Science*, **333**, 1104-1105 (2011).
152. Ariga, K. & Kunitake, T. Supramolecular Chemistry –Fundamentals and Applications Advanced Textbook. Springer-Verlag Berlin Heidelberg, Germany. (2006).

153. Li, Z.-T. & Wu, L.-Z. Hydrogen Bonded Supramolecular Structures. Volume 87. Zhang, D-W, Wang, H, and Li, Z-T. Chapter 1. Hydrogen Bonding Motifs: New Progresses. Springer-Verlag GmbH Berlin Heidelberg (2015).
154. Steed, J.W., Turner, D.R. & Wallace, K.J. Core Concepts in Supramolecular Chemistry and Nanochemistry. Jeffery, G. A., An Introduction to Hydrogen Bonding, Oxford University. Press, Oxford, UK, 1997. (2007).
155. Watson, D.J. Molecular Biology of the Gene, Fifth Edition. Chapter 6: The Structures of DNA and RNA. Person Benjamin Cuommings (2004).
156. Li, X., Gao, Y., Boott, C.E., Winnik, M.A. & Manners, I. Non-covalent synthesis of supermicelles with complex architectures using spatially confined hydrogen-bonding interactions. *Nature Communications*, **6**, 8127 (2015).
157. Scheiner, S. Noncovalent Forces. Biswal, Himansu S. Chapter 2. Hydrogen Bonds Involving Sulfur: New Insights from ab Initio Calculations and Gas Phase Laser Spectroscopy. Springer International Publishing Switzerland. 15-45 (2015).
158. Biswal, H.S. & Wategaonkar, S. Nature of the N-H...S Hydrogen Bond. *The Journal of Physical Chemistry A*, **113**, 12763-12773 (2009).
159. Perrin, C.L. & Nielson, J.B. "Strong" Hydrogen Bonds In Chemistry And Biology. *Annual Review of Physical Chemistry*, **48**, 511-544 (1997).
160. Rajagopal, S. & Vishveshwara, S. Short hydrogen bonds in proteins. *Federation of European Biochemical Societies (FEBS)*, **272**, 1819-1832 (2005).

Chapter 2. Experimental Methods

2.1 Chemicals and Materials

All chemicals were purchased from Sigma Aldrich and were used as received without further purification. Deionized water (nominal resistivity 18 M Ω cm) was obtained from a NanopureTM purification system, Barnstead). 2'Deoxy-6-thioguanosine was prepared under N₂ using standard Schlenk techniques. ¹H and ¹³C NMR spectra were performed on a Bruker Advance 300 spectrometer at 300 MHz and 500 MHz, with DMSO-*d*₆ and D₂O as a solvent. Electrospray mass spectra (MS-ESI) were recorded on a Waters Micromass LCT Premier mass spectrometer and Matrix-assisted laser desorption and ionization time-of-flight mass spectrometry (MALDI-TOF-MS) with matrix HCCA (α -Cyano-4-hydroxycinnamic acid). Elemental analysis, % C.H.N, was performed with a Carlo-Erba CE1108 in the School of Chemistry at Newcastle University and by the elemental analysis service (Stephen Boyer, London Metropolitan University).

2.2 Silicon Chips preparation for AFM, XPS, and FTIR

p-type silicon (100) chips were used as the substrate for AFM, XPS and FTIR measurements. Silicon wafers were cut into chips approximately 1 cm² for AFM, XPS, and 4 cm² for FTIR analysis, and were cleaned by placing in piranha solution (1:4, H₂O₂:H₂SO₄) for 1 h, then washed with deionised water and dried with nitrogen gas.

2.3 Characterization of gels

The composition of the gels was characterized by various techniques: UV-Vis-spectroscopy, Fourier transform infrared (FTIR), circular dichroism (CD), X-ray photoelectron spectroscopy (XPS), powder X-ray diffraction (XRD), fluorescence spectroscopy, and elemental (C.H.N) analysis. Atomic force microscopy (AFM), transmission electron microscopy (TEM), and epifluorescence microscopy were used to determine the morphology of the xerogels. The electrical conductivity measurements of the xerogel fibres were measured using a probe station (Cascade Microtech with Agilent B1500A semiconductor parameter analyser and a Model ETC-200L, ESPEC-Japan temperature controller). In general, few of the compounds produced crystals of a size and quality suited to single crystal X-ray diffraction and those which did required a high intensity source to obtain usable data. These samples were investigated at the

Diamond Light Source, which was used to collect the single crystal diffraction data for the products produced from the reaction of some substituted nucleosides with silver ions.

2.3.1 Fourier transform infrared (FTIR) spectroscopy

Due to the large number of absorption bands in the mid IR range, infrared spectroscopy can provide detailed information about chemical structure. These bands may be assigned to vibrations of functional groups in a compound and provide evidence for particular chemical bonds in the structure. The traditional IR spectrometer consists of: 1- a radiation source using electrical heating (1000-1800°C) of a Nernst filament (zirconium or cerium oxide) or globar (silicon carbide) to produce black-body radiation; 2- a sample cell which normally comprises alkali metal halides such as NaCl, KCl, etc, because these materials are transparent in the IR region of the spectrum; 3- a monochromator which disperses the beam into different frequencies or wavenumbers and 4- a detector which measures the radiant energy. The spectra are presented as either transmittance ($\%T = 100 \cdot I_{\text{sample}}/I_{\text{blank}}$) or absorbance ($A = \log_{10} I_{\text{blank}}/I_{\text{sample}}$) against wavenumber. The FTIR instrument has many of the same elements, but includes a Michelson interferometer,¹ Fig. 2.1. The beam splitter directs half the incident light to a moving and half to a fixed mirror. After the beams are reflected from the mirrors they are combine into a single beam, passed to the sample and recorded by the detector. As the pathlength is changed with the movement of one mirror, different wavenumbers of light come into constructive interference when the beams recombine; this results in a time-varying light intensity at the sample and detector. Fourier transformation by the FFT algorithm converts the time-varying signal to a spectrum (intensity against wavenumber or frequency). The FT spectrometer now dominates because all frequencies are present at the sample at once and this results in advantages of speed and signal-to-noise ratio over traditional instruments.

Molecular vibration frequencies depend on atomic masses and the bond force constants, $\bar{\nu} = \frac{1}{2\pi c} \sqrt{\frac{k}{\mu}}$ where c is the speed of light, k the force constant and μ the reduced mass. High wavenumber vibrations are typically stretching modes of groups containing light atoms. Bending/deformation modes have low k and appear at lower wavenumbers.² In this project, FT-IR spectroscopy was carried out using a Varian 800 FT-IR instrument in transmittance mode with 60 scans co-added and averaged and 16 cm^{-1} spectral resolution in the range from 400 to 4000 cm^{-1} . Typically, the sample was prepared by depositing $10 \text{ }\mu\text{L}$ of freshly prepared gel on a clean p-Si (100) wafer ($2 \text{ cm} \times 2 \text{ cm}$) and left to dry by air overnight prior to analysis.

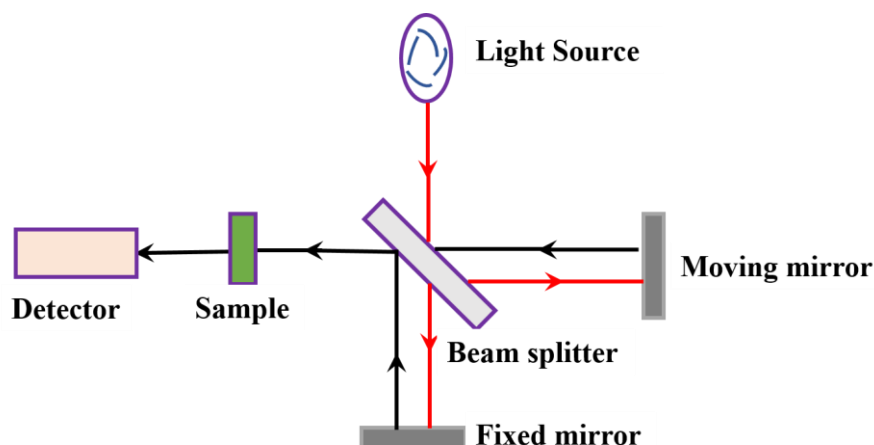


Figure 2.1. Schematic diagram of an FTIR spectrometer.¹ Interference between the beams shown as the pathlength is adjusted by the moving mirror produces a time-varying intensity at the sample. The variation of intensity with time can be Fourier-transformed into a variation with wavenumber in order to display the spectrum.

2.3.2 UV-Visible absorption spectroscopy

UV-Vis absorption spectroscopy refers to absorption spectra of light with wavelengths in range about 200-800 nm. Strictly, the visible region is 400-700 nm, but many spectrometers extend the longer wavelength range slightly. Below 200 nm is the vacuum ultraviolet region.³ A typical UV-Vis spectrometer consists of a radiation source, monochromator, detector, amplifier, and recorder, as shown below in Fig.2.2. The radiation source for the UV region may be a hydrogen or deuterium discharge lamp. A separate source is usually required for the visible region, e.g., a tungsten filament lamp for the wavenumber range 400 nm to 800 nm. Directly after the light source, a monochromator disperses the light into different wavelengths and, unlike FT instruments, a narrow band of wavelengths is directed to the sample at any one time. Quartz optical components are most commonly used for this task as they are transparent in UV region, while glass may be used in visible region. In a double beam instrument, the light is passed to a beam divider in order to generate two equivalent intensity beams: the sample beam and the reference (blank) beam which pass through the sample cell and the reference (blank) cell, respectively. The other component is the detector which is normally a photomultiplier tube. UV-Vis spectra are recorded by scanning the monochromator through the desired wavelength range and the data are presented as absorbance ($A = \log_{10} I_{\text{blank}}/I_{\text{sample}}$) against wavenumber.

The metal-ligand complexation reactions in this work were monitored by UV-Vis absorption spectroscopy and the absorbance spectra of the ligands (nucleobases and nucleosides) and the

gels (metal- nucleobases, nucleosides) were recorded *in situ* on a Cary 100 Bio UV-Visible Spectrophotometer at room temperature with a typical wavelength range 200-600 nm. A quartz cuvette was used to measure the absorbance of the gel by dropping cast 10 μL of the gel on the one side of the cuvette to form a thin layer in a cavity in the quartz slide. The sample was left overnight at room temperature to dry by air prior to measurement.

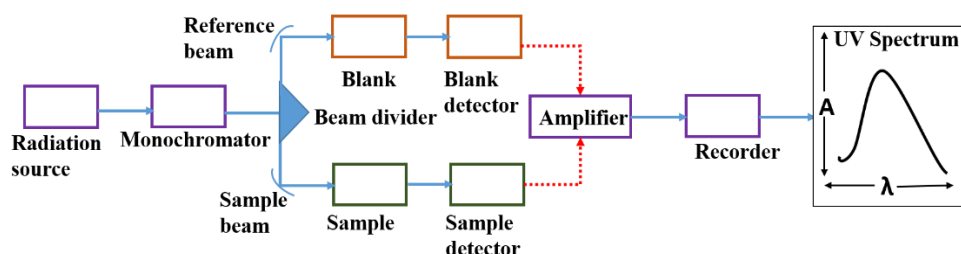
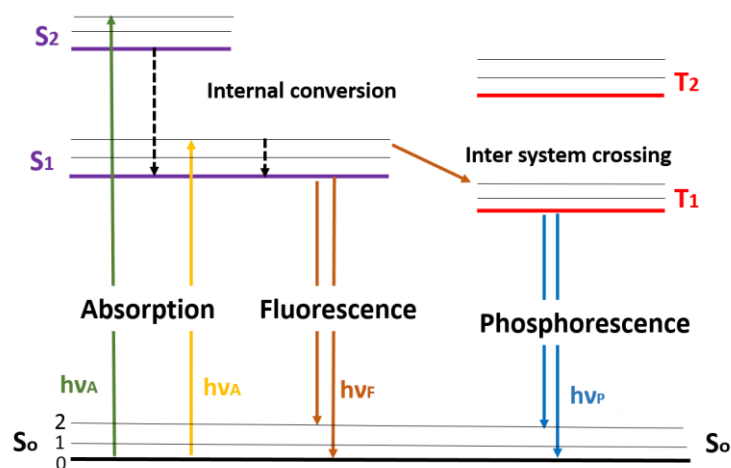


Figure 2.2. Schematic diagram of a double-beam UV-Vis spectrometer.²

2.3.3 Fluorescence spectroscopy

A typical Perrin-Jablonski diagram is shown in Scheme 2.1; it illustrates three processes: absorption, phosphorescence, and fluorescence. S_0 , S_1 , and S_2 refer to the singlet ground state, first and second singlet excited electronic states, respectively. The vertical lines depict the transitions between the electronic states—the Franck Condon principle states that because nuclei are so much more massive than electrons, the electronic transition takes place before the nuclei can respond. The transition from lowest vibrational energy level of the ground electronic state (S_0) to vibration energy levels in the S_1 and S_2 excited electronic states, occurs in very short times (10^{-15} s) this process is called absorption. However, a consideration of the fact that the equilibrium geometry of the upper state is usually different than of the ground state and the Franck-Condon shows that the transition is to vibrationally excited states of S_1 or S_2 . Return to the ground vibrational state of S_1 by vibrational relaxation (smaller dashed arrow) occurs within 10^{-12} s. Fluorescence emission (typical lifetime 10^{-8} s) occurs from S_1 with wavelength higher than that for absorption because of the energy lost as heat in vibrational relaxation and because the transition to S_0 does not go directly to the ground vibrational level (Franck-Condon principle again), but to a vibrationally excited state followed by relaxation to the original ground vibrational state of S_0 . Internal conversion is illustrated by the larger dashed arrow, it occurs rapidly (10^{-12} s) and usually much faster than fluorescence from S_2 , this gives rise to Kasha's rule that fluorescence occurs from S_1 even if the initial absorption event reaches a higher excited electronic state. Another process of importance is the crossing from S_1 to the first excited triplet state T_1 , this is called inter system crossing. After vibrational relaxation in

T_1 , emission from T_1 is called phosphorescence which occurs at higher wavelength (lower energy) compared to fluorescence. The transition from T_1 to the ground state is spectroscopically “forbidden” and occurs at a much slower rate / with a longer lifetime than fluorescence (μs or longer). However, the presence of heavy halide atoms such as iodine and bromine increases spin-orbit coupling and normally enhances the rates of inter crossing system and phosphorescence.⁴



Scheme 2.1. Perrin-Jablonski diagram⁴. $h\nu_A$ indicates energy changes associated with absorption processes; $h\nu_F$ is the energy of the photon produced by fluorescence and $h\nu_P$ is the energy of a photon produced by phosphorescence (involves a non-zero spin change).

A typical instrument is shown in Fig. 2.3. It comprises a light source (xenon arc lamp), monochromators for excitation and emission, a sample chamber, prism polarizers, and detector.⁵

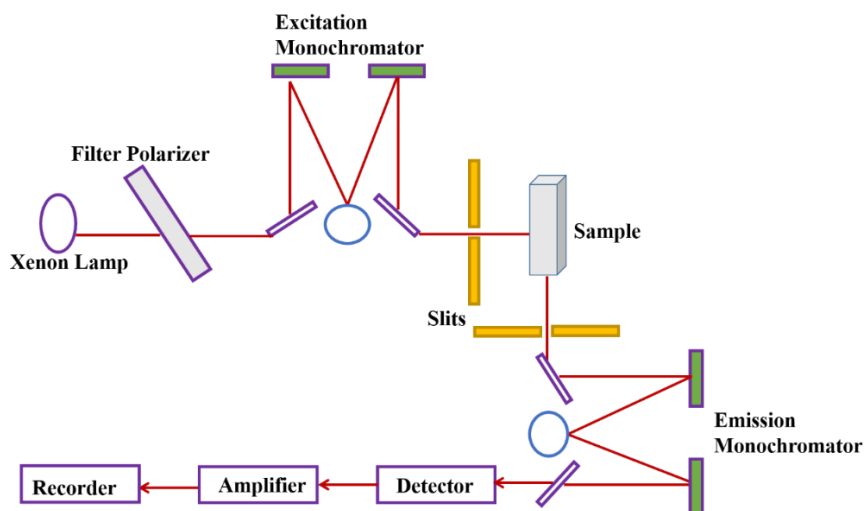


Figure 2.3. Fluorescence spectrometer block diagram.⁶

2.3.4 Circular Dichroism spectroscopy (CD)

Circular dichroism can be described as the difference between the absorption spectrum that is produced using left and right circularly polarized light.⁷ By applying Beer's law, equation (2.1) is obtained:

$$\Delta\varepsilon = \varepsilon_L - \varepsilon_R = \frac{A_L - A_R}{cl} = \frac{\Delta A}{cl} \dots\dots\dots(2.1)$$

Where $\Delta\varepsilon$ and ΔA are the difference between the molar extinction coefficients and the the absorbance for left and right circularly-polarized light respectively. c is the molar concentration in mol/L, and l is the pathlength of the cuvette. The unit that used for measuring the CD signal is degree of ellipticity (θ); the origin of this unit relates to the means of obtaining the spectra before photoelastic modulators became available that produce alternating beams of left and right circularly polarized light⁸. Molar ellipticity $[\theta] = 3298.2\Delta\varepsilon$ traditional $\text{deg cm}^2 \text{dmol}^{-1}$.

Circular dichroism (CD) is an important technique for the study of chiral structures in part of this work. Circular dichroism spectra were recorded on a Jasco J-810 spectrometer with conditions: path length 0.01mm, sensitivity 100 mdeg, data pitch 0.2 nm, scan speed 10 nm/min, response time 2 secs, bandwidth 2 nm, and 3 accumulations. Fig. 2.4 displays a block diagram of a CD spectrometer; Scheme 2.2 illustrates left and right circularly polarized light.⁹

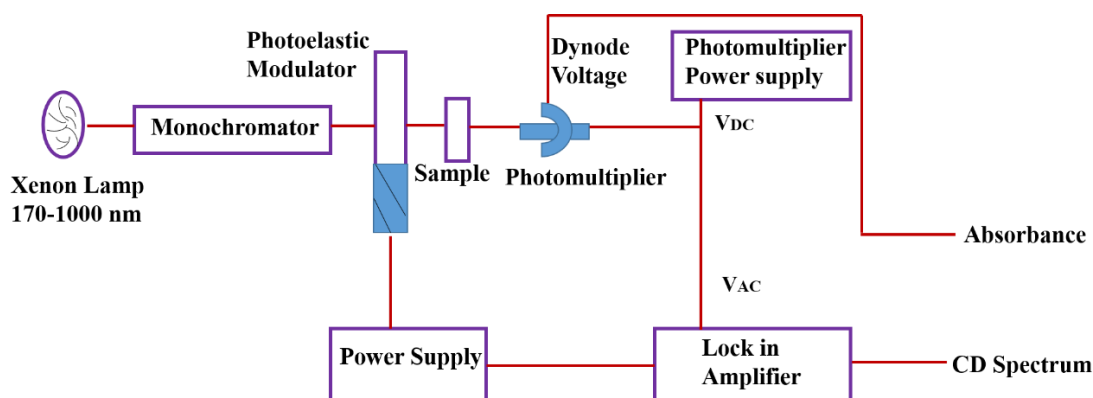
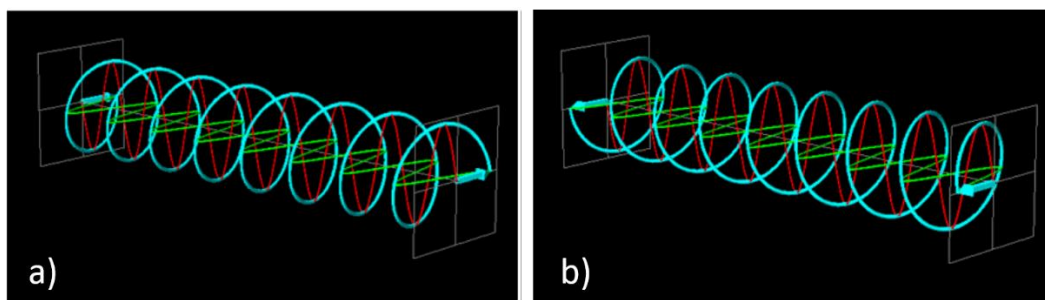


Figure 2.4. CD spectrometer block diagram.⁷



Scheme 2.2. Diagram of left (a) and right (b) circularly polarized light.⁹

2.3.5 X-Ray Photoelectron Spectroscopy (XPS)

XPS spectra were acquired using a Thermo Scientific K-Alpha X-ray photoelectron spectrometer (Thermo Electron Corp., East Grinstead, UK), equipped with an Al K α X-ray source (1486.6 eV). A take-off angle of 90° was used during data acquisition, and a charge neutralisation gun was used to compensate for surface charging. The CasaXPS software (Casa, <http://www.casaxps.com>, USA) was used to analyse the XPS spectra. All binding energies were calibrated with either the Au 4f signal at 84.8 eV or the C1s peak at 284.6 eV as reference. Wide scan (survey) spectra were recorded at a pass energy of 150 eV and 1 eV/step, while narrow scan (higher resolution) spectra were recorded at a pass energy of 50 eV and 0.1 eV/step. The sample was prepared by depositing 10 μ L of the gel onto a clean Si (100) chip (1 cm x 1cm), followed by air drying at room temperature prior to analysis.

2.3.6 Crystal and Powder X-Ray Diffraction (XRD)

XRD is used to characterize the chemical structure of crystalline compounds. The energies of X-rays are in range of 100eV-10MeV and correspond to wavelengths in range of 0.01 -10 nm.¹⁰ There are two principal ways used to generate X-rays.¹¹ Laboratory sources employ a metal target bombarded with high energy electrons which are characteristic of the metal chosen. Synchrotron sources accelerate high electron energy electrons in a circular ring and produce X-rays at tangents to the ring. Synchrotron sources have high brightness and produce a range of X-ray wavelengths. In this work, they have been used to study some weakly-diffracting crystals not amenable to analysis by lab-based technology. As well as structural analysis, XRD may also be used to determine the size of crystallites in a powder by using Scherrer's equation (eq. 2.2)¹⁰ which takes into account the incompleteness of constructive/destructive interference in small particles and predicts a finite breadth to the diffraction peaks. Diffraction from a macroscopic single crystal occurs at a specific angle (θ) because of interference effects

according to Bragg's Law (eq. 2.3). However, in a small crystal or microcrystalline powder, incomplete interference (and instrumental limitations) result in finite diffracted intensity at angles slightly different from the Bragg angle. Smaller crystals yield broader, less intense peaks and the quantitative relation is:

$$t = \frac{K\lambda}{B_{1/2} \cos \theta_B} \quad (2.2)$$

Where t is diameter of the crystallites, K is the Scherrer constant which is ≈ 0.9 , $B_{1/2}$ is the full width at half maximum (FWHM) of the diffraction peak. θ is the Bragg angle (eq. 2.3).

$$n\lambda = 2d \sin \theta \quad (2.3)$$

Where n is order of reflection, λ is the wavelength of the X-ray beam, d is the distance between lattice planes, and θ is the angle of diffraction. The scattering of X-rays depends on the atomic number; generally, only a small fraction of the incident beam is scattered of each lattice plane. Most of the beam can penetrate to lower planes and a portion will be scattered from each of these. All the scattered beams will interfere constructively when their pathlengths are different by an integer multiple of the X-ray wavelength. The bold lines in Fig. 2.5 refer to the path length difference as:

$$AB = d \sin \theta, \quad AD = d \sin \theta, \quad \text{then:} \quad AB + AD = 2d \sin \theta$$

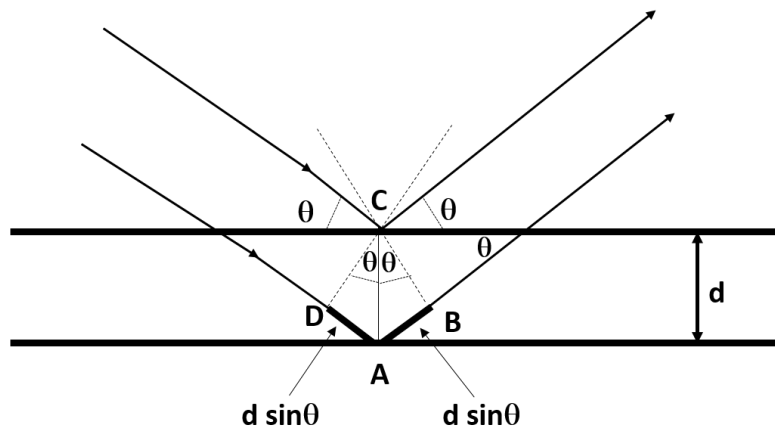


Figure 2.5. Bragg diffraction describes the scattering of an incident beam from crystal planes separated by a distance d and constructive/destructive interference of the scattered beams at an angle θ to the normal. The pathlength difference is $AB + AD$ and constructive interference occurs when this is an integer multiple of the X-ray wavelength.¹²

In this work, powder XRD data was acquired using a PANalytical X'Pert Pro diffractometer (PANalytical) using Cu $K\alpha$ radiation source ($\lambda = 1.54 \text{ \AA}$). Samples were prepared by drop-

casting 10 μL of the gel onto a glass slide and leaving it to dry in air prior to analysis. Some crystals of coordination complexes were investigated by single crystal diffraction at the Diamond Light Source.

2.4 Gel characterization with the scanning probe microscope (SPM)

2.4.1 Atomic force microscope (AFM)

Atomic force microscopy is a technique that is used to image the topography of a sample surface with high resolution and produces a three-dimensional image; it was invented by Binnig¹³ in 1986. AFM is one of the scanning probe microscopes (SPMs), a family of techniques that includes the scanning tunnelling microscope (STM) and scanning near field optical microscope (SNOM). All these techniques use a sharp probe (tip) which interacts with the sample as it is scanned over the sample surface. Originally, the motivation was to defeat the diffraction limit, because the spatial resolution is limited by tip size which may be much smaller than the wavelength of visible light. Novel modes of operation have since been developed which allow imaging of various properties (charge, current, adhesion force, mechanical properties, friction etc). The AFM can be classified according to the contact, tip motion, and the nature of the application.¹⁴ There are two common classes of AFM operation contact and non-contact. In contact mode, the tip “touches” the sample (a high tip-sample force is present corresponding to very close contact); this may be destructive towards soft samples. In non-contact modes, the tip oscillates or taps the sample and these modes often result in less sample damage, but sometimes lower resolution. In tapping mode TM, the cantilever is in intermittent contact with the sample, as it is vibrated. During scans both the oscillation amplitude and phase are recorded and no horizontal force is applied to the sample surface, consequently less damage occurs to the sample surface. AFM senses the force on the tip via the deflection of the cantilever to which it is attached. In principle, the deflection x of the tip is related to the force f by Hooke’s law $f = kx$ and the absolute force can be measured after determination of the cantilever spring constant k . However, it is usual to detect the deflection directly using a split photodiode and employ that signal in the feedback loop to control the tip/sample force. The common compositions of the tip & cantilever are silicon or silicon nitride (Si_3N_4).¹³ In general, an AFM will measure both vertical and horizontal deflection of the cantilever, using an optical lever / split photodiode which is cheap and easy to use, and obtains resolution similar to that of an interferometer. The principle of this lever is to reflect a laser beam from the back of the cantilever onto the centre of a photodetector which consists of four

sections. The difference in light intensity on the sections is related to the vertical and horizontal deflection of the light beam and hence the cantilever. In this work, AFM data was acquired using a Multimode 8 atomic force microscope with a NanoscopeV controller (Bruker), and an “E” scanner. Nanoscope software version 9.1 was used to control the microscope. The system was operated in ScanAsyst in Air mode as a peak force tapping mode at ultra-low forces to minimise damage to the samples. To reduce vibrational noise, an isolation table/acoustic enclosure was used (Veeco Inc., Metrology Group). Silicon tips on silicon nitride cantilevers (ScanAsyst, Bruker) were used for imaging. The nominal tip radius was approximately 2 nm, resonant frequency 150 kHz and spring constant $k \sim 0.7 \text{ N m}^{-1}$. The AFM data were analysed with NanoScope Analysis 1.5 software (Bruker). The sample was prepared by adding 2 μl of the gel onto a clean silicon wafer (1 cm x 1 cm) and drying in air. Fig. 2.6 shows the main parts of the AFM.

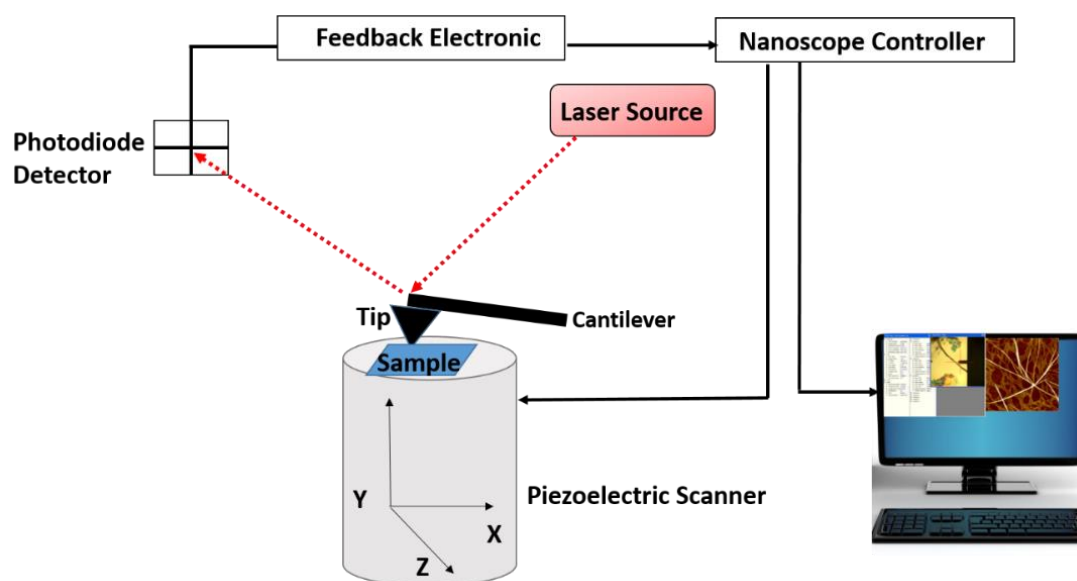


Figure 2.6 Atomic Force Microscope (AFM) components & block diagram.

2.4.2 Epifluorescence Microscope

Fluorescence images were obtained by using Zeiss Epifluorescence Microscope. The excitation light was provided by a mercury lamp with a filter to select wavelengths from 300 to 400 nm with 65% maximum transmission at 365 nm. A long-pass filter was used to separate the emitted light from the scattered light with a cut off at 420 nm and the image was collected with a

monochrome CCD camera. The samples were prepared by depositing 2 μL of diluted hydrogel on silicon wafer and were dried in air.

2.4.3 Transmission electron microscope (TEM)

Transmission electron microscopy is a technique that is used to record images of a thin sample with magnification in the range 10^3 - 10^6 , it is also can be used to analyse crystalline samples by producing an electron diffraction pattern. All these processes are done using a source of electrons accelerated to a high energy called an electron gun.¹⁵ In TEM a beam of electrons is used to irradiate a thin film of sample with acceleration voltage in range of 100-200 kV, in some cases acceleration voltages of 200-500 kV is used to enhance the resolution and voltage of 500 kV-3MV is the highest voltage electron microscopy can be used (HVEM).¹⁶ Higher voltages produce shorter wavelength electrons via the de Broglie relation and, in principle, higher resolution images. Fig. 2.7 displays the components of a TEM microscope. In this work, TEM measurements were acquired using Philips CM100 electron microscope at accelerating voltage 100 kV with high resolution digital image. The sample was prepared by dropping 2 μL of diluted gel onto a carbon coated copper grid and left to dry overnight in air prior to analysis.

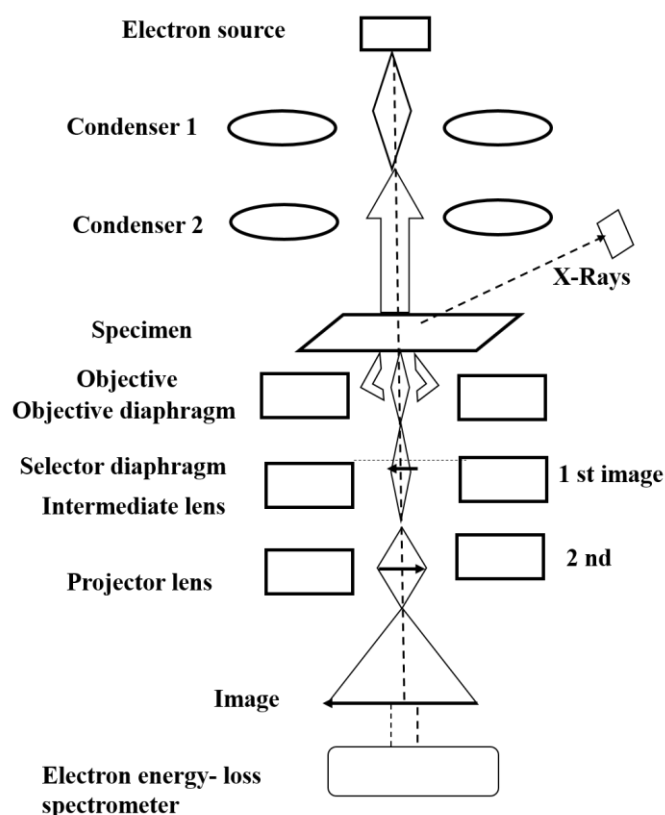


Figure 2.7. A block diagram of a TEM.¹⁶

2.5 Electrical measurements

All the electrical measurements were carried out under dry nitrogen without light illumination. Current-voltage measurements at different temperatures were measured on the probe station (Cascade Microtech, Inc., Oregon, USA) using a thermal chuck system (Model ETC-200L, ESPEC, Japan). Platinum microband electrodes (MBEs) (MBEs; Smart Microsystems Pt MB-4000, Windsor Scientific Ltd. Slough, UK) were used to fabricate electronic devices for electrical characterisation of Au:6-thioguanosine gel. The MBEs were made up of Si/SiO₂ substrates. Four independent platinum electrodes were patterned on the top of the SiO₂ layer. The height of the electrodes is 200 nm and their width is 10 μ m with 10 μ m spaces between them. The surfaces of the MBEs were electrical insulated except 2 x 2 mm² area for depositing the gel, as shown in Fig. 2.8 (A). Devices were fabricated by depositing the gel onto the Platinum MBEs. The platinum MBEs were washed with ethanol and dried with nitrogen gas. The clean platinum electrodes were analysed on a probe station and reference current/voltage curves were recorded which showed the background currents to be less than 100 fA at 2 V. For the device, A drop (~1 μ l) of Au:6-thioguanosine gel was casted onto the uninsulated area on the MBE. The device was left to dry for a week in Schlenk flask, which was maintained on a vacuum line (~750 mbar) at a temperature of 45 °C. The gel droplet dried to produce a film of the Au:6-thioguanosine fibres across the Pt-electrodes, as shown in Fig. 2.8 (B) and (D). The electrodes were connected to the probe station and current / voltage curves were collected. For doping, the xerogel was exposed to iodine or tris(4-bromophenyl)ammoniumyl hexachloroantimonate ([Br(C₆H₄)₃N]SbCl₆). In the former case, the xerogel on platinum MBEs was exposed to iodine vapor for 1h by heating 0.1 g of iodine to 45 °C in a 50 ml round bottom glass flask. For the latter, the xerogel on MBEs was treated with a drop (~1 μ l) of 0.1 M of ([Br(C₆H₄)₃N]SbCl₆) in anhydrous acetonitrile. The gel was left to dry for 30 min before the current/voltage curve was collected. Control experiments where iodine or ([Br(C₆H₄)₃N]SbCl₆) was applied to MBEs in the absence of Au:6-thioguanosine xerogel showed negligible background currents.

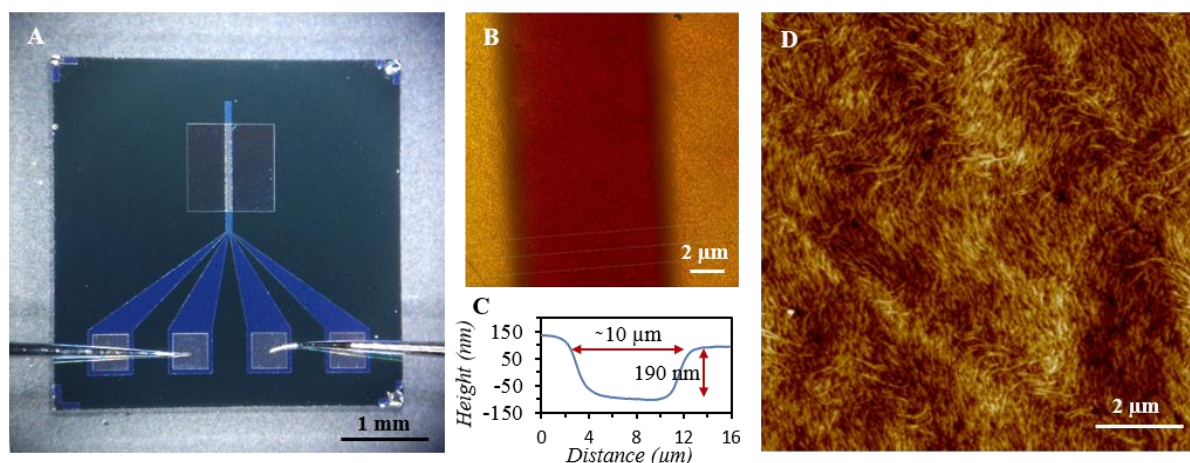


Figure 2.8. (A) An optical microscopy image of the microband electrodes (MBE) on the probe station, showing the contact pads and needle probes at the bottom and the 10 μm -spaced Pt electrodes in the square region above, (B) AFM height image of a Au:6-TGR xerogel drop-cast onto the area between two microelectrodes, (C) a profile of the electrode gap region and (D) AFM height image of the xerogel between the microelectrodes.

References

1. Smith, B.C. Fundamentals of Fourier Transform Infrared Spectroscopy, Second Edition-CRC Press. Taylor and Francis Group, LLC. (2011).
2. Yadav.L. Organic Spectroscopy. Springer-Science+Business Media, B. V. (2005).
3. Anderson, R.J. & Bendell, D.J. Organic Spectroscopic Analysis. The Royal Society of Chemistry, Thomas Graham House. Science Park. Milton Road, Cambridge CB4 0WF, UK. (2004).
4. Lakowicz, J.R. Principles of Fluorescence Spectroscopy.Third Edition. Springer Science+Business Media, LLC. (1983).
5. Müllertz, A., Perrie, Y. & Rades, T. Analytical Techniques in the Pharmaceutical Sciences. Bagatolli, L. A. Chapter 2, Fluorescence Spectroscopy: Basic Foundations and Methods. Springer Science+Business Media LLC New York., 29-59 (2016).
6. Resch-Genger, U. Standardization and Quality Assurance in Fluorescence Measurements I,Techniques. Zwinkels, J. Surface Fluorescence: the Only StandardizedMethod of Measuring Luminescence. Springer-Verlag Berlin Heidelberg. 5, 163-192 (2008).
7. Jones, C., Mulloy, B. & Thomas, A.H. Methods In Molecular Biology, Vol 22. Microscopy, Optical Spectroscopy, and Macroscopic Techniques. Drake, A. E. Circular Dichroism, Chapter 16, p. 219. Humana Press Inc , Totowa, NJ (1994).

8. Nagao, K., Atsuya, M. & John, M. Circular Dichroism and Magnetic Circular Dichroism Spectroscopy for Organic Chemists. The Royal Society of Chemistry, Thomas Graham House. Science Park. Milton Road, Cambridge CB4 0WF, UK. (2012).
9. <https://www.chem.uci.edu/~dmitryf/manuals/Fundamentals/CD%20spectroscopy.pdf>. Download 17/8/2017.
10. Waseda, Y. & Shinoda, K. X-Ray Diffraction Crystallography. Springer-Verlag Berlin Heidelberg. (2011).
11. Pecharsky, V.K. & Zavalij, P.Y. Fundamentals of Powder Diffraction and Structural Characterization of Materials. Springer Science+Business Media, Inc. (2003).
12. Fultz, B. & Howe, J. Transmission Electron Microscopy and Diffractometry of Materials. Fourth Edition. Springer-Verlag Berlin Heidelberg. (2013).
13. Binnig, G., Quate, C.F. & Gerber, C. Atomic force microscope. *Physical Review Letters*, **56**, 930-933 (1986).
14. Bhushan, B. Scanning Probe Microscopy in Nanoscience and Nanotechnology. Springer-Verlag Berlin Heidelberg. (2010).
15. Egerton, R.F. Physical Principles of Electron Microscopy. An Introduction to TEM, SEM, and AEM. Second Edition. Springer International Publishing Switzerland. (2016).
16. Reimer, L. & Kohl, H. Transmission Electron Microscopy Physics of Image Formation. Springer Science+Business Media, LLC. (2008).

Chapter 3. Au (I):6-Thioguanosine Hydrogel

3.1 Introduction

Gold is known as a noble metal and often cited as the most noble, or least reactive¹ among all metals. It is the most electronegative metal on the Pauling scale and its cations are strong oxidants. The red-yellow colour of the gold is assigned to the transition from filled orbital 5d to 6s (Fermi level) upon the absorption of blue and violet light in the visible reign around 2.4 eV. Gold is a soft metal and easy to stretch to form a wire (ductile); it is also very malleable. The common oxidation state of gold is (III) and (I).²⁻⁴

Nucleosides display a rich coordination chemistry because of the different binding sites available in these nitrogen bases; these include metal-ion binding modes that give rise to multinuclear, oligo, and polymeric structures.^{5,6} The resulting metal complexes can exhibit additional supramolecular interactions due to hydrogen bonding and such properties are important in the formation of metallogels.⁷⁻⁹

Simple thiopurines are sulfur-containing analogues of natural nucleosides, commonly used in treating a variety of medical conditions. They are readily incorporated into nucleic acids which, in fact, is a feature of their mode of action upon metabolism.¹⁰ Their metal-ion specificity and binding modes are different from the natural derivatives, most notably in their aurophilicity and an ability to form coordination chain polymers *via* a single-atom-bridge as $\{-\text{metal}-\mu\text{S}-\}_n$.^{11,12} This was the basis of the hypothesis that synthesis of a gold-based polymer with such a nucleoside variant could provide a material with the required extended bonding motif for gel formation and even conductivity. Importantly, the aurophilicity of the thiol group would avoid competing reactions with metal ion binding sites on the natural nucleosides and so could be readily integrated into the framework of duplex DNA structures. The reaction of equimolar equivalents of Au(I) ions with the sulfur-modified nucleoside, 6- thioguanosine (6-TGR) in aqueous-based solution at basic pH spontaneously forms a luminescent hydrogel. The broad luminescence ~606 nm is characteristic of the formation of oligomeric gold-thiolate species.^{13,14} Further characterization by a range of techniques was used to establish that the reaction yields a gold(I)-thiolate coordination polymer of general formula $\{-\text{Au}-\mu\text{-6-TGR}-\}_n$.

3.2 Experimental

3.2.1 Synthesis of Gold:6-Thioguanosine (Au:6-TGR) gel with 10 mg /ml 6-TGR

Au:6-TGR gel was prepared with a 1:1 metal / nucleoside molar ratio. Gelation was observed when an Au(I) solution, prepared by reduction of HAuCl_4 with two equivalents of thiodiglycol ($\text{HO}(\text{CH}_2)_2\text{S}(\text{CH}_2)_2\text{OH}$), was added to the TGR solution. A typical sample of gel was prepared by adding the solution of HAuCl_4 (13 mg, 0.033 mmol in 40 μL MeOH and 160 μL H_2O), after reduction with 5 μL of thiodiglycol, to the warm solution of TGR (10 mg, 0.033 mmol in 400 μL 0.1 N NaOH, 200 μL MeOH, and 200 μL H_2O) after gently shaking the mixture, the resulting was 1 ml of yellow gel, that was stable to inversion in a vial.

3.2.2 Synthesis Gold:6-Thioguanosine (Au:6-TGR) solutions with concentration 1, 0.1, and 0.01 mg of 6-TGR

To study the morphology of the Au:6-thioguanosine polymer, a series of Au:6-TGR solutions with mole ratio 1:1 and with concentrations 1, 0.1, and 0.01 mg/ml of TGR were prepared by the same procedure that was used to prepare the Au:6-TGR gel at a concentration of 10 mg/ml of TGR. The sole difference in procedure was that both the solutions of Au(I) and TGR were diluted with water and then mixed with each other to give solutions of Au:6-TGR diluted by factors of: 10, 100, or 1000 times compared to the 10 mg/ml Au:6-TGR gel. The concentration of TGR in these preparations were 1, 0.1, 0.01 mg/ml. The Au:6-TGR was synthesised with the mole ratio 1:1, the solution of HAuCl_4 (13 mg, 0.033 mmol in 40 μL MeOH and 160 μL H_2O) was reduced with 5 μL thiodiglycol then diluted with water.

TGR solution (10 mg, 0.033 mmol in 400 μL 0.1 N NaOH, 200 μL MeOH, and 200 μL H_2O) was prepared and diluted with water. After appropriate dilution, the Au(I) solution and the TGR solution were mixed, gently shaking the mixture and clear yellow solutions were formed with the concentrations 1, 0.1, 0.01 mg/ml of Au:6-TGR respectively. The samples were prepared for AFM measurement by drop casting 2 μL of the sample on a clean p- Si < 100 > chip and left to dry in air for 24h before AFM. Some samples were taken after different reaction times of 1 min, 1 h, 2 h, and 3 h, drop casted and dried immediately in a stream of N_2 and then investigated by AFM.

3.2.3 Electrical measurements

A drop ($\sim 1 \mu\text{L}$) of Au:6-thioguanosine gel was cast onto the uninsulated area on platinum microband electrodes (MBEs). The MBEs were $10 \mu\text{m}$ wide and with $10 \mu\text{m}$ gaps between. The gel drop was dried under vacuum to produce a thin film of the Au:6-thioguanosine fibres on and between the Pt-electrodes. The electrodes were connected to a probe station and current/voltage curves were collected. For doping, the gel on Platinum MBEs was exposed to iodine vapour for 1h by heating 0.1 g of iodine to 45°C in a 50 ml round bottom glass flask. Current-voltage curves were also collected after oxidation. Control experiments where iodine was applied to MBEs in the absence of gel showed negligible current above background. Treatment with alternative oxidant tris(4-bromophenyl)ammoniumylhexachloroantimonate $[(\text{BrC}_6\text{H}_4)_3\text{NSbCl}_6]$ was also found to result in linear current-voltage characteristics similar obtained with iodine. The xerogel on the MBEs was treated with a drop ($\sim 1 \mu\text{L}$) of 0.1 M of $(\text{BrC}_6\text{H}_4)_3\text{NSbCl}_6$ in anhydrous acetonitrile. The gel was left to dry for 30 min before the current/voltage curve was collected.

3.3 Results & Dissociation

3.3.1. Gold:6-thioguanosine (Au:6-TGR) gel synthesis and characterisation

The reaction of equimolar equivalents of Au(I) ions with the sulfur-modified nucleoside, 6-thioguanosine (6-TGR) in basic solution spontaneously forms a luminescent hydrogel, Fig. 3.1 & 3.5. The broad luminescence $\sim 600 \text{ nm}$ is characteristic of the formation of oligomeric gold-thiolate species.^{13,14} Further characterization by a range of techniques established the reaction to yield a gold(I)-thiolate coordination polymer of general formula $\{-\text{Au}-\mu\text{-6-TGR}-\}_n$.

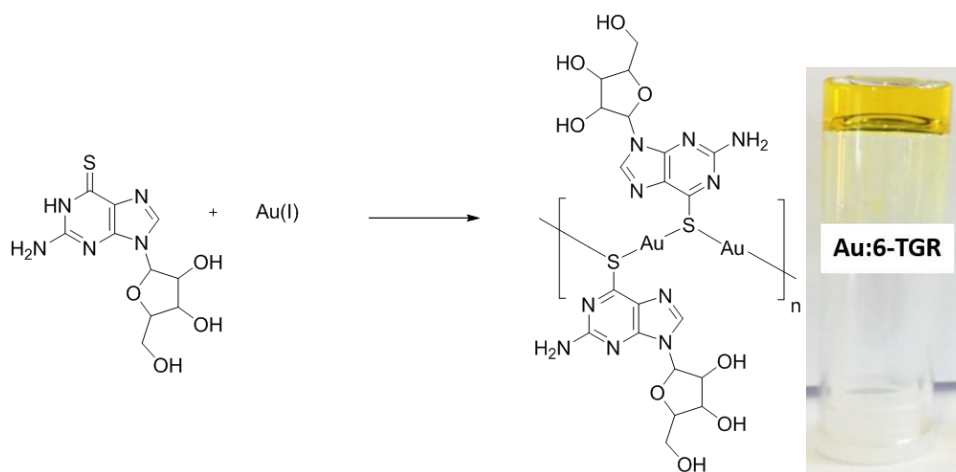


Figure 3.1. Route synthesis of 1:1 Au:6-TGR hydrogel with photograph for the gel.

3.3.2 Fourier transform infrared spectroscopy (FTIR) characterisation

The FTIR spectrum of 6-thioguanosine (6-TGR) in Fig. 3.2 shows stretching band at 1205 cm^{-1} assigned to C=S,¹⁵ this band was absent in the spectrum of Au:6-TGR gel indicating that S atom was involving in the binding by forming charge transfer complex with Au(I), no band was shown in the spectrum of (6-TGR) at 2600 cm^{-1} which belongs to the stretch mode S-H^{16,17} and that confirms that 6-thioguanosine was at thione form rather than thiol tautomeric form.^{15,18}

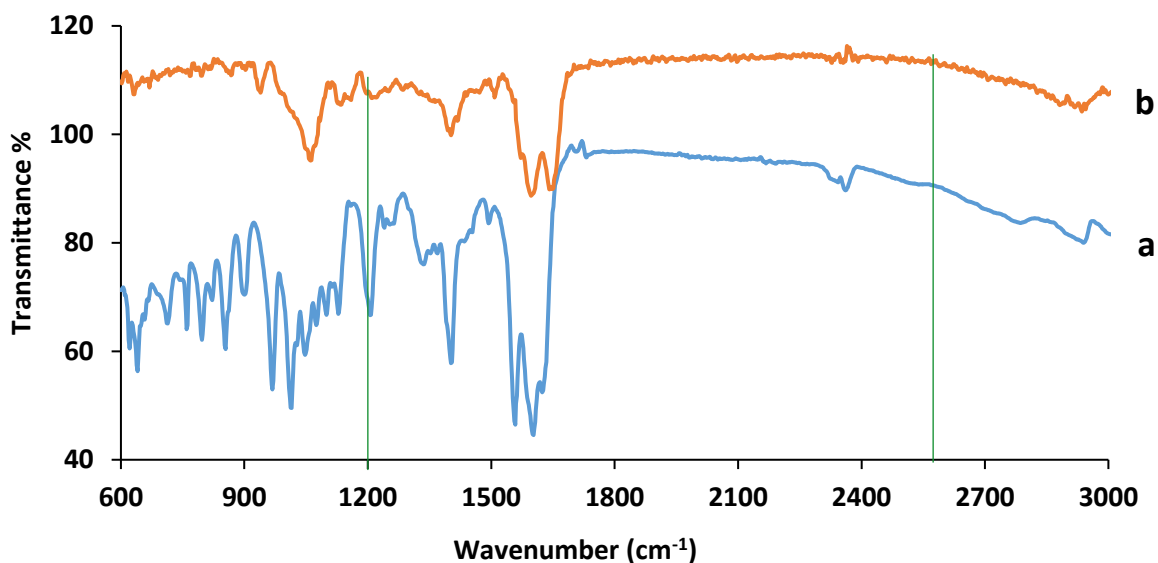


Figure 3.2. Comparison between the FTIR spectra of: a) 6-thioguanosine and b) Au-6-thioguanosine gel.

3.3.3 UV-Vis Absorption spectroscopy

The absorbance spectrum of the 6-thioguanosine nucleoside (6-TGR) solution was investigated at pH 12, the spectrum showed a peak at 326 nm which is typically assigned to π - π^* transitions of the thiol form, Fig. 3.3, however, on going to pH 2, the spectrum was shifted to lower energy (345 nm) indicating that the 6-TGR solution was in the thione form. These data were in good agreement with Zhang.¹⁹ The spectrum of basic solution of 6-TGR at pH 9 that used to react with Au(I) solution showed a peak at 325 nm indicates that the solution was in thiol form as a result of the deprotonation that occurred at N1-H before coordinating with Au(I). A new band was observed at 360 nm after complexation with Au (I), Fig. 3.4. and this suggests the ligand-metal charge transfer transitions (LMCT)^{13,20} of a complex of the thiol form.

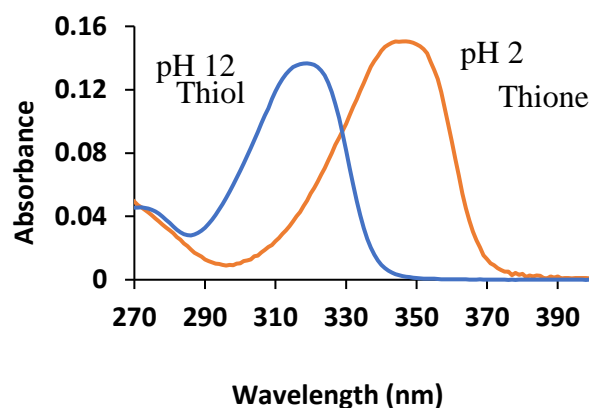


Figure 3.3. Shows absorption spectra of the thione and the thiol forms of 6-thioguanosine (6-TGR) solution at pH 2 (orange line) and pH 12 (blue line), respectively.

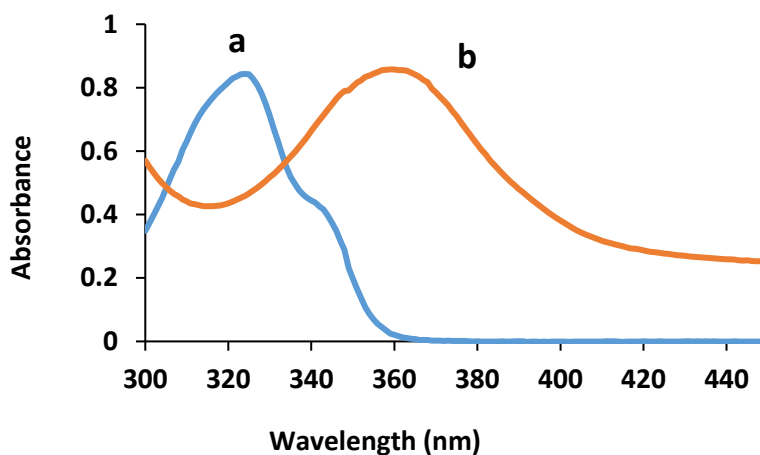


Figure 3.4. UV-Vis absorbance spectrum of: a) 6-thioguanosine (6-TGR) nucleoside and b) spectrum of 50 μM Au:6-TGR gel. A new band was observed at 360 nm after complexation of Au (I) with 6-TGR.

3.3.4 Fluorescence spectroscopy characterization of Au:6-TGR

Luminescent metal complexes are recently of growing interest for their different applications in photochemistry. It is well known that metallophilic interactions are observed with group 11 (Au, Ag, and Cu) where the absolute value of ΔG with Au(I) complexes, for instance, is higher than that of hydrogen bonding, and the Au...Au interaction strength measurement, $V(Re)$, was found to vary from 29-46 kJmol^{-1} .²¹ The strength of Au...Au are observable in the short Au...Au distances. Relativistic effects are considered to be important in strengthening this interaction; such efforts are prominent for heavier elements because they depend on the electron velocity compared to the speed of light and the electron kinetic energy increases with the atomic number. Such interactions can play an interesting role in the photophysics features of the

complexes.²² In addition, the luminescence of gold (I) thiolate complexes can be interpreted in terms of charge transfer transitions from sulfur atom to gold ion ($p\pi(S) \rightarrow p\sigma(Au)$) in which the effect of metallophilic interactions causes stabilization the empty bonding orbital $p\sigma$.^{13,20} Gold also has a very high spin-orbital coupling (5104 cm^{-1}), which contributes to the low triplet state energy;² all these factors strongly affected at the luminescence of gold (I) complexes. The fluorescence emission spectrum of 6-thioguanosine (6-TGR), Fig. 3.5, with excitation at 326 nm indicated a broad band around 347 nm to 514 nm and centred at 416 nm assigned to $\pi-\pi^*$ transitions. While the spectrum of Au:6-TGR gel with excitation at 360 nm showed an emission around 600 nm covering the area from 519 nm to 716 nm; this broad peak suggests that the interaction between Au(I) ions and 6-TGR leads to formation of a complex with lower lying charge transfer excited states (LMCT).

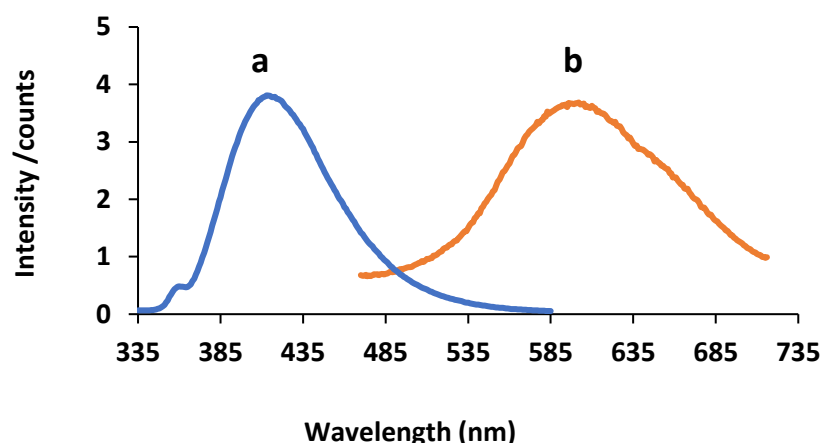


Figure 3.5. The emission spectra of: a) 6-thioguanosine(6-TGR) nucleoside with excitation 320 nm and b) the spectra of Au:6-TGR gel with excitation 360 nm.

The large Stokes shift (11276 cm^{-1}) of the absorption and emission for Au:6-TGR suggest that the emission of the Au:6-TGR hydrogel was from a triplet excited state. Access to the triplet excited state is easy because the presence of Au increases the spin-orbital coupling in Au complexes.^{23,24} According to theoretical calculations of emission spectra, the emission in complexes of the gold(I) is attributed to the triplet state of the metal centre.²⁵

3.3.5 Circular dichroism (CD)

The CD spectrum of the 6-thioguanosine (6-TGR) solution in Fig. 3.6 displays a positive and negative band at 256 and 324 nm assigned to $\pi-\pi^*$ and $n-\pi^*$ transitions of the nucleoside, respectively. However, the corresponding CD spectrum of the Au:6-TGR hydro gel shows a

red shift for the band at 256 nm at the 6-TGR to lower energy (274 nm) alongside with a dramatic increase of intensity of the ellipticity upon the binding with Au(I) ions; this is attributed to increasing base stacking which causes ordering of the bases.^{26,27} In addition the spectrum of the gel shows formation of new negative and positive bands at 384 nm and 420 nm, respectively which are not been seen in the CD spectrum of 6-TGR. This suggests the arrangement of left-handed helical structures for the fibres at the hydrogel.^{28,29} Based on these findings, the Au:6-TGR hydrogel has a highly organized helical structure which is produced by forming a 1D polymer by coordinating Au(I) ions with 6-TGR nucleoside followed by self-assembly of the polymer chains.

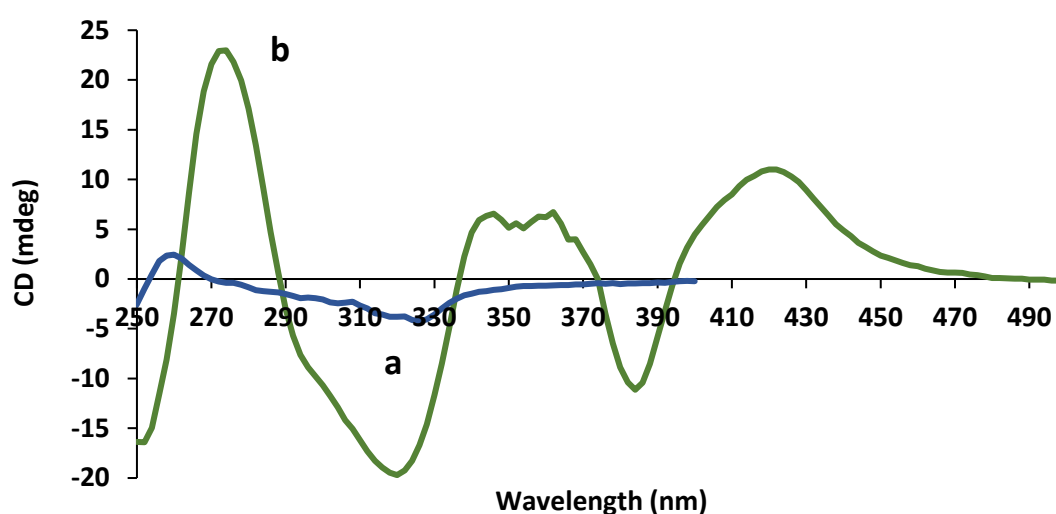


Figure. 3.6 Comparison of CD spectra of: a) 6-thioguanosine (6-TGR) nucleoside (blue line) and b) Au:6-thioguanosine hydrogel (green line), the measurement was carried out with concentration 10 mg / 1.8 ml using quartz cell with path length 0.1 mm for both 6-TGR and the hydrogel.

3.3.6 Powder x-ray diffraction

No sharp Bragg peaks were found in the X-ray diffraction pattern for Au:6-TGR hydrogel in Fig. 3.7 indicating that the sample was amorphous, but instead the data showed broad peaks in the range $20 < Q < 40$. These correspond to distances $d=2\pi/Q$ of 0.318, 0.231, and 0.187 nm which can be assigned to Au...Au, Au-S, and C-S respectively, the data is presented in Table 3.1, this data was a good agreement with the literature that showed the same distances in various other gold complexes.³⁰⁻³³ Larger values of d at distances 0.574 & 0.854 nm which can be assigned to intramolecular Au-Au, and 1.755 nm distance, which can be interpreted as the diameter of the helix, are also can be seen in the range $Q < 15$, as shown in Fig.3.7.

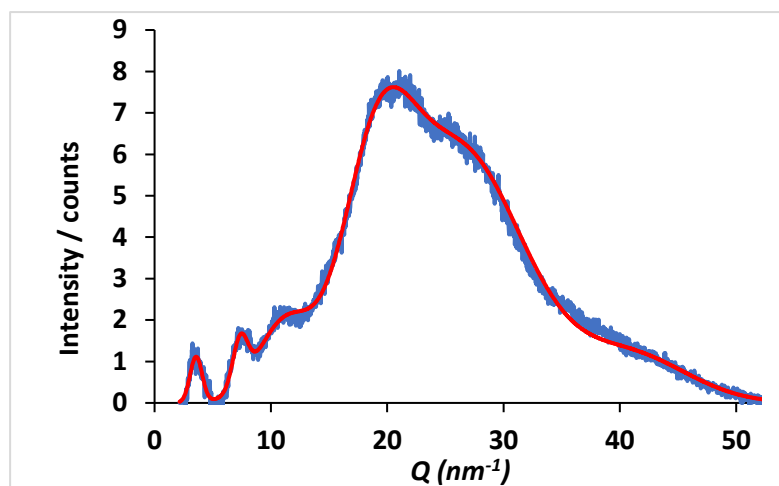


Figure 3.7. XRD pattern for Au:6-TGR hydrogel. The blue line is the experimental diffraction data and the orange line is the theoretical fit to a sum of Gaussian function.

Table 3.1. Distance d_i extracted from the analysis of the XRD data for Au:6-TGR gel.

Distance / nm	Suggested Assignment
0.318	Au-Au
0.231	Au-S
1.757	Fibre diameter
0.854	Intramolecular Au-Au
0.574	Intramolecular Au-Au
0.187	C-S

3.3.7 X-ray photoelectron spectroscopy (XPS) of Au:6-TGR

Survey scans of xerogel samples of Au:6-TGR identifying the elemental composition are shown in Fig. 3.8 c-h before and after oxidative treatment with iodine; the latter was used to effect oxidative doping for electrical conduction. Along with the gelating product Au:6-TGR, elements derived from starting materials are also observed. The survey spectra show the expected elemental composition of Au:6-TGR (i.e. C, N, O, S and Au) along with Cl 2p at a binding energy (BE) of ~198 eV, attributed to chloride ions from the starting material (HAuCl₄.3H₂O). The I 3d peak appears in the survey spectrum after the oxidation treatment, at a BE of 618 eV.

Fig. 3.8 c and d shows the high-resolution spectra of Au 4f_{5/2} and 4f_{7/2} for Au:6-TGR. Au 4f_{5/2} and 4f_{7/2} peaks are separated by 3.67 eV and the ratio of the component band areas is 6:8. Prior

to treatment with iodine the component at 84.6 eV is attributed to Au 4f_{7/2} and that at 88.3 eV to Au 4f_{5/2}.^{34,35} The BE value of the 4f_{7/2} peak indicates the +1 formal oxidation state for the Au ions³⁶ (typical range 84.3-85.5 eV).^{37,38} After doping with iodine, both the Au 4f_{5/2} and 4f_{7/2} peaks are shifted to higher binding energy by 0.2 eV.

The high resolution XPS spectra for sulfur were fitted with two spin-orbit components (2p_{1/2} and 2p_{3/2}) with a fixed splitting ~1.2 eV and with the ratio between the band areas fixed at 1:2. The S 2p_{3/2} at BE 163 eV is attributed to sulfur in Au(I)-thiolate form.³⁵ This value, in fact, suggests a bridging thiolate mode in Au:6-TGR based on previous reports which show higher S 2p_{3/2} binding energy (~163 eV)^{39,40} for this compared to comparable terminal thiol binding (~162 eV).⁴¹ The S 2p_{3/2} peak at 166 eV is attributed to sulfoxide^{42,43} (R-SO-R) formed by oxidation of the thiodiglycol, used to reduce Au(III) in the HAuCl₄·3H₂O starting material to Au(I) ions. After iodine doping (Fig. 3.8f), a new S 2p_{3/2} peak appears at a BE of 169.2 eV that is attributed to sulfone^{35,43} (R-SO₂-R). From the calculation of the area of S 2p_{3/2} peaks before oxidation by iodine, on average 68.1 % of the sulfur in the samples is thiolate and the rest is sulfoxide. After the oxidation, both of these components are reduced with 63.8 % thiolate, 27.3 % sulfoxide and 8.8 % sulfone. These values show that only small fraction (~7 %) of the thiolate in the Au:6-thioguanosine has been oxidized to the corresponding sulfoxide- and sulfone-Au(I) complexes after treatment with iodine.⁴⁴ Additionally, the S 2p_{3/2} spectra is shifted after oxidation to a higher BE by 0.2-0.3 eV. The high resolution scan of XPS spectra for iodine were fitted with two spin-orbit components (3d_{3/2} and 3d_{5/2}) separated by 11.5 eV and with a component band area ratio of 2:3.³⁵ The I 3d_{5/2} spectrum of 1 was fitted with two components (619.4 and 621.1 eV), as shown in Fig. 3.8 h. The peak at 619.4 eV is attributed to I₃⁻,^{45,46} while the other peak at 621.1 eV is in the range of both I₂^{45,46} and I₅⁻.⁴⁶⁻⁴⁹ as the binding energies of both are within a small range and can overlap. The presence of the I₅⁻ is possible in the presence of I₂ and I₃⁻ (I₂ + I₃⁻ ⇌ I₅⁻). The iodine doping process is expected to initially form I₃⁻, which reacts subsequently through a reversible reaction with further I₂ to form relatively stable species of polyiodide.^{48,49} Since the XPS spectra do not show Au(III) it indicates that the Au-thioguanosine xerogel is doped by injecting charge into Au:6-TGR forming polyiodide as counter anions rather than oxidative-addition of the I₂ to the metal centers.⁵⁰ Fig. 3.8i-l shows high resolution C 1s and N 1s spectra of Au:6-TGR xerogel before and after doping. The C 1s spectra were fitted with four components. The first peak at 285 eV is attributed to contributions from both C–C and C=C.⁵¹ The peak at 286.3 eV is attributed to C–O and C–N^{35,51} and the peak at 287.6 eV is attributed to carbon atoms in N=C–N.⁵² The peak

at binding energy 292.6 eV is attributed to $\pi-\pi^*$ shake up satellite peak.^{51,53,54} This peak disappears after doping, Fig. 3.8 i and j. The N 1s spectra were fitted with two peaks at BE of 400.4 and 398.8 eV that are assigned to conjugated sp^2 (C=N) and non-conjugated sp^3 (C-N< and -NH₂) nitrogen atoms, respectively.⁵⁵ The high resolution XPS spectra of the xerogel Au:6-TGR show little observable change in the chemical composition, except the noted oxidation of 7 % of thiolate, after iodine treatment. The binding energy shift in the Au 4f, S 2p, and N 1s spectra by 0.2 eV compared to C 1s after treatment is indicates of oxidative doping of the coordination polymer Au:6-TGR. In addition, the loss of the shake up satellite peak in the C 1s spectrum after doping confirms the change in electronic configuration upon oxidation.⁵⁶

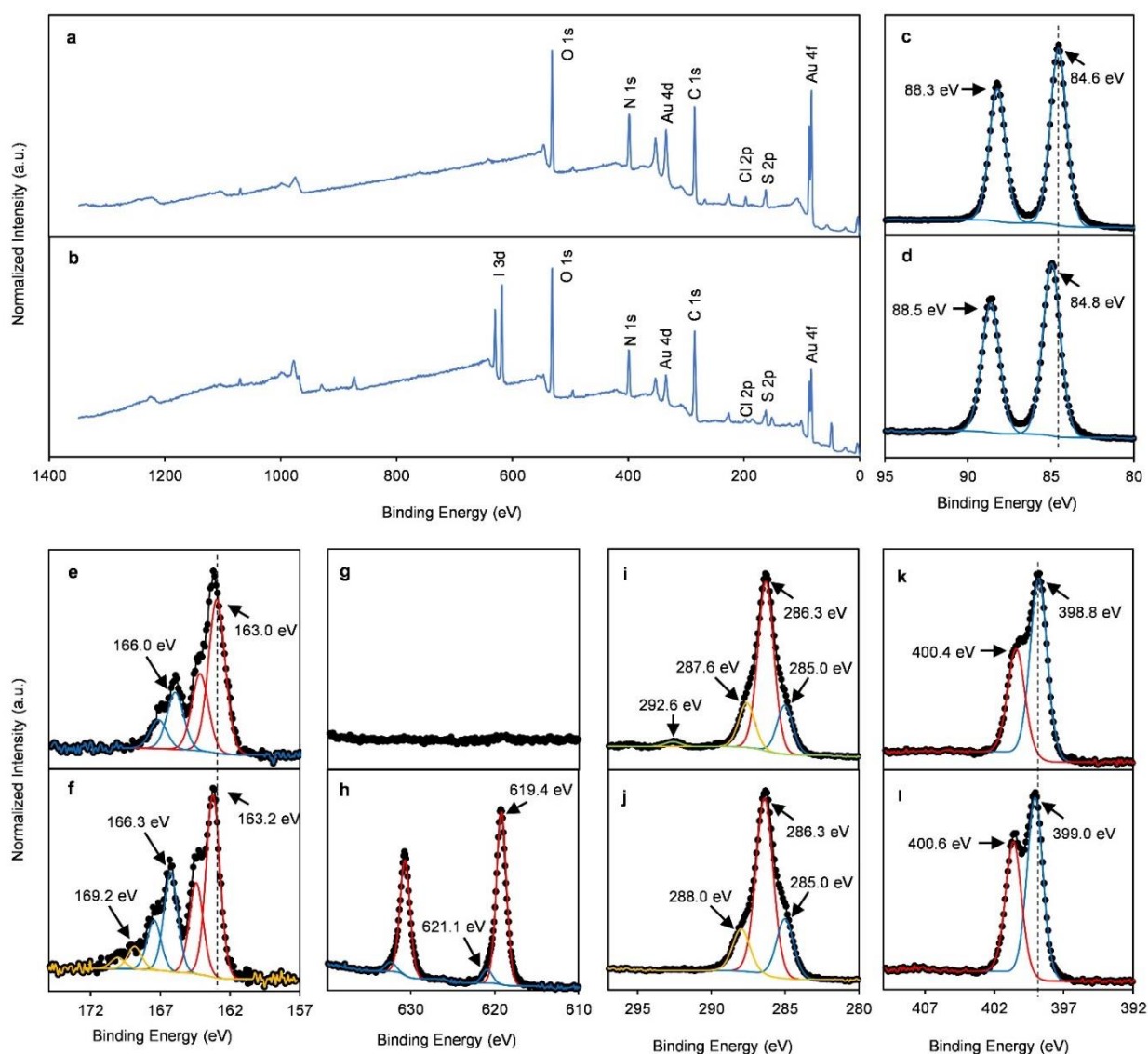


Figure 3.8. XPS spectra of (dried) Au:6-thioguanosine gel samples. XPS survey spectra of Au-6-thioguanosine gel samples (a) before and (b) after oxidation with iodine. High-resolution XPS spectra

of Au 4f, S 2p and I 3d. (c and d) Au 4f_{5/2} and 4f_{7/2}, (e and f) S 2p_{1/2} and 2p_{3/2}, (g and h) I 3d_{3/2} and 3d_{5/2}, (i and j) C 1s and (k and l) N 1s regions of the XPS spectra of Au:6-thioguanosine gel samples (c, e, g, i and k) before and (d, f, h, j and l) after doping with iodine.

3.4 Atomic force microscopy (AFM)

In order to probe the morphology and the size of the fibres in the gel, 2 μ L of Au:6-TGR hydrogel was drop-cast onto a silicon wafer (1 x 1 cm), dried in air, and imaged using tapping mode AFM. The AFM images (a) & (b) in Fig. 3.9 revealed the formation of 1D strands spanning many microns in length. The alternating highly ordered waves with pitch 28 nm that are apparent in the cross section in Fig. 3.9 (d) which is a profile along the sloping white line along the individual fibre, in image (c) are consistent with a helical arrangement. The regular spacing reflects a highly-organized self-assembly for Au:6-TGR polymer to form a structured fibre. Image (c) also shows that the dried xerogel comprises one-dimensional molecular strands extending many microns in length with the smallest feature heights of *ca.* 3 nm. These strands entangle to form the necessary 3D network required for gel formation; the alternating light-dark features along individual fibres are consistent with a highly organised helical structure.¹³ A statistical analysis was carried out to show the height (diameter) distribution of the fibres in the gel. The data in Fig. 3.10, shows that the diameter is \sim 3 nm, some bars were with higher heights in range between 4–5 nm but with less frequency, and some were with more less frequency with heights up to 7 nm also were present at the histogram, in addition, lower height up to 2 nm with less frequency, corresponding to individual polymer strands, also can be seen.

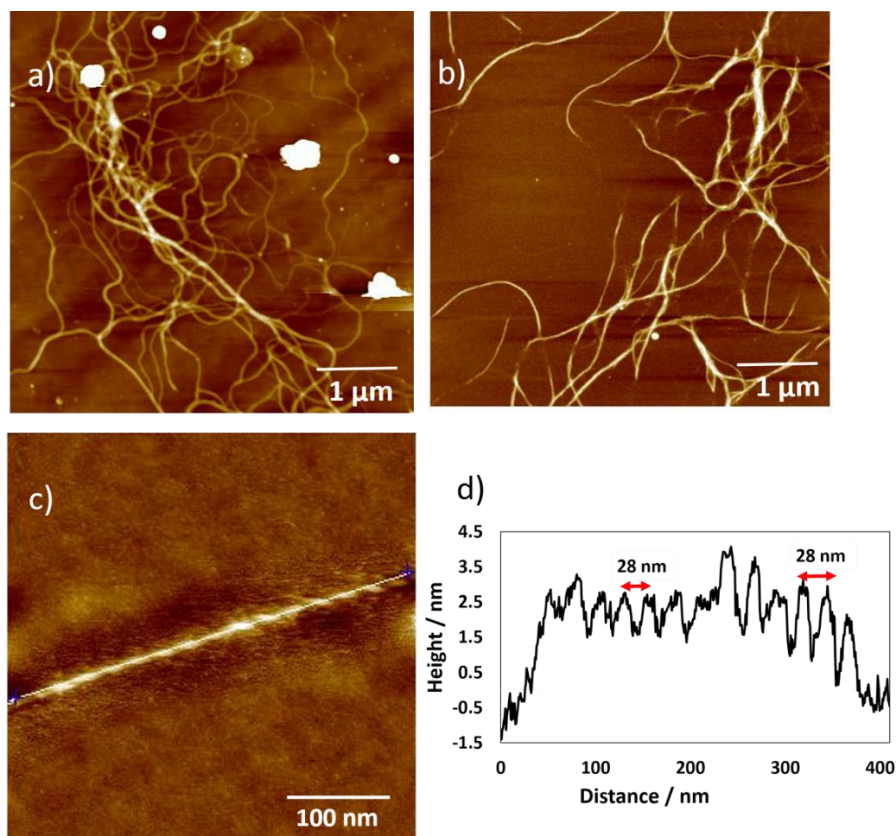


Figure 3.9. Tapping mode AFM images of 1:1 gold:6-thioguanosine hydrogel drop-cast onto a silicon wafer and dried in air. The scale bars in (a), (b), and (c) are 1 μm , 250 nm, and 100 nm respectively. (a) Height image, the grayscale, corresponds to 11 nm at, (b) 9.7 nm, and (c) 3.9 nm. (d) The associated cross-section along the slopping white line in (c). shows the height of the fibres ~ 3 nm and the distance between the alternating waves of the spiral is 28 nm which reflects highly helical arrangement.

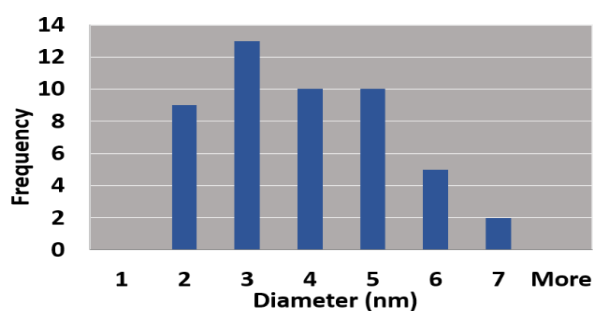


Figure 3.10. The histogram shows the size distribution of the fibres.

The architectures of helical structure are present in nature, for instance, the α -helical in proteins and double strands of DNA, where helical structures are formed spontaneously. In synthetic chemistry, researchers try to control the helical structure in order to use it in different applications for example, electronics and catalysis.⁵⁷ A chiral molecule has a potential route to form helical structure via supramolecular self-assembly. In contrast, an achiral molecule has less opportunity to form helical compound.⁵⁸⁻⁶¹ 6-Thioguanosine nucleoside is chiral and this

gives rise to helical structure when coordinated with Au(I) and then self-assembled to form 3D network. The AFM images (a), (b), and (c) in Fig. 3.11 with scale bars 400, 120, and 100 nm respectively show more clearly helical fibres structure for Au:6-TGR hydrogel.

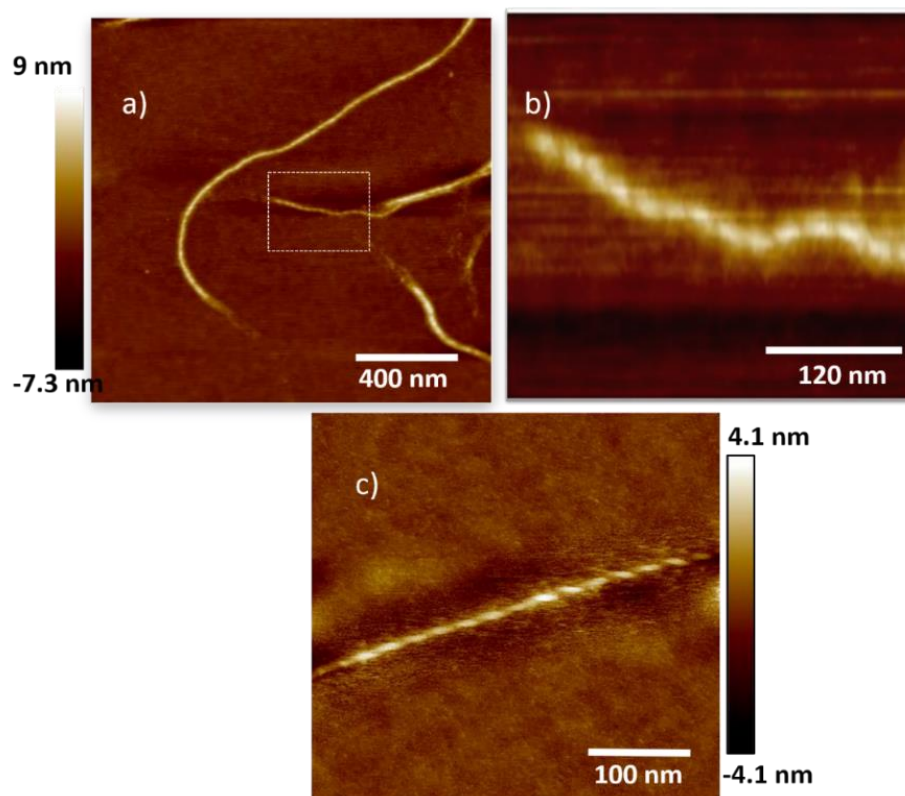


Figure 3.11. Higher resolution AFM images of a single fibre for Au:6-TGR hydrogel, the images are suggestive a helical structure of the fibre. The scale bars at (a), (b), and (c) are 400 nm, 120 nm, and 100 nm respectively, (b) a small area of (a).

The height of the alternating light-dark features along individual fibres in the AFM image in Fig. 3.12 b, indicates that they contain several individual strands and the apparent periodicity seen by AFM arises from intertwining in some relatively ordered supramolecular structure-the pitch is too large to be easily explained on the basis of single polymer chains. The profile (c) is associated with the sloping blue and red lines across image (b), the difference at the thickness and the height between the individual and the twin fibres is very clear, as the height at the twin is ~ 7.5 nm which two times higher than that at the single fibre.

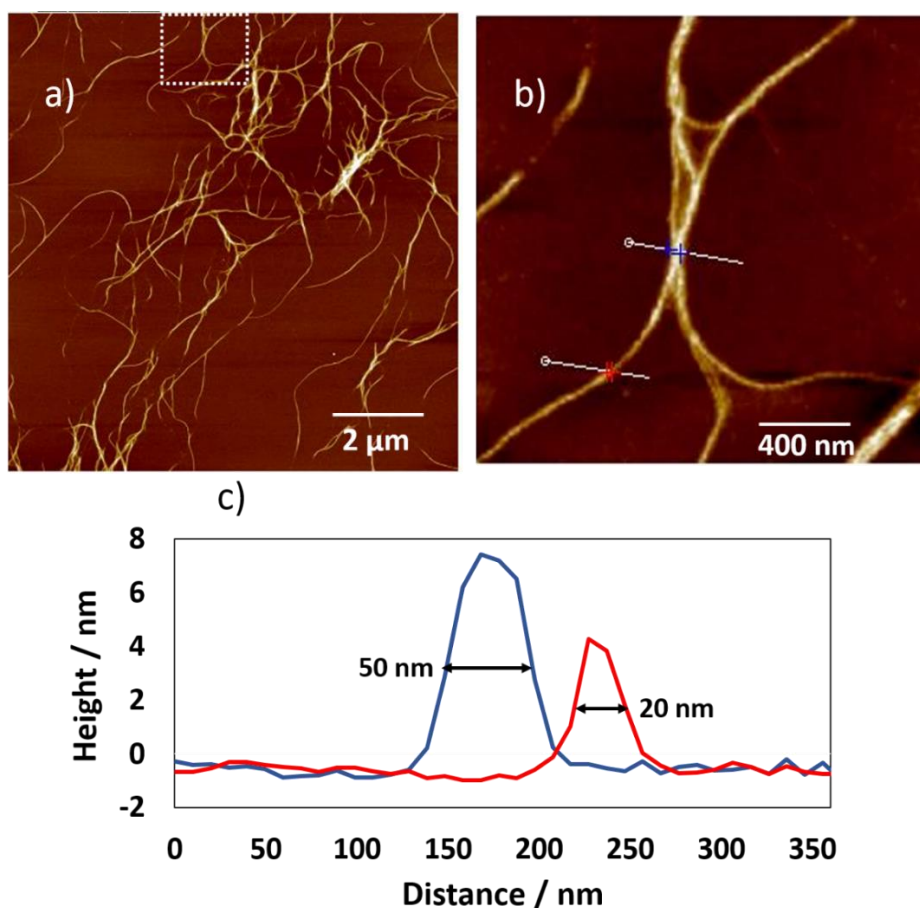


Figure 3.12. AFM images of Au:6-TGR drop-cast onto a silicon wafer, (a) with scale bar 2 μm, (b) a small area of (a) with scale bar 400 nm shows intertwining of two strands of helical fibres. (c) The associated cross section along the two white slopping lines in (b), showing larger diameter with height ~ 6 nm as a result of twining (blue curve) and smaller diameter with height ~ 3 nm of individual fibre (red curve).

3.5 Transmission electron microscopy (TEM)

TEM measurement was performed with a Philips CM100 electron microscope at accelerating voltage 100 kV and the sample was prepared by casting 2 μL of 1:1 Au:6-TGR hydrogel onto a clean carbon coated copper grids followed by air drying prior to analysis. Fig. 3.13 reveals very long nano fibres, in some areas, some nano fibres can be seen entangled with each other.

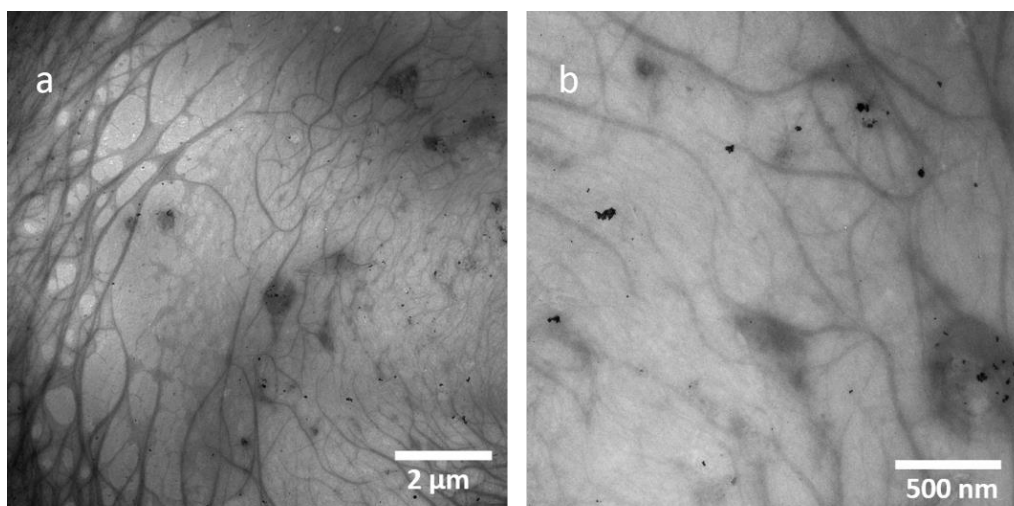


Figure 3.13. TEM images of 1:1 Au-6-TGR hydrogel, the scale bar was 2 μm and 500 nm and the magnification was 10500x and 34000x at (a) and (b), respectively.

3.6 Fluorescence microscopic imaging

Optical fluorescence microscopic images were taken showing long luminescent fibres are produced; this morphology is consistent with the structures that observed by both AFM and TEM techniques. The most analysed area by microscopy displayed long fibres which was easily identified, however, helical features was not easily accessed by microscopy, as shown in Fig. 3.14. The luminesce of the gel can be also seen in this sample. The sample was prepared by depositing 2 μL of the gel on a clean Si substrate, leaving to dry in air prior to analysis using Zeiss Epifluorescence Microscope. The excitation was provided by a mercury lamp with bandpass filter to select wavelength between 300-400 nm and the emitted light was filtered by a longpass filter with cut-off at 420 nm. The scale bar was 10 μm .

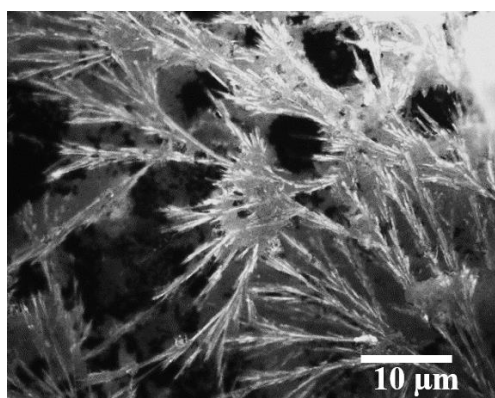


Figure 3.14. Fluorescence microscopic images of 1:1 Au:6-TGR measured using Zeiss Epifluorescence Microscope, excitation light was provided by mercury lamp with bandpass filter 300-400 nm, while longpass filter was used to filter the emitted light with cut-off at 420 nm.

3.7 Conductivity of Au:6-TGR hydro gel

Conductive polymers are organic or inorganic electrical conductors that have an extended π electron system. Very early, Letheby⁶² prepared poly aniline as a partly conductive polymer by oxidation aniline in sulphuric acid in 1862, and later many organic conductive polymers were synthesised. However, polyacetylene was the most important among all these compounds for it showed high conductivity (10^{-8} - 10^{-7} and 10^{-3} - 10^{-2} S m⁻¹ for *cis* and *trans* polyacetylene, respectively).⁶³ Conducting films of Au:6-TGR xerogel were prepared by exposure of the sample of Au xerogel to the vapor of I₂. X-ray photoelectron (XPS) spectroscopy was used to characterize the oxidation states in the Au xerogel-I₂. Since the XPS spectra did not show Au(III) it indicates that the Au:6-thioguanosine xerogel is doped by injecting charge into the xerogel forming polyiodide as counter anions rather than oxidative-addition of the I₂ to the metal centers.⁶⁴ There were two species of iodine forms I₃⁻ ions and I₅⁻ complex (I₂ + I₃⁻), the presence of the I₅⁻ is possible in the presence of I₂ and I₃⁻ (I₂ + I₃⁻ \rightleftharpoons I₅⁻). The iodine doping process is expected to initially form I₃⁻, which reacts subsequently through a reversible reaction with further I₂ to form relatively stable species of polyiodide.^{65,66}

3.7.1 Two-terminal I–V characteristics and temperature dependence of the Au:6-TGR conductance

The conductivity of Au:6-TGR hydrogel before and after oxidation by doping with I₂ was recorded by using two-terminal I–V technique with a probing station (Cascade Microtech) and a B1500A semiconductor analyser (Agilent) under dry nitrogen at room temperature. Fig.3.15 shows the resulting data where the current is varying with potential at a constant temperature (298 K). The test was carried out with applied voltage from -3 to 3V in steps of 0.2 V with a constant rate 100 m s /0.2 V. Prior to aligning the fibres of the hydrogel at the electrode, the platinum electrodes were analysed on a probe station and reference current/voltage curves were recorded which showed the background currents less than 100 fA at 2 V. Nonlinearity can be seen at the current–voltage curve for the Au:6-TGR xerogel before oxidation process, however a straight line (ohmic behaviour) can be observed upon doping the xerogel with I₂.

Using alternative oxidants such as tris(4-bromophenyl)ammoniumyl hexachloroantimonate ([Br(C₆H₄)₃N]SbCl₆) produced similar behaviour confirming the conductive nature of the doped coordination polymer and that the observed conductivity was not due simply to the presence of the polyiodide species.⁶⁷

The I-V curve in Fig. 3.15 shows little evidence of conductivity for the undoped material. The differential conductance at zero bias was estimated as < 30 pS. The current at high bias, greater than about 1.5V, shows some increase, but this shape of I-V curve, which has almost zero slope at the origin, is not evidence of conductivity in the usual sense. Oxidative doping of Au xerogel does produce a material with finite zero bias conductance, whether the oxidant employed is a vapour such as I_2 (7.1 ± 0.05 nS) or a liquid such as a dry acetonitrile solution containing $([Br(C_6H_4)_3N]SbCl_6)$ (12.9 ± 0.09 nS). The XPS data of the doped and undoped material (Fig. 3.8) indicate that the positive charge introduced by oxidation resides mainly on Au and S atoms.

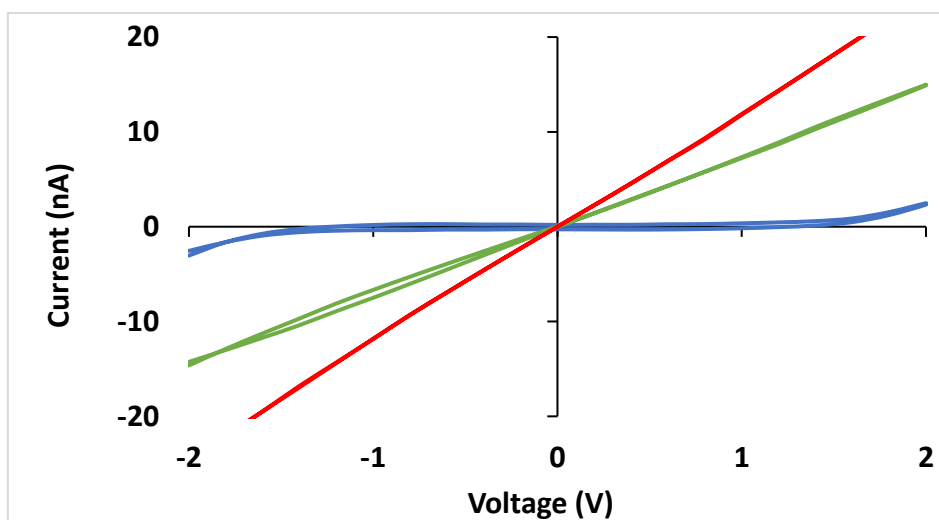


Figure 3.15. Electrical characterisation of the Au:6-thioguanosine coordination polymer, I-V curves before (blue) and after doping with Tris(4-bromophenyl)ammoniumyl hexachloroantimonate (red) and iodine (green) at 298 K taken over a constant rate 100 ms / 0.2 V.

The I-V curve of Au:6-TGR hydrogel at various temperatures over the range of 223 to 323 K, as shown in Fig. 3.16 was carried out with two-terminal I-V technique using a probe station under dry nitrogen and the temperature was controlled by a thermal chuck system (Model ETC-200 L, ESPEC, Japan), this technique allows characterisation the conductance that temperature dependence. Upon using two cycles of cooling and heating measurements, as can be observed, the conductance (G) increased with temperature. Increasing conductivity with temperature is frequently observed with conducting polymers, however the structure of the polymer, dimensionality, and the degree of the crystallinity are the factors that may affected the details of the measurements. By moving from cooling to heating, no significant change at the

conductance value have been shown versus temperature (T) and that confirms thermal stability of Au:6-TGR xerogel.

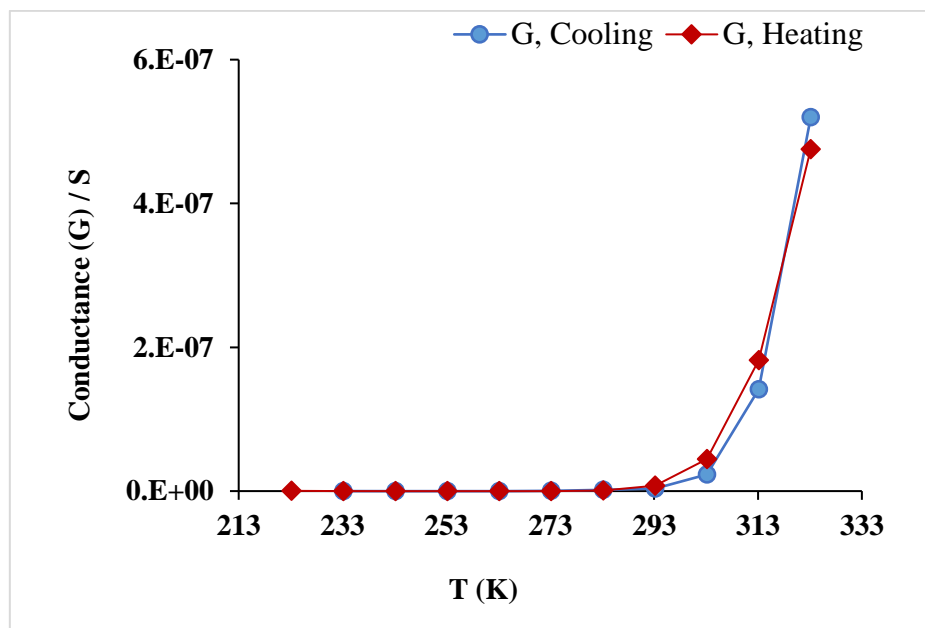


Figure 3.16. Conductance Vs. temperature of the Au:6-TGR hydro gel for cooling and heating over a temperature range of (223–323 K).

3.7.2 Calculation the activation energy from Arrhenius plot

The Arrhenius plot that corresponding to the conductance in Fig. 3.16 is presenting in Fig. 3.17. It can be seen clearly that Arrhenius behaviour explains the conductance over range of temperatures that measured by plotting the $\ln G$ versus T^{-1} and a straight line was obtained.

The data in Fig. 3.17 shows that the zero-bias conductance increases with temperature in accordance with an equation of Arrhenius form. This is characteristic of a semiconductor or hopping conductor and not of a metallic conductor. In principle, the increase in conductance could be explained in terms of thermal excitation across a gap, which would result in an activation energy of $\frac{1}{2}E_{\text{gap}}$. However, the activation energy of about 0.97 eV does not match the data from optical spectroscopy. Fluorescence excitation spectra show an optical gap of 360 nm which is about 3.44 eV. Instead, the nature of the conductivity in doped xerogel is more like that of the conjugated polymers than crystalline inorganic semiconductors. Typically, conjugated polymers are poorly conducting when undoped and have optical gaps of several eV, but conduct via a hopping mechanism when doped. Although bulk samples of conjugated polymers typically show temperature-dependent conductances which follow variable range hopping models,⁶⁸ simple Arrhenius behaviour was observed when they are constrained to form as one dimensional structures.⁶⁹ In these systems, and doped polymer, the activation energy

extracted from the Arrhenius plot is much smaller than the optical gap because it corresponds to thermally-assisted tunnelling between somewhat localised states rather than carrier generation by excitation across the gap as in crystalline inorganic semiconductors. Finally, it is worth noting to observe essentially identical Arrhenius plots for both heating and cooling cycles and the doped polymer is stable up to 50 °C.

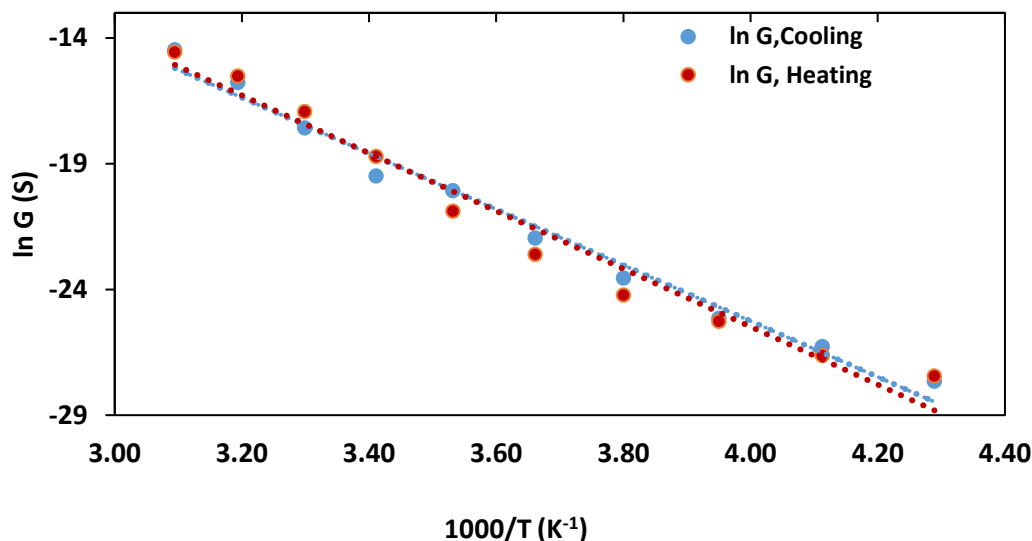


Figure 3.17. An Arrhenius plot for the zero-bias conductance of the I₂-doped Au:6-thioguanosine xerogel. Activation energy (E_a) = 0.97 ± 0.02 eV obtained from two independent heating (red)/cooling (blue) cycles.

Table 3.2 Activation energy (E_a) of cooling and heating cycles for Au:6-TGR hydrogel.

Energy	Cooling	Heating	Average	Error \pm
E_a (kJ mol⁻¹)	92.36	95.65	94.01	1.65
E_a (eV)	0.96	0.99	0.97	0.02

E_a (kJmol⁻¹): Free standard cell voltage.

E_a (eV): The activated energy.

AFM imaging after treatment with I₂ vapor showed that no notable structural changes occurred and the molecular strands remained intact (Fig. 3.18 a and b). The chemical effects of this treatment, judged by XPS, indicated the reaction generally proceed *via* a redox mechanism with the formation of a polyiodide-doped coordination polymer.

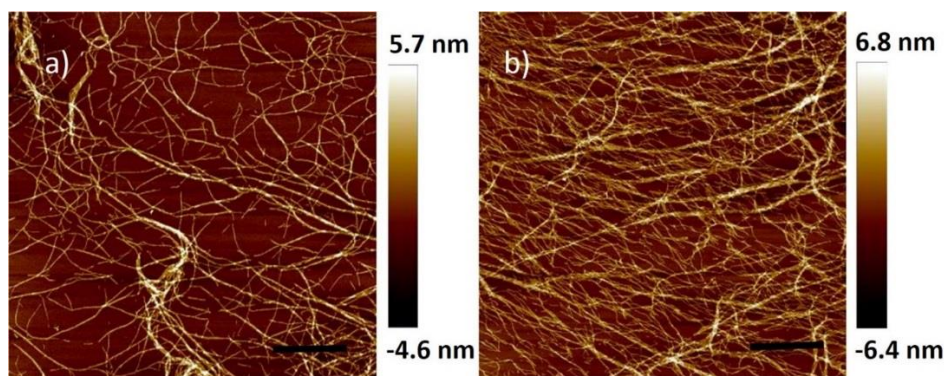


Figure 3.18. AFM images of Au:6-thioguanosine hydrogel before (a) and after (b) oxidation with iodine. The scale bar was 2 μm .

In conclusion, the Au:6-TGR shows electronic conductivity upon oxidation and the charge carriers are dominantly associated with the Au-S chains of the structure and not the nucleobase. The I-V curves show ohmic behaviour, i. e., the slope of the I-V curve is the same no matter how small or large the deviation from equilibrium. This behaviour is distinct from photoinduced electron transfer experiments (in DNA) in which long range electron transfer is observed for photon energies sufficient to populate the initial excited state and distinct from electrochemical experiments where the applied potential must exceed the formal potential of the relevant couple to drive electron transfer.

Current-voltage curves collected before and after oxidation (Fig. 3.15) reveal a dramatic increase in conduction upon treatment. Essentially ohmic behaviour is observed over the $\pm 2\text{V}$ range with an increase of at least two orders of magnitude in conductance upon treatment. The temperature-dependent I-V measurements (Fig. 3.16) show Arrhenius behaviour characteristic of a thermally-activated conduction mechanism with an activation energy of 94 kJ mol^{-1} .

The linearity and lack of hysteresis of the I-V data in Fig. 3.15 strongly argues against the interpretation in terms of electrochemical oxidation of the bases. The lack of hysteresis (doped or undoped polymer) and the linear I-V characteristic (doped polymer) are inconsistent with an electrochemical process driven by the interfacial potential and especially with the electrochemistry of the DNA bases where chemical steps following the electron transfer prevent observation of the reverse process except at scan rates ($10 - 100 \text{ V s}^{-1}$) orders of magnitude greater than applied in this work.⁷⁰ Instead, the lack of hysteresis is a piece of evidence in favour interpretation of the measurements in terms of electron transport in the film.

3.8 Diluted solutions of 1:1 Au-6-TGR with con. 1, 0.1, and 0.01 mg/ml 6-TGR

In this section, the effect of preparing Au:6-TGR at different concentrations was explored. In particular, the effect of dilution on the self-assembly of the material was investigated by AFM. The UV-Vis absorbance spectra of Au:6-TGR solution with concentrations 0.01 mg/ml of 6-TGR was measured and a high intensity peak was found at 345 nm indicating that the compound was in the thione form as a result of the dilution, another peak (less pronounced) at 360 nm was found assigned to form ligand metal charge transfer complex (LMCT) between Au(I) ion and 6-TGR via S atom, as shown in the Fig. 3.19 below. This result indicates that the dilution process which leads to reduction of the pH and disfavours the deprotonation at N1-H which is very necessary to produce the thiol form prior to binding with Au(I) and consequently the solution of 6-TGR was in a thione form before binding with Au(I) and no gel was formed. A broad peak at a similar wavelength (360 nm) was seen in the spectrum of Au:6-TGR hydrogel which was prepared with conc. 10 mg / ml of 6-TGR. The solutions with concentrations 1 mg / ml & 0.1 mg / ml gave noisy spectra and the absorbance values for both were too small to acquire good data.

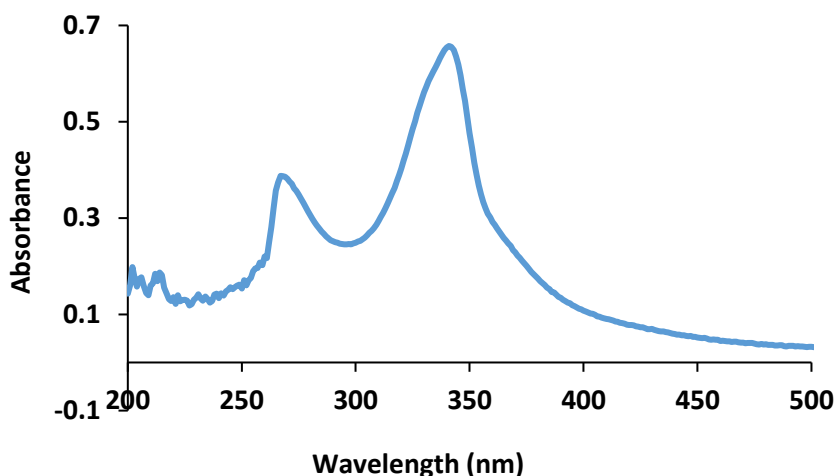


Figure 3.19. The Absorbance spectrum of Au:6-TGR solution with conc. 0.01 mg / ml 6-TGR.

3.9 Fluorescence spectra of Au:6-TGR solutions

Fig. 3.20 shows the fluorescence emissions spectra of 1:1 Au:6-TGR gel and the solutions with concentrations 10 mg / ml and 1, 0.1, 0.01 mg / ml of 6-TGR, respectively. The data shows that the intensity of the fluorescence emission of the Au:6-TGR solutions decreased with the decline in the concentration, however a large reduction the intensity was found for the gel with concentration 10 mg / ml compare to the intensity of the more dilute solutions due to the inner-

filter effects and that indicates that the gel with high concentration absorbs a large part of the energy of excitation or emission.

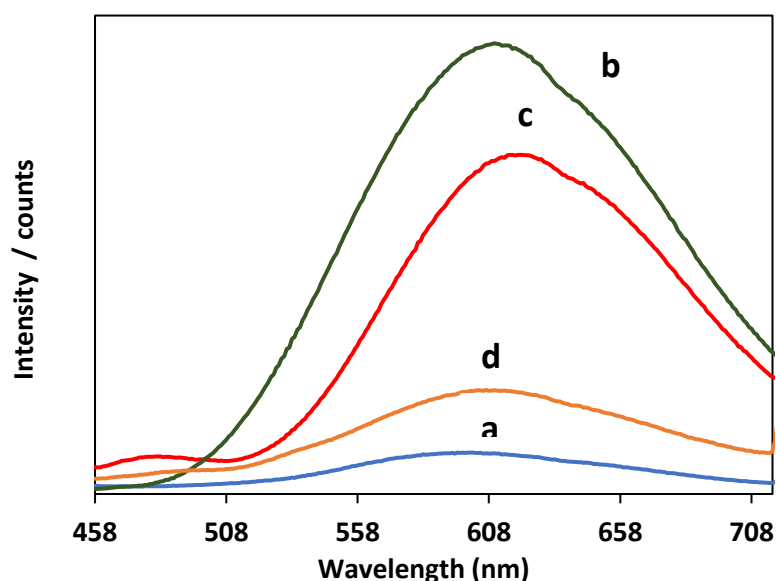


Figure 3.20. The fluorescence emission spectrum of: a) 1:1 Au:6-TGR gel with concentration 10 mg / ml and b), c), and d) the solutions with concentrations 1, 0.1, 0.01 mg/ml of 6-TGR, respectively.

3.10 Atomic force microscopy (AFM)

The AFM images of diluted solutions of Au:6-TGR with concentrations 1, 0.1, 0.01 mg / ml revealed different morphology depending upon the concentration, time taken after sample preparation, and the speed of drying. For instance, the AFM images of the sample with conc. 1 mg / ml of 6-TGR that have been taken 24 h after preparation and dried by air showed circularly organized fibres with clockwise and anticlockwise morphology and a height of 3 nm. The chirality of the compound, which normally leads to helical fibres, can be considered the reason for the clockwise and anticlockwise spiral morphology, this phenomenon was observed with numerous fibres.⁷¹⁻⁷⁵ In addition, the morphology of spiral was also seen with different fibres⁷⁶ and crystalline compounds.⁷⁷⁻⁷⁹ The practical experiment which was carried out with different conc. of Au:6-TGR has shown that the solutions with conc. 0.01 & 0.1 mg / ml were not able to form spiral fibres, however, upon increasing the conc. to 1 mg / ml both clockwise and anticlockwise fibres are formed, as shown in Fig. 3.21, 3.22 and this indicates that the morphology of Au:6-TGR can be controlled by the concentration.

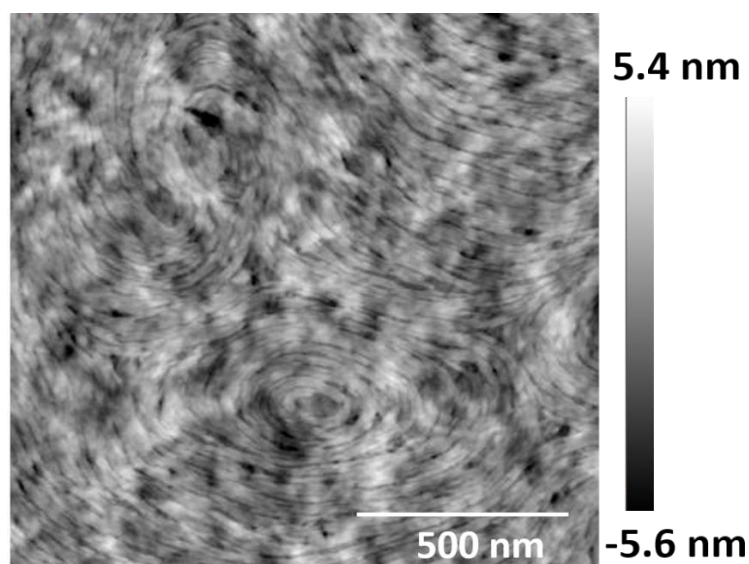


Figure 3.21. Tapping mode AFM images of 1:1 gold:6-thioguanosine solution with con. 1 mg / ml, the sample was taken 24h after preparation and drop-cast into a silicon wafer followed by drying in air with scale bar 500 nm and height (grayscale) 5.4 nm, the image shows both clockwise and anticlockwise fibrous morphology.

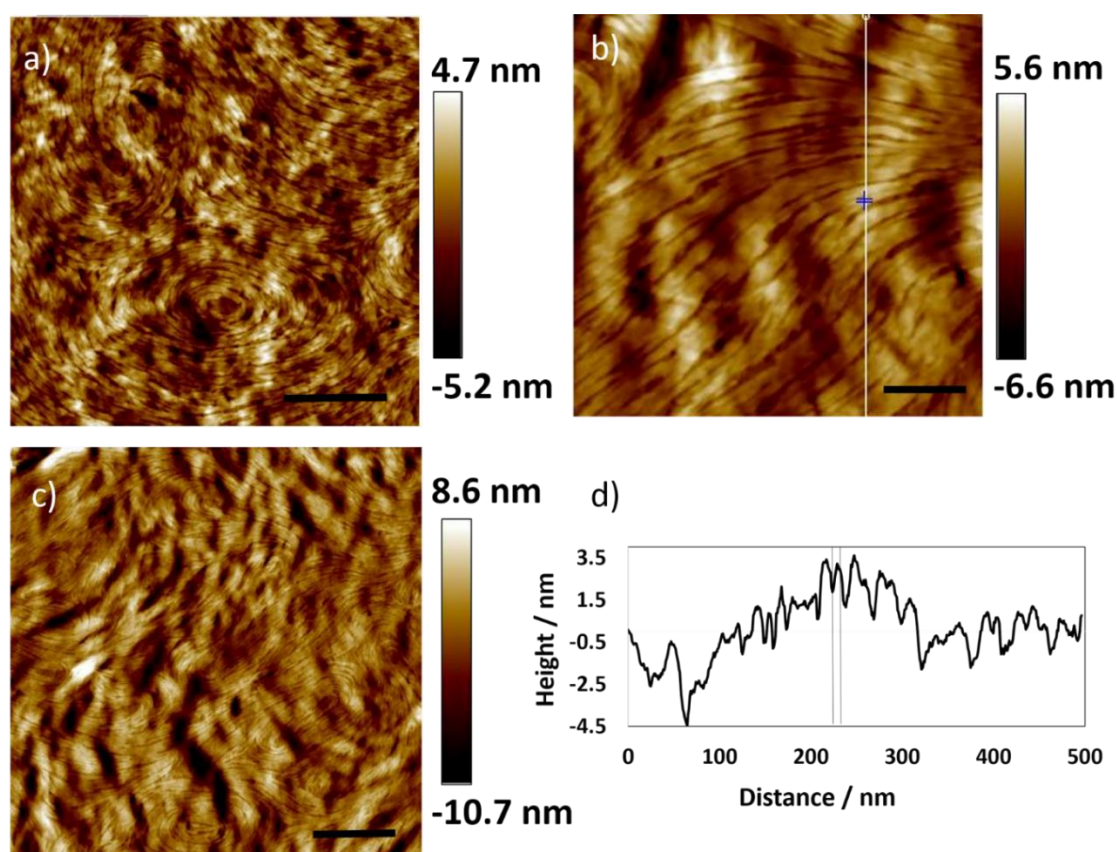


Figure 3.22. Tapping mode AFM images of 1:1 gold:6-thioguanosine solution with con. 1 mg / ml, the sample was taken 24h after preparation and drop-cast onto a silicon wafer followed by drying in air. The scale bars in (a), (b) & (c) are 350 nm, 100 nm, and 400 nm, respectively and (d) the associated cross-section along the white vertical line in (b) shows the height of the fibres ~ 3 nm. The morphology of the fibres in these images is circularly organised fibres.

Upon taken the sample of solution of 1:1 Au:6-TGR with conc. 1 mg / ml one min after preparation, drop casting onto a substrate and drying by N₂ prior to analysis with AFM, no spiral was formed at the AFM images as a result of increasing the speed that used to dry the sample. This suggests that time is another factor that can be added to control the morphology in addition to the concentration as mentioned before. Fig. 3.23 shows the AFM images of this sample with the cross section. The height of the fibres (~ 6.5 nm) in this sample is higher than that at the same concentration but with air drying (~3 nm) this difference can be attributed to the stream of N₂ which may be causes bundling the fibres with each other.

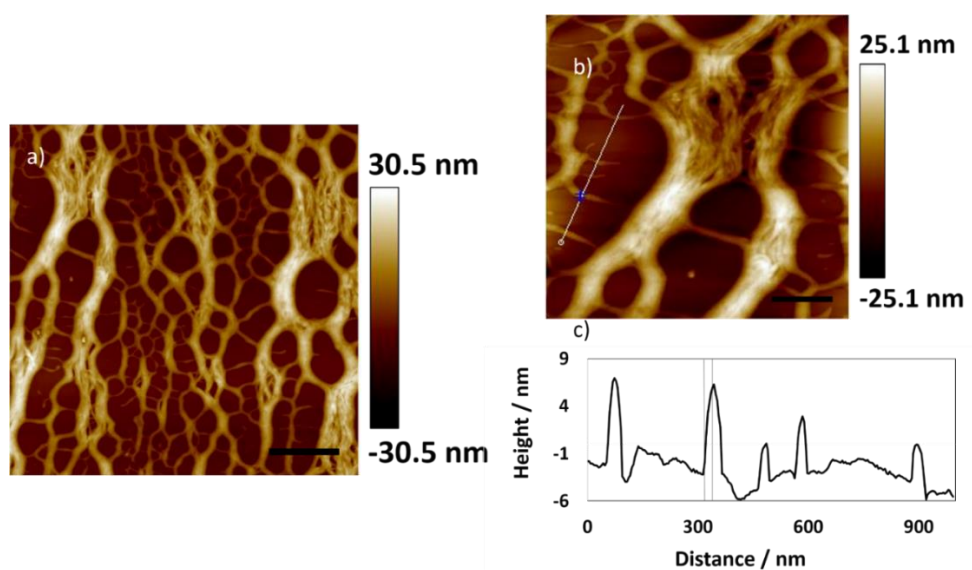


Figure 3.23. Tapping Mode Height AFM images of 1:1 Au-6-TGR solution with con. 1 mg / ml, the sample was taken 1 min after preparation and was dried with N₂. The scale bar and the height (grayscale) at (a) & (b) were 1 μm, 30.5 nm, and 400 nm, 25.1 nm, respectively. (d) The height profile measured along the white line of the corresponding fibre ~ 6.2 nm in image (b).

The AFM images of the diluted sample with conc. 0.1 mg / ml that was drop cast onto a substrate 1 min after preparation and dried by air demonstrated a dense network of fibres with height 1 nm but no spiral was seen and that indicates a strong effect of the factors aforementioned on the morphology of the fibres, Fig. 3.24.

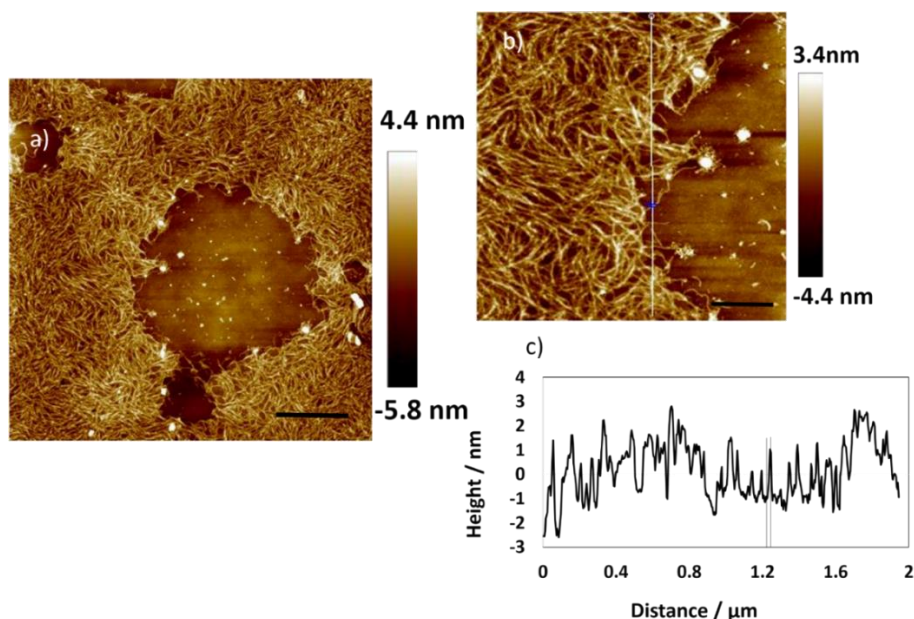


Figure 3.24. Tapping Mode AFM Height images of Au:6-TGR solution with con. 0.1 mg / ml, the sample was taken 1 min after preparation and dried by air. Scale bars and height (grayscale) at (a) & (b), 1 μ m, 4.4 nm and 400 nm, 3.4 nm, respectively. (c) The associated cross section along the vertical line at (b) shows the height of fibres \sim 1 nm.

Upon increasing the speed of drying by using dry N₂ and the period of time taken for sample preparation from 1 min to 1 h for sample 0.1 mg / ml, a less dense network was obtained, as shown in Fig. 3.25. By using the same condition of drying with N₂ gas and period 1 min for sample 1 mg / ml, the circular fibres (clockwise and anticlockwise) were disappeared and honeycomb cell-like network was formed instead as observed in Fig. 3.23.

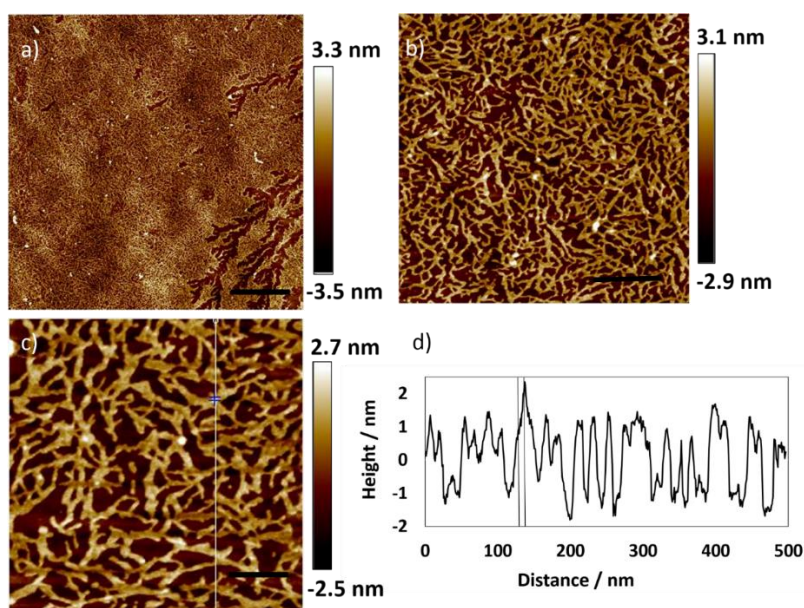


Figure 3.25. Tapping Mode AFM image of Au:6-TGR solution with con. 0.1 mg / ml, the sample was taken 1h after preparation thereafter drying by N₂ gas and drop -casted onto a substrate. The scale bar in image (a), (b), and (c) were 1 μ m, 250 nm, and 100 nm, respectively, d) is the profile of the vertical white line across image (c) shows that the height of the fibres is \sim 2.3 nm.

Preparing the Au:6-thioguanosine solution with greater dilution (0.01 mg /ml) and drying by air leads to form thick fibres with height ~ 3 nm, Fig. 3.26. It is worthwhile to note here that, the speed of sample's drying effect on the morphology of the fibres and that can be observed at the AFM images of samples Au:6-TGR solutions with different concentrations.

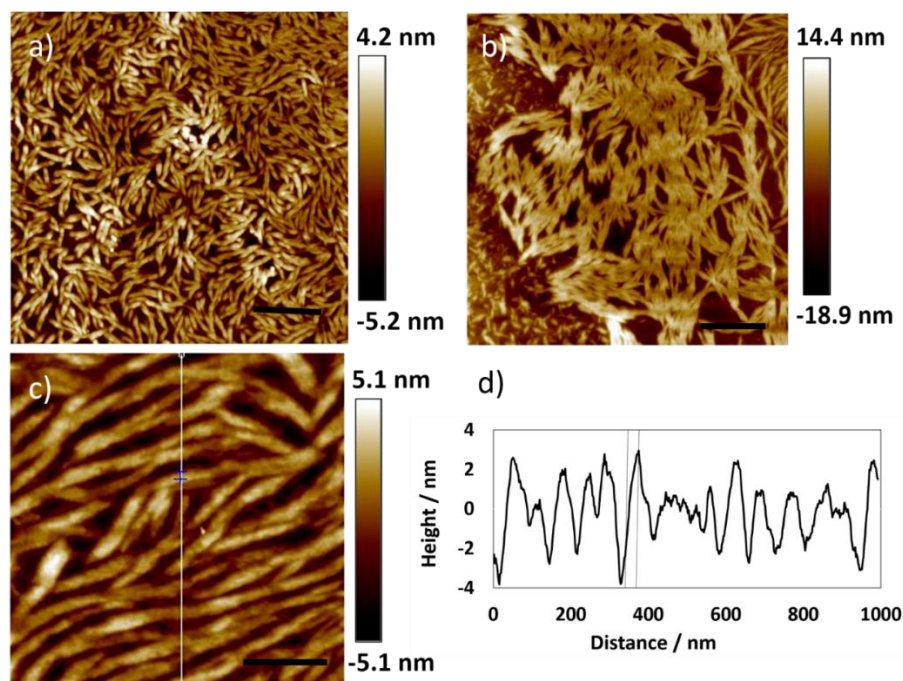


Figure 3.26. Tapping Mode AFM Height images of 1;1 Au:6-thiouanosine solution (Au:6-TGR) with con. 0.01 mg /ml, the sample was taken 1 min after preparation and drop cast onto a silicon wafer followed by drying by air. The scale bar is 1 μ m at: (a) & (b) and 250 nm at (c), respectively. (d) The associated cross-section along the white vertical line in (c) shows the height of fibres ~ 3 nm.

3.11 Fluorescence microscopic imaging

Fluorescence images which were carried out for samples prepared from solutions of Au:6-thioguanosine with concentration 0.01, 0.1, and 1 mg /ml, showed important differences of morphology. Fibres formed with concentration 0.01 and 0.1 mg /ml were very thin while entangle sheet-like structures can be seen for samples with concentration 1 mg /ml. The difference of the morphology depending on the concentration reflects the possibility to control the size, thickness and the morphology of the polymer Au:6-TGR by control the concentration. Fig. 3.27 presents the data.

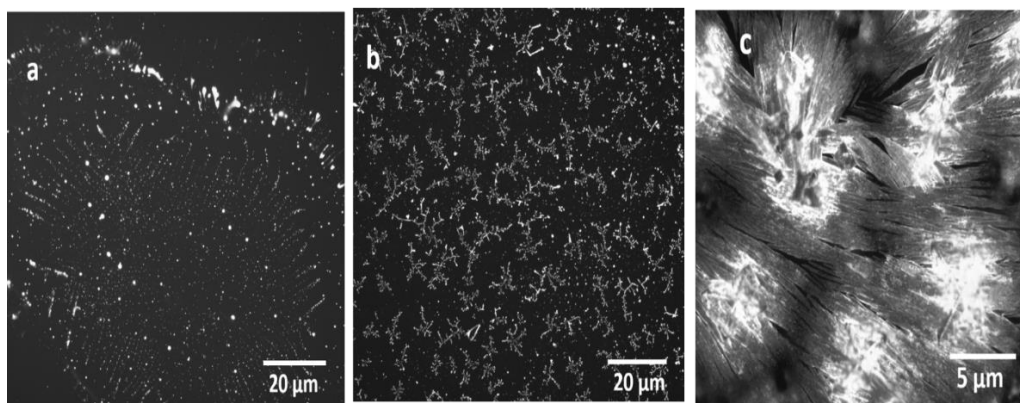


Figure 3.27. Fluorescence microscopic images of 1:1 Au: 6-TGR solutions, the concentrations were 0.01, 0.1, and 1 mg / ml 6-TGR in images (a), (b), and (c), respectively, the sample in image (c) was taken 24 h after preparation.

3.12 Templating 6-thioguanosine polymer on DNA

3.12.1 Synthesis Au(I):6-TGR hydrogel in the presence of DNA

Au:6-TGR gel was prepared with concentration 10 mg/ ml of 6-TGR, after two min of the gel synthesis, 40 μ L of 1 mg/ml of calf thymus DNA solution was added to the gel, shaking gently and incubated for 10 min at room temperature. 1.5 μ L of the gel was drop casted onto a clean silicon wafer (n-Si<100> 1 x 1 cm), dried in air for 24h and then imaged by AFM. The aim of these experiments was to observe the effect of DNA as a template for the structures formed by the Au:6-TGR complex

3.12.2 Atomic force microscopy studies

Using DNA as scaffold with different metals which leads to form nanowires is reported in numerous papers,^{69,80-82} however, in this work the fibres that obtained from the coordinated polymer of Au:6-TGR hydrogel was used as a template for DNA to shed light on the molecular interactions in these supramolecular nano fibres by adding a small volume of DNA to the Au:6-TGR hydrogel 10 min after preparation the hydrogel. After deposition of the gel with DNA onto a substrate followed by air drying, the morphology of the hydrogel was investigated by Tapping Mode AFM; the results revealed that the morphology of the hydrogel was transferred from helical nano fibres to a long, regular, and uniform fibres coated with DNA with a beads-on-a-string morphology.⁸³⁻⁸⁵ The AFM image (a) in Fig. 3.28 shows more clearly the aforementioned features. The mechanism of this interesting morphology is not understood very well but it possibly be owing to the interactions of the DNA with the 6-thioguanosine at the Au:6-TGR hydrogel via hydrogen bonding. The analysis for the cross section along image (c)

shows that the height of the fibres is ~ 8.5 nm, and the statistical analysis for image (a) in Fig. 3.29 displays that the size distribution of the fibres is between 10-12 nm, some of lower structure heights between 6-8 nm and lower than that up to 2 nm can be observed but with less frequency, in addition, some of higher structures heights between 14-16 nm can be seen but with lower frequency. These heights are substantially greater than the apparent height of duplex DNA in AFM images, which is typically about 1nm; the height data therefore suggests the DNA molecules are coated with Au:6-TGR polymer. The addition of DNA to the hydrogel increased the surface roughness up to height 8.5 nm compare to the height of the hydrogel which was 3 nm by forming new hierarchical structure. It is worthwhile to note here that, electrospinning technique⁸⁵ is the method that used with most preparations to produce beads-on-string structures.

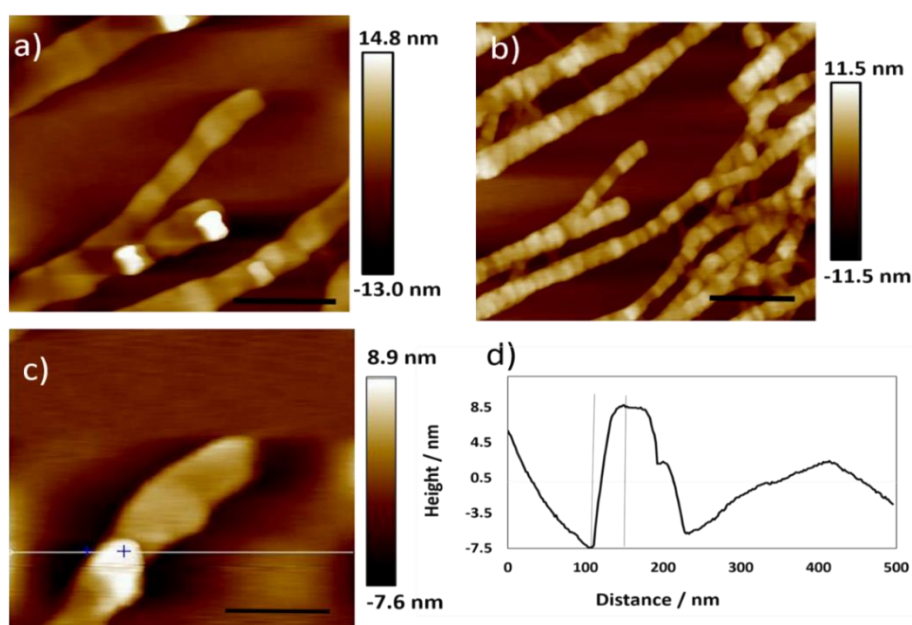


Figure 3.28. Tapping Mode AFM Height images of Au-6-TGR gel with DNA. Scale bars and height (grayscale) at (a), (b), and (c) are 300 nm, 500 nm, 150 nm and 14.8 nm, 11.5 nm, 8.9 nm, respectively. (d) The associated cross section along the white line at (c) shows the height of fibres ~ 8.5 nm.

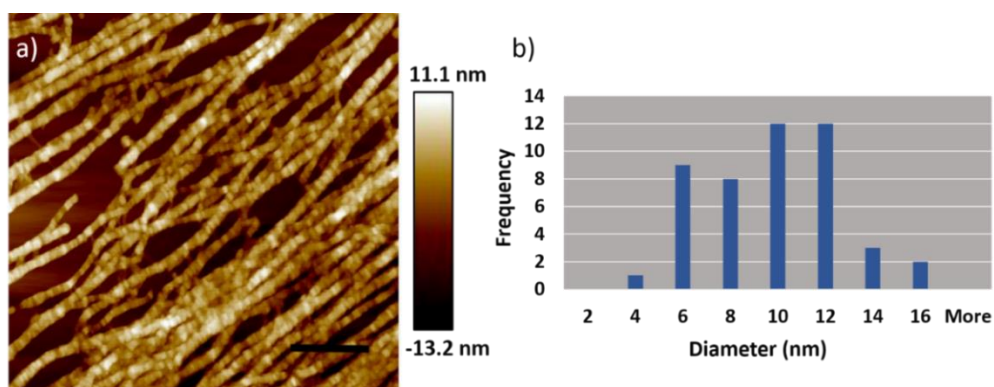


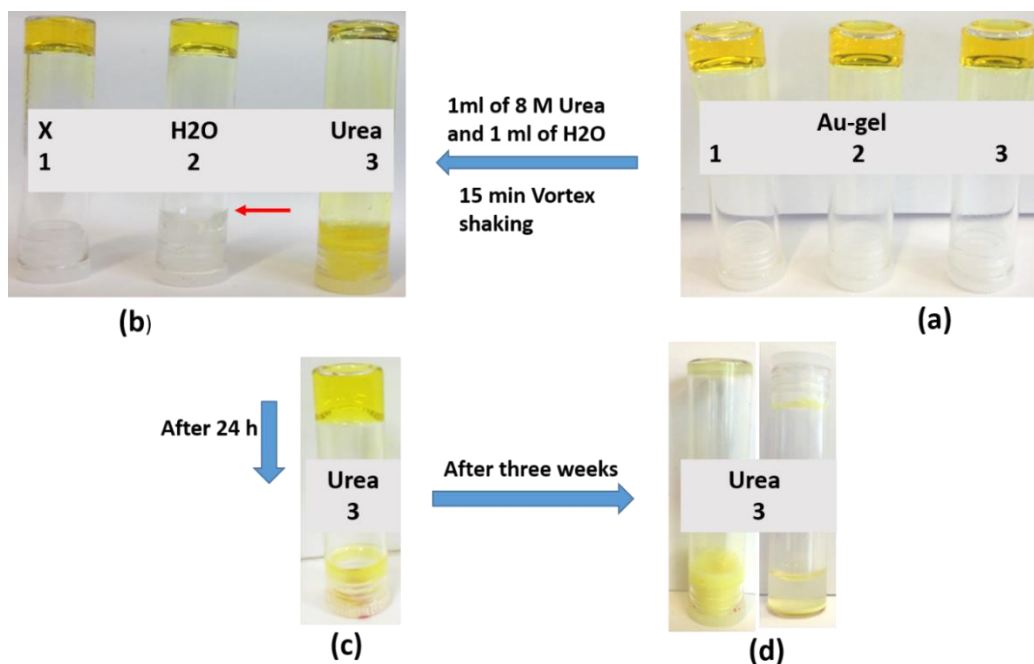
Figure 3.29. (a) Height AFM image with scale bar 1 μm and height (grayscale) 11.1 nm shows the fibrous morphology of Au-6-TGR gel as a consequence of addition DNA to Au-6-TGR gel, (b) the histogram shows the size distribution of the fibres.

3.13 Synthesis of gold:6-thioguanosine (Au:6-TGR) gel with urea

To assess the role of hydrogen bonding in the gel formation, urea solution was used as a denaturing agent. The working hypothesis was that urea could compete with 6-TGR hydrogen-bonding interactions and disrupt the gel in an analogous manner to the well-known effect of urea on proteins. 1 ml of 8M urea solution was added to 1 ml of Au:6-TGR gel with concentration 10 mg of 6-TGR, in a similar manner, 1 ml of water was added to 1 ml of gel while the third vial with gel left without additive (indicated with symbol X at the schematic which refers that it was left with no additive).

3.13.1 Interaction Au:6-TGR gel with urea

Scheme 3.1 below shows four parts, part (a) shows three vials of 1:1 Au:6-TGR gel labelled with (1), (2), and (3), at part (b) 1 ml of H_2O and 1 ml of 8 M urea solution was added to vials (2) and (3) respectively, while the third vial (3) left without additive (indicated with symbol X at the schematic which refers that it was left with no additive). The contents of the three vials were shaken with a vortex mixer for 15 min, after vigorous mixing, the gel with urea solution (vial 3) became a viscous liquid and mixed with the solution of urea, while the other two vials (1&2) were not affected. However, the solution with urea reformed a gel again after leaving to stand for 24 h at room temperature, as shown at part (c). The reformed gel was drop-cast onto a clean silicon chip and dried in air prior to imaging by AFM. After three weeks, the gel with urea transformed into a yellow powder and a clear solution (part d). Testing the powder under microscope showed crystals of urea, the powder was imaged by AFM and characterised by powder X-ray diffraction. This experiment was designed to study the effect of hydrogen bonding on the formation of Au:6-TGR hydrogel.



Scheme 3.1. Shows three vials of 1:1 Au:6-TGR gel (part a), 1 ml of H₂O and 1 ml of 8 M urea solution was added to vial (2) and (3), respectively, while vial (1) left without additive, marked with x, the three vials was shaken for 15 min causes collapsed the gel at vial (3), no change was occurred for the gel at vial (1&2) (part b). After 24h the gel with urea reformed again (part c), and after three weeks reformed gel was collapsed (part d).

3.13.2 AFM images of reformed gel with urea solution

The right-handed helical morphology of the reformed gel of Au:6-TGR with urea is very clear in Fig. 3.30. It is interesting that the reformed gel, that produced by reaction of Au:6-TGR gel with 8 M urea, retains the helical morphology and the height of the fibres (~ 3.5 nm) which is very close to that at the gel without urea (2–4 nm) as shown in Fig. 3.30. However, the distances between the pitches along a single fibre are decreased from 28 nm in the Au:6-TGR hydrogel without urea to 16 nm in the reformed gel with urea and that may be assigned to reduce the concentration of the Au:6-TGR hydrogel upon adding the urea solution to the half of the original concentration (10 mg/ ml). It is suggested that urea breaks up the innerchain hydrogen bonds, but the Au:6-TGR coordination polymer -Au-S-Au-S- backbone is unaffected.

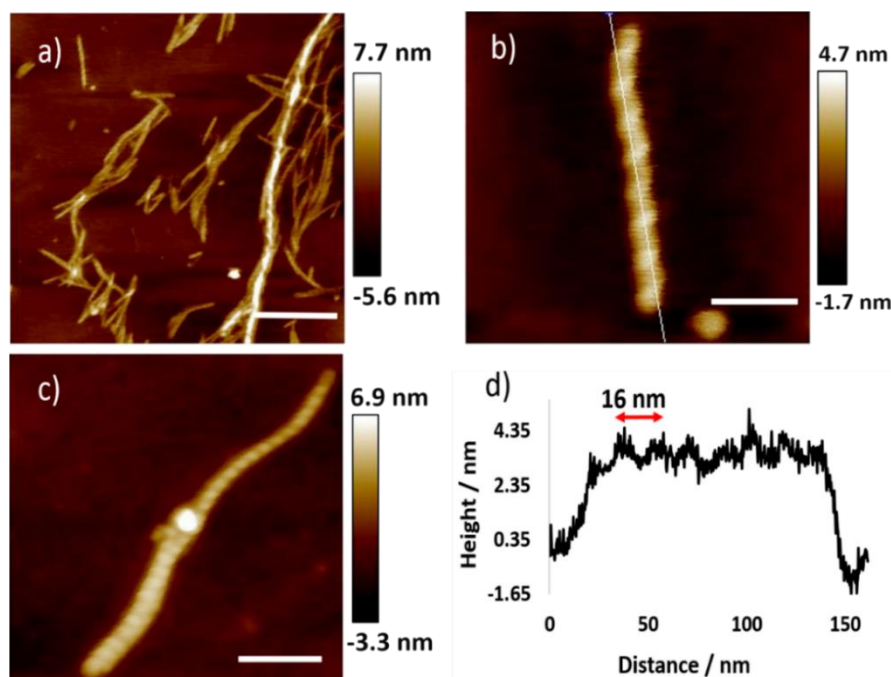


Figure 3.30. Tapping Mode Height AFM images of 1:1 Au:6-TGR gel after reformed gel with 8 M urea solution. The scale bar and the height (grayscale) at (a), (b), and (c) are 250 nm, 40 nm, 100 nm and 7.7 nm, 4.7, 6.9 nm, respectively, (d) the height profile measured along the white vertical line of the corresponding helical fibre ~ 3.5 nm in image (b). The distance between the top waves of the helix fibre is 16 nm as shown at the cross section.

3.13.3 Fluorescence microscopy

Fig. 3.31 displays fluorescence microscopic images for the re-formed Au(I):6-thioguanosine gel with 8 M urea (a), and the final product of the gel after collapsing (b) as a consequence of denaturing by urea solution. Image (a) showed very long fibres and it seems that the urea is connected to the Au(I) gel by hydrogen bonding, however, after three weeks, the gel collapsed and turned to yellow precipitate and crystals. These crystals represent the urea that gathered after losing the hydrogen bonding (cross-link) with the gel after collapse.

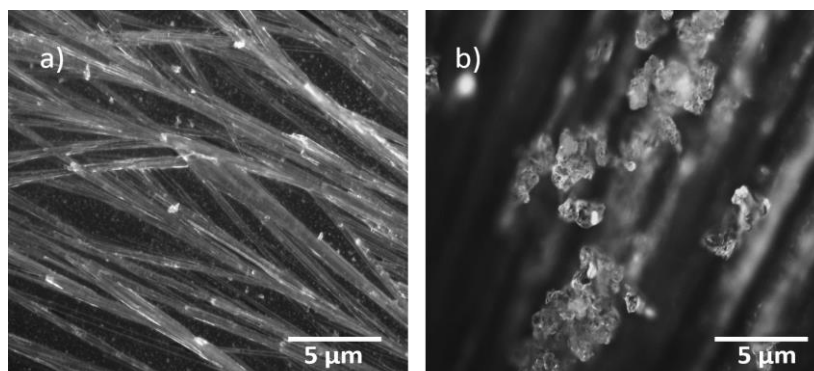


Figure 3.31. Shows the fluorescence microscopic image of: a) gold:6-thioguanosine gel that reformed with 8 M urea, b) the collapse gold:6-thioguanosine gel with urea after three weeks of reformation.

3.14 Conclusion

A new luminescent 1D coordination polymer based on the self-assembly of Au(I) ions with the sulfur-modified nucleoside, 6-thioguanosine have been prepared. The material's molecular structure is highly analogous to duplex DNA and, as a gold-thiolate polymer uniquely exhibits electrical conduction upon oxidative doping. This semiconducting motif can to be readily incorporated, co-axially, into the framework of DNA structures due to the metal-ion binding that assembles the chain being specific for the "mutant" nucleoside. This work advances the field of DNA-materials towards further complexity by allowing the incorporation of semiconducting properties co-axial *via* an alternative method and making possible new types of construction protocols, compositional architectures and material combinations.

The work in this chapter has been published.

Lamia L. G. Al-Mahamad, Osama El-Zubir, David G. Smith, Benjamin R. Horrocks, Andrew Houlton "A coordination polymer for the site-specific integration of semiconducting sequences into DNA-based materials" *Nature Communications*, 8, 2017.

doi:10.1038/s41467-017-00852-6.

References

1. Hammer, B. & Norskov, J.K. Why the gold is the noblest of all the metals. *Nature*, **376**, 238-240 (1995).
2. Barbieri, A., Accorsi, G. & Armaroli, N. Luminescent complexes beyond the platinum group: the d¹⁰ avenue. *Chemical Communications*, , 2185-2193 (2008).
3. Laguna, A. Modern Supramolecular Gold Chemistry: Gold-Metal Interactions and Applications. Gimeno, M .C. Chapter 1.The Chemistry of Gold. WILEY-VCH Verlag GmbH & Co. KGaA, Weinheim. 1-64 (2008).
4. Yang, W. & Li, T. From Achiral Molecular Compenents to Chiral Supermolecles and Supercoil Self-Assembly *Chemistry - A European Journal*, **5**, 1144-1149 (1999).
5. Lippert, B. Multiplicity of metal ion binding patterns to nucleobases. *Coordination Chemistry Reviews*, **200-202**, 487-516 (2000).

6. Amo-Ochoa, P., Castillo, O., Welte, L., Gomez-Herrero, J. & Zamora, F. Synthesis of designed conductive one-dimensional coordination polymers of Ni(II) with 6-mercaptopurine and 6-thioguanine. *Inorganic chemistry*, **48**, 7931-7936 (2009).
7. Tam, A.Y.-Y. & Yam, V.W.-W. Recent advances in metallogels. *Chemical Society Reviews*, **42**, 1540-1567 (2013).
8. Piepenbrock, M.-O.M., Clarke, N. & Steed, J.W. Metal Ion and Anion-Based “Tuning” of a Supramolecular Metallogel. *Langmuir*, **25**, 8451-8456 (2009).
9. Liu, K. & Steed, J.W. Triggered formation of thixotropic hydrogels by balancing competitive supramolecular synthons. *Soft Matter*, **9**, 11699-11705 (2013).
10. Aarbakke, J. & Elion, G.B. Thiopurine biology and pharmacology. *Trends in Pharmacological Sciences*, **18**, 3-7 (1997).
11. Olea, D. & Gomez-Herrero, J. From Coordination Polymer Macrocrystals to Nanometric Individual Chains *Advanced Materials*, **17**, 1761-1765 (2005).
12. Houlton, A., Amo-Ochoa, P., Hribesh, S., Pike, A.R. & Zamora, F. Coordination chemistry of 6-thioguanine derivatives with cobalt: toward formation of electrical conductive one-dimensional coordination polymers. *Inorganic chemistry*, **52**, 5290-5299 (2013).
13. Lavenn, C., Guillou, N., Fateeva, A. & Demessence, A. A luminescent double helical gold(i)–thiophenolate coordination polymer obtained by hydrothermal synthesis or by thermal solid-state amorphous-to-crystalline isomerization. *Journal of Materials Chemistry C*, **3**, 4115-4125 (2015).
14. Odriozola, I., Loinaz, I., Pomposo, J.A. & Grande, H.J. Gold–glutathione supramolecular hydrogels. *Journal of Materials Chemistry*, **17**, 4843-4845 (2007).
15. Kasened, O.E. Infrared spectra of 6-thioguanine tautomers. An experimental and theoretical approach. *Spectrochimica Acta Part A*, **58**, 1793-1808 (2002).
16. Rostkowska, H. & Adimowicz, L. Theoretical and matrix-isolation experimental studies on 2-thiocytosine and 5-fluoro-2-thiocytosine. *Biochimica et biophysica Acta*, **1172**, 239-246 (1993).
17. Odriozola, I., Ormategui, N., Loinaz, I., Pomposo, J.A. & Grande, H.J. Coinage Metal–Glutathione Thiolates as a New Class of Supramolecular Hydrogelators. *Macromolecular Symposia*, **266**, 96-100 (2008).
18. Singh, K., Yadav, R., A & Yadav, J.S. Vibrational studies of biomolecules-III. 6-Tbioguanine. *Spectrochimica Acta*, **47A**, 819-820 (1991).

19. Zhang, Y., Zhu, X., Smith, J., Haygood, M.T. & Gao, R. Direct observation and quantitative characterization of singlet oxygen in aqueous solution upon UVA excitation of 6-thioguanines. *The Journal of Physical Chemistry B*, **115**, 1889-1894 (2011).
20. Fernandez, E.J., Laguna, A., Lopez-de-Luzuriaga, J.M., Monge, M. & Sanchez-Forcada, E. Different phosphorescent excited states of tetra- and octanuclear dendritic-like phosphine gold(I) thiolate complexes: photophysical and theoretical studies. *Dalton Transactions*, **40**, 3287-3294 (2011).
21. Pyykko, P. Strong Closed-Shell Interactions in Inorganic Chemistry. *Chemical Reviews*, **97**, 597-636 (1997).
22. Kishimura, A. & Aida, T. Phosphorescent Organogels via "Metallophilic" Interactions for Reversible RGB-Color Switching. *Journal of the American Chemical Society*, **127**, 179-183 (2005).
23. Yam, V.W. & Cheng, E.C. Highlights on the recent advances in gold chemistry-a photophysical perspective. *Chemical Society Reviews*, **37**, 1806-1813 (2008).
24. Ma, Y., Zhou, X., Chan, W.-H. & Shen, J. High Luminescence Gold(I) and Copper(I) Complexes with a Triplet Excited State for Use in Light-Emitting Diodes. *Advanced Materials*, **11**, 852-857 (1999).
25. Yuguang, M. & Jiacong, S. Triplet luminescent dinuclear-gold(I) complex-based light-emitting diodes with low turn-on voltage. *Applied Physics Letters*, **74**, 1361-1363 (1999).
26. Agris, P.F. & Lam, A.T. Modified nucleoside-dependent transition metal binding to DNA analogs of the tRNA anticodon stem/loop domain. *BioMetals*, **8**, 290-296 (1995).
27. Holy, A. & Luck, G. CD studies on the conformation of oligonucleotides complexed with divalent metal ions: interaction of Zn^{+2} with guanine favours syn conformation. *Nucleic Acids Research*, **10**, 2757-2770 (1976).
28. Jonkheijm, P. & Meijer, E.W. Transfer of π -Conjugated Columnar Stacks from Solution to Surfaces. *Journal of the American Chemical Society*, **125**, 15941-15949 (2003).
29. Lee, C.C. & Schenning, A.P.J. Preparation and characterization of helical self-assembled nanofiber. *Chemical Society Reviews*, **38**, 671-683 (2009).
30. Bachman, R.E. & Bodolosky-Bettis, S.A. Construction of Luminescent Gold(I) Aryl Thiolates via Isonitrilegold(I) Complexes: Influence of Synthetic Methodology and the

- Thiolate Ligand on Structure and Properties. *Verlag der Zeitschrift für Naturforschung Tübingen*, **64b**, 1491-1499 (2009).
31. Mansour, M.A. & Eisenberg, R. Linear Chain Au(I) Dimer Compounds as Environmental Sensors: A Luminescent Switch for the Detection of Volatile Organic Compounds. *Journal of the American Chemical Society*, **120**, 1329-1330 (1998).
 32. Vickery, J.C. & Balch, A.L. Solvent-Stimulated Luminescence from the Supramolecular Aggregation of a Trinuclear Gold(I) Complex that Displays Extensive Intermolecular Au...Au Interactions. *Angewandte Chemie International Edition*, **36**, 1179-1181 (1997).
 33. Parker, D. & Roy, P.S. Crystal and Molecular Structure of Chloro-1,4,7-trithiacyclononane Gold(I): Adoption of a Strained [225] Conformation by the Macrocyclic Ligand. *Inorganica Chimica Acta*, **155**, 227-230 (1989).
 34. Battistoni, C. & Mattogno, C. XPS Photoelectron Spectra of Cluster Compounds of Gold. *Inorganica Chimica Acta*, **24**, 207-210 (1977).
 35. Moulder, J.F. & Chastain, J. Handbook of X-ray Photoelectron Spectroscopy: A Reference Book of Standard Spectra for Identification and Interpretation of XPS Data. Perkin-Elmer Corporation, Physical Electronics Division. (1992).
 36. Bourg, M.-C. & Lennox, R.B. Gold-Sulfur Bonding in 2D and 3D Self-Assembled Monolayers: XPS Characterization. *The Journal of Physical Chemistry B*, **104**, 6562-6567 (2000).
 37. McNeillie, A. & Smith, W.E. X-Ray Photoelectron Spectra of Some Gold Compounds. *Journal of the Chemical Society. Dalton transactions, Inorganic chemistry*, , 767-770 (1980).
 38. Kitagawa, H. & Nakajima, T. Studies of Mixed-valence States in Three-dimensional Halogen-bridged Gold Compounds, $\text{Cs}_2\text{Au}^{\text{I}}\text{Au}^{\text{III}}\text{X}_6$ (X = Cl, Br or I). Part 2.¹ X-Ray Photoelectron Spectroscopic Study. *Journal of the Chemical Society. Dalton transactions, Inorganic chemistry*, , 3121-3125 (1991).
 39. Best, S.A. & Walton, R.A. X-Ray Photoelectron Spectra of Inorganic Molecules. 18.¹Observations on Sulfur 2p Binding Energies in Transition Metal Complexes of Sulfur-Containing Ligands. *Inorganic Chemistry*, **16**, 1976-1979 (1977).
 40. Walton, R.A. The X-Ray Photoelectron Spectra Of Metal Complexes Of Sulfur-Containing Ligands: Sulfur 2p Binding Energies. *Coordination Chemistry Reviews*, **31**, 183-220 (1980).

41. Castner, D.G. X-ray Photoelectron Spectroscopy Sulfur 2p Study of Organic Thiol and Disulfide Binding Interactions with Gold Surfaces. *Langmuir*, **12**, 5083-5086 (1996).
42. Lindberg, B.J. & Siegbahn, K. Molecular Spectroscopy by Means of ESCA II. Sulfur compounds. Correlation of electron binding energy with structure. *Physica Scripta.*, **1**, 286-298 (1970).
43. Manceau, M., Gaume, J., Gardette, J.-L. & Bideux, L. Further insights into the photodegradation of poly(3-hexylthiophene) by means of X-ray photoelectron spectroscopy. *Thin Solid Films*, **518**, 7113-7118 (2010).
44. Almukhlifi, H.A. & Burns, R.C. Gold nanoparticles on metal oxide surfaces derived from *n*-alkanethiolate-stabilized gold nanoparticles; investigations of the adsorption mechanism and sulfate formation during subsequent thermolysis. *Applied Catalysis A: General*, **502**, 174-187 (2015).
45. Chilkoti, A. & Ratne, B.D. X-ray Photoelectron Spectroscopy of Iodine-Doped Nonconjugated Polymers. *Chemistry of Materials*, **5**, 786-792 (1993).
46. Salaneck, W.R., Plummer, E.W., Heeger, A.J. & MacDiarmid, A.G. Photoelectron spectroscopy of iodine-doped polyacetylene. *The Journal of Chemical Physics*, **72**, 3674-3678 (1980).
47. Hsu, S.L., Signorelli, A.J., Pez, G.P. & Baughman, R.H. Highly conducting iodine derivatives of polyacetylene: Raman, XPS and X-ray diffraction studies. *The Journal of Chemical Physics*, **69**, 106-111 (1978).
48. Polzonetti, G. & Russo, M.V. X-ray photoelectron spectroscopy of iodine-doped polyethynylferrocene. *Synthetic Metals*, **25**, 375-384 (1988).
49. Polzonetti, G. & Marsich, N. Evidence of reacting iodine species at the surface of a polyphenylacetylene film investigated by xps. *Journal of Electron Spectroscopy and Related Phenomena*, **52**, 581-588 (1990).
50. Moulay, S. Molecular iodine/polymer complexes. *Journal of Polymer Engineering*, **33**, 389-443 (2013).
51. Briggs, D. Surface Analysis of Polymers by XPS and Static SIMS. Cambridge University Press, Cambridge. (1988).
52. Sam, S.S. & Gabouze, N.N.-e. Peptide immobilisation on porous silicon surface for metal ions detection. *Nanoscale Research Letters*, **6**, 412-419 (2011).
53. Kondo, M., Mates, T.E., Fischer, D.A., Wudl, F. & Kramer, E.J. Bonding structure of phenylacetylene on hydrogen-terminated Si(111) and Si(100): surface photoelectron spectroscopy analysis and ab initio calculations. *Langmuir*, **26**, 17000-17012 (2010).

54. Seifert, S., Gavrilu, G.N., Zahn, D.R.T. & Braun, W. The molecular orientation of DNA bases on H-passivated Si(111) surfaces investigated by means of near edge X-ray absorption fine structure spectroscopy. *Surface Science*, **601**, 2291-2296 (2007).
55. Sapirgin, A.V., Thomas, C.W., Dulcey, C.S., Patterson, C.H. & Spector, M.S. Spectroscopic quantification of covalently immobilized oligonucleotides. *Surface and Interface Analysis*, **37**, 24-32 (2005).
56. Yue, J. & Epstein, A.J. XPS Study of Self-Doped Conducting Polyaniline and Parent Systems. *Macromolecules*, **24**, 4441-4445 (1991).
57. Engelkamp, H. & Nolte, R.J.M. Self-Assembly of Disk-Shaped Molecules to Coiled-Coil Aggregates with Tunable Helicity. *Science*, **284**, 785-788 (1999).
58. Song, B., Liu, B., Wu, G. & Yin, S. Controlled self-assembly of helical nano-ribbons formed by achiral amphiphiles. *Nanoscale*, **7**, 930-935 (2015).
59. Cao, H., Yuan, Q., Zhu, X., Zhao, Y.P. & Liu, M. Hierarchical self-assembly of achiral amino acid derivatives into dendritic chiral nanotwists. *Langmuir*, **28**, 15410-15417 (2012).
60. Jeong, J., Kang, L., Lubensky, T.C. & Yodh, A.G. Chiral structures from achiral liquid crystals in cylindrical capillaries. *Proceedings of the National Academy of Sciences (PNAS) USA*, **112**, E1837-1844 (2015).
61. Li, Y., Wong, K.M., Wong, H.L. & Yam, V.W. Helical Self-Assembly and Photopolymerization Properties of Achiral Amphiphilic Platinum(II) Diacetylene Complexes of Tridentate 2,6-Bis(1-alkylpyrazol-3-yl)pyridines. *ACS Applied Materials & Interfaces*, **8**, 17445-17453 (2016).
62. Letheby, H. On the Production of a Blue Substance by the Electrolysis of Sulfate of Aniline. *Journal of the Chemical Society*, **15**, 161-163 (1862).
63. Hirakawa, H., Macdiarmid, A.G. & Heeger, A.J. Synthesis of Electrically Conducting Organic Polymers: Halogen Derivatives of Polyacetylene, (CH)_x. *Journal of the Chemical Society, Chemical Communications*, , 578-580 (1977).
64. Moulay, S. *Journal of Polymer Engineering*, **33**, 389-443 (2013).
65. Pozonetti, G. & Russo, M.V. X-Ray Photoelectron Spectroscopy Of Iodine-Doped Polyethynylferrocene. *Synthetic Metals*, **25**, 375-384 (1988).
66. Cao, R. & Spicer, W.E. Investigation of Interface States and Fermi Level Pinning Mechanisms with Metals on InP(110) Surfaces. *Journal of Electron Spectroscopy and Related Phenomena*, **51**, 581-589 (1990).

67. Hardy, L.C. & Shriver, D.F. Poly(ethylene oxide)-Sodium Polyiodide Conductors: Characterization, Electrical Conductivity, and Photoresponse. *Journal of the American Chemical Society (ACS)*, **108**, 2887-2893 (1986).
68. Joo, J. & Epstein, A.J. Physical Characterization of Electrochemically and Chemically Synthesized Polypyrroles. *Macromolecules*, **33**, 5131-5136 (2000).
69. Hassanien, R. & Horrocks, B.R. Preparation and Characterization of Conductive and Photoluminescent DNATemplated Polyindole Nanowires. *ACS Nano- American Chemical Society*, **4**, 2149-2159 (2010).
70. Trnkova, L. & Palecek, E. Electrochemical Behaviour of Guanine and its Derivatives. I. Fast Cyclic Voltammetry of Guanosine and Calf Thymus DNA. *Bioelectrochemistry and Bioenergetics*, **7**, 643-658 (1980).
71. Yoshii, Y., Hoshino, N. & Akutagawa, T. The Formation of Organogels and Helical Nanofibers from Simple Organic Salts. *Chemistry a European Journal*, **20**, 16279-16285 (2014).
72. Epstein, I.R. & Xu, B. Reaction-diffusion processes at the nano-and microscale. *Nature Nanotechnology*, **11**, 312-319 (2016).
73. Tsuda, A. Hydrodynamic Helical Orientations of Nanofibers in a Vortex. *Symmetry*, **6**, 383-395 (2014).
74. Shen, Q.T., Schuh, A.L., Cui, Q. & Audhya, A. Structural analysis and modeling reveals new mechanisms governing ESCRT-III spiral filament assembly. *The Journal of Cell Biology*, **206**, 763-777 (2014).
75. Godeau, G. & Barthelemy, P. Glycosyl-Nucleoside Lipids as Low-Molecular-Weight Gelators. *Langmuir*, **25**, 8447-8450 (2009).
76. Kyotani, M. & Akagi, K. Helical Carbon and Graphitic Films Prepared from Iodine-Doped Helical Polyacetylene Film Using Morphology-Retaining Carbonization. *Journal of the American Chemical Society*, **130**, 10880–10881 (2008).
77. Brar, B. & Leonard, D. Spiral Growth of GaSb on (001) GaAs using Molecular Beam Epitaxy. *Applied Physics Letters*, **66**, 463-465 (1995).
78. Bennett, B.R. & Shanabrook, B.V. Molecular Beam Epitaxy of Sb-based Semiconductors. Electronics Science and Technology Division, Naval Research Laboratory, Washington, DC, Chapter 10. (1998).
79. Smereka, P. Spiral crystal growth. *Physica D*, **138**, 282-301 (2000).

80. Watson, S.M., Wright, N.G., Horrocks, B.R. & Houlton, A. Preparation, Characterization and Scanned Conductance Microscopy Studies of DNA-Templated One-Dimensional Copper Nanostructures. *Langmuir*, **26**, 2068-2075 (2010).
81. Hassanien, R., Almaky, M.M., Houlton, A. & Horrocks, B.R. Preparation and electrical properties of a copper-conductive polymer hybrid nanostructure. *RSC Advances*, **6**, 99422-99432 (2016).
82. Watson, S.M., Pike, A.R., Pate, J., Houlton, A. & Horrocks, B.R. DNA-templated nanowires: morphology and electrical conductivity. *Nanoscale*, **6**, 4027-4037 (2014).
83. Sostarecz, M.C. & Belmonte, A. Beads-on-String Phenomena in Wormlike Micellar Fluids. *Physics of Fluids*, **16**, L67-L70 (2004).
84. Clasen, C., Eggers, J., Fontelos, M.A., Li, J.I.E. & McKinley, G.H. The Beads-on-String Structure of Viscoelastic Threads. *Journal of Fluid Mechanics*, **556**, 283-308 (2006).
85. Wang, Y., Lai, C., Fei, B. & Xin, J.H. Beads-on-String Structured Nanofibers for Smart and Reversible Oil/Water Separation with Outstanding Antifouling Property. *ACS Applied Materials & Interfaces*, **8**, 25612-25620 (2016).

Chapter 4. Synthesis and Structural Study of Copper and Silver Complexes of 6-Thioguanosine

Abstract

This chapter demonstrates the synthesis and the characterization of 3D coordination polymers of a thiolated metal-nucleoside, 6-thioguanosine. Two hydrogels were prepared by complexation of copper and silver with 6-thioguanosine (6-TGR). The morphology of the hydrogel was examined by atomic force microscopy and confirmed with TEM images which showed the formation of dense fibres. The copper hydrogel displays strong luminescence, however the silver gel did not. Circular dichroism measurements for both Cu and Ag hydrogel displayed formation of new bands upon metal complexation indicating an ordered chiral structure. The coordination polymers were formed via Cu-S6 and Ag-S6 binding, respectively.

4.1 Introduction

A hydrogel of guanosine was prepared in 1962¹ by using 5'-guanosine mono phosphate (5'-GMP). This nucleoside and its derivatives are able to self-assemble under suitable conditions of concentration and pH to form a helical structure of G-quartets via hydrogen bonding. Recently, all types of interactions were found to be involved in the formation of the structure including π - π stacking, cation-dipole coordination, and metal ion-phosphate (electrostatic binding).² Most guanosine hydrogels that are prepared with metals ions were based on binding to guanosine via O6/N7 and the hydro-gels of its derivatives use binding modes via the sugar group³, C8⁴, and derivatives via N9.⁵ Houlton⁶ synthesised a chelate ring of Co- 6-thioguanosine complex ion, he found that the coordination occurred via S6 and N7, while Zamora⁷ was able to prepare a 1D polymer of Cd with 6-mercaptapurine via S6 and N7. Adhikari⁸ studied the effect of a series of monovalent cations including silver(I) ion which induce deoxy guanosine (d Gs) and guanosine (Gs) purine to form hydrogels. No complex has yet been observed for 6-thioguanosine (6-TGR) with coinage ions and this indicates specific properties of group 11 to self-assemble and aggregate to form supramolecular compounds of 3D hydrogels with 6-thioguanosine. In this work, we demonstrate for the first time the metal hydrogel of the thio analogue of O6-guanosine, that is 6-thioguanosine (6-TGR), which was capable to coordinate with coinage metal ions, copper and silver via the S6 atom. Interestingly, using this nucleoside with other metals showed different results, and the formation of gels

based on the concept of coordination polymer was not shown with other metals ions and it was only found with group 11.

4.2 Experimental

4.2.1 Synthesis of copper:6-thioguanosine (Cu:6-TGR) hydrogel

A Cu:6-TGR hydrogel was prepared with the mole ratio 1:2. $\text{Cu}(\text{CO}_2\text{CH}_3)_2$ solution (6 mg, 0.033 mmol in 40 μL MeOH and 160 μL H_2O) was added to warm solution of TGR (20 mg, 0.066 mmol in 400 μL NaOH (0.1N), 200 μL MeOH, and 200 μL H_2O), after gently mixing the two solutions and leaving to stand for 5 min, 1 ml of an orange gel was formed.

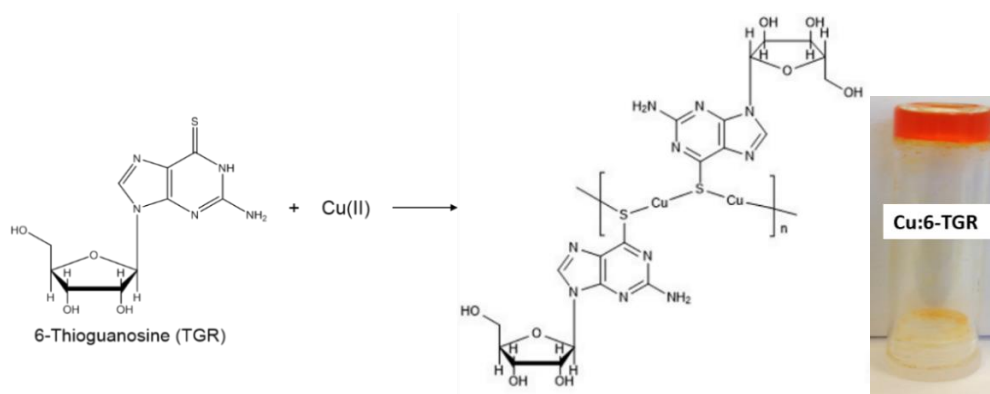
4.2.2 Synthesis of silver: 6-thioguanosine (Ag:6-TGR) hydrogel

Ag-TGR hydrogel was prepared with 1:1 mole ratio Ag:6-TGR, by adding solution of AgNO_3 (9 mg, 0.0534 mmol in 40 μL MeOH and 160 μL H_2O) to warm solution of 6-TGR (16 mg, 0.0534 mmol in 400 μL NaOH(0.1N), 200 μL MeOH, and 200 μL H_2O) the two solutions were gently mixed. 1 ml of a stable, transparent yellow hydrogel was formed immediately. To prepare hydrogel in the ratio 2:1 of Ag:6-TGR, the same procedure was followed, except the mass of AgNO_3 used was 1.8 mg.

4.3 Results & Discussion

4.3.1 Copper:6-thioguanosine (Cu:6-TGR) hydrogel

The reaction of Cu (acetate)₂ with 6-thioguanosine(6-TGR) with mole ratio 2:1 ligand to metal was necessary to produce the hydrogel as using 1:1 was failed to obtain the gel. In addition, the reaction was performed in basic medium, and this was important to dissolve the ligand 6-TGR which is difficult to dissolve in water, and it assists to make deprotonation at N1-H. The ligand is expected to be in the thiol form (-SH). A simple inversion test was used to indicate the stability of the gel. Scheme 4.1 presents the reaction route and a photo-graph of the gel.



Scheme 4.1. Proposed structure for Cu(I):6-thioguanosine hydrogel with an image of the gel inverted in a glass vial.

4.3.1.1 Fourier transform infrared spectroscopy (FTIR) characterisation

The spectrum of 6-thioguanosine nucleoside (6-TGR) in Fig. 4.1 shows a band at 1205 cm^{-1} , which is typically assigned to the C=S stretch, this band was changed to 1222 cm^{-1} after complexation with Cu(II) ions. In addition, the two bands at 1604 cm^{-1} and 1558 cm^{-1} that belong to C=C and C=N stretching mode at the nucleoside (TGR) was shifted to 1587 cm^{-1} and 1564 cm^{-1} , respectively, in Cu:6-TGR. These changes are assigned to the effects of complexation with metal ions. This data indicates the involvement of exocyclic S6 atom with Cu (I) ion, based on this it is suggested that complexation leads to a 1D polymer of form -S-Cu-S-Cu-. Fig. 4.1 shows the FTIR spectrum of 6-TGR before and after complexation with Cu(II) ions. Zamora⁹ found that the reaction between Cu(II) and 6-thioguanine leads to form tetramer complex of Cu(I) via S6 and the reduction of the Cu(II) to Cu(I) was occurred by 6-thioguanine. Odriozola¹⁰⁻¹⁴ prepared thiolate hydrogels with Au, Ag, and Cu via -S-M-S-M- systems. Based on the observations mentioned above, the binding site for the reaction of Cu ion with 6-thoguanosine is S6 atom.

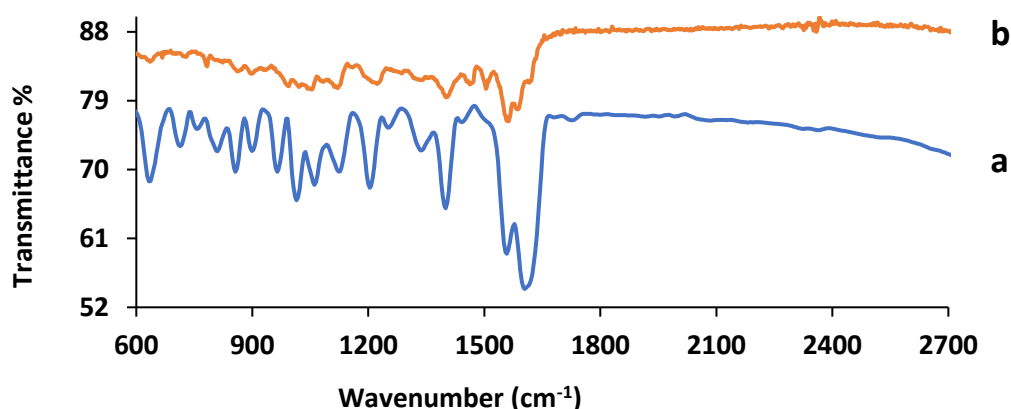


Figure 4.1. FTIR spectrum of: a) 6-thioguanosine (TGR) and b) Cu:6-TGR gel.

4.3.1.2 UV-Vis absorption spectroscopy

Spectroscopic characterization of 6-thioguanosine (6-TGR) in pH 2 and pH 12 showed that 6-TGR can exist thione (C=S) and thiol (-SH) forms by forming bands at 348 nm and 320 nm, respectively, as shown in Fig. 4.2, this data was consistent with reports in this area.¹⁵⁻¹⁷ The UV-Vis spectrum of the basic solution (pH 10.7) of 6-thioguanosine (6-TGR) showed characteristic peaks at 273 nm, 326 nm and 345 nm associated with π - π^* transitions, the peak at 326 nm is due to the excitation energy of the π - π^* transition of the thiol form, may be deprotonation was occurred to NH1 at basic medium and that revealed the ligand appears at thiol form, in addition the band at 345 nm is frequently relates to the emerging of the thiol base π - π^* transitions and the transition of the stacked π - π^* of the neighbours nucleosides.¹⁸ The spectrum of the 6-TGR showed dramatically red shift for the bands at 273 nm and 326 nm to lower energy (324 nm and 380 nm respectively) after complexation with Cu ions, the change in the spectrum is due to the formation of ligand to metal charge transfer complex via binding of Cu ion with S6 at the nucleoside 6-thioguanosine, as shown in Fig. 4.3.

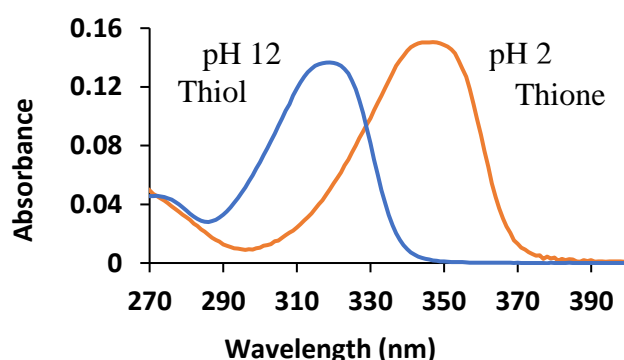


Figure 4.2 Comparison UV-Vis absorbance spectra of 6-thioguanosine (6-TGR) solution at pH 2 and pH 12 and showed that 6-thioguanosine (6-TGR) was in thione and thiol form, respectively.

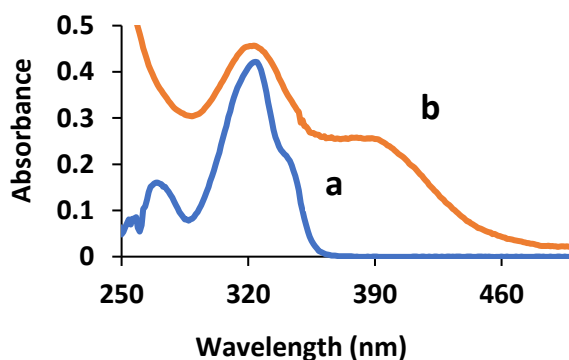


Figure 4.3. Comparison UV-Vis spectrum of: a) basic solution of 50 μ M 6-thioguanosine (6-TGR) vs b) Cu:6-thioguanosine (Cu:6-TGR) gel.

4.3.1.3 Fluorescence spectroscopy

Fig. 4.4 displays the fluorescence emission spectrum of the basic solution of 6-thioguanosine (6-TGR) nucleoside with excitation at 326 nm and the fluorescence emission spectrum of Cu-TGR gel with excitation at 380 nm. The spectrum of 6-TGR solution showed a broad peak centred at 420 nm covering the area from 347 nm to 514 nm associated with π - π^* transitions, while the spectrum of Cu:6-TGR gel showed red shift to lower energy and exhibited a broad peak centred at 580 nm over the range 494 nm to 727 nm indicating the strong interactions between Cu(I) ion and the nucleoside 6-TGR. The emission is tentatively assigned to metal–ligand charge transfer transitions because the oxidation state of the Cu is (I) at the gel as shown by XPS data below.¹⁹ It is known that the aggregation via metallophilic interactions tends to reduce the HOMO–LUMO gap^{20,21} and hence, the strong luminescence of Cu(I):6-TGR complex is suggestive of strong Cu...Cu intermolecular interactions because of the large Stokes shift (9074 cm⁻¹). Such large Stokes shifts are known for Cu(I) complexes²²⁻²⁴ and no overlap may be observed for the absorbance and emission bands in these complexes.¹⁹

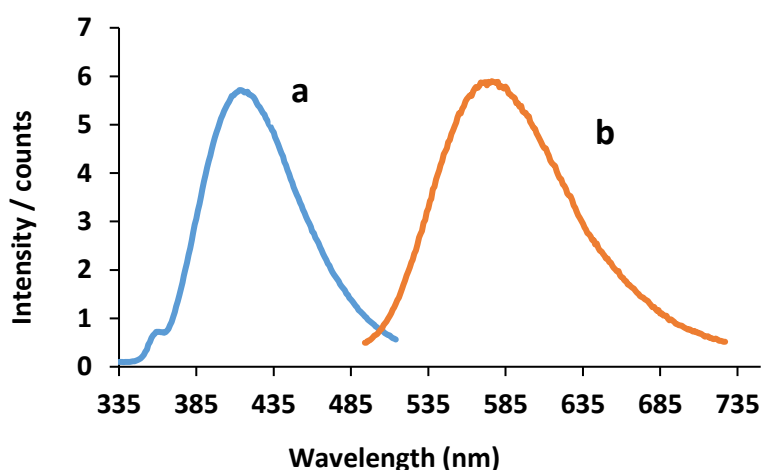


Figure 4.4. Fluorescence spectra of: a) basic solution of 50 μ M 6-thioguanosine (6-TGR) nucleoside, and b) the spectrum of Cu:6-TGR gel. The excitation wavelength was 326 nm and 380 nm for 6-TGR and Cu:6-TGR, respectively.

4.3.1.4 Circular dichroism spectroscopy (CD) characterization

CD spectroscopy was used to investigate the optical and chiral properties of the gels. Fig. 4.5 displays the optical activities of 6-TGR solution and Cu:6-TGR gel. The CD spectrum of the 6-thioguanosine nucleoside (6-TGR) showed a negative band ellipticity under 200 nm that is attributed to the ribose moiety,²⁵ and two bands, positive and negative, at 228 nm and 246 nm that are associated with n - π^* , along with two bands, positive and negative, at 262 nm and 326

nm that due to π - π^* transitions, respectively. However, the spectrum of 1:2 Cu:6-TGR gel showed remarkably hyperchromicity and marked red shift in the bands of n- π^* transition to 232 nm and higher intensity and red shift to the bands of π - π^* transitions at negative 262 nm and positive 330 nm. Increasing the intensity of the ellipticity after complexation with metal ions is assigned to increases in the base stacking and thereby increasing the molecular ordering.^{26,27} Chantot²⁸ suggested that the optical activity of the bromo guanosine gel is assigned to the formation of a highly ordered helical structure.

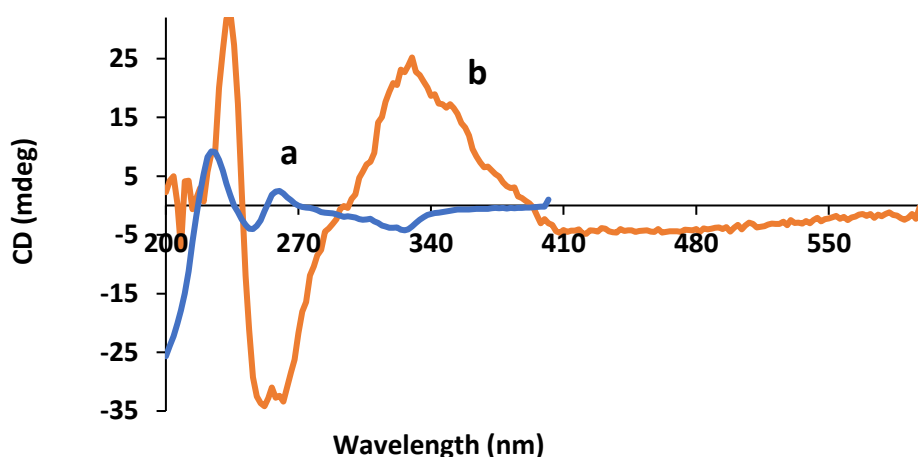


Figure 4.5. CD spectra of: a) the aqueous solution of 6-thioguanosine (6-TGR) (blue line) vs b) CD spectrum of 1:2 Cu:6-TGR gel (orange line).

4.3.1.5 X-Ray photoelectron spectroscopy (XPS) characterization of Cu:6-thioguanosine gel (Cu:6-TGR)

The colour change upon addition of the blue solution of Cu(II) to the solution of the 6-thioguanosine (6-TGR) suggests that the oxidation state of the Cu(II) ion was changed from (+2) to (+1) in the orange Cu:6-TGR gel. In order to establish the oxidation state of the Cu ion at the gel, X-ray photoelectron spectroscopy (XPS) was carried out. The XPS spectrum of Cu:6-TGR xerogel, Fig. 4.6, detected the Cu 2p_{3/2} and Cu 2p_{1/2} at binding energy 932.78 with FWHM 1.8 eV and 952.58 eV with FWHM 2.3 eV respectively with a splitting of 19.8 eV, and this agrees with the separation value of Cu 2p_{3/2} and Cu 2p_{1/2} for Cu(I).²⁹⁻³¹ Distinguishing between Cu(II) and Cu(I) in XPS is not difficult, as Cu(II) shows shake-up satellites^{32,33} due to interaction of the photoelectron with the incomplete d-shell of nearby Cu atoms, this satellite peak usually appears at 942 eV which is absent in the XPS spectrum of Cu:6-TGR gel, suggesting that Cu(II) is not present and the oxidation state of the copper at the gel is (+1).

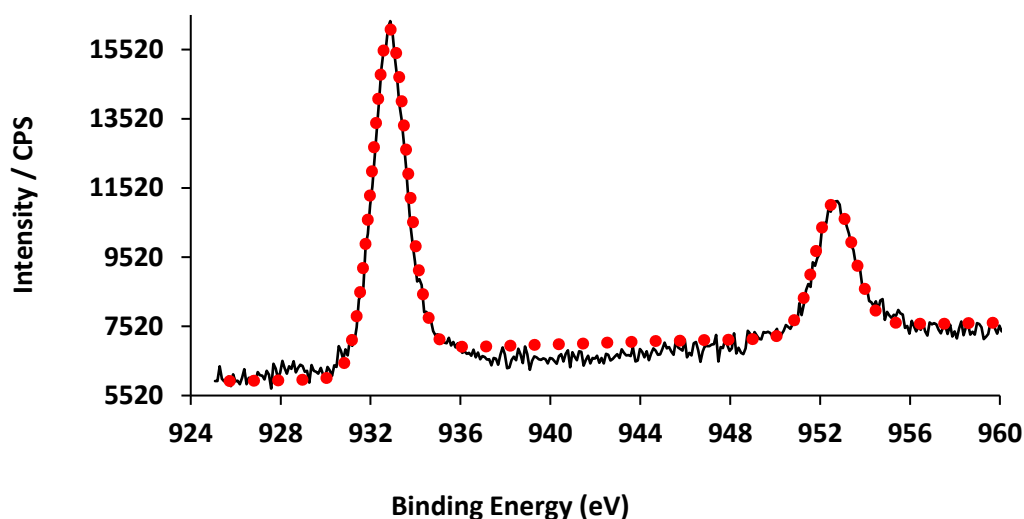


Figure 4.6. The XPS spectra of Cu:6-TGR shows the photoelectron for Cu2p_{3/2} and Cu2p_{1/2} at binding energy 932.78 eV, FWHM 1.8 eV and 952.58 eV, FWHM 2.3 eV, respectively with a splitting of 19.8 eV.

To ensure no Cu(0) was formed at the gel, Auger Parameter data (AP) was used to distinguish between Cu(0) and Cu(I); the appearance a peak at 915.6 K.E which is lower than that associated with Cu(0) by ~3 eV indicates that the oxidation state of Cu at the gel is Cu(I) , as shown in Fig. 4.7 , and this consistent with the literature.³⁴

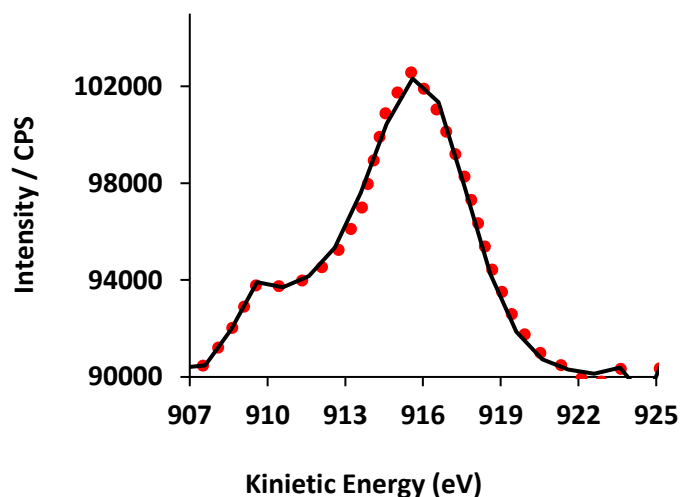


Figure 4.7. The XPS spectrum of auger parameter for L₃M₄₅M₄₅ Kinetic Energy (eV) of Cu:6-TGR shows the Auger parameter (AP) data at 915.5 K.E.

To confirm no Cu₂O at the sample, O1s XPS was measured, Fig. 4.8 shows no component centred at 530.4 eV that belongs to Cu₂O and the band at 532.7eV with FWHM 1.68 eV belongs to the oxide layer at silicon substrate^{35,36} and possibly to water/acetate. The above observations confirm that copper acetate (Cu(CH₃COO)₂) was reduced by the purine compound (6-

thioguanosine), and that agrees with studies³⁷⁻³⁹ which showed reduction of Cu(II) by purine to Cu(I).

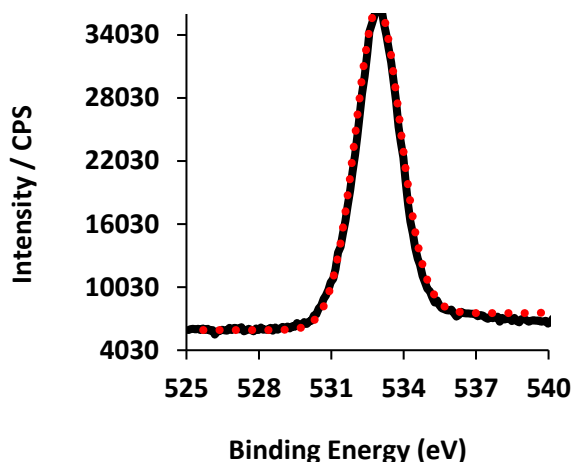


Figure 4.8. XPS spectrum of Cu:6-TGR shows the photoelectron of O1s with FWHM 1.68 eV.

4.3.1.6 Powder x-ray diffraction (XRD)

Cu(I) is soft acid has affinity towards S atom (soft base), the Cu-S⁴⁰⁻⁴² distance is found in the range 0.247-0.268 nm, and the S...S⁴⁰ interdimer was found at 0.327 nm. Other reports found that the distance of Cu-S at thiourea is 0.231-0.242 nm, Cu-Cu^{43,44} was found 0.255 nm, while Saxena⁴⁵ observed that Cu-Cu distance at 0.269 nm and 0.2722 nm. Cu-N7 distance was found at 0.1992 nm by Sletten⁴⁶ who prepared dichloro-(6-thio-9-methyl purine)copper(II) monohydrate, this band was not found here suggests that Cu(I) was not binding via N atoms. Fig. 4.9 and Table 4.1 below show the XRD pattern and the distance (*d_i*) that extracted from analysis XRD data for Cu:6-TGR gel.

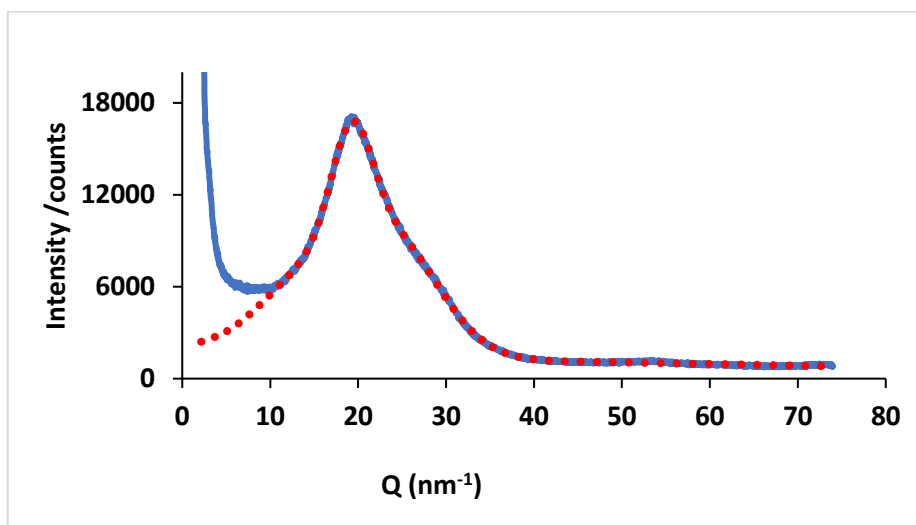


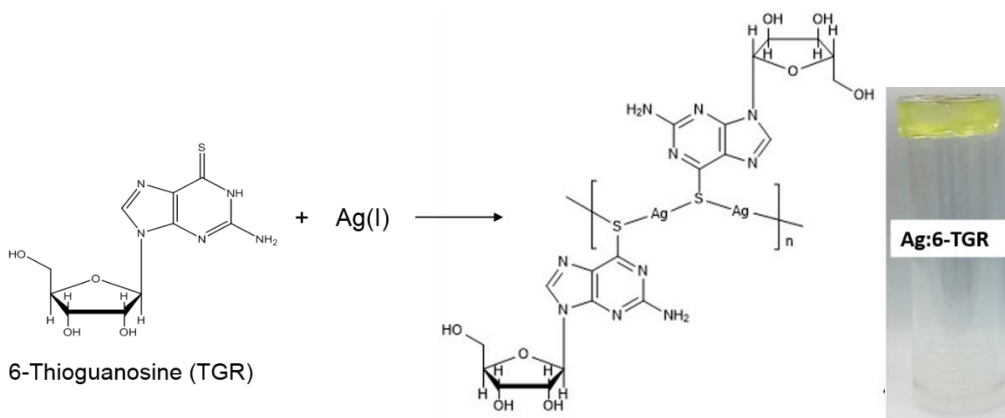
Figure 4.9. XRD pattern for Cu:6-TGR hydrogel. The blue line is the experimental diffraction data and the red dotted line is the theoretical fit to a sum of Gaussian functions.

Table 4.1. Distances extracted from the analysis of the XRD data for Cu:6-TGR gel.

Distance / nm	Suggested Assignment
0.257	Cu-S
0.325	S...S
0.394	π - π distance ⁴⁵ between layers

4.3.2 Silver: 6-thioguanosine (Ag:6-TGR) hydrogel

The reaction of AgNO₃ with 6-thioguanosine (6-TGR) in basic medium leads to form a stable hydrogel. The classic inversion test was used to confirm the formation of the gel as shown in Scheme 4.2. Using basic medium to achieve this reaction was important to dissolve the 6-TGR, at the same time it helps to make deprotonation at N1-H and this reveals 6-TGR in a thiol form.



Scheme 4.2 Proposed structure for Ag(I):6-thioguanosine hydrogel and photo image for the yellow hydrogel.

4.3.2.1 Fourier transform infrared spectroscopy (FTIR) characterisation

The IR spectra of Ag:6-TGR gel in Fig. 4.10 shows shifts for the band at 1205 cm⁻¹ that we attribute to the C=S stretch mode to higher frequency (1211 cm⁻¹) indicates that the binding occurred via the S6 atom. No change was observed for the bands at 1604 cm⁻¹ and 1558 cm⁻¹ at the 6-TGR nucleoside that assigned to stretch mode C=C and N=C and that suggests that no binding was occurred via N7. No broad band at 1319 cm⁻¹ in the complex indicating that nitrate group was not take part in the binding. The above observations indicate that Ag(I) is binding to S6 and forming 1D polymer of -Ag-S-Ag-S-, this data was consistent with Odriozola^{10,13} who prepared thiolate hydrogels with coinage metal ions. Orioli¹⁵ and Tu⁴⁷ prepared a complex of Ag:6-guanosine and they suggested that forming a chelate ring stabilized Ag complexes,

while Mann², Gancharova⁴⁸, and Loo⁴⁹ found that the coordination of Ag(I) to guanosine monophosphate (GMP) occurred via O6 and N7 by forming a dimeric structure.

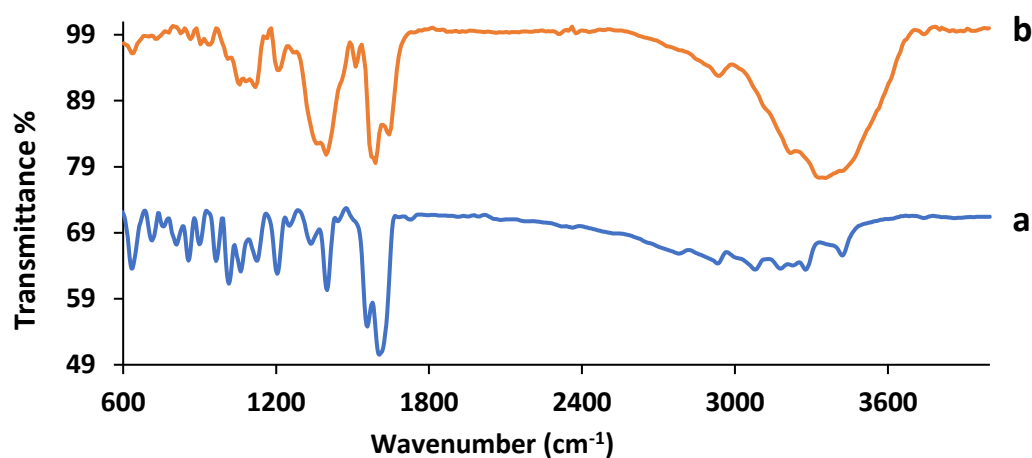


Figure 4.10. FTIR spectrum of: a) 6-thioguanosine (6-TGR) nucleoside vs b) silver:6-thioguanosine (Ag:6-TGR) xerogel.

4.3.2.2 UV-Vis absorption spectroscopy

The UV-Vis spectrum of a basic (pH 10.3) solution of 6-thioguanosine nucleoside (6-TGR) showed a band at 326 nm that belongs to π - π^* transitions of the thiol form as a result of the deprotonation at NH1. This band was shifted to lower energy (340 nm) after complexation with Ag (I) ions, Fig. 4.11.

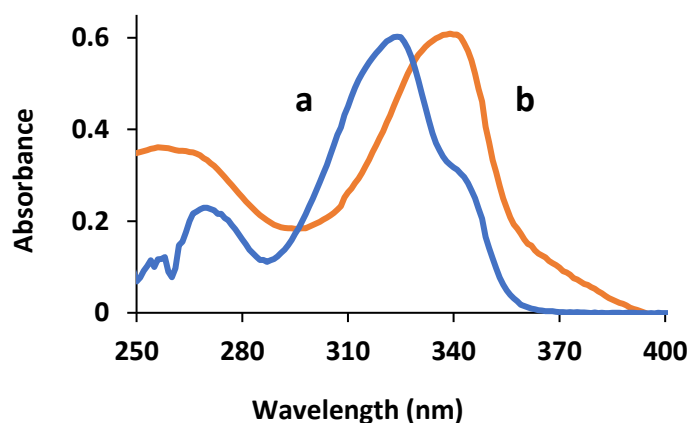


Figure 4.11. UV-Vis spectrum of: a) basic solution of 6-thioguanosine nucleoside (6-TGR) vs b) spectrum of Ag:6-TGR gel.

4.3.2.3 Fluorescence spectroscopy

In contrast to the fluorescence spectrum of the copper-6-thioguanosine gel, the silver-nucleoside gel shows a weak fluorescence band from 495 nm to 630 nm. It has been suggested

that the absence the Ag...Ag interactions increases the HOMO-LUMO gap ²¹ and weak luminesce, similar to the free ligand, is at least consistent with this. A very few reports that prepared silver nucleoside compounds have shown no fluorescence,^{2,8} and numerous papers on different Ag(I) complexes showed no fluorescence,⁵⁰ except for the dimeric complexes of silver and gold that prepared by Ray.⁵¹ He observed fluorescence for a dimeric Ag complex and he claimed that as a result of shorter Ag...Ag contacts. Fig. 4.12 shows the fluorescence emission spectrum of Ag:6-TGR.

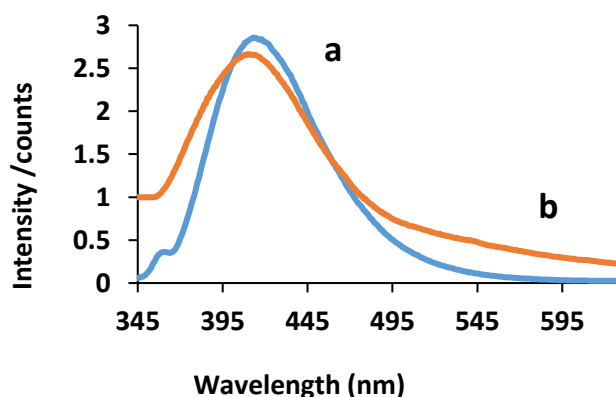


Figure 4.12. Fluorescence emission spectra of: a) basic solution of 50 μ M 6-thioguanosine (6-TGR) nucleoside (blue line), and b) the spectrum of Ag:6-TGR gel (orange line), the excitation was 326 nm and 340 nm for 6-TGR and Ag:6-TGR, respectively.

4.3.2.4 Circular dichroism spectroscopy (CD) characterization

The positive and negative bands at 228 nm and 246 nm that belongs to $n-\pi^*$ transition in the spectrum of the nucleoside 6-thioguanosine (6-TGR) showed red shift in the spectrum of Ag:6-TGR to negative bands at 238 nm and 300 nm with high intensity as a result of binding Ag ion with the nucleoside 6-TGR, Fig. 4.13. The positive and negative bands at 262 nm and 328 nm that belongs to $\pi-\pi^*$ were shifted with high intensity to negative and positive bands at 342 nm and 406 nm respectively in the spectrum of the complex. The CD spectrum of the 6-TGR ligand is dramatically altered upon the addition of Ag(I) and that reflects the ordered structure of the coordination polymer.

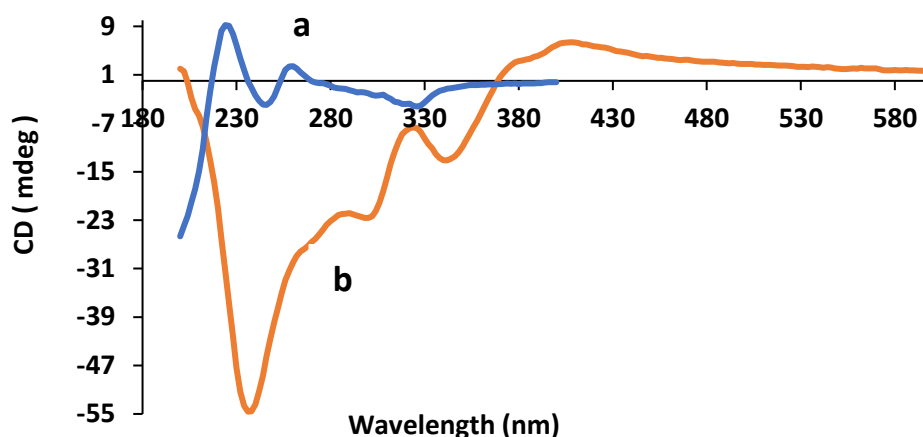


Figure 4.13. Comparison between the CD spectra of: a) 6-thioguanosine nucleoside (6-TGR), and b) CD spectrum of 1:1 Ag:6-TGR gel.

4.3.2.5 Powder X-ray diffraction (XRD)

Ag(I) is a relatively soft acid that prefers to coordinate with soft bases such as sulfur but also coordinates to nitrogen.⁵² Fig. 4.14 displays the X-ray diffraction data of Ag:6-TGR hydrogel; the scattering is typical of amorphous systems with partial order and can be analysed by fitting sums of Gaussian functions to the data. The peak positions to these fitted components are related to the interatomic distances by Bragg's law and Table 4.2 represents the distance between the atoms in the polymer. The distances of Ag-S and Ag-Ag were found 0.272 and 0.374 nm, respectively, the data were consistent with the literature.^{53,54} The absence of Ag-N7 distance indicates that the binding site in the Ag(I) gel was only through S6 atom.

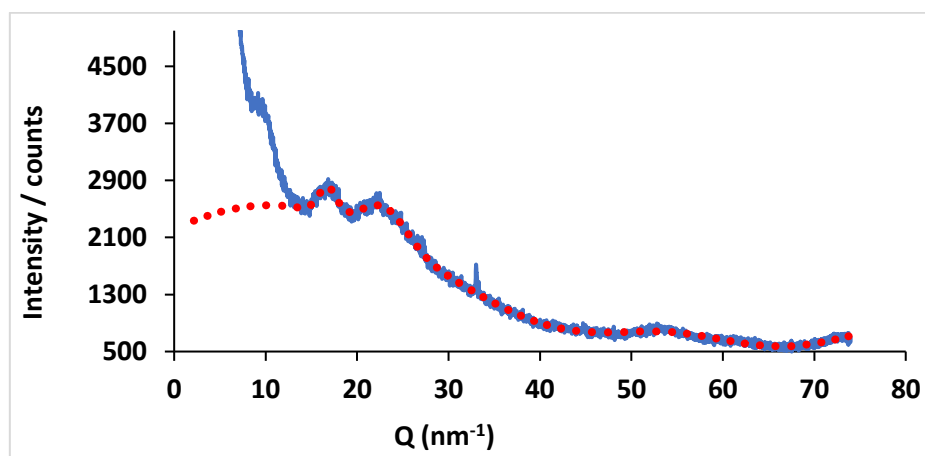


Figure 4.14. XRD pattern for Ag:6-TGR hydrogel. The blue line is the experimental diffraction data and the red dotted line is the theoretical fit to a sum of Gaussian functions.

Table 4.2. Distances extracted from the analysis of the XRD data for Ag:6-TGR gel.

Distance / nm	Suggested Assignment
0.272	Ag-S ⁵³
0.374	Ag-Ag

4.3.3 Atomic force microscopy (AFM)

In order to probe the morphology and the size of the fibres in the gels, surface topographic imaging was carried out using tapping mode AFM by depositing 2 μ L of Cu:6-TGR and Ag:6-TGR gels onto a clean silicon (100) wafer (1cm x 1cm). The samples were left to dry overnight in air prior to analysis. All AFM images showed a network of long fibres. A statistical analysis was carried out to show the height and the size (diameter) distribution of the fibres in the gel.

A typical AFM image of the Cu:6-TGR xerogel in Fig. 4.15, shows a very dense, entangled fibres with heights in range 10 - 34 nm. The size distribution of the fibres was calculated as shown in the histogram, and the modal height was ~28 nm, some lower structure heights between 10 - 16 nm with lower frequency can be seen, in addition to a few larger structures with heights between 31- 46 nm. These larger structures can be assigned to bundles of two or more single fibres. As shown in the section analysis, some of the peaks are single fibres and some peaks are most likely two or more fibres on top of another. This likely also explains the bimodal distribution of Fig. 4.15 b.

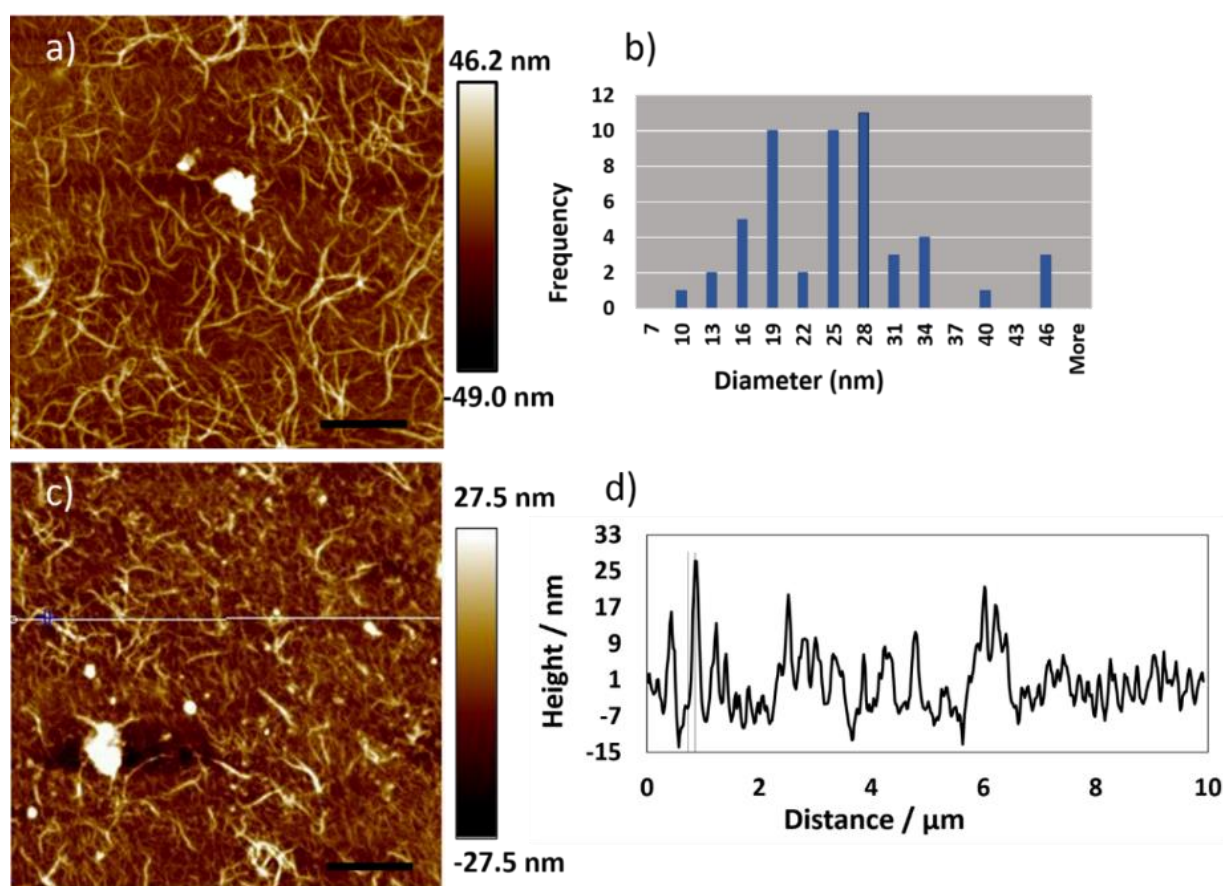


Figure 4.15. Tapping Mode AFM Height image of 1: 2 Cu-6-thioguanosine gel (Cu:6-TGR), (a)&(c) the scale bar was 2 μm and the height (grayscale) were 46.2 nm & 27.5 nm, (b) the histogram shows the size (diameter) distribution of the fibre. (d) A cross section associated the white horizontal line in (c) shows the height of the fibres ~ 28 nm, as shown at the section, some of the peak is a single fibre and some peaks are corresponding to two fibres on top of the other and for this reason the distribution looks bimodal.

In the AFM image that is shown in Fig. 4.16, a regular needle-like morphology can be observed; it is apparent from image (b) that some fibres are entangled with each other but, in general the images show that the common morphology of the fibres was needle-like. A statistical analysis shows that the modal height of the fibres was 3 nm and the range observed was 2-7 nm, much thinner than for the Cu fibres of Fig. 4.15. The profile of the white section in image (c) shows that the height of the fibres is 2-3 nm and the regular nature of the heights suggests fibres whose heights match individual polymer chain dimensions.

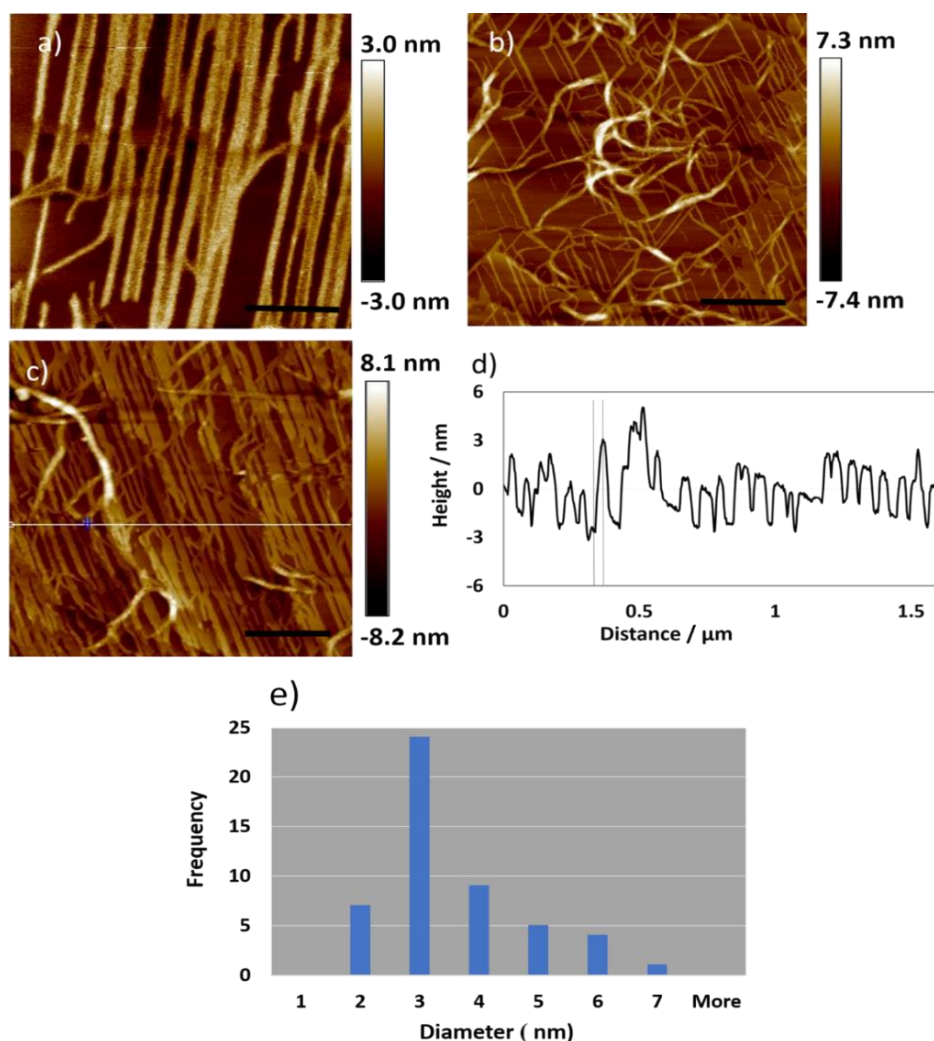


Figure 4.16. Tapping Mode AFM Height images of 1:1 Ag:6-thioguanosine gel (Ag:6-TGR). The scale bars and the heights (grayscale) were 200 nm & 3 nm, 400 nm & 7.3 nm, and 400 nm & 8.1 nm at a), b), and c), respectively, d) the associated cross-section along the white horizontal line in (c) shows the height of the fibres ~ 3 nm, e) the histogram shows the size (diameter) distribution of the fibres.

In Fig. 4.17, silver: 6-thioguanosine was prepared with mole ratio 2:1, by increasing the concentration of silver ions, the morphology of the gel was changed compared to the gel with ratio 1:1. It is not clear if another silver ion was coordinated to a second binding site of the nucleobase, though an experiment was done to test if the excess of silver ions were free or binding, by reducing the gels with both ratios with DMAB (Dimethylamine Borane) at the same conditions. The results showed that the gel with ratio 2:1 was reduced very fast (formation of black, metallic Ag), however the gel with ratio 1:1 was very difficult to reduce and that suggested that the excess of silver ions in the gel with ratio 2:1 were free, even though, the reason that causes the different morphology of this gel is still not clear.

The AFM images in Fig. 4.18 show lattice-like fibre network. The white line across image (a) along several microns of fibres displays structure height ~ 3 nm, while the histogram in Fig.

4.18 (d) demonstrates the average fibre height for ~ 50 fibres of Ag:6-TGR gel, the structure height was observed at 3 nm, some larger structure height up to 5 nm was seen in much lower frequency, in addition, to lower structure height up to 2 nm in much lower frequency was also seen. Interestingly, the height of the fibres was similar at both stoichiometry (3 nm).

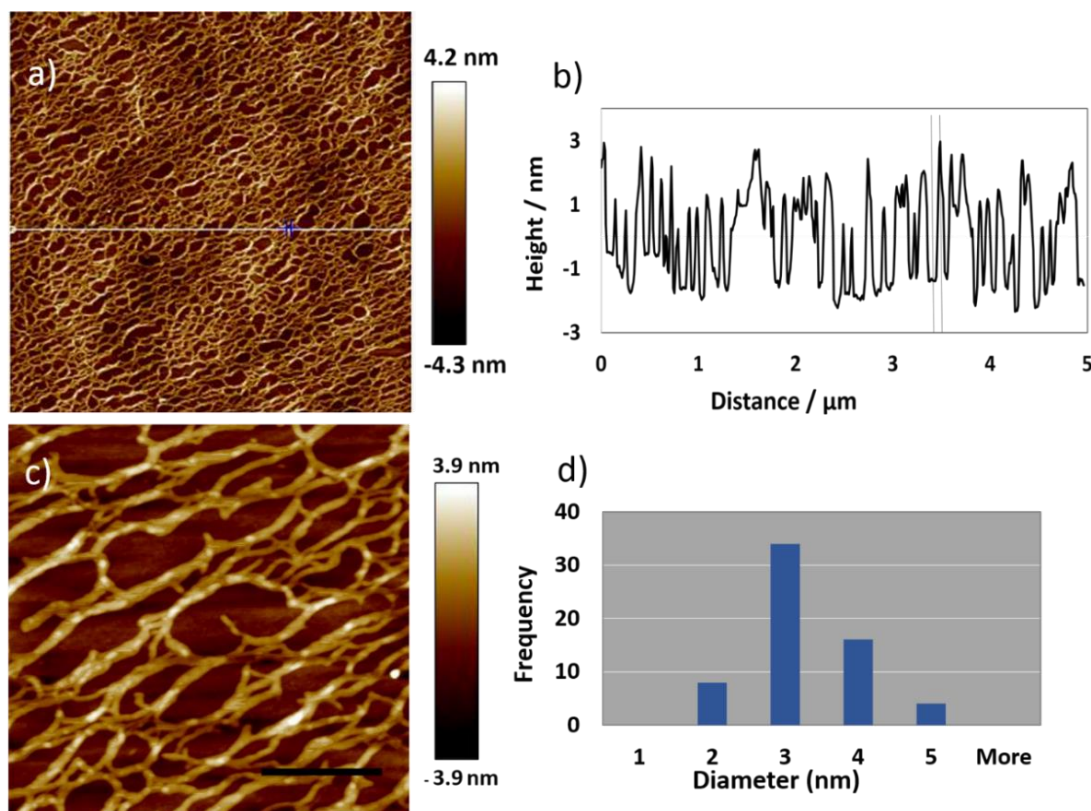


Figure 4.17. Tapping Mode AFM Height images of 2:1 Ag:6-thiouanosine gel (Ag:6-TGR) drop casted onto a silicon wafer and drying by air. The scale bars are $1\mu\text{m}$ & 300 nm and the height (grayscale) are 4.2 nm and 3.9 nm in (a) and (c), respectively. (b) The associated cross- section along the white horizontal line in (a) shows the height of fibrous $\sim 3\text{ nm}$, (d) the histogram of the size (diameter) distribution of ~ 50 fibres of Ag:6-TGR.

4.3.4 Transmission electron microscopy (TEM)

The morphology of Ag & Cu:6-TGR xerogels were examined using TEM, based on this approach, two types of substrate were used to prepare the samples, carbon coated copper grids and holy carbon copper grids. The sample was prepared by drop casting $1.5\mu\text{L}$ of the gel onto the substrate, followed by air drying prior to imaging. The inspection of the Ag:6-TGR samples with concentrations 2:1 and 1:1 as shown in Fig. 4.18 and 4.19, respectively, revealed the formation of very dense, entangled networks of fibres.

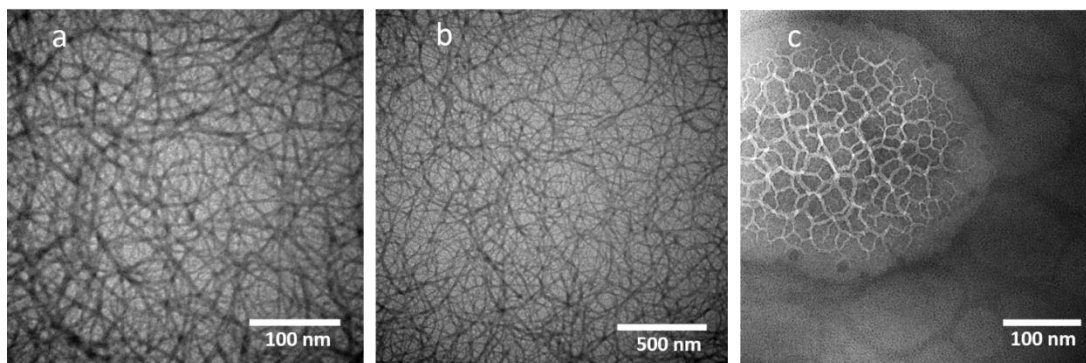


Figure 4.18. TEM of 2:1 Ag:6-TGR xerogel, the scale bar was 100 nm, 500 nm, 100 nm at (a), (b), and (c), while the magnification was 64000x, 34000x, and 180000x, respectively.

It is worthwhile to note here that; no silver nanoparticles were seen at the TEM images for Ag:6-TGR gel that prepared with metal to ligand stoichiometry 2:1.

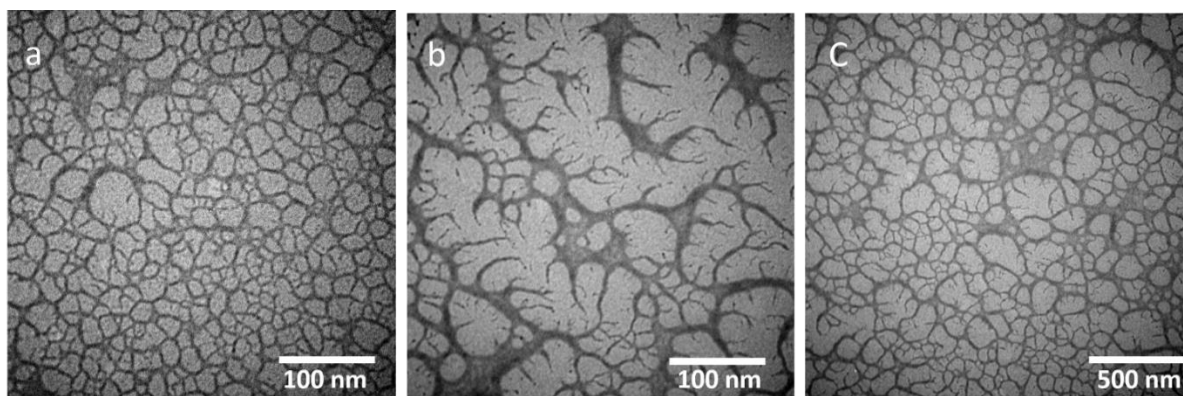


Figure 4.19. TEM images of 1:1 Ag:6-TGR hydrogel, the scale bar and the magnification was 100 nm and 64000x at (a)& (b), and 500 nm and 46000x at (c)

Fig. 4.20 shows the TEM images of Cu xerogels using carbon-copper grids (a & b), further inspection was carried out by preparing the sample with holey carbon (c & d), all the images display networks of highly uniform fibres consist of entangled thin nano fibres.

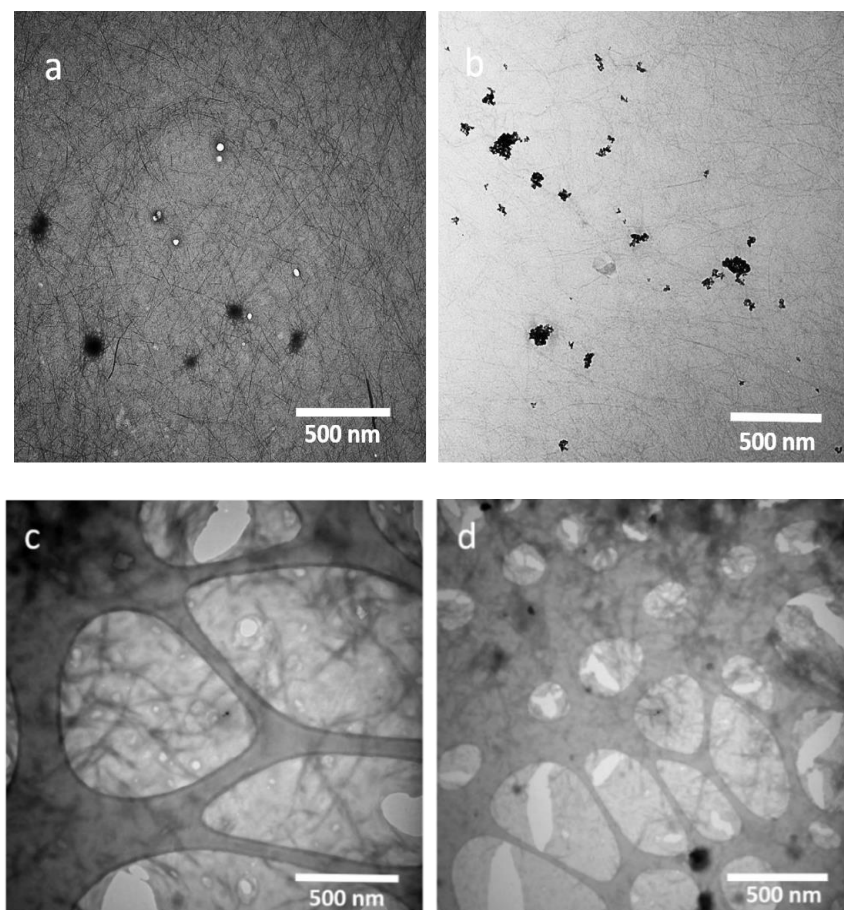


Figure 4.20. TEM of 1:2 Cu:6-TGR hydrogel, the scale bar was 500 nm at (a) and (b), while the magnification was 13500x and 19000x, respectively. Images (c)&(d) were measured by holey copper grids with scale bar 500nm and magnification 34000x &13500x, respectively.

4.4 Conclusion

This study demonstrates synthesis of 3D hydrogels for Cu (I) & Ag (I) with 6-thioguanosine nucleoside based on coordination polymer formation and metal binding via the S6 atom. The data suggested forming 1D polymer of $-\{ -S-M-S-M- \}_n$ for Cu and Ag hydrogels, respectively, entanglement of the polymer chains leads to form 3D hydrogels via hydrogen bonds. The fluorescence measurements showed that Cu hydrogel has a very strong luminescence, which may be due to the strong Cu...Cu interactions and a small HOMO-LUMO gap. The Ag hydrogel showed weak fluorescence and small Stokes shift which may indicates weak Ag...Ag interactions. The AFM data was consistent with TEM data as both techniques show formation of very long fibres (many micrometres).

References

1. Davies, D.R. & Gellert, M. Helix Formation by Guanylic Acid. *Proceedings of the National Academy of Sciences (PNAS) USA*, **48**, 2013-2018 (1962).
2. Dash, J., Patil, A.J., Das, R.N., Dowdall, F.L. & Mann, S. Supramolecular hydrogels derived from silver ion-mediated self-assembly of 5'-guanosine monophosphate. *Soft Matter*, **7**, 8120-8126 (2011).
3. Peters, G.M. Guanosine -Borate Hydrogels- Form and Function. Thesis, University of Maryland, USA. (2015).
4. Das, R.N., Kumar, Y.P., Pagoti, S., Patil, A.J. & Dash, J. Diffusion and birefringence of bioactive dyes in a supramolecular guanosine hydrogel. *Chemistry a European Journal*, **18**, 6008-6014 (2012).
5. Peters, G.M., Brown, S.P., Raghavan, S.R. & Davis, J.T. G4-quartet.M⁺borate hydrogels. *Journal of the American Chemical Society*, **137**, 5819-5827 (2015).
6. Houlton, A., Amo-Ochoa, P., Hribesh, S., Pike, A.R. & Zamora, F. Coordination chemistry of 6-thioguanine derivatives with cobalt: toward formation of electrical conductive one-dimensional coordination polymers. *Inorganic chemistry*, **52**, 5290-5299 (2013).
7. Zamora, F. & Amo-Ochoa, P. Assembling of Dimeric Entities of Cd(II) with 6-Mercaptopurine to Afford One-Dimensional Coordination Polymers: Synthesis and Scanning Probe Microscopy Characterization. *Inorganic Chemistry*, **45**, 7642-7650 (2006).
8. Adhikari, B., Shah, A. & Kraatz, H.-B. Self-assembly of guanosine and deoxyguanosine into hydrogels: monovalent cation guided modulation of gelation, morphology and self-healing properties. *Journal of Materials Chemistry B*, **2**, 4802-4810 (2014).
9. Amo-Ochoa, P., Castillo, O., Guijarro, A., Sanz Miguel, P.J. & Zamora, F. Supramolecular architectures based on 6-purinethione complexes. *Inorganica Chimica Acta*, **417**, 142-147 (2014).
10. Odriozola, I., Loinaz, I., Pomposo, J.A. & Grande, H.J. Gold–glutathione supramolecular hydrogels. *Journal of Materials Chemistry*, **17**, 4843-4845 (2007).
11. Casuso, P., Carrasco, P., Loinaz, I., Grande, H.J. & Odriozola, I. Converting drugs into gelators: supramolecular hydrogels from N-acetyl-L-cysteine and coinage-metal salts. *Organic & Biomolecular Chemistry*, **8**, 5455-5458 (2010).

12. Casuso, P., Carrasco, P., Grande, H.J. & Odriozola, I. Argentophilic hydrogels: elucidating the structure of neutral versus acidic systems. *Soft Matter*, **7**, 3627-3633 (2011).
13. Odriozola, I., Ormategui, N., Loinaz, I., Pomposo, J.A. & Grande, H.J. Coinage Metal–Glutathione Thiolates as a New Class of Supramolecular Hydrogelators. *Macromolecular Symposia*, **266**, 96-100 (2008).
14. Odriozola, I., Casuso, P., Loinaz, I., Cabanero, G. & Grande, H.J. Designing neutral metallophilic hydrogels from di- and tripeptides. *Organic & Biomolecular Chemistry*, **9**, 5059-5061 (2011).
15. Orioli, P.L. & Cini, R. A Proton Magnetic Resonance Investigation on 1: 1 Cytidine and Guanosine Silver (I) Complexes. *Biolnorganic Chemistry*, **7**, 345-349 (1977).
16. Zhang, Y., Zhu, X., Smith, J., Haygood, M.T. & Gao, R. Direct observation and quantitative characterization of singlet oxygen in aqueous solution upon UVA excitation of 6-thioguanines. *The Journal of Physical Chemistry B*, **115**, 1889-1894 (2011).
17. Hribesh, S. 2'-Deoxy-6-Thioguanosine: Synthesis of Monomer, Oligomers and Long DNA, and their Binding with Metal Ions. Thesis, Newcastle University, UK. (2013).
18. Repges, R., Beuck, C., Weinhold, E., Raabe, G. & Fleischhauer, J. 6-Thioguanine in DNA as CD-spectroscopic probe to study local structural changes upon protein binding. *Chirality*, **20**, 978-984 (2008).
19. Henary, M. & Zink, J.I. Structure and Assignment of the Luminescence of a New Mixed-Ligand Copper(I) Polymer. *Inorganic Chemistry*, **36**, 796-801 (1997).
20. White-Morris, R.L. & Balch, A. New Insights into the Effects of Self-Association of the Cation $[\text{Au}\{\text{C}(\text{NHMe})_2\}_2]^+$ on Its Solid State Structure and Luminescence. *Inorganic Chemistry*, **41**, 2313-2315 (2002).
21. Kishimura, A. & Aida, T. Phosphorescent Organogels via "Metallophilic" Interactions for Reversible RGB-Color Switching. *Journal of the American Chemical Society*, **127**, 179-183 (2005).
22. Rasika Dias, H.V. & Omary, M.A. Bright Phosphorescence of a Trinuclear Copper(I) Complex: Luminescence Thermochromism, Solvatochromism, and "Concentration Luminochromism". *Journal of the American Chemical Society*, **125**, 12072-12073 (2003).

23. Vitale, M. & Ford, P.C. Ab Initio Studies of the Copper(I) Tetramers $\text{Cu}_4\text{X}_4\text{L}_4$ (X = I, Br, Cl). Effects of Cluster Structure and of Halide on Photophysical Properties. *Inorganic Chemistry*, **33**, 561-566 (1994).
24. Hollingsworth, G. & Zink, J.I. Optical Memory in Cu^+ -Doped β'' -Alumina. *Journal of the American Chemical Society*, **110**, 6569-6570 (1988).
25. Zhou, P. & Li, H. Chirality delivery from a chiral copper(II) nucleotide complex molecule to its supramolecular architecture. *Dalton Transactions*, **40**, 4834-4837 (2011).
26. Agris, P.F. & Lam, A.T. Modified nucleoside-dependent transition metal binding to DNA analogs of the tRNA anticodon stem/loop domain. *BioMetals*, **8**, 290-296 (1995).
27. Holy, A. & Luck, G. CD studies on the conformation of oligonucleotides complexed with divalent metal ions: interaction of Zn^{+2} with guanine favours syn conformation. *Nucleic Acids Research*, **10**, 2757-2770 (1976).
28. Chantot, J.-F. & Guschlbauer, W. North-Holland Publishing Company - Amsterdam. *Febs Letters*, **4**, 173-176 (1969).
29. Wang, J.-J. & Wang, Y.-Q. Synthesis of Monodispersed Wurtzite Structure CuInSe_2 Nanocrystals and Their Application in High-Performance Organic-Inorganic Hybrid Photodetectors. *Journal of the American Chemical Society*, **132**, 12218-12221 (2010).
30. Hsu, W.-H., Hsiang, H.-I. & Yu, S. Crystallite formation mechanism of $\text{CuIn}(\text{Se},\text{S})_2$ synthesized using solvothermal method. *Ceramics International*, **41**, 3208-3213 (2015).
31. Llanos, J. & Ramirez, R. Electron transfer and electronic structure of KCuFeS_2 . *Journal of Alloys and Compounds*, **234**, 40-42 (1996).
32. Platzman, I. & Tannenbaum, R. Oxidation of Polycrystalline Copper Thin Films at Ambient Conditions. *The Journal of Physical Chemistry C*, **112**, 1101-1108 (2008).
33. Wang, L., Wei, G., Yang, X. & Li, Z. Electrostatic assembly of Cu_2O nanoparticles on DNA templates. *Applied Surface Science*, **252**, 2711-2716 (2006).
34. Battistoni, C. & Paparazzo, E. An XPS and Auger Study of some Polynuclear Copper Compounds. *Inorganica Chimica Acta*, **102**, 1-3 (1985).
35. Watson, S.M., Wright, N.G., Horrocks, B.R. & Houlton, A. Preparation, Characterization and Scanned Conductance Microscopy Studies of DNA-Templated One-Dimensional Copper Nanostructures. *Langmuir*, **26**, 2068-2075 (2010).

36. Pate, J., Zamora, F., Horrocks, B.R. & Houlton, A. Solution-based DNA-templating of sub-10 nm conductive copper nanowires. *Journal of Materials Chemistry C*, **2**, 9265-9273 (2014).
37. Trnkova, L. & Navratil, R. Comparative Voltammetric Analysis of Adenine and Xanthine on a Pencil Graphite Electrode in the Presence of Copper Ions. *International Journal of Electrochemical Science*, **8**, 4397-4408 (2013).
38. Ernando, Q. & Cheney, G.E. Metal Complexes of Purine and Some of its Derivatives. [Contribution from the Department of Chemistry, University of Pittsburgh] **81**, 2611-2615 (1959).
39. Nagapradeep, N., Venkatesh, V., Tripathi, S.K. & Verma, S. Guanine-copper coordination polymers: crystal analysis and application as thin film precursors. *Dalton Transactions*, **43**, 1744-1752 (2014).
40. Okamoto, H. & Kanehama, R. Novel ET-Coordinated Copper(I) Complexes: Syntheses, Structures, and Physical Properties (ET=BEDT-TTF=Bis(ethylenedithio)tetrathiafulvalene). *Inorganic Chemistry*, **42**, 7173-7181 (2003).
41. Kwon, S.-Y., Cho, J.-H., Lee, H.-I., Lee, U. & Noh, D.-Y. Cu(I) coordination complex with TTF-based radical cation ligand. *Inorganic Chemistry Communications*, **8**, 510-512 (2005).
42. Kitamura, N. & Araki, H. Synthesis, Structure, and Emissive Properties of Copper(I) Complexes $[\text{Cu}^{\text{I}}(\mu\text{-X})_2(\mu\text{-1,8-naphthyridine})(\text{PPh}_3)_2](\text{X}=\text{I}, \text{Br})$ with a Butterfly-Shaped Dinuclear Core Having a Short Cu–Cu Distance. *Inorganic Chemistry*, **46**, 10032-10034 (2007).
43. Johnson, K. & Steed, J.W. Effects of non-molecular forces on molecular structure in tris(thiourea)-copper(I). *Journal of the Chemical Society, Dalton Transactions*, 2601-2602 (1998).
44. Liu, J.F., Pan, F.X., Pan, Q.J. & Sun, Z.M. Ligand-controlled syntheses of copper(I) complexes with metal-metal interactions: crystal structure and relativistic density functional theory investigation. *Inorganic Chemistry*, **53**, 11068-11074 (2014).
45. Saxena, A., Dugan, E.C., Liaw, J., Dembo, M.D. & Pike, R.D. Copper(I) complexes of heterocyclic thiourea ligands. *Polyhedron*, **28**, 4017-4031 (2009).
46. Sletten, E. & Apeland, A. Crystallographic Studies on Metal-Nucleotide Base Complexes. VI. Dichloro-(6-thio-9-methylpurine)copper(II) Monohydrate. *Acta Crystallographica*, **B31**, 2019-2022 (1975).

47. Tu, T.A. & Reinoso, J. The Interaction of Silver Ion with Guanosine, Guanosine Monophosphate, and Related Compounds. Determination of Possible Sites of Complexing. *Biochemistry*, **5**, 3375-3383 (1966).
48. Goncharova, I. Ag(I)-mediated homo and hetero pairs of guanosine and cytidine: monitoring by circular dichroism spectroscopy. *Spectrochimica Acta Part A: Molecular and Biomolecular Spectroscopy*, **118**, 221-227 (2014).
49. Loo, K. & Petty, J.T. Ag⁺-Mediated Assembly of 5'-Guanosine Monophosphate. *The Journal of Physical Chemistry B*, **114**, 4320-4326 (2010).
50. Arulraj, A.D., Devasenathipathy, R., Chen, S.-M., Vasantha, V.S. & Wang, S.-F. Highly selective and sensitive fluorescent chemosensor for femtomolar detection of silver ion in aqueous medium. *Sensing and Bio-Sensing Research*, **6**, 19-24 (2015).
51. Ray, L. & Ghosh, P. Shorter Argentophilic Interaction than Auophilic Interaction in a Pair of Dimeric {(NHC)MCl}₂ (M = Ag, Au) Complexes Supported over a N/O-Functionalized N-Heterocyclic Carbene (NHC) Ligand. *Inorganic Chemistry*, **47**, 230-240 (2008).
52. Xie, L.-X., Wei, M.-L., Duan, C.-Y., Sun, Q.-Z. & Meng, Q.-J. Structures, fluorescent properties of the Ag(I) compounds based on molecular clips with biphenyl core. *Inorganica Chimica Acta*, **360**, 2541-2548 (2007).
53. Wang, R.-H., Cao, R., Zhao, Y.-J. & Weng, J.-B. Two silver(I)-thiolate polymers with zigzag chain and lamellar structures. *Polyhedron*, **20**, 3165-3170 (2001).
54. Bell, R.A. & Hu, M. Silver Complexes of Environmental and Related Thiols: Structural Studies. McMaster University, Hamilton , Ontario, Canada. 13-18 (1997).

Chapter 5. Complexation of Coinage Metal Ions with 2'-deoxy-6-Thioguanosine (d TGR)

Abstract

Coordination polymers of 2'-deoxy-6-thiopurine riboside with coinage metal ions were prepared as 3D networks. The polymers entangle via hydrogen bonding to form 3D networks and hydrogels. 2'-Deoxy-6-guanosine (Gs) was used to synthesize the corresponding 6-thio purine derivative, 2'-deoxy-6-thioguanosine (d TGR). Upon coordination the metal ions of Au, Cu, and Ag with d TGR stable hydrogels were formed.

5.1 Introduction

Metal thio purine complexes have been of recent research interest partly because of the potential applications of these compounds in the pharmaceutical field^{1,2} but also some gels have been reported. A 2-deoxyadenosine derivative with alky chain and urea linker was prepared as a gel under ultrasonic treatment. The formation of the gel occurred by the balance of hydrophilic-hydrophobic interactions³. Deoxy guanosine gels with monovalent cations (Na^+ , K^+ , Ag^+ , Au^+ , Hg^+ , and Tl^+) have prepared by Adhikair.⁴ For 5'-azido-2'- deoxy thymidine lipids the gelation occurred by hydrogen bonding, π - π stacking, and hydrophobic interactions.⁵ Zhao⁶ demonstrated a very clear example to present the influence of a lack of hydroxyl group(2'OH) from the sugar structure, he found that the 2'OH group has the main role at the orientation of the supramolecular structure by forming flower-shaped structures with pyrimido[4,5-*d*]pyrimidine nucleoside. Coinage metals or group 11, which include Au, Ag, and Cu, displayed highly affinity towards thio purine by forming hydrogels with 6-thioguanosine as mentioned in chapter three.

5.2 2'-Deoxy-6-thioguanosine nucleoside metal ions complexation

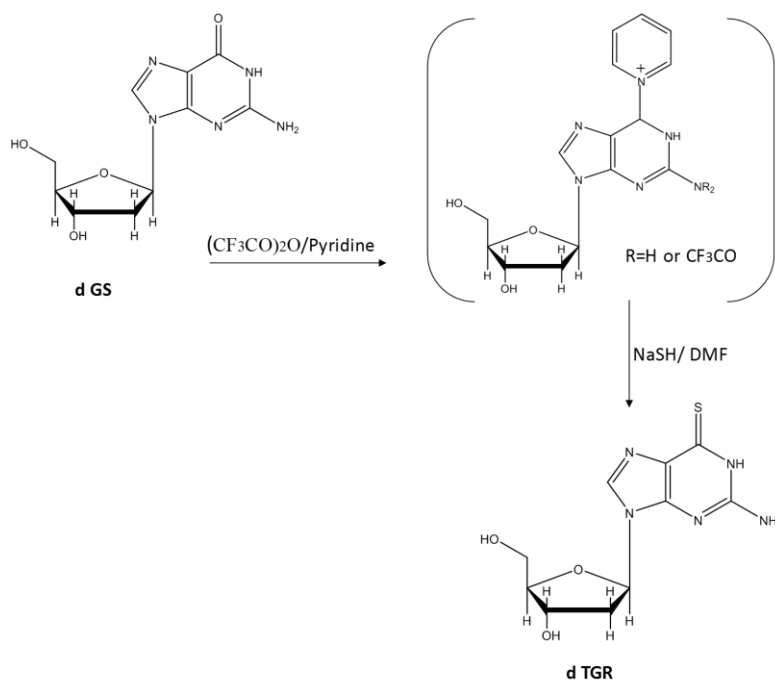
To prepare coinage metals ions:2'-deoxy nucleoside gels, 2'-deoxy-6-thioguanosine (d TGR) was synthesised by thiolation of 2'-deoxy-6-guanosine and characterized using NMR, Mass spectroscopy, FTIR, and UV-Vis spectroscopy. The commercial d TGR is very expensive (£ 2860.00 for 250 mg, Sigma), and for this reason it was synthesised.

5.2.1 Synthesis of 2'-deoxy-6-thioguanosine (d TGR)

The method of A. Jones⁷ (1991) was used to prepare 2'-deoxy-6-thioguanosine (d TGR). The reaction was carried out in a Schlenk flask under nitrogen by adding 30 ml of cooled pyridine anhydrous to 2'-deoxy-6-guanosine (0.4 gm, 150 mmol) in ice bath, then 1.8 ml (12.6 mmol) of trifluoroacetic anhydride was added drop wise and left stirring for 40 min. Then a suspension of NaSH (2.6 gm, 23 mmol) in 45.2 ml of anhydrous DMF was added and stirred for 24 h. After that, 76 ml of ammonium bicarbonate was added with vigorous stirring, then the mixture was concentrated and the residue was dissolved in methanol and filtered. After concentrated the filtrate to dryness, 0.1 M of TEAA buffer (triethylammonium acetate) was added and the product was recrystallized with H₂O: MeOH to give a yellow powder (60%).

5.2.2 Mechanism of the reaction

The mechanism of Jones⁷ reaction involves the formation of a pyridinium intermediate as a result of adding trifluoroacetic anhydride to d Gs in dry pyridine. After that, adding sodium sulfide in anhydrous dimethylformamide to the pyridinium intermediate gives d TGR with yield 40%, as shown in Scheme (5.1).



Scheme 5.1. Jones⁷ route for synthesis of 2'-deoxy-6-thioguanosine (d TGR).

5.3 2'-Deoxy-6-thioguanosine (d TGR) characterization

To characterize 2'-deoxy-6-thioguanosine (d TGR), ESI-MS on a Waters LCT -Premier mass spectrometer, NMR spectra on a 300 and 500 MHz Delta Jeol, UV-Vis-spectroscopy, and Fourier transform infrared (FTIR) were used.

5.3.1 Mass spectroscopy characterization

Mass spectroscopy (ESI-MS) was carried out in methanol with concentration 100 $\mu\text{g/ml}$ with Waters LCT-Premier mass spectrometer. The major peak at ES-Mass spectra, Fig. 5.1, (positive mode) for 2'-deoxy-6-guanosine (d Gs) was found at 290.0850 m/z corresponding to the formula $\text{C}_{10}\text{H}_{13}\text{N}_5\text{O}_4\text{Na}$ (calculated 290.086), while the positive mode peak in Fig. 5.2 corresponding to deoxy 6-thioguanosine with formula $\text{C}_{10}\text{H}_{13}\text{N}_5\text{O}_3\text{SNa}$ displayed at 306.067 m/z (the calculated 306.0639). Based on these data the synthesis of d TGR was successfully achieved.

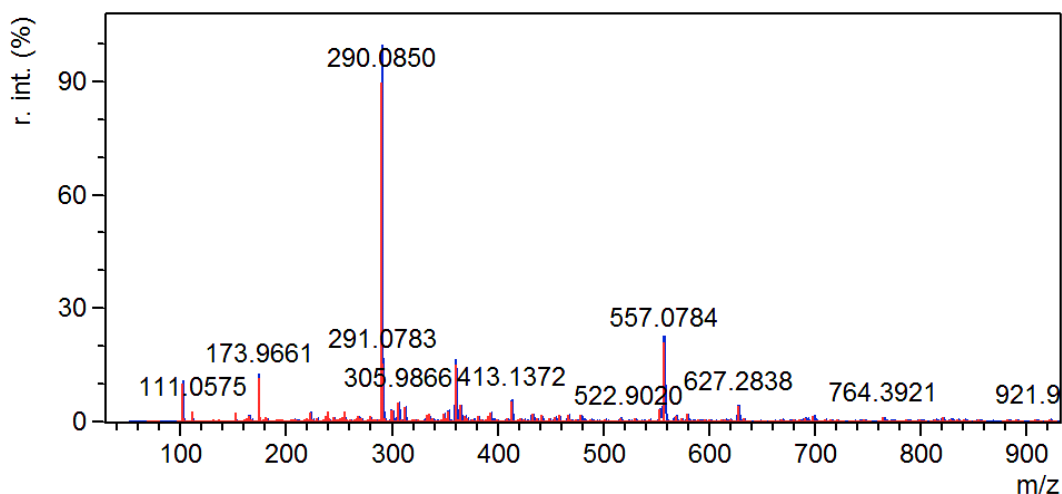


Figure 5.1. Mass spectrum (ESI-MS) of 2'-deoxy-6-guanosine (d Gs). The solvent was methanol and the concentration was 100 $\mu\text{g/ml}$.

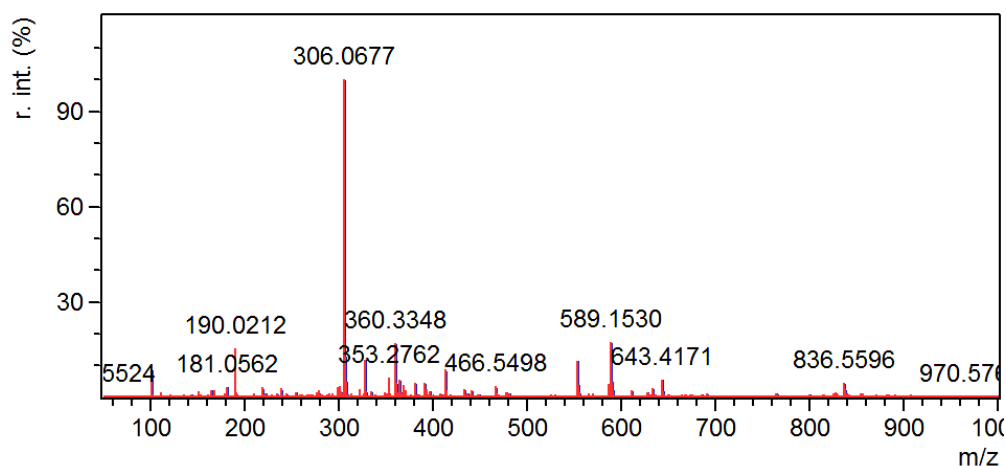


Figure 5.2. Mass spectrum (ESI-MS) of 2'-deoxy-6-thioguanosine (d TGR). The solvent was methanol and the concentration was 100 $\mu\text{g/ml}$.

5.3.2 NMR studies

The ^1H NMR (300 MHz, $\text{DMSO-}d_6$, 25°C) spectrum in Fig. 5.3 confirmed the data of FTIR and UV-Vis which showed successful formation of 2'-deoxy-6-thioguanosine. Comparison of the ^1H -NMR data of synthesized d TGR with corresponding d Gs, Table 5.1, showed that N1-H was observed at 11.94 ppm while at d Gs it was found at 10.63 ppm, this data was consistent with that reported by Jones.⁷ Small chemical changes have been seen at the protons of NH_2 and C8-H at d TGR compared to d Gs as a result of the distance from S6.

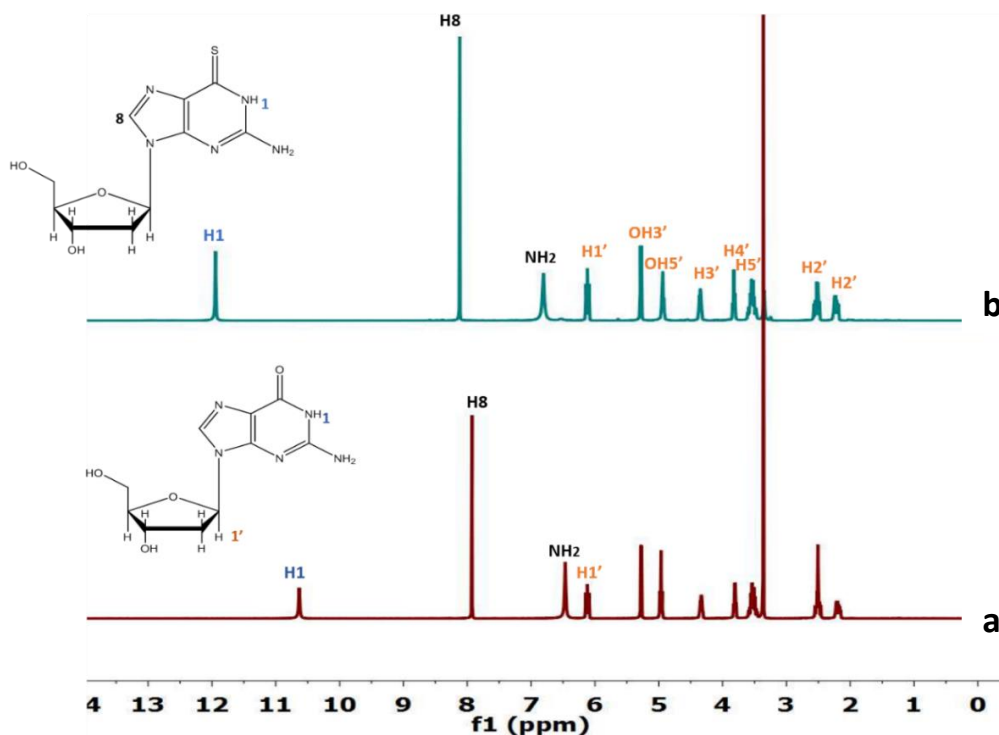


Figure 5.3. Comparison between ^1H -NMR for a) d Gs and b) d TGR in $\text{DMSO-}d_6$.

Table 5.1. Comparison of H signals in ^1H - NMR spectra of d Gs and d TGR.

Number of H atom	^1H in d Gs δ/ppm	^1H in d TGR δ/ppm
H1	10.63	11.94
H8	7.95	8.12
NH2	6.46	6.81
H1'	6.14	6.14
H2'	2.55, 2.23	2.55, 2.23
H3'	4.35	4.35
H4'	3.83	3.83
H5'	3.55, 3.56	3.55, 3.56
OH3'	5.28	5.28
OH5'	4.98	4.98

The ^{13}C -NMR spectrum of d TGR displayed that a signal for C6 at 175.94 ppm, while the signal of the corresponding atom of d Gs before modification was found at 157.19 ppm. Fig. 5.4. The data was comparable with Jones⁷ and that indicates successful synthesis of d TGR. The peak of C'2 was found at 40.02 and 40 ppm at d Gs and d TGR, respectively. Table 5.2. shows comparison C signal in ^{13}C NMR spectra between d Gs and d TGR.

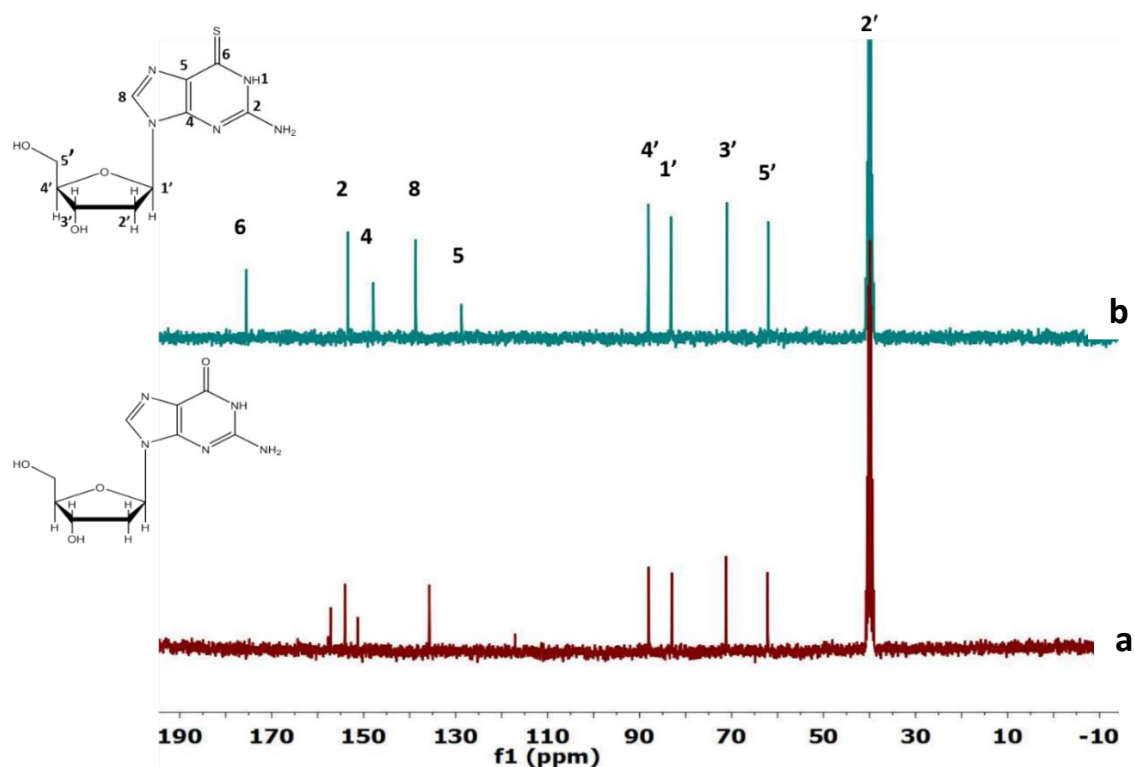


Figure 5.4 ^{13}C -NMR spectra comparison between a) d Gs and b) d TGR in DMSO- d_6 .

Table 5.2. Comparison of C atom signals in ^{13}C - NMR spectra of d Gs and d TGR.

Number of C atom	^{13}C -NMR of d Gs δ/ppm	^{13}C -NMR of d TGR δ/ppm
1'	83	83.16
2'	40.02	40
3'	71.19	71.05
4'	88.01	88.13
5'	62.16	62.02
2	154.09	153.47
4	151.33	147.91
5	117.10	128.79
6	157.19	175.49
8	135.72	138.69

5.3.3 UV-Vis absorption characterization

A comparison of UV-Vis spectra of basic solutions of d Gs and d TGR (Fig. 5.5) displayed a peak at 273 nm assigned to a π - π^* transition of the C=O moiety. This peak was red shifted to 320 nm in the spectrum of d TGR and indicates successful substitution of the O atom of the carbonyl group by S. Formation of the new peak in the spectrum of a basic solution of d TGR at 320 nm which is assigned to the π - π^* , indicates that the d TGR was in thiol (-SH) form.⁸ This peak that appears for the solution of d TGR is comparable with that found to the basic solution of 6-TGR.

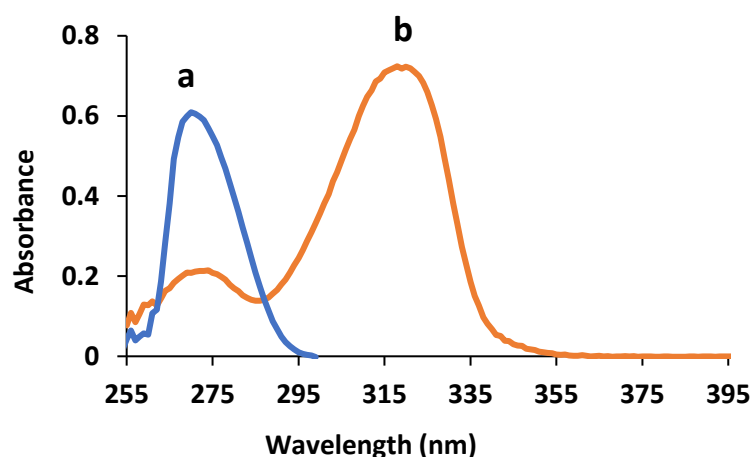


Figure 5.5. Comparison absorption spectrum between: a) 50 μM of 2'-deoxy-6-guanosine (d Gs) (blue line) and b) 50 μM of 2'-deoxy-6-thioguanosine (d TGR) (orange line) in basic aqueous solution (pH=9).

5.3.4 Fourier transform infrared (FTIR) Characterization

The C=O stretching mode⁹⁻¹¹ was a good band to distinguish between d Gs and d TGR, as this band was seen at 1681 cm^{-1} in the FTIR spectrum of d Gs and absent in the spectrum of d TGR (Fig. 5.6). In addition, the band at 1200 cm^{-1} which assigned to the stretching mode¹² C=S was apparent in the spectrum of d TGR, while the band at 2600 cm^{-1} that belongs to the stretching mode¹²⁻¹⁴ S-H was absent in the spectrum of d TRG, these data clearly support forming d TGR and indicates that it was in thione form. The above observation data of mass, NMR, UV-Vis, and FTIR show that the conversion of d Gs to d TGR was performed successfully.

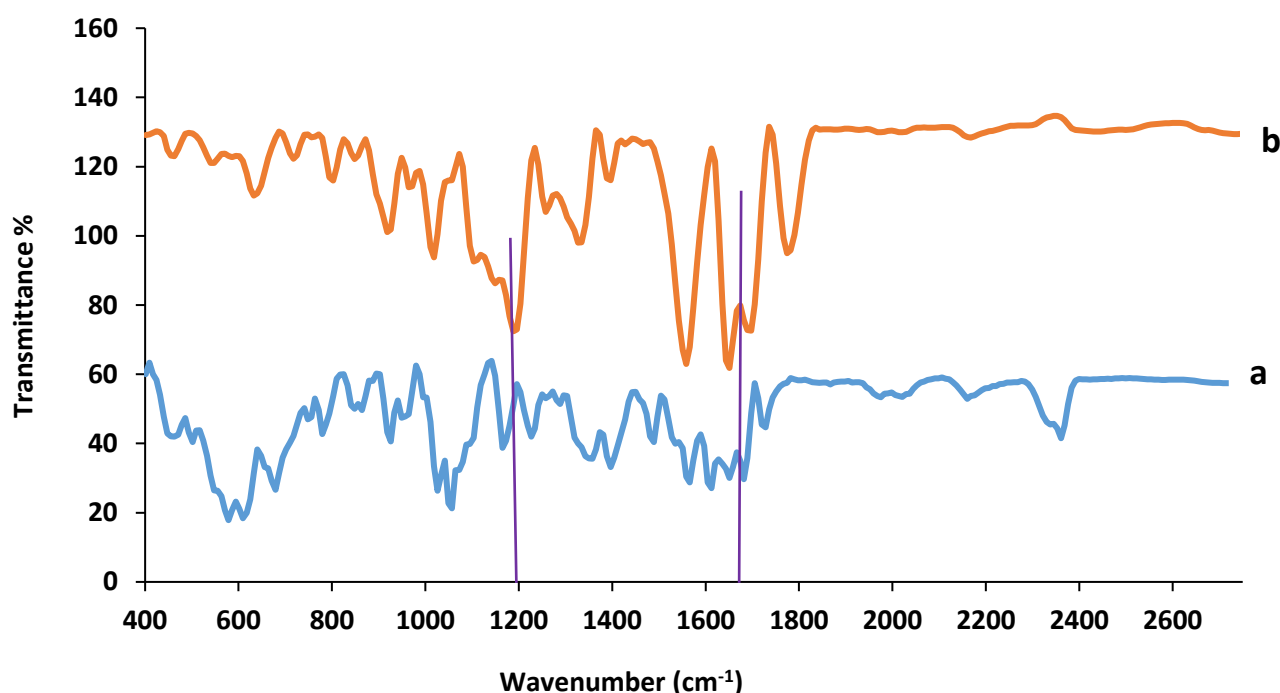


Figure. 5.6. Comparison FTIR spectra between: a) 2'-deoxy-6-guanosine (d Gs) (blue line) and b) 2'-deoxy-6-thioguanosine (d TGR) (orange line).

5.4 Synthesis of Au, Ag, and Cu:d TGR hydrogels

The same procedure that used to prepare hydrogels of Au, Ag, and Cu:6-TGR was used to prepare the gels of Au, Ag, and Cu:d TGR and the colour of the obtained hydrogels were yellow, transparent yellow, and orange, respectively, Fig. 5.7.

5.5 Results & Dissociation

The stability of 6-thioguanosine (6-TGR) gels with time is higher than that in 2'-deoxy-6-thioguanosine (d TGR) gel which suggests an important role for hydrogen bonding involving the 2'OH groups. The stability of metal:d TGR gels is reduce with time with the order Au:d

TGR < Cu:d TGR < Ag:d TGR. It was found¹⁵ that no significant affect for the absence of 2'OH group at the monohydrate structure of 2'-deoxy-6-guanosine (d Gs) compared to the corresponding 6-guanosine(Gs) , however, at dihydrated cluster d Gs reveals less stability. The driving forces in the gelation process involve hydrogen bonding, π - π interactions, van der Waal¹⁶, and dipole-dipole interactions, however it seems that hydrogen bonding¹⁷ plays the key role in the forming of hydrogel.¹⁸ Hydrogen bonding and perpendicular π - π stacking are responsible of the high arrangement at nucleic acid structure, in addition that makes nucleosides as a good template for making hydrogels.¹⁹

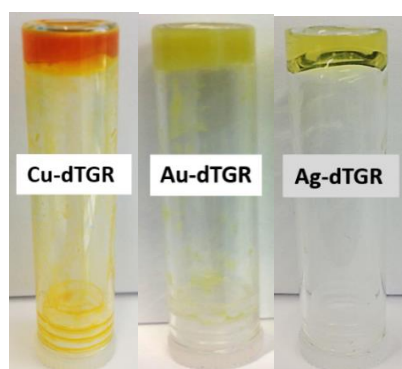


Figure 5.7 Photographs of Au, Ag, and Cu:d TGR hydrogels.

5.5.1 Atomic force microscopy (AFM) characterization

The morphology of the 2'-deoxy-6-thioguanosine (d TGR) hydrogels that were prepared with metal ions of group 11 (Au, Cu, Ag) were investigated to study the effect of the absence of the 2'OH group from the sugar structure on the morphology of the gels. AFM tapping mode was used to carry out this study on the xerogels. The morphology of the polymer that forming upon coordination Au(I) with 2'-deoxy-6-thioguanosine is apparent in the height AFM images in Fig. 5.8. Image (a) shows individual fibres with close imaging (scale bar 250 nm), the fibre was found to be long, uniform, and has breakages in the structure make it seems to be a granular linear fibre with height ~10 nm as shown in image (b) which is associated with the cross section of the horizontal white line along image (a). Image (d) displays the linearity at the morphology of the fibres clearly. 2'-Deoxy-6-thioguanosine exhibits ability to form 3D networks, as shown by image (c), in spite of the absence of the 2'OH group. A statistical analysis was carried out to evaluate the size distribution of the fibres in the gel, the data which is presenting in the histogram (e) shows structures up to 11 nm in height recorded, in addition some higher height structures up to 23 nm but with low frequency is observed, and a number of smaller height structure in range 5-8 nm also can be seen with less frequency. Comparison the AFM images

in Fig. 5.8 for Au:d TGR with those for the Au:6-TGR gel (chapter 3) showed drastically different in the height and the diameter of the fibres; as the height was ~ 10 nm and the diameter was 11 nm in the former, while the latter displayed 3 nm for both. This indicates the effect of a lack of 2'OH group on the morphology of the gel.

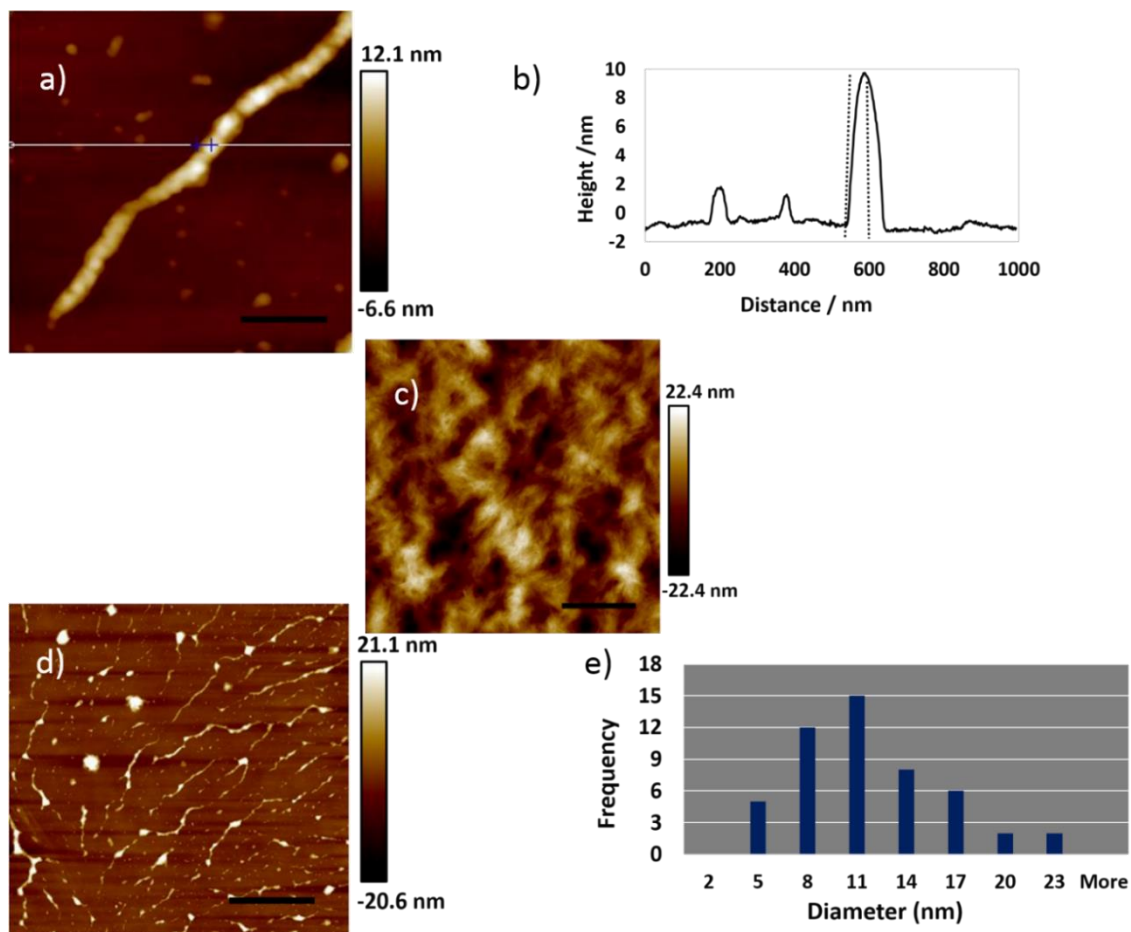


Figure 5.8. Tapping Mode AFM images of (a) height image of a section of a single fibre of Au:d TGR, the scale bar 250 nm and the height (grayscale) 12.1 nm. (c) & (d) are height images of the Au:d TGR gel show the entangle and single fibres, the scale bar was 500 nm and 2 μ m and the height (grayscale) was 22.4 nm and 21.1 nm at (c) & (d), respectively. (b) Cross section of the white line at (a) shows the height of the fibres ~ 10 nm. (e) Height distribution of Au:d TGR fibres. The difference between images (c) & (d) is assigned to the area of imaging, as image (c) was imaged from a thick area to show the network while image (d) was imaged from a thin area to display single fibres.

The AFM image (a) in Fig. 5.9 for the Ag:d TGR hydrogel shows that the fibre is very smooth with height ~ 1.4 nm, as shown in the profile (b). There is evidence of entwining of some fibres with each other in the cross section from left to right along image (c) which obviously shows the height structure of ~ 7.5 nm, (d) is the profile of the cross section along image (c). The height of the fibres for this gel is different from that for Ag(I):6-TGR that obtained with concentration 1:1 of metal to ligand stoichiometry (chapter 4). The Ag(I):6-TGR was needle-

like fibres with 3 nm height and diameter. While the Ag:d TGR gel is more thinner and has lower height and diameter (1.5 nm). In addition, this gel showed entwining their fibres with each other to produce fibres with height 7 nm as shown in Fig. 5.9.

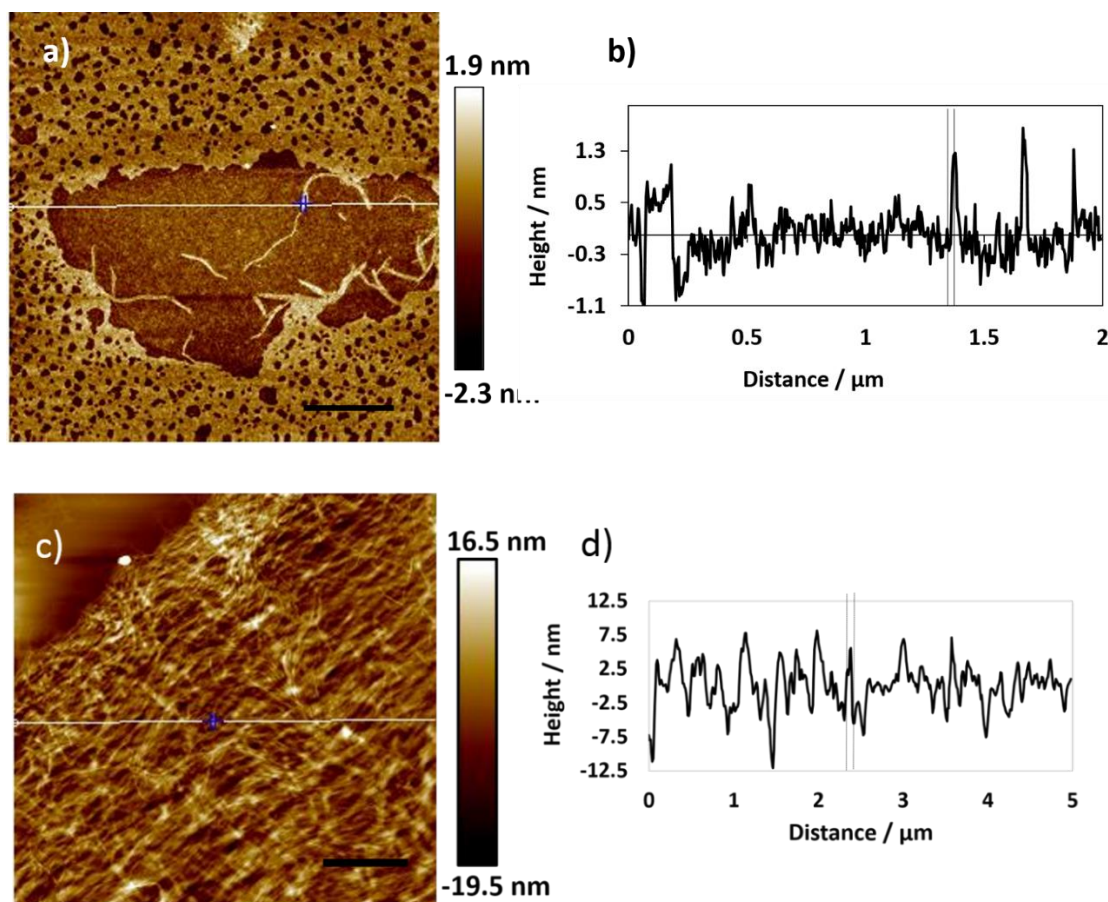


Figure 5.9. (a) Height image of Ag:d TGR gel drop cast onto a silicon wafer and air drying, the scale bar and the height (grayscale) in (a) was 400 nm and 1.9, the image were taken by Tapping Mode AFM image. (b) is the profile of the cross section along image (a) show the height is ~ 1.4 nm. The cross section from left to right shows the regions highlighted in (c), scale bar 1 μm , height (grayscale) 16.5 nm. (d) Showing the profile of the corresponding cross section of (c).

AFM images of Cu:d TGR hydrogel is shown in Fig. 5.10, it is clear that the fibre is linear and no branching was seen at the images, the result of the statistical analysis displays that the diameter of the fibre was 7 nm as shown at the histogram (b), some higher height in range of 9-13 nm can be seen and some lower height between 5-3 nm also was found at the histogram, but both the higher and the lower height were with less frequency. The profile (d) of the individual fibre along the cross section in image (c) shows a height of ~ 7 nm. Comparison the AFM images for this gel with that for Cu:6-TGR (chapter 4) revealed that the fibres for Cu-gel with a lack of hydroxyl group is thinner and has less height (7 nm) as shown in Fig. 5.10, while Cu:6-TGR has fibres with height ~ 28 nm.

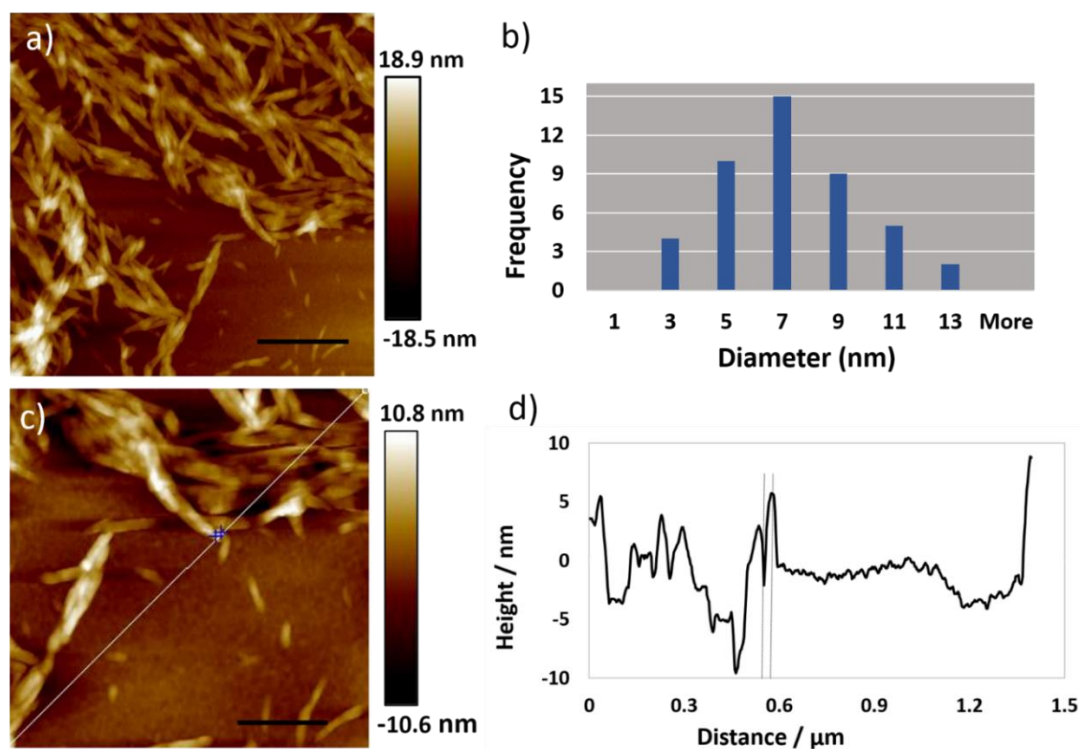


Figure 5.10. Tapping mode AFM image of 1:2 Cu- deoxy 6-thioguanosine gel drop cast onto a silicon wafer and drying by air. (a) Height images with scale bar 500 nm and the height (grayscale) is 18.9 nm, (c) a small area of (a) with scale bar 250 nm and 10.8 nm height (grayscale). (b) The histogram of the size (diameter) distribution of the fibres, (d) the associated cross section along the white line in (c) shows the height of the fibres at ~ 7 nm.

In conclusion, the influence of a lack of 2'OH group on the polymer morphology was very clear with Au:d TGR among other hydrogels of Cu and Ag.

5.5.2 Transmission electron microscope (TEM) characterization

The morphology of the metal ions deoxy hydrogels was inspected by TEM. Samples were prepared by drop casting 2 μL of the hydrogel onto a TEM grid, followed by drying prior to inspect. A typical TEM images of Ag:d TGR casted onto a carbon coated copper grids was indicated in Fig. 5.11, the TEM images revealed very long, linear, and uniform fibre and the fibre was stretching along the substrate. This fibrous morphology is a good evidence to support the data of AFM images.

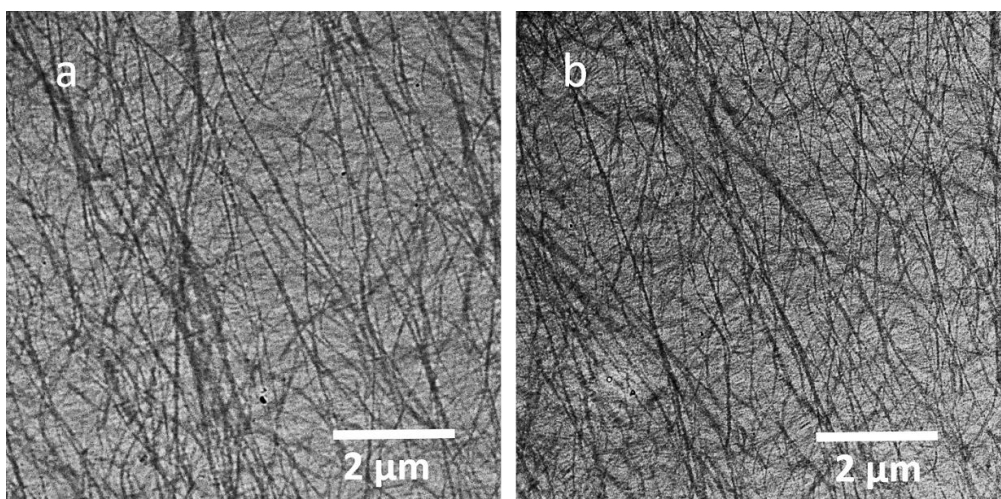


Figure 5.11. TEM of Ag:d TGR gel. The scale bar was 2 μm , and the magnification was 10500x and 7900x at (a) and (b), respectively.

The TEM images of Au:d TGR in Fig. 5.12 display long highly continuous fibres and it is clearly apparent that the fibres were avoiding the holes of the carbon substrate as there was no bridge across the holes in the substrate.

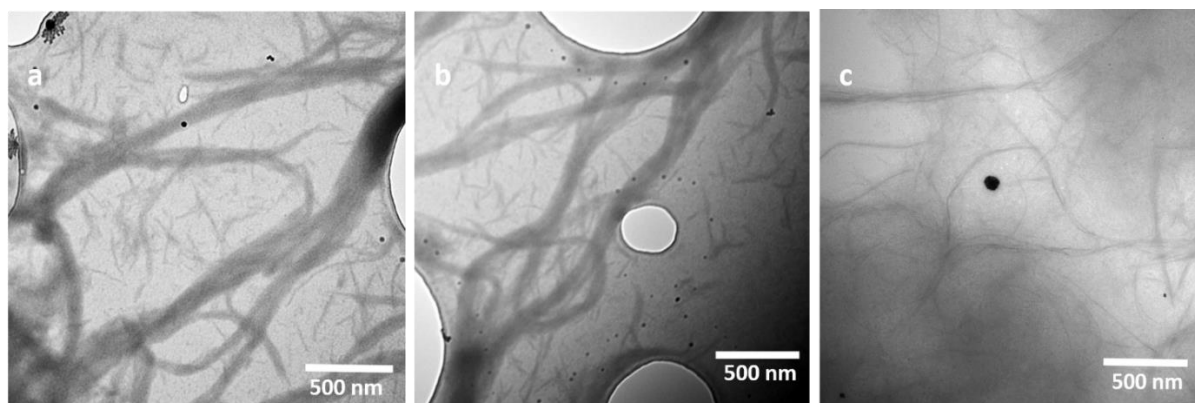


Figure 5.12. TEM of Au:d TGR gel. The scale bar and the magnification were 500 nm and 46000x at (a) and (b), 500 nm and 34000x at (c), respectively.

The morphology of TEM of Cu:d TGR in Fig. 5.13 revealed thick linear continuous fibres. These appear to consist of two or more fibres entwined with each other, as shown in image (a), the red arrow refers to roughly three fibres. The morphology of these images is a good agreement to that obtained by AFM where the fibre was found long and thick.

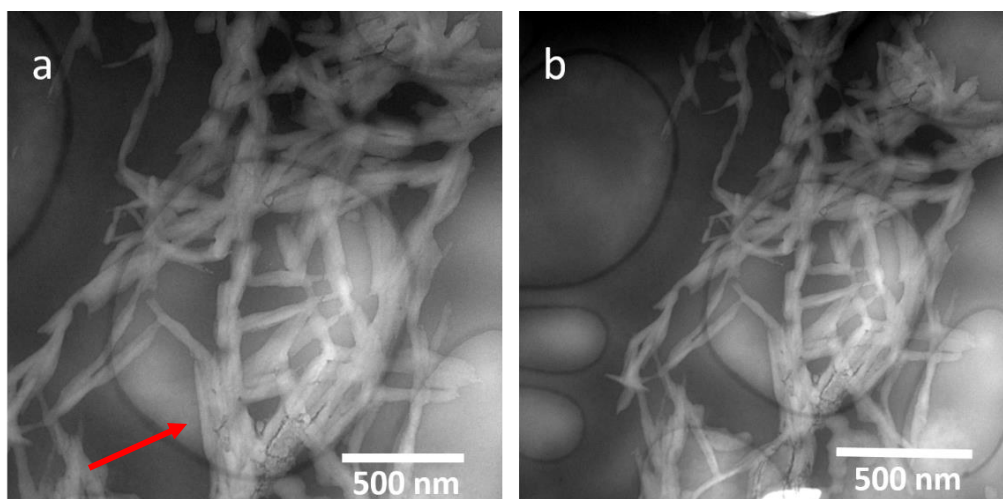


Figure 5.13. TEM of Cu -d TGR gel. The scale bar was 500 nm at (a) and (b), and the magnification was 46000x and 34000x, respectively.

5.6 Conclusion

2'-Deoxy-6-thioguanosine (d TGR) was successfully synthesis from 2'-deoxy-6-guanosine via thiolation reaction and characterised by NMR, Mass spectroscopy, FTIR, and UV-Vis. The characterisation's data of the pale powder product showed a good agreement with the compound that prepared by Jones⁷. The reaction of d TGR with group 11 (Au, Ag, Cu) in aqueous solutions revealed formation 3D hydrogels. A combination of AFM and TEM techniques that used to inspect the morphology of the gels displayed long, linear, uniform fibres. The AFM images for Ag:d TGR and Cu:d TGR showed the formation of fibres with less height compare to that for Ag:6-TGR and Cu:6-TGR (chapter 4). However, some changes have been seen with Au:d TGR fibre as the height increased (11 nm) compare to the fibres' height for Au:6-TGR (3 nm), these observations indicate that the coordination of d TGR with group 11 was not affected by the lack of hydrogen bonding which assigned to absence 2'OH group from the structure of sugar group.

References

1. Ansari, A., Patel, N., Duley, J.A. & Florin, T.H. Low-dose azathioprine or mercaptopurine in combination with allopurinol can bypass many adverse drug reactions in patients with inflammatory bowel disease. *Alimentary Pharmacology & Therapeutics*, **31**, 640-647 (2010).

2. Yamanari, K. & Kaizaki, S. Synthesis and stereochemistry of cobalt(III) complexes containing purine-6- thione and related ligands. *Journal of the Chemical Society, Dalton Transactions*, , 305-309 (1996).
3. Park, S.M. & Kim, B.H. Ultrasound-triggered water gelation with a modified nucleoside. *Soft Matter*, **4**, 1995–1997 (2008).
4. Adhikari, B., Shah, A. & Kraatz, H.-B. Self-assembly of guanosine and deoxyguanosine into hydrogels: monovalent cation guided modulation of gelation, morphology and self-healing properties. *Journal of Materials Chemistry B*, **2**, 4802-4810 (2014).
5. Godeau, G. & Barthelemy, P. Glycosyl-Nucleoside Lipids as Low-Molecular-Weight Gelators. *Langmuir*, **25**, 8447-8450 (2009).
6. Zhao, H., Guo, X., Chu, L., He, Y. & Chen, Q. Complex self-assembly of pyrimido[4,5-*d*]pyrimidine nucleoside supramolecular structures. *Nature Communications*, **5**, 3108-3018 (2014).
7. Kung, P.-P. & Jones, R.A. One-Flask Syntheses of 6-Thioguanosine and 2'-Deoxy-6-Thioguanosine *Tetrahedron Letters*, **32**, 3919-3922 (1991).
8. Zhang, Y., Zhu, X., Smith, J., Haygood, M.T. & Gao, R. Direct observation and quantitative characterization of singlet oxygen in aqueous solution upon UVA excitation of 6-thioguanines. *The Journal of Physical Chemistry B*, **115**, 1889-1894 (2011).
9. Barth, A. Infrared spectroscopy of proteins. *Biochimica et biophysica Acta*, **1767**, 1073-1101 (2007).
10. Gunasekaran, S. & Kumaresan, S. FTIR, FT Raman spectra and molecular structural confirmation of isoniazid. *Indian Journal of Pure & Applied Physics*, **47**, 12-18 (2009).
11. Manton, A. & Taubert, A. Metal-Peptide Frameworks (MPFs): “Bioinspired” Metal Organic Frameworks. *Journal of the American Chemical Society*, **130**, 2517-2526 (2008).
12. Fulara, J. & Nowak, M.J. Theoretical and Infrared Matrix Isolation Study of 4(3H)-Pyrimidinethione and 3(2H)-PyrMazlnethione. Tautomerism and Phototautomerism. *Journal of Physical Chemistry*, **95**, 2404-2411 (1991).
13. Lapinski, L., Nowak, M.J. & Rostkowskam, H. Infrared spectra of 2-thiocytosine and 5-fluoro-2-thiocytosine; experimental and *ab initio* studies. *Spectrochimica Acta*, **49A**, 551-565 (1993).

14. Qian, W. & Krimm, S. Conformation Dependence of the SH and CS Stretch Frequencies of the Cysteine Residue. *Biopolymers*, **32**, 1503-1518 (1992).
15. Asami, H., Urashima, S.H. & Saigusa, H. Hydration structures of 2'-deoxyguanosine studied by IR-UV double resonance spectroscopy: comparison with guanosine. *Physical Chemistry Chemical Physics*, **11**, 10466-10472 (2009).
16. Esch, J. & Feringa, B.L. New Functional Materials Based on Self-Assembling Organogels: From Serendipity towards Design. *Angewandte Chemie International Edition*, **39**, 2263-2266 (2000).
17. Wang, Q., Lee, E., Kinbara, K. & Aida, T. High-water-content mouldable hydrogels by mixing clay and a dendritic molecular binder. *Nature*, **463**, 339-343 (2010).
18. Sukul, P.K. & Malik, S. Supramolecular hydrogels of adenine: morphological, structural and rheological investigations. *Soft Matter*, **7**, 4234-4241 (2011).
19. Dodd, D.W., Jones, N.D. & Hudson, R.H. Hydrogelation abilities of nucleobase-modified cytidines possessing substituted triazoles. *Artificial DNA: PNA & XNA*, **1**, 90-95 (2010).

Chapter 6. Synthesis and Characterisation of Supramolecular Hydrogels formed by Silver Thionucleobases

Abstract

This work demonstrates synthesis and characterization of silver: 6-thio purine & 2-thio pyrimidine nucleobase hydrogels. The coordination polymers of silver-nucleobases were prepared by complexation of Ag(I) with 6-mercaptopurine (6-MP), 6-thioguanine(6-TG), and 2-thiocytosine (2-TC). The FTIR spectra of the hydrogels show that the fundamental coordination site the S6 and S2 atoms of the purine and pyrimidine nucleobases, respectively. The coordination polymer of silver:2-TC nucleobase was followed by formation tiny amount of silver sulphide which turns the colour of the compound to black with the time. Studying the morphology for the three types of the hydrogels by AFM and TEM show very long linear fibre with dense networks for the hydrogels.

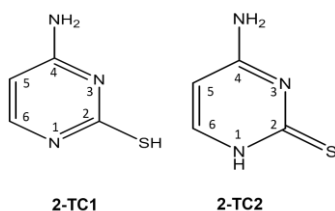
6.1 Introduction

Using biomolecules as ligands can lead to formation a coordination polymer (CP) which has features that are compatible with the original ligand. Normally the biomolecular ligand has multiple binding sites and that can increase the diversity of coordination polymers in accordance with the kind of the metal ions because the orientation of metal ion towards the binding site is usually affected by different conditions such as the oxidation state of the metal ion, the pH of the reaction, the mole ratio, etc. Nucleobases are ideal biomolecules to form different CPs with metal ions as they have different binding sites with electron lone pairs on atoms such as N, O, and S, and they have a hydrogen bonding system that helps to drive self-assembly of CPs. However, biomolecules are difficult to form crystals with metal ions and most of these compounds form amorphous particles. Davidson¹ was able to prepare a 2D linear polymer by coordinating Ag(I) with adenine via N7 and N9, while Zamora was able to prepare 1D polymer of $[\text{Cd}(\text{6-MP})_2 \cdot 2\text{H}_2\text{O}]_n$ by reaction of Cd ions with 6-mercaptopurine(6-MP), the binding occurred via S6 and N7². Houlton³ synthesised a chelate ring of Co:6-thioguanine complex, and he found that the coordination was occurred via S6 and N7. Gagnon⁴ prepared a dimeric structure of adenine nucleobase and silver ion in which silver atoms were bonded via N3 and N9 atoms of bridging bidentate adeninium ligands.

6-Mercaptopurine (6-MP) and 6-Thioguanine (6-TG) nucleobases are analogues of hypoxanthine and guanine obtained by replacing the O6 with S6. Both of the nucleobases are

used as anticancer agents for patients who suffer from acute lymphoblastic leukaemia.^{5,6} The potentiometric studies show that the proton at S6 at 6-TG and 6-MP is more acidic than that at N9⁷, and the behavior of silver atom as soft acid to soft base was studied by Sigel⁸ who confirms in his report the rule of affinity hard bases to hard acids and vice versa, and he found that the binding of Mn⁺² as hard base was very weakly towards sulfur compared to Cu⁺². At guanine, N7 is the favoured site for binding due to higher basicity and higher dipole moment $> 7D^9$ of guanine. Adhikari¹⁰ studied the effect of a series of monovalent cations including silver(I) ion which induce deoxy guanosine (dGs) and guanosine (Gs) to form hydrogels. A supramolecular hydrogel of guanosine 5'-monophosphate (Na₂5'GMP) with Ag(I) was prepared by Mann¹¹ who suggested the formation of dimer of Ag-GMP via N7 and O6, Mann's result was reported before by Loo¹² who used several nucleobases including guanine, he suggested that it forms a dimer with silver ion via N7 and O6 and recently by Goncharova¹³, who suggested the same result with 5'-guanosine monophosphate. Previously studies by Oriol¹⁴ and Tu¹⁵ at Ag-guanosine complex were suggested forming a chelate ring involving N7 and O6.

2-Thiosytocine (2-TC) is a derivative of a natural nucleic acid base cytosine by replacement of the exocyclic oxygen of cytosine with sulphur atom. It is found in the tRNA of some organisms (*E.coli*) but not in mammals.¹⁶ This nucleobase exhibits strong biological effects such as antitumor,^{17,18} antifungal, and anti-inflammatory activity.¹⁹ Due to thiol-thione and amino-imino equilibria, 2-TC presents six tautomeric forms,¹⁹ the most common forms are thiol (2-TC1) and thione (2-TC2) with an exocyclic amino group. According to Latosinska,¹⁹ the stability order in the solid phase is 2-TC2 $>$ 2-TC1 as shown in Scheme 6.1, while Vetter²⁰ and Lapinski²¹ found that 2-TC exhibits the thiol form in the solid state. Reports of interaction of pyrimidines with metals ions showed that 2-thiocytosine act as bidentate while isocytosine act as monodentate upon coordination with Pt and Pd ions.²² It was found that Ruthenium (III) ion and Cu(II) ion coordinated with 2-thiocytosine via N3 and S atoms.^{23,24} Complexes of 2-thiocytosine and 1-methyl-2-thiocytosine with trimethylplatinum(IV) was prepared and it was found that the coordination of these monodentate ligands was occurred via the S atom of the nucleobase.²⁰ Here, we demonstrated for the first time the morphology structure of a new 3D polymers of 6-thio purine and 2-thio pyrimidine of 6-mercaptopurine (6-MP), 6-thioguanine (6-TG), and 2-thiocytosine(2-TC), respectively, with Ag(I) via S atom.



Scheme 6.1. Amine–thiol(2-TC1) and amine- thione (2-TC2) of 2-thiocytosine tautomers.

6.2 Experimental

6.2.1 Synthesis of Silver: 6-Thioguanine (Ag:6-TG) hydrogel

1:1 mole ratio was used to prepare the Ag:6-TG hydrogel by Adding the solution of AgNO_3 (16.2 mg, 0.0956 mmol in 40 μL MeOH and 160 μL H_2O) to the warm solution of 6-TG (16 mg, 0.0956 mmol 400 μL DMSO, 200 μL MeOH, and 200 μL H_2O (the % of DMSO that used for dissolving 6-TG was represented 40% of the total volume of the gel), 1 ml of constant yellow hydrogel was formed at once.

6.2.2 Synthesis of Silver: 6-Mercaptopurine (Ag:6-MP) gel

Ag:6-MP gel was prepared with 1:1 mole ratio by adding the solution of AgNO_3 (8.1 mg, 0.047 mmol in 40 μL MeOH, and 160 μL H_2O) to the warm solution of 6-MP (8.12 mg, 0.047 mmol in 400 μL DMSO, 200 μL MeOH, and 200 μL H_2O), after mixing the solution 1 ml of a clear yellow gel was formed.

6.2.3 Synthesis of Silver: 2-Thiocytosine (Ag:2-TC) gel

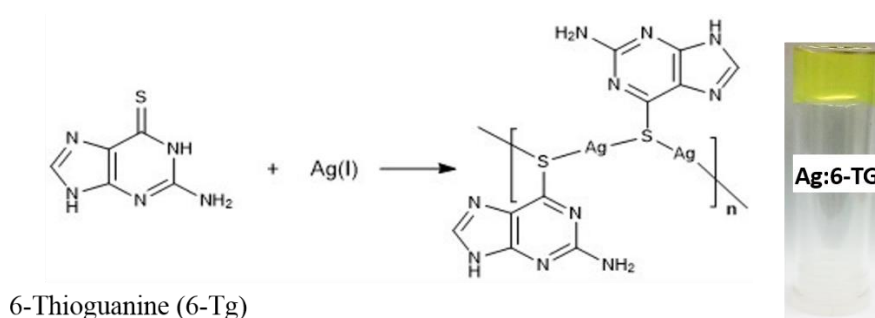
Ag:2-TC was prepared with 1:1 mole ratio, AgNO_3 (0.1132 g, 0.666 mmol in 400 μL MeOH, and 1.6 ml H_2O) was added to the solution of 2-TC (0.0847 g, 0.666 mmol in 2 ml DMSO, 2 ml MeOH, and 4 ml H_2O) after gently shaking, a clear pale solution was formed at once, after two mins a small aggregation was formed, testing these aggregations under the microscope showed long filaments, pale solid Ag:2-TC (yield 0.0768 g with respect to the weight of the ligand, ~91%) was collected by filtering the precipitate. However, leaving the precipitate at the solution leads to increase the size of the filaments after two weeks, and followed two weeks later the filaments be more grown and entangled with each other and the colour turned to brown. At the end of 30 days as a total period since preparing time, the compound was completely black and the entangled filaments converted to long bundles belts ribbon as shown by fluorescent microscope then converted to fibres after six weeks. Scheme 6.4 showing the

route reaction to synthesis the pale Ag:2-TC, while Fig. 6.11 displays photo image for black Ag:2-TC hydrogel

6.3 Results & Discussion

6.3.1 Silver: 6-Thioguanine (Ag:6-TG) hydrogel

Silver:6-thioguanine hydrogel was synthesised by reaction of AgNO_3 with 6-thioguanine (6-TG), the product would be expected to have a linear geometry²⁵ with coordination number 2, and the chains of the polymer will be in form $-\text{S}-\text{Ag}-\text{S}-\text{Ag}-$. The product of the reaction was a stable hydrogel which was characterized with a range of spectroscopic techniques aiming to address the chemical structure of the complex, while the morphology was characterized by using the AFM and TEM. Scheme 6.2 presents the reaction route to the hydrogel. The photograph shows a simple inversion test of a glass vial containing a sample of the gel.



Scheme 6.2. Synthetic route for Ag:6-TG hydrogel, and photograph of the gel.

6.3.1.1 Fourier transform infrared spectroscopy (FTIR) of Ag:6-thioguanine (Ag:6-TG)

The sharp band at 1226 cm^{-1} that observed in the spectrum of the 6-thioguanine nucleobase, Fig. 6.1, is characteristic of the stretching mode of $\text{C}=\text{S}$, this band was absent in the spectrum of the Ag:6-TG gel after complexation indicating that the binding of Ag ion to the nucleobase occurred via S the atom, Moreno-Sanchez²⁶ found that 6-thioguanine bound via S6 with Ag (I) and the ligand acts as unidentate and monoanionic (but his preparation was not a gel). A new band at 1317 cm^{-1} that relates to the nitrate group³ was observed in the spectrum of the complex confirms the presence of the nitrate group in the structure of the gel. The bands at 1535 cm^{-1} and 1612 cm^{-1} which are typically assigned to stretching modes of $\text{C}=\text{N}$ and $\text{C}=\text{C}$ in the ligand 6-TG are shifted to form one band at 1660 cm^{-1} in the complex, changes at the vibrations spectra

regions²⁷ of the nucleobase are apparent for both the intensities and the band positions around 1570-1700 cm^{-1} , and that was not evidence to take part N7 atom at the complexation.

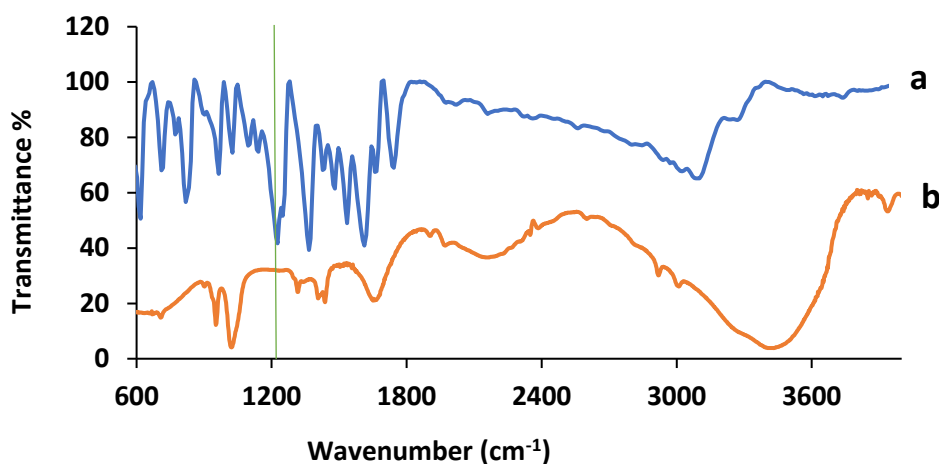


Figure 6.1. Compression FTIR spectra between: (a) the spectrum of the nucleobase 6-TG and (b) the spectrum of Ag:6-TG gel. The green vertical line indicates the position of the C=S stretch.

6.3.1.2 UV-Vis absorption spectroscopy of Ag:6-thioguanine hydrogel (Ag:6-TG)

The spectrum of 6-thioguanine at pH 2 and pH 12, Fig. 6.2, showed two bands at 345 and 320 nm assigned to thione (C=S) and thiol (SH), respectively, Zhang²⁸ found the same result. The spectrum of the aqueous solution of 6-thioguanine (6-TG) at pH (7.3), Fig. 6.3, showed a band at 342 nm that associated with π - π^* transitions assigned to thione form (C=S) which is observed at neutral or acidic pH.^{28,29} The spectrum of the complex demonstrated similar band at 342 nm. Khizhnya³⁰ found that Ag(I) binding with N-acetyl-L- cysteine(NAC) via the S atom and forms linear chains of $-\text{Ag}-\text{S}-\text{Ag}-\text{S}-$ and he assigned the weak absorbance peak that forms upon complexation to participate the electrons of one of pairs of S atom with the orbital of Ag(I).

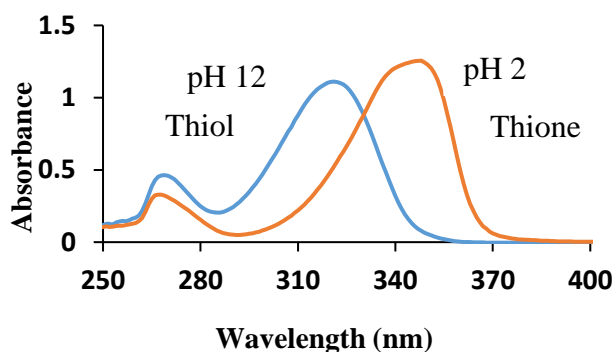


Figure 6.2. Shows the thione and the thiol forms of 6-thioguanine (6-TG) solution at pH 2 (orange line) and pH 12 (blue line), respectively.

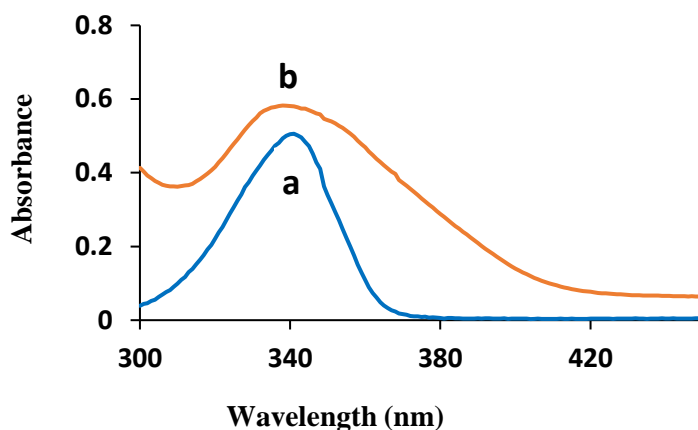


Figure 6.3. Displays comparison between UV-Vis absorption spectra of: (a) 60 μM 6-Thioguanine (6-TG) nucleobase at pH 7.3 and (b) Ag:6-thioguanine (Ag:6-TG) gel.

6.3.1.3 Fluorescence spectroscopy of Ag: 6-thioguanine (Ag:6-TG)

The fluorescence spectrum of 6-thioguanine(6-TG) with excitation 340 nm, Fig. 6.4 shows a broad emission covered the area from 355 nm to 590 nm and centred at 417 nm, while the fluorescence spectrum of Ag:6-thioguanine (Ag:6-TG) displayed a weak emission over the range from 493 nm to 660 nm. This emission, though it was not very strong, is very interesting as most of silver compounds with nucleobases, nucleosides, and other ligands that prepared before^{10,11,31} were non-fluorescent. Gelation leads to a red-shift of the λ_{em} . this is known for supramolecular structures.³²

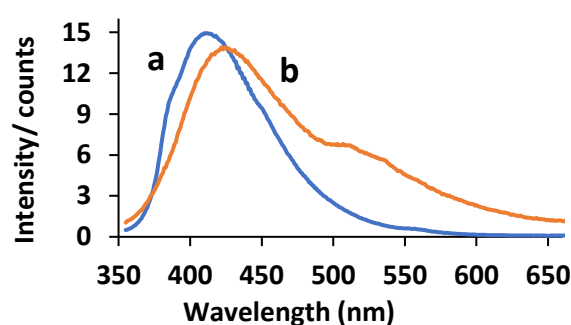


Figure 6.4. Comparison between the fluorescence emission spectrum of (a) aqueous solution of 50 μM 6-thioguanine (6-TG) vs the spectrum of (b) 1:1 Ag:6-TG gel, the excitation wavelength was 342 nm for both 6-TG and Ag:6-TG, respectively.

6.3.1.4 Powder x-ray diffraction (XRD)

The X-ray diffraction patterns for Ag: 6-TG hydrogel, Fig. 6.5 displayed that the distances of Ag-S were 0.276 nm, while the length bands of Ag-Ag were 0.395 nm and 0.488 nm ,respectively, Table 6.1. These data were a good agreement with the literature which gives typical lengths of Ag-S bonds in range 0.237-0.272^{33,34} nm and Ag-Ag was 0.374 -0.458^{34,35} nm. The intramolecular Ag...Ag separation^{35,36} was found at 0.453 nm. A short Ag...Ag distance was found by Bosch³⁷ from 0.288 to 0.297 nm.

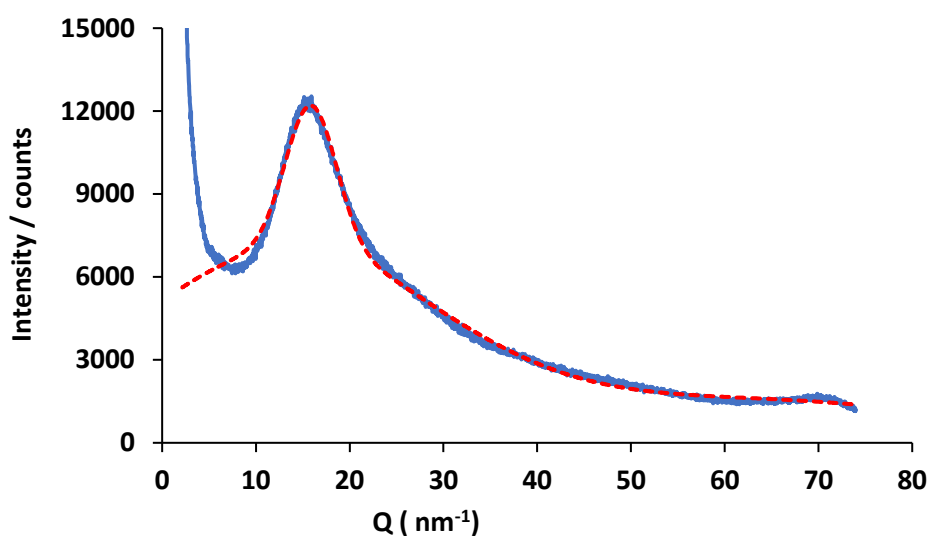


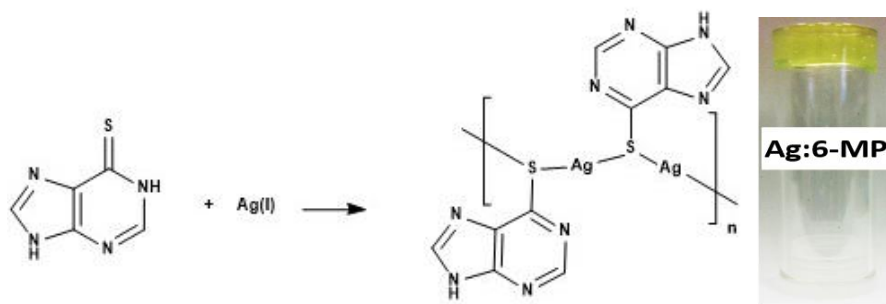
Figure 6.5. XRD pattern for Ag:6-TG hydrogel. The blue line is the experimental diffraction data and the red dotted line is the theoretical fit to a sum of Gaussian functions.

Table 6.1. Distances extracted from the analysis of the XRD data for Ag:6-TG gel.

Distance /nm	Suggested Assignment
0.488	Ag....Ag
0.276	Ag-S
0.395	Ag...Ag

6.3.2 Silver: 6-Mercaptopurine (Ag:6-MP) gel

In similar manner to the synthesis of Ag:6-TG hydrogel, the reaction of AgNO₃ with 6-mercaptopurine (6-MP) leads to a stable hydrogel, Scheme 6.3 shows the chemical reaction route with photograph of an inversion test of the gel.



Scheme 6.3. Chemical reaction route for synthesis of Ag:6-MP hydrogel, and photograph of a gel inversion test.

6.3.2.1 Fourier transform infrared spectroscopy (FTIR) of Ag:6-mercaptopurine hydrogel (Ag:6-MP)

The stretching band at 1273 cm^{-1} which belongs to C=S in the spectrum of the nucleobase (6-MP)³⁸⁻⁴⁰ was not seen in the spectrum of the complex Ag:6-MP, Fig. 6.6, which suggests that the binding of Ag ion to the nucleobase occurred via the S6 atom. The stretching band observed around 1566 cm^{-1} due to C=C and C=N in the spectrum of 6-MP nucleobase was significantly shifted to higher frequency (1658 cm^{-1}) in the spectrum of the complex. The change of the vibrations in the region $1570\text{--}1700\text{ cm}^{-1}$ was apparent in the nucleobase spectra,²⁷ however, this was not evidence that N7 participated in the complexation. A new band at the 1319 cm^{-1} indicating the presence of nitrate group at the molecular structure of the polymer in the gel.

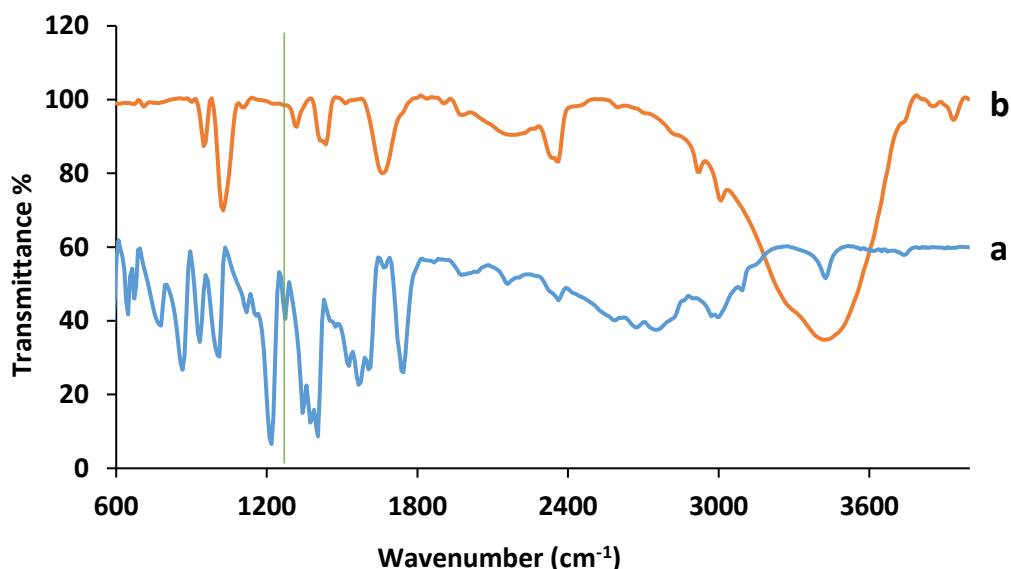


Figure 6.6. FTIR spectrum of the 6-Mp nucleobase (a) vs the spectrum of Ag:6-MP complex (b) in the $600\text{--}4000\text{ cm}^{-1}$ region. The green vertical line indicates the position of the C=S stretch.

6.3.2.2 UV-Vis absorption of Ag:6-mercaptopurine hydrogel (Ag:6-MP)

The spectrum of the 6-MP, Fig. 6.7, was carried out at pH 2 and pH 12. The data showed absorption peak at 320 nm relates to π - π^* which observed at natural and acidic medium associated with the thione form (C=S) and a peak at 300 nm which assigned to the thiol form (SH),^{28,29} respectively, furthermore, Kiefer³⁹ found that 6-MP at a basic medium has a thiol form (SH). Fig. 6.8, shows the spectrum of aqueous solution of 6-MP at pH (6) which displays a peak at 320 nm assigned to thione (C=S), this peak was red-shifted in the spectrum of Ag:6-MP hydrogel to 330 nm after complexation with Ag (I).

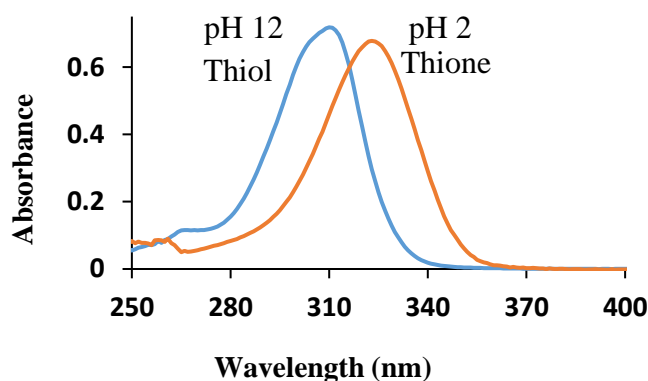


Figure 6.7. UV-Vis absorption spectra of 6-MP at pH 2 and pH 12 show the thione and thiol form, respectively.

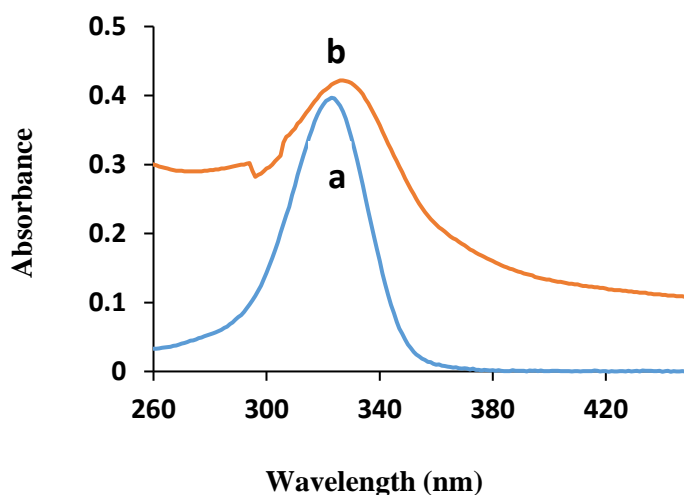


Figure 6.8. UV-Vis spectrum of: (a) 60 μ M 6-Mercaptopurine (6-MP) nucleobase at pH 6 and (b) spectrum of Ag:6-Mercaptopurine (Ag:6-MP) gel.

6.3.2.3 Fluorescence spectroscopy of Ag:6-mercaptopurine (Ag:6-MP)

The fluorescence spectrum of an aqueous solution of 6-mercaptopurine(6-MP) with excitation 320 nm (absorption peak 320 nm) showed a broad emission covered the area from 372 nm to 510 nm and centred at 412 nm, this data was a good agreement with Selvaraj⁴⁰ who displayed strong fluorescence for 6-MP at around 380 nm with excitation at 320 nm, while Shen⁴¹ reported that the fluorescence of 6-MP is weak and no peak was seen at area 340-390 nm. However, our data shows a good fluorescence for 6-MP. Weak emission was found to the spectrum of Ag:6-MP gel at 495-630 nm as shown in Fig. 6.9, most complexes of silver with nucleosides that known or with other ligands were either non-fluorescence or very weak fluorescence.

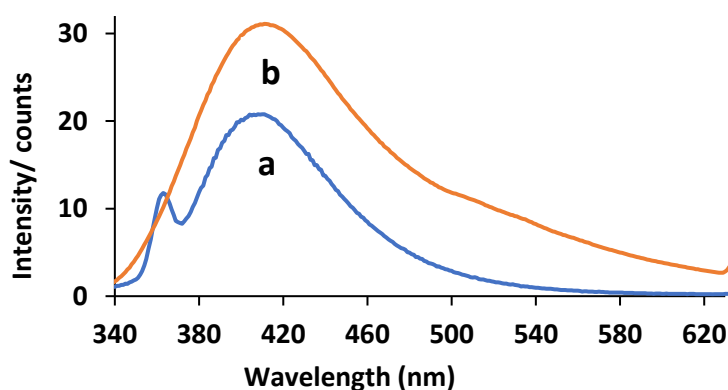


Figure 6.9. Comparison between the fluorescence emission spectrum of (a) aqueous solution of 6-Mercaptopurine (6-MP) vs the spectrum of (b) 1:1 Ag:6-MP gel, the excitation was 320 nm and 328 nm for 6-MP and Ag:6-MP, respectively.

6.3.2.4 Powder x-ray diffraction (XRD)

The X-ray diffraction patterns for Ag: 6-MP hydrogel in Fig. 6.10 revealed that the distance of Ag-S was 0.273 nm^{33,34}, while the length band of Ag-Ag was 0.405 nm.^{35,36} Table 6.2 presents the data.

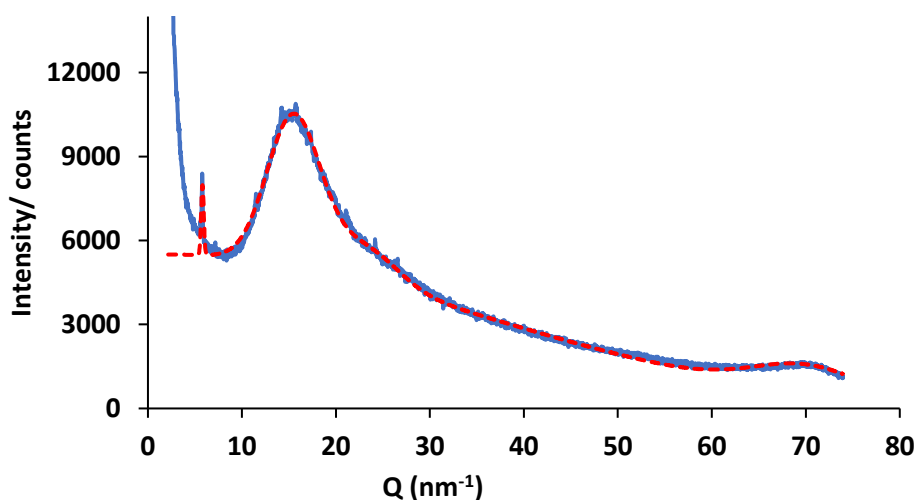


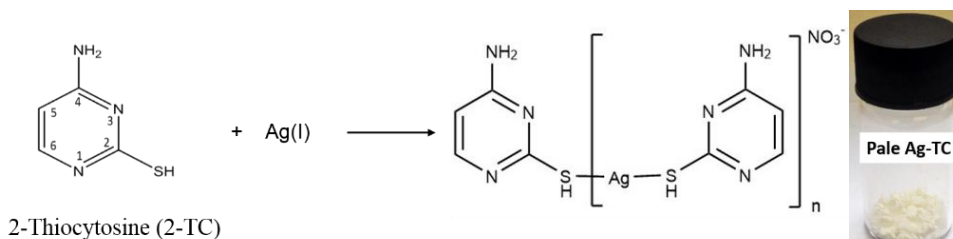
Figure 6.10. XRD pattern for Ag:6-MP hydrogel. The blue line is the experimental diffraction data and the red dotted line is the theoretical fit to a sum of Gaussian functions.

Table 6.2. Distances extracted from the analysis of the XRD data for Ag: 6-MP gel.

Distance/nm	Suggested Assignment
0.405	Ag-Ag
0.273	Ag-S

6.3.3 Silver: 2-Thiocyto $sine$ (Ag:2-TC) gel

The reaction of AgNO_3 with 2-thiocyto $sine$ with mole ratio 1:1 of metal to ligand in mixture solvents of DMSO, MeOH, and H_2O leads to prepare pale polymer of Ag:2-thiocyto $sine$, testing the polymer under microscope showed formation of a very long fibres. Scheme 6.4 displays the reaction route. The solid isolated by filtration after forming and dried at 45°C for 2 h. Leaving the solid in the solvents produces black gel after six weeks, as shown in Fig. 6.11.



Scheme 6.4. Chemical reaction route for synthesis Ag:2-TC.

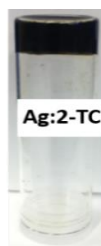


Figure 6.11. Photo images for black Ag:2-thiocyctosine (Ag:2-TC) hydrogel that produced after six weeks when pale Ag:2-TC was left with solvents mixture that used for preparation. Inversion classic test was used to confirm the formation of the hydrogel.

6.3.3.1 Fourier transform infrared spectroscopy (FTIR) of Ag:2-thiocyctosine(Ag:2-TC)

The spectrum of 2-TC, Fig. 6.12, shows a very weak band at 2546 cm^{-1} that assigned to the S-H⁴²⁻⁴⁴ stretching mode, this band was absent in the spectrum of the Ag:2-TC pale complex, in addition the bending mode S-H which was detected at the region from $925\text{--}850\text{ cm}^{-1}$ at the ligand²¹ was not seen in the spectra of the pale complex, these observations indicating coordination silver ion to the S atom of 2-TC. Furthermore, no band was observed at 3400 cm^{-1} , 1206 cm^{-1} & 1098 cm^{-1} related to stretching modes N1-H and C=S, respectively, in the spectrum of the ligand indicates that the ligand was at thiol form.⁴⁵ The two narrow bands at 3101 and 3317 cm^{-1} that assigned to stretch symmetric (*sym*) and asymmetric (*asym*) modes of NH_2 were found in the spectra of 2-TC^{46,47} and black complex and that confirms no binding was occurred via N atom of NH_2 .

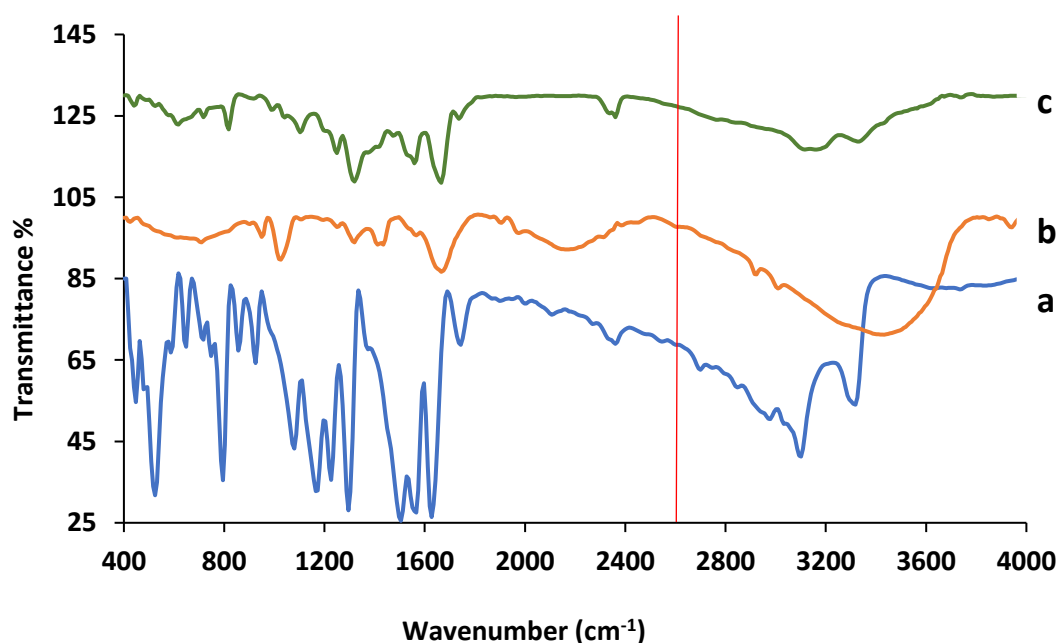


Figure 6.12. FTIR spectra of: (a) 2-Thiocyctosine (2-TC) nucleobase, (b) pale complex of Ag:2-TC, and (c) black complex of Ag:2-TC. The red vertical line indicates the position of the S-H stretch.

6.3.3.2 UV-Vis absorption spectroscopy of Ag:2-TC

The UV-Vis spectrum of the 2-TC, Fig. 6.13, shows two bands at 280 nm and 241 nm assigned to π - π^* ,⁴⁸ the band at 280 nm was shifted at the pale colour complex that formed after complexation between 2-TC and Ag(I) to lower energy (295 nm), this new band can be assigned to π - π^* transitions, the same band that formed for pale complex can be seen at the black complex.

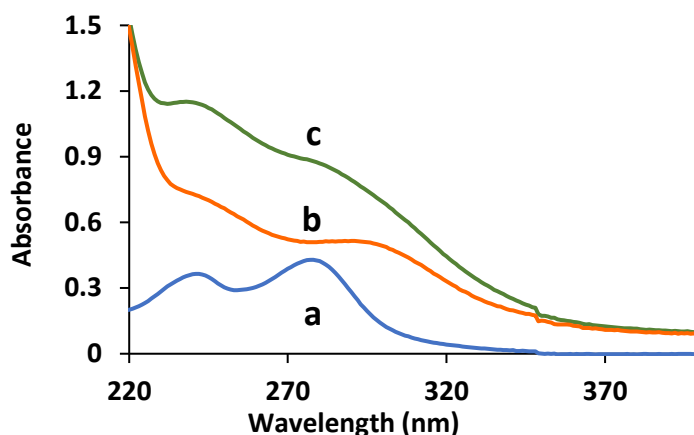


Figure 6.13. UV-Vis absorbance spectra of (a) 2-Thiocytoosine (2-TC) nucleobase with concentration 50 μ M, (b) pale complex of Ag:2-TC, and (c) black complex of Ag:2-TC.

6.3.3.3 Powder X-ray diffraction (XRD)

The XRD data showed formation of two species of microcrystalline and amorphous. The microcrystalline is belong to the compound that produces from coordination 2-thiocytoosine with Ag(I) ions, isolated this compound from the mixture solvents DMSO, MeOH, and H₂O leads to produce pale stable compound. However, leaving this compound in the mixture solvents for six weeks leads to loss the microcrystallinity and forms amorphous structure alongside with forming black gel.

The X-ray diffraction pattern for pale Ag:2-TC in Fig. 6.14 revealed sharp Bragg peaks in range between $5 < Q < 30$ corresponding to distance (d), $d = 2\pi/Q$. Higher distances where found in range of $4 < Q < 19$.

The sharp Bragg peaks that apparent in Fig. 6.14 for the pale compound indicates that the compound has microcrystalline structures. Table 6.3 displays the d for pale Ag:2-TC.

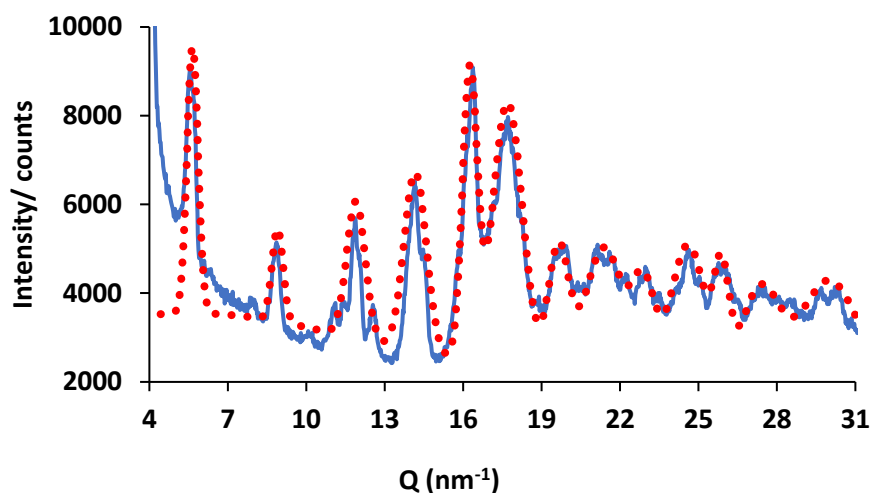


Figure 6.14. XRD pattern for pale Ag:2-TC. The blue line is the experimental diffraction data and the red dots line is the theoretical fit.

Table 6.3. Distance d_i extracted from the analysis of the XRD data for pale Ag:2-TC.

Distance/nm	Suggested Assignment
0.386	Intramolecular Ag-Ag
0.274	Ag-S
0.255	Ag-S
0.242	Ag-S

The X-ray diffraction data for the black compound of Ag:2-TC in Fig. 6.15 shows amorphous structure and no Bragg peaks were found compared to the pale Ag:2-TC compound which showed microcrystalline structure. Fitting the data displays that the Ag-Ag distance was found at 0.39 nm, however, no distance for Ag-S was observed which is expected to be found at 0.27 nm according to the literature, and that can be reasoned to the small size of Ag₂S that formed. Table 6.4 displays the d for black Ag:2-TC.

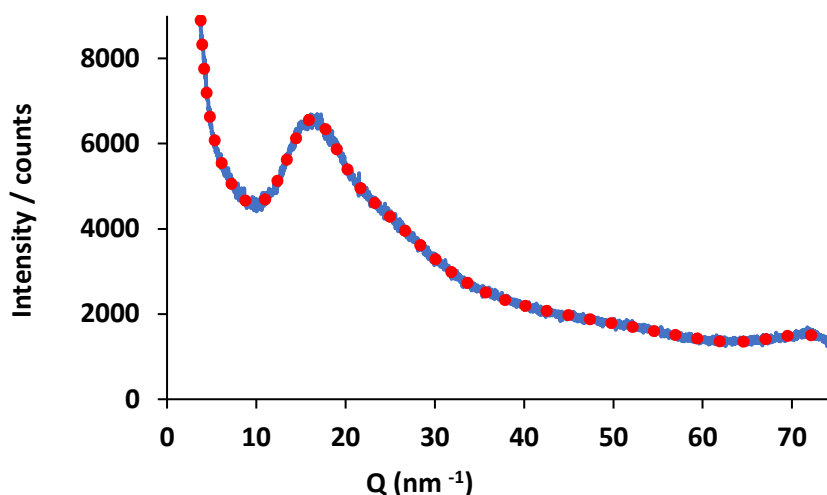


Figure 6.15. XRD pattern for black Ag:2-thiocyto-sine hydrogel. The red dots line is the theoretical fit and the blue line is the experimental diffraction data.

Table 6.4. Distance d_i extracted from the analysis of the XRD data for black Ag:2-TC gel.

Distance / nm	Suggested Assignment
0.317	Ag-Ag
0.457	Ag-Ag
0.392	Ag-Ag

6.3.3.4 X-ray photoelectron spectroscopy (XPS) of 2-thiocyto-sine

The contradiction in the binding energy value for $3d_{5/2}$ at Ag in different oxidation states make it difficult to use it for distinguishing between them because the small difference (1.2 eV) between the three oxidation states of binding energy values for instance the Ag $3d_{5/2}$ at Ag^0 , Ag_2O , and AgO were found to be 367.9-368.4, 367.6-368.5, and 367.3-368.1, respectively,⁴⁹ thus, the Auger Parameter (AP) is more useful to distinguish between silver species. The AP is independent on the charge of the sample, as it represents the difference between photoelectron energy and Auger electron energy. Furthermore, the chemical shifts at the peaks is higher than that for photoelectron peaks,⁵⁰⁻⁵³ for instance, the AP for Ag^0 is higher by 2 eV than the values for other oxidation states.⁴⁹ However, it is difficult to use it to distinguish the Ag(I) from other oxidation states for silver, for instance in Ag_2O and AgO , the shape of photoelectron peaks use to distinguish between them as they appear as a complex doublet in AgO and a single doublet in Ag_2O .^{49,51} Fig. 6.16, shows the XPS spectrum of photoelectron for Ag $3d_{5/2}$ and $3d_{3/2}$ in Ag-TC, as shown in the figure a doublets peaks with binding energy 368.28 eV and 374.28 eV

with separation 6.0 eV and FWHM= 1.10 eV assigned to Ag 3d_{5/2} and Ag 3d_{3/2}, respectively, indicating that the oxidation state of Ag at Ag:2-TC is (+1).⁵¹

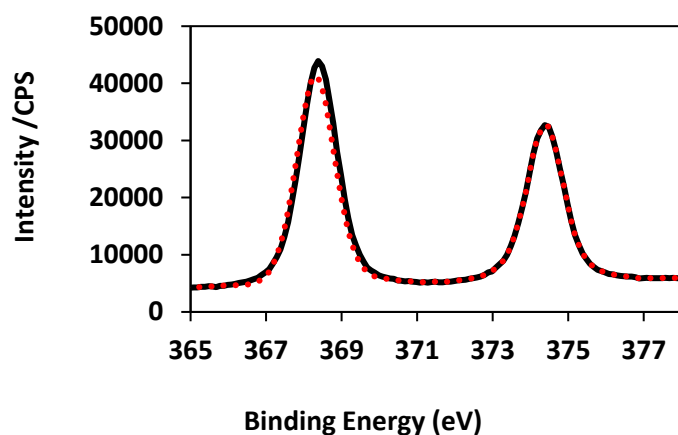


Figure 6.16. The XPS spectrum of Ag:2-TC shows the photoelectron for 3d_{5/2} and 3d_{3/2} with separation 6.0 eV and FWHM 1.1 eV.

To establish the oxidation state of the silver at the sample with more reliable evidence, AP parameter have been measured also. Fig. 6.17 shows the Ag Auger peaks with BE values 1137.41 and 1129.64 eV which correspond to KEs of Auger lines for Ag 3d_{5/2} M₄N₄₅N₄₅ and Ag 3d_{3/2} M₅N₄₅N₄₅ of 357.04 and 349.27 eV and the Auger Parameter (AP) can be calculated as 725.32 eV and 723.55 eV, respectively, and this suggests bonding Ag-S, these data are a good agreement with the data of Kaushik⁵¹ who found that AP value of Ag 3d_{5/2}, M₄N₄₅N₄₅ for Ag(I) at Ag₂S was 724.8 eV which is close to the value in this thesis.

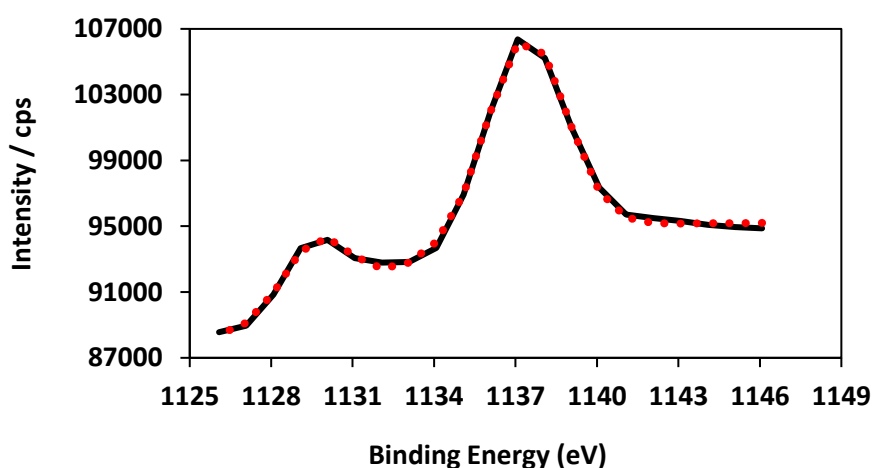


Figure 6.17. The XPS spectrum of Ag-TC shows the Auger lines for Ag 3d_{5/2}, M₄N₄₅N₄₅ and Ag 3d_{3/2}, M₅N₄₅N₄₅ for Ag-TC at 349.27 eV and 357.04 eV, AP = 725.32, and 723.55 eV, respectively.

Fitting S 2p XPS peaks as shown in Fig. 6.18, displayed two sets of doublet bands, the first doublet at 162.28 eV and 163.78 are assigned to $2p_{3/2}$ and $2p_{1/2}$, respectively, while the second doublet set for the same electronic configuration was apparent at 165.88 eV, 167.28 eV. The apparent of those sets of peaks at these positions are attributed to the presence of Ag_2S .⁵⁴

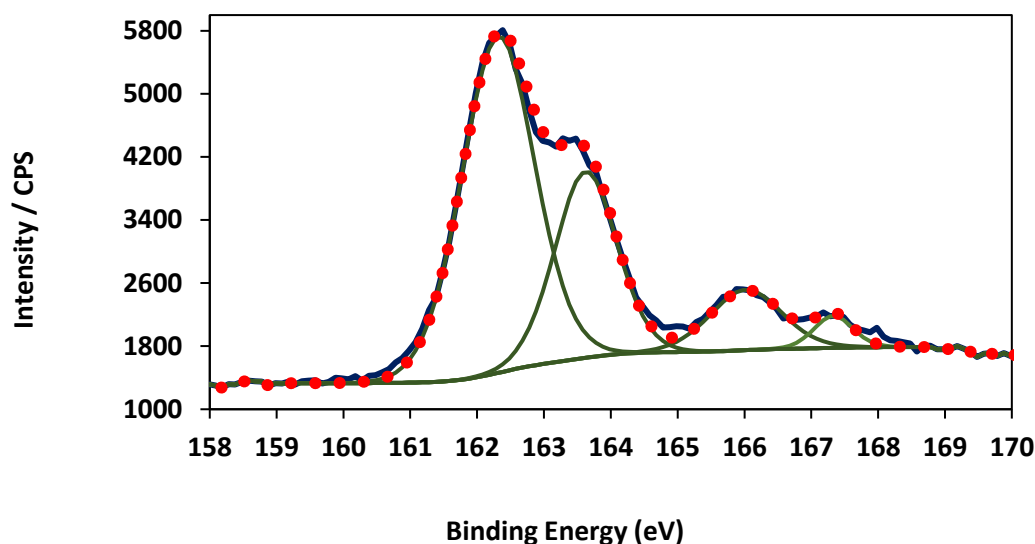


Figure 6.18. XPS spectrum of S 2p for $2p_{3/2}$ and $2p_{1/2}$ shows doublet sets of peaks.

Moreover, to confirm that the sample does not have silver oxide, examining Ag O $1s$ showed one component assigned to O $1s$ located at 532 eV which is attributed to the surface oxide layer of the silicon substrate²⁷ and no peak was centred at 530.4 eV^{55,56} that is normally observed when the oxide is present in the sample, the absence of this peak indicating that no oxide was at the sample, as shown in Fig. 6.19.

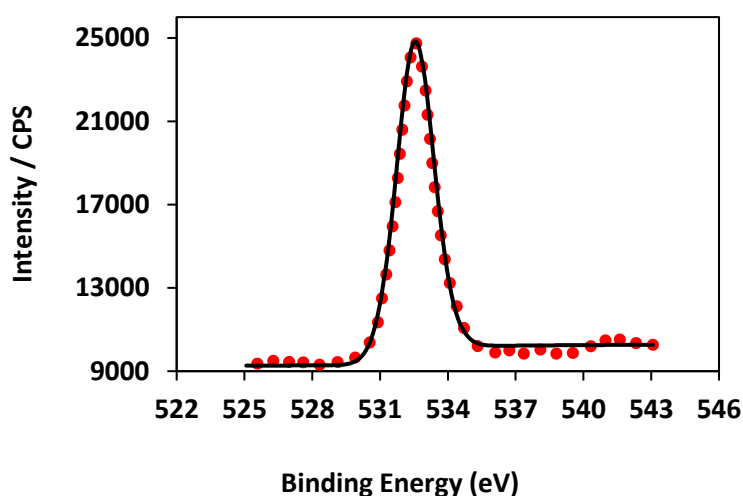


Figure 6.19. XPS spectrum of Ag:2-TC shows the photoelectron of O1s.

6.3.3.5 Mass spectra characterization for pale Ag:2-TC

The data of mass spectra that carried out at Sheffield University using matrix-assisted laser desorption and ionization time-of-flight mass spectrometry (MALDI-TOF-MS) for pale Ag:2-TC in acetonitrile revealed presence of $[L + Ag + NO_3^-]$ and confirms the proposal formula $C_4H_4N_4SAgO_3$, m/z found: 295.9607 (calculated: 295.8688), the data confirms the proposal structure for pale Ag:2-TC. The isotope at m/z 485.0079 is attributed to $[2L+Ag+2NO_3^-]$. Fig. 6.19 presents the mass spectrum.

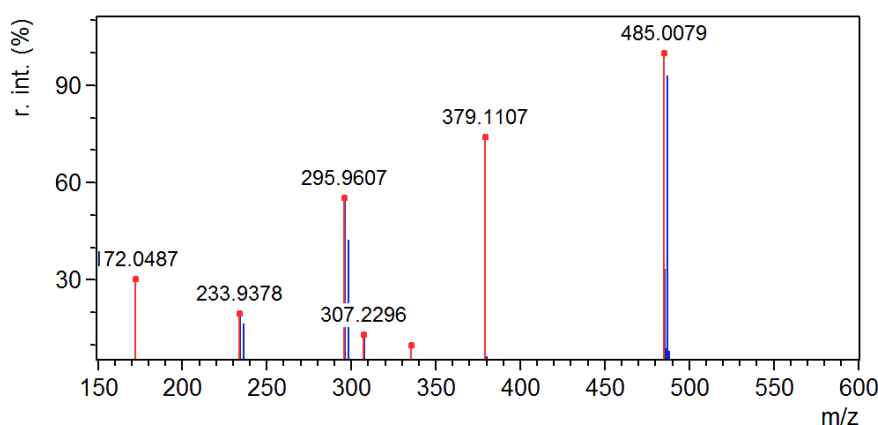


Figure 6.19. Matrix-assisted laser desorption and ionization time-of-flight mass spectrometry (MALDI-TOF-MS) mass spectrum for pale Ag-2TC in acetonitrile.

6.4 Atomic force microscopy (AFM)

6.4.1 Atomic force microscopy (AFM) characterization of the Ag: 6-TG & 6-MP hydrogels

Self- assembly helps to synthesis a new class of material with multiple length scales. Both natural biomolecules⁵⁷ and synthetic molecules are capable to assemble and form nanofibres by supramolecular aggregates. The term nanofiber refers to the fibres with a diameter <100 nm.⁵⁸ Nanofibres can be found as a helix structure by twisting fibre or produce from twisting of two or more fibres to form bundles, in this case the possibility to observe the helix by AFM will be only for one fibre and the helical must be not ruled out from describing the structure. The helical structure is possible to seen by AFM, however the formation of dens networks sometimes makes observation of the helix difficult. In order to probe the morphology and the size of the fibres in the gels, surface topography imaging was carried out using tapping mode AFM on samples prepared by depositing 2 μ L of Ag:6-TG & Ag:6-MP hydrogels onto a silicon substrates. The AFM images revealed the formation of extremely long polymer molecules (>10 μ m the maximum scan range) with a dense network. A statistical analysis was carried out to show the size (diameter) distribution and the height of the fibres in the Ag:6-TG & 6-MP

hydrogels. Fig. 6.20 image (c) shows the histogram of the Ag:6-TG hydro gel structure, the peak height is revealed to be 9-11 nm. Peaks with heights larger than that, up to 15 nm, were appeared at low frequency, some peaks lower than 9 nm, from 3-7 nm, are also seen at the histogram. The profile of the individual fibre structure on the surface, Fig. 6.20 (b) showed that the height was typically in range of 9 nm. Interestingly, the shape of the fibres was linear, and there was no branching have been observed at all AFM images that have been measured and that indicates that the chains have a linear structure.

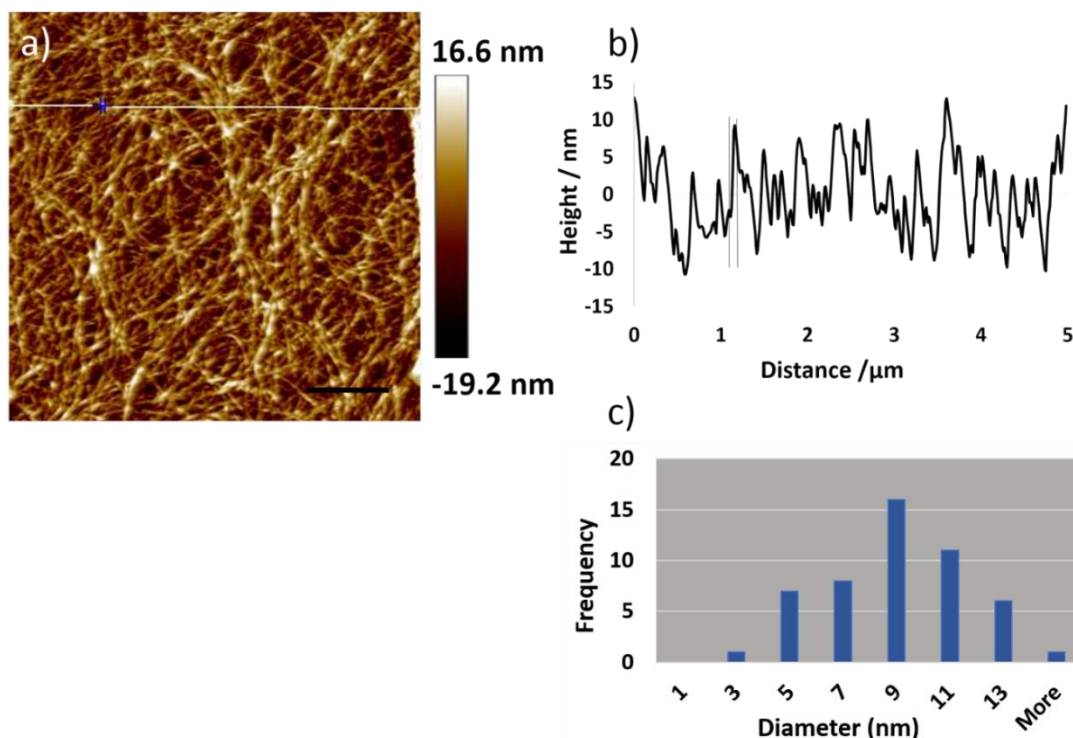


Figure 6.20. AFM of Ag:6-TG gel drop cast onto a silicon wafer and air drying, the image was taken in tapping mode. (a) Height image, the grayscale 16.6 nm and scale bar 1 μm. (b) the cross section of (a) shows the height of the fibres at a diameter ~9 nm, (c) the histogram of the size(diameter) distribution of the fibres of Ag:6-TG gel.

The size distribution of the fibres at Ag:6-MP gel is shown in Fig. 6.21 d, the common (modal) diameter is observed to be about 7-9 nm, number of peaks at low frequency with larger heights, up to 17 nm, or lower heights, down to 3 nm, are also apparent at the histogram.

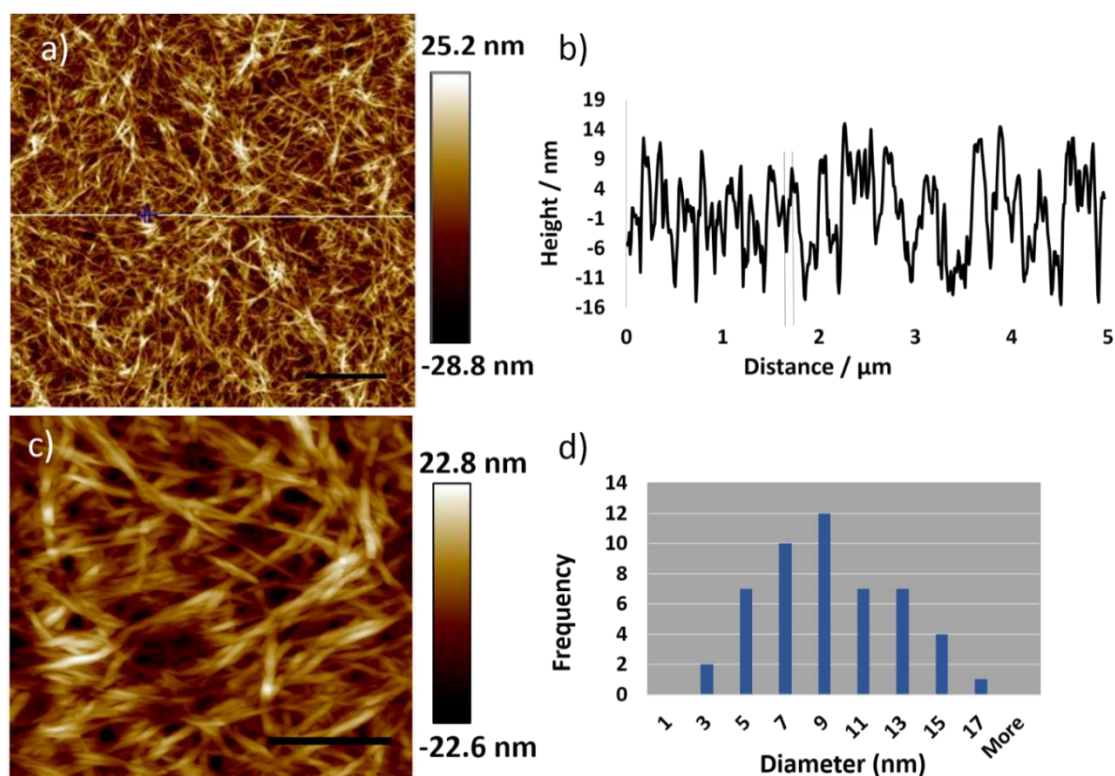


Figure 6.21. Tapping mode AFM images of 1:1 silver 6-mercaptopurine hydrogel drop-cast onto a silicon wafer and dried in air. The scale bars in (a) & (c) are 1 μm and 300 nm, respectively. (a) Height image, the grayscale corresponds to 25.2 nm (b) the associated cross-section along the white horizontal line in (a) shows the height of the fibres at a diameter ~ 9 nm, (c) a small area of (a) with height (grayscale) 22.8 nm, and (d) the size distribution of ~ 50 Ag:6-MP fibres.

6.4.2 Atomic force microscopy (AFM) of Ag:2-TC

The intermolecular potentials represent one of the most important factors that help the molecules to form a polymer structure, furthermore the interactions of dipolar moments that involve hydrogen bonding, van der Waals, and π - π stacking lead to form fibre and supramolecular polymers.⁵⁹ To understand the factors that limit the length and the rate formation of fibres, the light must be first shed on the growth process which includes self-assembly of the chains of the polymer into fibre depending on intermolecular interactions.⁶⁰ The AFM image in Fig. 6.22 was taken from the pale Ag:2-TC. Image (a) shows the microfibre structure, (b) is the profile of the white vertical line along image (a) which revealed that the height was ~ 300 nm. While the AFM images in Figs. 6.23 & 6.24 were taken from the black compound of Ag:2-TC. The images showed nano fibre structure, the histogram (d) displays the distribution size of the fibres. The profile of image (a) in Fig. 6.24. indicates the height of the fibres which was ~ 12 nm.

The difference in the AFM images between the pale compound (Fig.6.22) and the black compound (Figs. 6.23 & 6.24) in the morphology and the height of the fibres is assigned to the microcrystalline structure of the pale compound and the amorphous structure of the black compound. These observations are consistent with the XRD data which shows conversion the structure from microcrystalline to amorphous upon conversion the Ag:2-TC from pale compound to black gel.

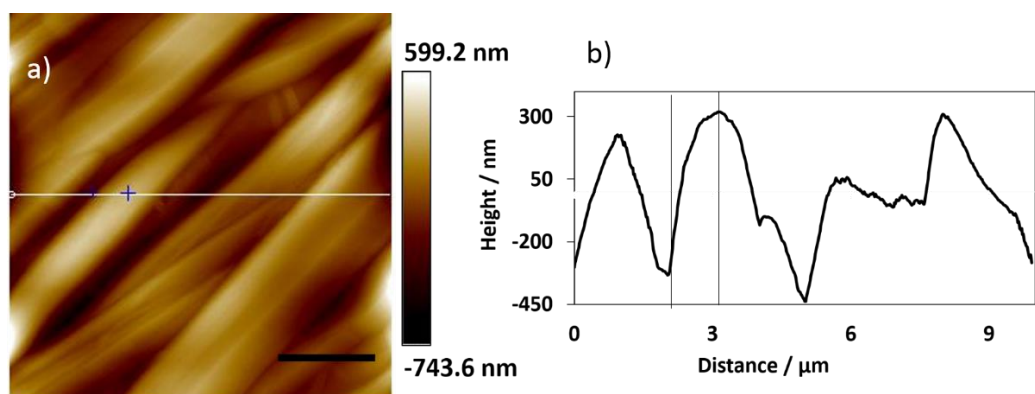


Figure 6.22. a) Height AFM image for pale Ag:2-TC with scale bar 2.5 μm, b) the profile of the white vertical line in image (a) shows the height ~300 nm. The high value for the height in this image reflects the microcrystalline structure for the pale Ag:2-TC.

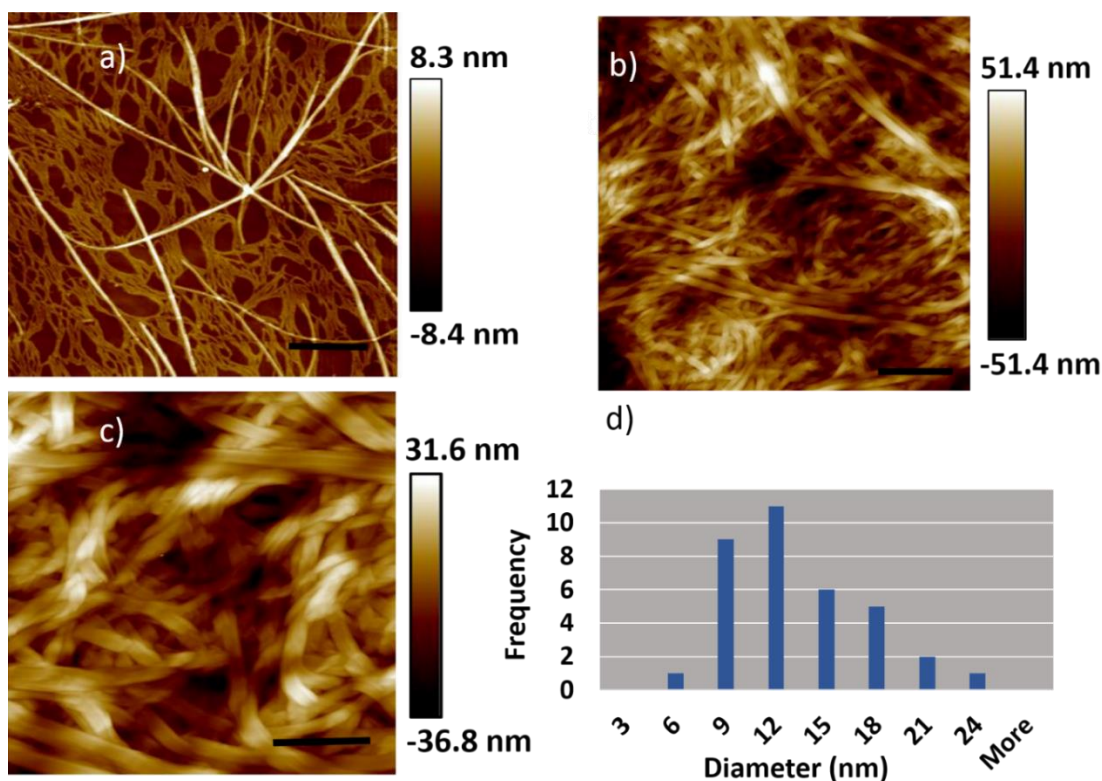


Figure 6.23. Tapping Mode AFM Height images of 1:1 Ag-2-thiocytosine gel, the scale bar was 1 μm in images (a) and (b), and 500 nm in image (c), the mean height was 8.3 nm, 51.4nm, and 31.6 nm at (a), (b), and (c), respectively. d) The histogram shows the size (Diameter) distribution of the fibres.

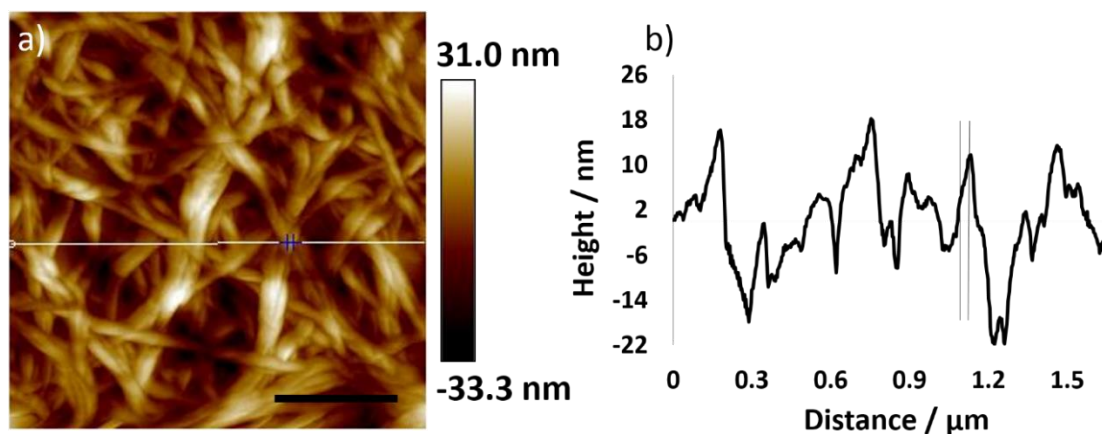


Figure 6.24. a) Height AFM image with scale bar 500 nm and height 31 nm, b) the profile of the white vertical line in image (a) shows the height ~12 nm.

6.5 Transmission electron microscopy (TEM) characterization

Transmission Electron Microscopy (TEM) was used to assess the morphology of the gel, identical sample was prepared by placing 1.5 μL of the gel onto a carbon coated copper grid substrate, after drying at ambient conditions, the sample was imaging by using Philips CM100 electron microscope at accelerating voltage 100 kV with high resolution, and a typical TEM images of networks of Ag: 6-TG & 6-MP hydrogels are shown in Fig. 6.25 & 6.26, it is apparent from the images that the gels have very long linear fibres with uniform distribution morphology upon the grids, it is also clearly apparent the absent of branching fibres and that was not occurred by chance, this finding strengthen the proposal that the binding site was only S6. These images show agreement with the morphology of the gels that obtained by AFM.

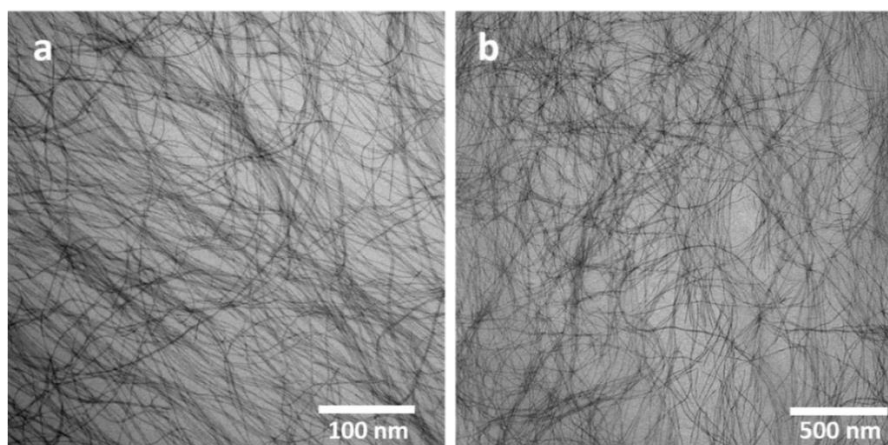


Figure 6.25. TEM of 1: 1 Ag:6-thioguanine (6-TG), the scale bar was 100 nm and 500 nm at (a)& (b), while the magnification was 64000x and 46000x, respectively.

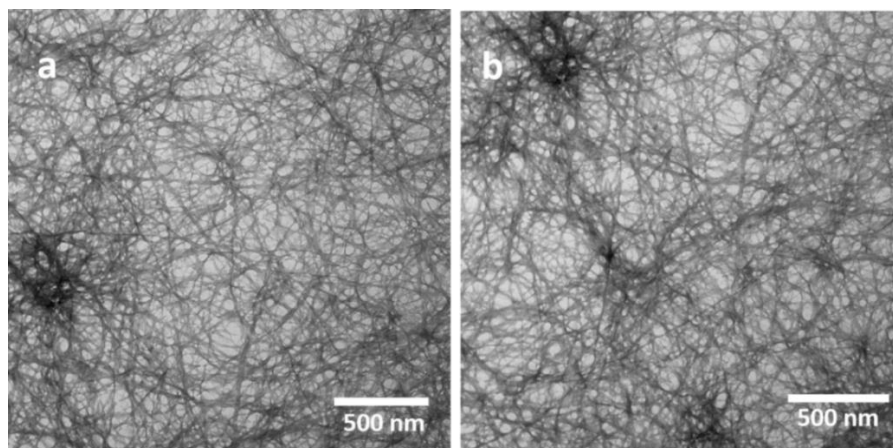


Figure 6.26. TEM of 1: 1 Ag- 6-mercapto purine (6-MP), the scale bar and the magnification was 500 nm 34000x at (a) & (b), respectively.

The TEM images for Ag:2-TC in Fig. 6.27 show very long fibres with tiny particles which may be attributed to the presence of Ag_2S .

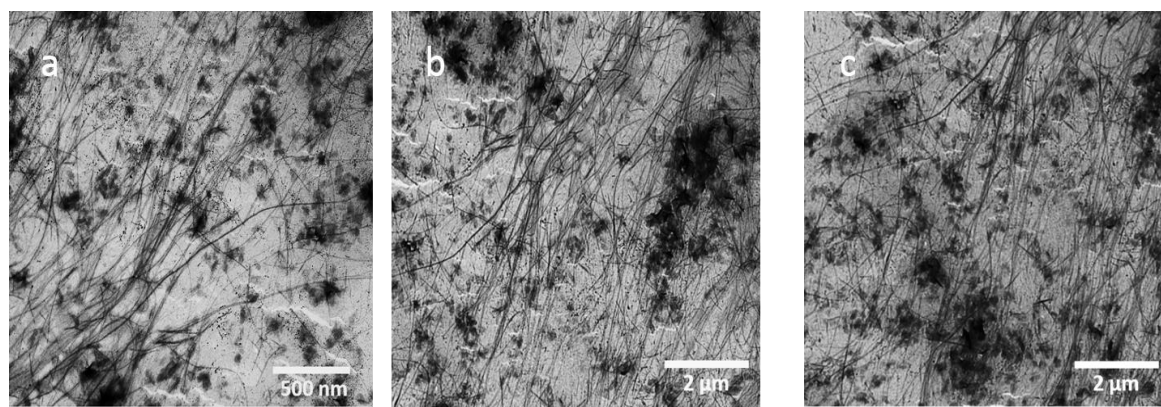


Figure 6.27. Transmission electron microscopy images of Ag:2-TC prepared with 1:1, the scale bar and the magnification were 500 nm, 13500x at (a) and 2 μm , 10500x at (b & c), respectively, the images which were for the black compound that formed after six weeks, show very long bundles with black particles that belongs to Ag_2S .

6.6 Fluorescence microscopic images

Studying the hierarchical process formation of polymer Ag:2-TC, Fig. 6.29, was carried out by using fluorescence microscope. Comparison between the morphology of 2-TC, AgNO_3 , and Ag:2-TC at mixture solvents of DMSO, MeOH, and H_2O showing the difference between the three compounds. As shown in Fig. 6.28, 2-TC (a, b) and AgNO_3 (c) have crystal structures, while the Ag:2-TC (d) has a polymeric structure. This comparison was achieved to confirm

that the polymer was belong to Ag:2-TC and not for 2-TC or AgNO₃, it was found that Ag(I) can form corrugated structure upon coordinated with DMSO.⁶¹ On the other hand, the chemical structure of 2-TC can form dimer, ribbons, and bundles as a result of the presence of two kinds of hydrogen bonding NH...N and NH...S.⁶²

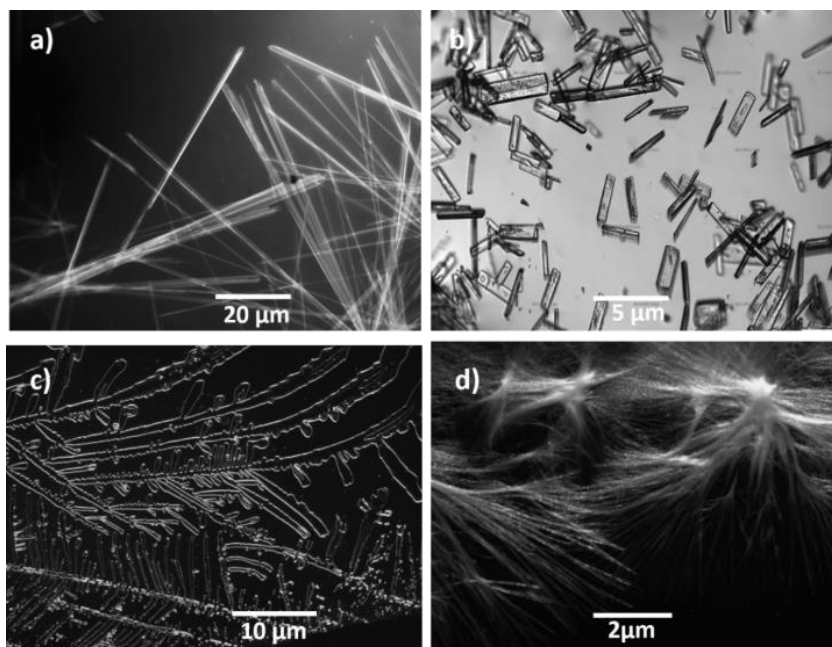


Figure. 6.28. Fluorescence image for 2-TC after 5 min (a) and optical image after 1h (b) of preparation in mixture solvents of DMSO, MeOH, and H₂O. Fluorescence image for AgNO₃ in solvents DMSO, MeOH, and H₂O (c), and Ag:2-TC(d) in a mixture of DMSO, MeOH, and H₂O solvents, showing crystal structure for (a, b) & (c) and polymer structure for (d), respectively.

The first stage was included formation of pale colour small clusters of micro filaments, Fig. 6.29 (images a & b) followed by growing these clusters into long branched micro fibres (c & d), next, the micro fibres begin converted into very thin fibres (e) which in turn forming a very thin layer (f) that represents a 3D network of hydrogel that indicted by using AFM. Remarkably, this process was accompanied by changing the colour of the mixture from pale to black, and the last stage (f) was not be formed before changing the colour completely to black indicating formation amount of Ag₂S, the total period from synthesis to obtained the gel was 6 weeks.

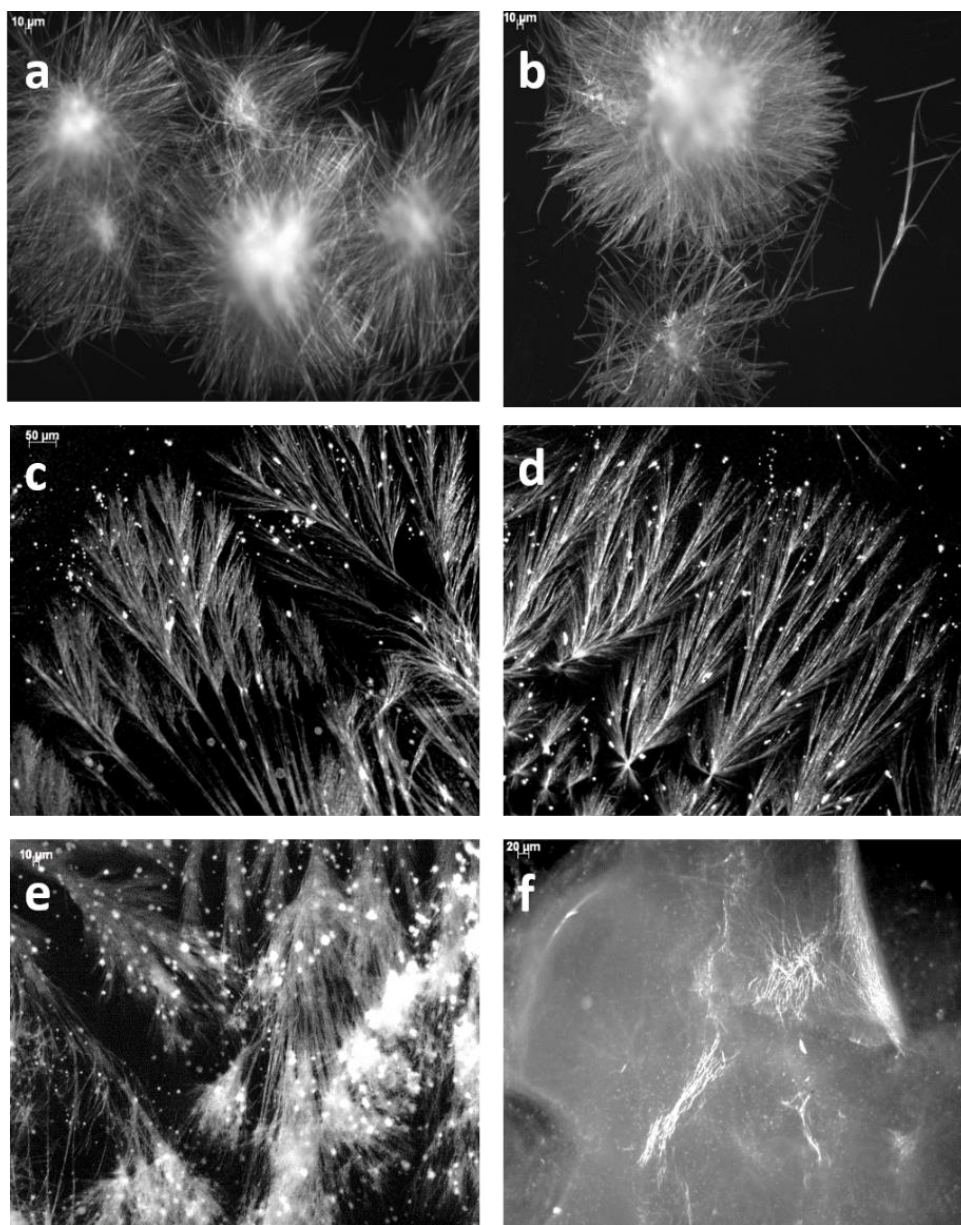


Figure 6.29. Fluorescence microscopic images of 1:1Ag:2-TC in different periods of polymerization, images a & b at the first week, images c & d after two weeks, and images e & f after eight weeks.

6.7 Conclusion

In summary, we prepared 3D hydrogels based on Ag-S bond with thio purine and thio pyrimidine, the coordination of metal ion to the nucleobase provide access to synthesis a new class of material by forming network consist of entanglement very long fibres. Importantly, the affinity of Ag(I) to form linear bonding with S atom leads to form very long chains of linear $-S-Ag-S-$. The X-ray data revealed formation two species compounds for the reaction of 2-thiocytoosine with Ag(I) ions, microcrystalline and amorphous, the former produces when isolated the pale product from the mixture solvents DMSO, MeOH, and H₂O, while the latter produces when leaving the pale compound in the mixture solvents which leads to loss the

microcrystallinity and forms amorphous structure alongside and forms black gel. The XPS data displayed that the black colour of the gel is due to the formation of Ag₂S.

References

1. Gillen, K., Jensen, R. & Davidson, N. Binding of Silver Ion by Adenine and Substituted Adenines. *Journal of the American Chemical Society*, **86**, 2792-2796 (1964).
2. Zamora, F. & Amo-Ochoa, P. Assembling of Dimeric Entities of Cd(II) with 6-Mercaptopurine to Afford One-Dimensional Coordination Polymers: Synthesis and Scanning Probe Microscopy Characterization. *Inorganic Chemistry*, **45**, 7642-7650 (2006).
3. Houlton, A., Amo-Ochoa, P., Hribesh, S., Pike, A.R. & Zamora, F. Coordination chemistry of 6-thioguanine derivatives with cobalt: toward formation of electrical conductive one-dimensional coordination polymers. *Inorganic chemistry*, **52**, 5290-5299 (2013).
4. Gagnon, C. & Beauchamp, A.L. Crystal Structure of Di-p-adeninium-disilver(1) Perchlorate Monohydrate. *Inorganic Chemistry*, **16**, 2469-2473 (1977).
5. Nishida, A. & Iga, T. Thiopurine S-methyltransferase activity in Japanese subjects: metabolic activity of 6-mercaptopurine 6-methylation in different TPMT genotypes. *Clinica Chimica Acta*, **323**, 147-150 (2002).
6. Dervieux, T. & Relling, M.V. HPLC Determination of Thiopurine Nucleosides and Nucleotides in Vivo in Lymphoblasts following Mercaptopurine Therapy. *Clinical Chemistry*, **48**, 61-68 (2002).
7. Taqui Khan, M.M.T. & Krishnamoorthy, C.R. Interaction of Metal Ions with Disubstituted Purines. *Journal of Inorganic and Nuclear Chemistry*, **35**, 1285-1292 (1973).
8. Sigel, H. & Prijs, B. "Hard and Soft" Behavior of Mn²⁺, Cu²⁺, and Zn²⁺ with Respect to Carboxylic Acids and Oxy-or orThio-Substituted Carboxylic Acids of Biochemical Significance. *Archives of Biochemistry and Biophysics*, **130**, 514-520 (1969).
9. Lippert, B. Multiplicity of metal ion binding patterns to nucleobases. *Coordination Chemistry Reviews*, **200-202**, 487-516 (2000).
10. Adhikari, B., Shah, A. & Kraatz, H.-B. Self-assembly of guanosine and deoxyguanosine into hydrogels: monovalent cation guided modulation of gelation,

- morphology and self-healing properties. *Journal of Materials Chemistry B*, **2**, 4802-4810 (2014).
11. Dash, J., Patil, A.J., Das, R.N., Dowdall, F.L. & Mann, S. Supramolecular hydrogels derived from silver ion-mediated self-assembly of 5'-guanosine monophosphate. *Soft Matter*, **7**, 8120-8126 (2011).
 12. Loo, K. & Petty, J.T. Ag⁺-Mediated Assembly of 5'-Guanosine Monophosphate. *The Journal of Physical Chemistry B*, **114**, 4320-4326 (2010).
 13. Goncharova, I. Ag(I)-mediated homo and hetero pairs of guanosine and cytidine: monitoring by circular dichroism spectroscopy. *Spectrochimica Acta Part A: Molecular and Biomolecular Spectroscopy*, **118**, 221-227 (2014).
 14. Orioli, P.L. & Cini, R. A Proton Magnetic Resonance Investigation on 1: 1 Cytidine and Guanosine Silver (I) Complexes. *Biolnorganic Chemistry*, **7**, 345-349 (1977).
 15. Tu, T.A. & Reinosa, J. The Interaction of Silver Ion with Guanosine, Guanosine Monophosphate, and Related Compounds. Determination of Possible Sites of Complexing. *Biochemistry*, **5**, 3375-3383 (1966).
 16. Carbon, J., David, H. & Studier, M.H. Thiobases in Escherchia coli Transfer RNA: 2-Thiocytosine and 5-Methylaminomethyl-2-thiouracil. *Science*, **161**, 1146-1147 (1968).
 17. Nagata, T. & Kawaguchi, T. Cytotoxicity and Pharmacokinetics of 1-β-D-Arabinofuranosyl-2-thiocytosine, a 2-Sulphur Substituted Derivative of Cytarabine. *Biological and Pharmaceutical Bulletin*, **22**, 100-102 (1999).
 18. Nagata, T. & Kawaguchi, T. Enzymatic Reactivity and Anti-tumor Activity of 1-(β-D-Arabinofuranosyl)-2-thiocytosine Derivatives. *Chemical and Pharmaceutical Bulletin*, **48**, 454-457 (2000).
 19. Latosinska, J.N., Seliger, J., Zagar, V. & Burchardt, D.V. A comparative study of the hydrogen-bonding patterns and prototropism in solid 2-thiocytosine (potential antileukemic agent) and cytosine, as studied by ¹H-¹⁴N NQDR and QTAIM/ DFT. *Journal of Molecular Modeling*, **18**, 11-26 (2012).
 20. Vetter, C., Wagner, C., Paschke, R. & Steinborn, D. Synthesis, characterization, and cytotoxicity of trimethylplatinum(IV) complexes with 2-thiocytosine and 1-methyl-2-thiocytosine ligands. *Inorganica Chimica Acta*, **362**, 189-195 (2009).
 21. Lapinski, L., Nowak, M.J. & Rostkowskam, H. Infrared spectra of 2-thiocytosine and 5-fluoro-2-thiocytosine; experimental and *ab initio* studies. *Spectrochimica Acta*, **49A**, 551-565 (1993).

22. Zakeeruddin, S.M. & Khan, B.T. Platinum(II) and palladium(II) complexes with substituted pyrimidines. *Transition Metal Chemistry*, **16**, 119-121 (1991).
23. Katsaros, N. & Tselepi-Kalouli, E. Ruthenium(III) Ion Complexes with Nucleic Acid Bases and Nucleosides. *Journal of Inorganic Biochemistry*, **34**, 63-74 (1988).
24. Nelson, H.C. Copper(II) Complexes of 2-Thiocytosine and 2,4-Dithiouracil. *Inorganica Chimica Acta*, **37**, L235-L237 (1979).
25. Cotton, F.A. & Wilkinson, G. Advanced Inorganic Chemistry A Comprehensive Text. Fourth edition. John Wiley & Sons. USA. (1980).
26. Moreno-Sanchez, J.M. & Sanchez-Sanchez, M.P. Thermal Studies on Purine Complexes. XVI. Thermal Behaviour of Some Metal Complexes of 6-Thioguanine. *Thermochimica Acta*, **144**, 347-356 (1989).
27. Watson, S.M., Wright, N.G., Horrocks, B.R. & Houlton, A. Preparation, Characterization and Scanned Conductance Microscopy Studies of DNA-Templated One-Dimensional Copper Nanostructures. *Langmuir*, **26**, 2068-2075 (2010).
28. Zhang, Y., Zhu, X., Smith, J., Haygood, M.T. & Gao, R. Direct observation and quantitative characterization of singlet oxygen in aqueous solution upon UVA excitation of 6-thioguanines. *The Journal of Physical Chemistry B*, **115**, 1889-1894 (2011).
29. Santhosh, C. & Mishra, P.C. Electronic Structures and Spectra of 6-Mercaptopurine and 6-Thioguanine. *Spectrochimica Acta*, **49A**, 985-993 (1993).
30. Khizhnyak, S.D., Ovchinnikov, M.M. & Pakhomov, P.M. Gel formation in low-concentration aqueous solutions containing N-acetyl-L-cysteine and silver nitrate. *Journal of Structural Chemistry*, **55**, 175-179 (2014).
31. Arulraj, A.D., Devasenathipathy, R., Chen, S.-M., Vasantha, V.S. & Wang, S.-F. Highly selective and sensitive fluorescent chemosensor for femtomolar detection of silver ion in aqueous medium. *Sensing and Bio-Sensing Research*, **6**, 19-24 (2015).
32. Kishimura, A. & Aida, T. Phosphorescent Organogels via "Metallophilic" Interactions for Reversible RGB-Color Switching. *Journal of the American Chemical Society*, **127**, 179-183 (2005).
33. Howard-Lock, H.E. Structures of Gold(I) and Silver(I) Thiolate Complexes of Medicinal Interest: a Review and Recent Results. *Inorganic Chemistry*, **6**, 201-209 (1999).
34. Engelhardt, L.M. & White, A.H. Lewis-base Adducts of Group IB Metal(I) Compounds. Part 12. Structural Studies of Some Bis(methyl-substituted pyridine)-

- copper(I) and -silver(I) Nitrates and Perchlorates. *Journal of the Chemical Society, Dalton Transactions*, 117- 123 (1985).
35. Eberhard, J., Stoll, I., Schmidt, W.G. & Mattay, J. Structural variety of 5-fluoroarene-2-aminopyrimidine in comparison to 2-aminopyrimidine silver(i) coordination polymers: progress report and overview. *CrystEngComm.*, **15**, 4225-4228 (2013).
 36. Li, J.R., Du, W.P., Xu, X.H. & Zhang, R.H. Novel dithioether-silver(I) coordination architectures: structural diversities by varying the spacers and terminal groups of ligands. *Dalton Transactions*, 464-474 (2005).
 37. Bosch, E. One- and Two-Dimensional Silver-Coordination Networks Containing π -Sandwiched Silver–Silver Interactions. *Inorganic Chemistry*, **41**, 2543-2547 (2002).
 38. Dorniani, D., Shaari, A.H. & Ahmad, Z. Preparation and characterization of 6-mercaptopurine-coated magnetite nanoparticles as a drug delivery system. *Drug Design, Development and Therapy*, **7**, 1015-1026 (2013).
 39. Szeghalmi, A.V., Leopold, L., Popp, J. & Kiefer, W. Adsorption of 6-mercaptopurine and 6-mercaptopurine riboside on silver colloid: a pH dependent surface enhanced Raman spectroscopy and density functional theory study. Part I. 6-Mercaptopurine. *Journal of Molecular Structure*, **735-736**, 103-113 (2005).
 40. Selvaraj, V., Alagar, M. & Hamerton, I. Analytical detection and biological assay of antileukemic drug using gold nanoparticles. *Electrochimica Acta*, **52**, 1152-1160 (2006).
 41. Shen, X.C., Lu, X., Zhang, L.J. & Liu, X.Y. Determination of 6-mercaptopurine based on the fluorescence enhancement of Au nanoparticles. *Talanta*, **69**, 456-462 (2006).
 42. Fulara, J. & Nowak, M.J. Theoretical and Infrared Matrix Isolation Study of 4(3H)-Pyrimidinethione and 3(2H)-PyrMazlnethione. Tautomerism and Phototautomerism. *Journal of Physical Chemistry*, **95**, 2404-2411 (1991).
 43. Leszczynski, J. & Nowak, M.J. Infrared experimental and ab initio quantum mechanical studies of 2-mercaptopurine tautomers. *Spectrochimica Acta*, **47A**, 339-353 (1991).
 44. Adamowicz, L. & Nowak, M.J. Theoretical and Matrix-Isolation Experimental Study on 2(1H)-Pyridinethione/2-Pyridinethioil. *Journal of Physical Chemistry*, **94**, 7406-7414 (1990).
 45. Adamowicz, L. & Rostkowska, H. Theoretical and matrix-isolation experimental studies on 2-thiocytosine and 5-fluoro-2-thiocytosine. *Biochimica et biophysica Acta*, **1172**, 239-246 (1993).

46. Mathlouthi, M. & Seuvre, A.M. FTIR and Laser-Raman Spectra of Cytosine and Cytidine. *Carbohydrate Research*, **146**, 1-13 (1986).
47. Rozenberg, M., Shoham, G., Reva, I. & Fausto, R. Low temperature FTIR spectroscopy and hydrogen bonding in cytosine polycrystals. *Spectrochimica Acta Part A: Molecular and Biomolecular Spectroscopy*, **60**, 463-470 (2004).
48. Loofbourow, J.R. & Sinsheimer, R.L. Ultraviolet Absorption Spectra at Reduced Temperatures: II. Pyrimidines and Purines. *Journal of Biological Chemistry*, **187**, 313-324 (1950).
49. Ferraria, A.M., Carapeto, A.P. & Botelho do Rego, A.M. X-ray photoelectron spectroscopy: Silver salts revisited. *Vacuum*, **86**, 1988-1991 (2012).
50. Briggs, D. & Grant, J. Surface Analysis by Auger and X-ray Photoelectron Spectroscopy. IM Publications, Chichester, UK. (2003).
51. Kaushik, V.K. Xps Core Level Spectra and Auger Parameters for Some Silver Compounds. *Journal of Electron Spectroscopy and Related Phenomena*, **56**, 273-277 (1991).
52. Lundwall, M., Rander, T., Svensson, S. & Björneholm, O. Enhanced surface sensitivity in AES relative to XPS observed in free argon clusters. *Surface Science*, **594**, 12-19 (2005).
53. Lundwall, M., Lindblad, A., Svensson, S. & Björneholm, O. Photon energy dependent intensity variations observed in Auger spectra of free argon clusters. *Journal of Physics B: Atomic, Molecular and Optical Physics*, **39**, 3321-3333 (2006).
54. Fenfang, Y. Template-assisted synthesis and assembly of nanoparticles. Chapter 3. PANi/Ag₂S nanocomposites. Thesis, National University of Singapore. (2008).
55. Kibis, L.S., Koscheev, S.V., Zaykovskii, V.I. & Boronin, A.I. The investigation of oxidized silver nanoparticles prepared by thermal evaporation and radio-frequency sputtering of metallic silver under oxygen. *Applied Surface Science*, **257**, 404-413 (2010).
56. Wei, W., Mao, X., Ortiz, L.A. & Sadoway, D.R. Oriented silver oxidenanostructures synthesized through a template-free electrochemical route. *Journal of Materials Chemistry*, **21**, 432-438 (2011).
57. Watson, J.D. The Structure of Tobacco Mosaic Virus. I. X-Ray Evidence of a Helical Arrangement of Sub-Units Around the Longitudinal Axis. . *Biochimica et biophysica Acta*, **13**, 10-19 (1954).

58. Lee, C.C. & Schenning, A.P.J. Preparation and characterization of helical self-assembled nanofiber. *Chemical Society Reviews*, **38**, 671-683 (2009).
59. Douglas, J.F. Theoretical issues relating to thermally reversible gelation by supramolecular fiber formation. *Langmuir*, **25**, 8386-8391 (2009).
60. Huisman, B.A., Bolhuis, P.G. & Fasolino, A. Phase transition to bundles of flexible supramolecular polymers. *Physical Review Letters*, **100**, 188301-188304 (2008).
61. Nasser, N., Boyle, P.D. & Puddephatt, R.J. A complex corrugated sheet structure is formed by self-assembly from the simple building block [Ag(dmsO)]⁺. *Inorganic Chemistry Communications*, **36**, 8-10 (2013).
62. Furberg, S. & Jensen, L. Crystal Structure of Thiocytosine. *Acta Crystallographica Section B*, **26**, 1260-1268 (1970).

Chapter 7. Synthesis and Crystal Structure Determination Complexes of Silver, Copper, and Cobalt with Thioether Purines

Abstract

Ag(I):6-methylmercaptapurineriboside (1) (Ag(I):6-MMPR), Cu(II):6-methylmercaptapurine (2 and 3) (Cu(II):6-MMP), and Co(II):6-methylmercaptapurine (4) (Co(II):6-MMP) were synthesised and characterized using UV-Vis, FTIR, fluorescence spectroscopy, elemental analysis (C.H.N), mass spectroscopy, NMR, fluorescence microscopy, and powder X-ray diffraction. The crystal structure data for $C_{22}H_{28}AgN_9O_{13}S_2$ (1) shows that Ag(I) lies on a crystallographic 2-fold rotation axis and the nitrate anion is loosely coordinated as a bidentate ligand in a discrete molecular complex. The complex and water molecules are connected by hydrogen bonding. The X-ray data revealed that the crystal of $C_{12}H_{12}N_8S_2Cl_4Cu_2$ (2) is triclinic, the structure is a partial methanol solvate, the methyl group and subsequently one proton bonded to nitrogen have been modelled as disordered over two positions. A dimeric Cu(II):6-MMP complex with proposed formula $C_{12}H_{12}Cu_2N_8O_2S_2$ (3) with 2:2 metal to ligand M_2L_2 stoichiometry was also isolated. X-ray data for $C_{12}H_{22}N_8S_2O_6Co$ (4) shows that the compound has monoclinic crystal system with an extensive 3D hydrogen bonding network.

7.1 Introduction

6-Thiopurines, which are derivatives of purine show antitumor activity¹⁻³ and for this reason the current studies are shedding light on these unnatural compounds to understand the coordination site and the bonding of metal ions in the purine complexes. In fact, the presence of multiple binding sites at the nucleobases and nucleosides compounds make these materials have special interesting as ligands towards numerous metal ions which give arise to obtain variable structures according to the site of coordination.^{4,5} The diversity of structure in these metal complexes has led to interest in various in different fields, *e.g.* luminescence,^{6,7} electronics,⁸ catalysis,⁹ gas adsorption,¹⁰ in addition to the pharmaceutical applications.¹¹⁻¹⁴ 6-methylmercaptapurine riboside (6-MMPR) is strong specific inhibitor of protein kinase N (PKN) and the activity of nerve growth factor (NGF).^{15,16} It was observed that 6-MMPR affects at the formation and conservation blood vessel.¹⁶ Hepatotoxicity was seen in patients who have very low concentration of 6-MMPR.¹⁷ 6-MMP is formed¹⁸ in patients who are suffering from leukaemia. Using oral dosing of the drug 6-mercaptopurine (6-MP), the metabolism of 6-MP that occurs in the liver by methyltransferase (TPMT) was shown to lead to leads to formation

of 6-MMP. The common metal binding site in purine is N7, however, N3 is a rare binding site,¹⁹⁻²¹ Houlton²² was able to prepare Na^+ and K^+ complexes with 9-ethyl adenine that attached to 18-aza-crown at the position of the deoxy ribose ring and he found that the coordination of the metal ions to the ligand was occurred via N3. The same researcher later, investigated the effect of 2-amino group at the orientation of metal ions towards binding at N3-position of purine.²³ He found that Cu(I) and Ag(I) bind to dithioether-derivatives of adenine via N3. M^+ bound to adenine (where M includes Li^+ , Na^+ , K^+ , and Cs^+) was investigated by Rajabi,²⁴ who found that this group of metal ions coordinate via N3 and N9. A dimeric adenine copper complex was synthesised²⁵ with a ligand to metal stoichiometry of 2:1, and the crystal structure was determined by Sletten,²⁶ who found that copper was binding via N9 and N3 and formed a chelating ring with Cu(II). Further study of magnetic properties of this compound were reported by Goodgame.²⁷ A distorted trigonal bipyramidal Cu(II) complex was prepared with 6-(2-chlorobenzylamino) purine by Marek;²⁸ in this complex, Cu ion adopted a penta coordinated geometry with two molecules of the ligands and three chloride ions, coordination Cu ion to the ligands molecules was occurred via N9 atoms.

Many complexes²⁹⁻³¹ were reported by the reaction of aliphatic or aromatic thioethers with metal ions; for example, the reaction of thianthrene (TA) with AuCl_3 in the presence of liquid SOCl_2 .³² The product of this reaction was a black crystalline compound of dichloridobis(thianthrene) gold(+1) tetrachloridoaurate(-1) with square planar geometry. The asymmetric unit showed that two cations $[\text{AuCl}_2(\text{TA})_2]^+$ and two inions $[\text{AuCl}_4]^-$ were located on inversion centres, and crystallographic *Ci* symmetry was resulted for all cations and anions. Fig. 7.1.

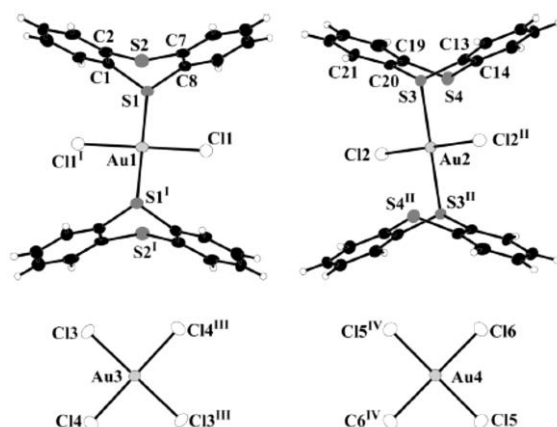


Figure 7.1. Structure of two cation $[\text{AuCl}_2(\text{TA})_2]^+$ and two inion $[\text{AuCl}_4]^-$ that prepared by Tjahjanto³².

Using an aliphatic thioether, Houlton³³ synthesised a Cu(I) complex. In this complex, the Cu(I) ion coordinated with (1-(N9-adenine)-3,6-dithiaheptane) via four S atoms to form Cu(I) complex which contains two adeninyl residues, Fig. 7.2.

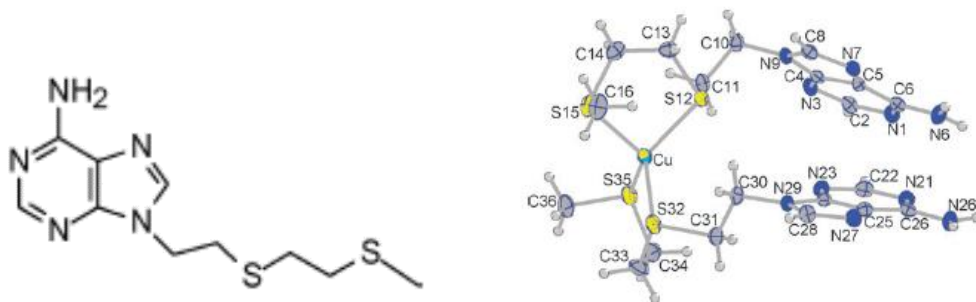


Figure 7.2. Showing: a) the ligand of (1-(N9-adenine)-3,6-dithiaheptane, and b) the Cu(I) complex that prepared with ligand (a) by Houlton.³³

No reports were found concerning the reaction of metal ions with 6-MMPR, while for 6-MMP, the complex of Zn:6-MMP was very recently prepared by Perea-Cachero,³⁴ Fig. 7.3. This complex has a polymeric structure of two dimensions with two Zn atoms which act as bridges between the molecules of the ligands via N atoms at the positions N9 and N7.

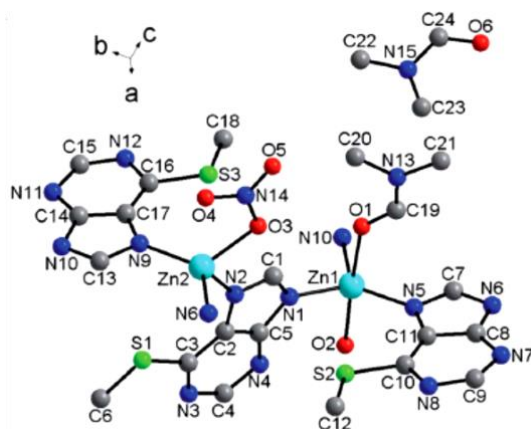


Figure 7.3. Crystal structure of $[Zn_2(6-MMP)_3(NO_3)(DMF)(H_2O)]_n \cdot nDMF$.³⁴

The work in this chapter presents the reaction of silver, copper, and cobalt ions with thio ether purines derivatives.

7.2 Experimental

7.2.1 Synthesis silver (I):6-methylmercaptapurine riboside

The solution of AgNO_3 (0.0569 g, 0.0335 mmol in 400 μL MeOH and 1.6 ml H_2O) was added to the warm solution of 6-MMPR (0.1 g, 0.0335 mmol, which was prepared by dissolving the 6-MMR in 2 mL DMSO, 2 mL MeOH, and 4 mL H_2O). After 5 min, small white crystals formed, the solution was left in dark for 3h then the crystals were isolated by filtering, washed with water and dried by air. The product was re-crystallised from 1:1 MeOH: H_2O then filtered and dried again by air (yield 0.075 g with respect to the ligand, 75%). Observation under microscope showed a regular, thick, and rectangular crystals. The crystals were examined by X-ray diffraction, UV-Vis, FTIR, NMR, mass spectra, and elemental analysis (C.H.N).

7.2.2 Synthesis of copper(II):6-methylmercaptapurine nucleobase $\text{C}_{12}\text{H}_{12}\text{N}_8\text{S}_2\text{Cl}_4\text{Cu}_2$ (2) and $\text{C}_{12}\text{H}_{12}\text{Cu}_2\text{N}_8\text{O}_2\text{S}_2$ (3)

Two methods can be used to prepare this compound with mole ratios (ligand to metal) of 1:4 and 1:2 as descibed below:

- 1- An olive-green $\text{C}_{12}\text{H}_{12}\text{N}_8\text{S}_2\text{Cl}_4\text{Cu}_2$ complex was prepared with 4:1 mole ratio metal to ligand by adding, with stirring, $\text{CuCl}_2 \cdot 2\text{H}_2\text{O}$ solution (0.209 g, 1.197 mmol in 200 μL MeOH and 800 μL H_2O) to a hot solution of 6-MMP (0.05 g, 0.3008 mmol in 4 ml MeOH). A further 2 ml of MeOH was added to the mixture and an olive-green precipitate formed after 2 min. The solution was heated and stirred for 5 min, then left to stand and afterwards filtered, washed with MeOH and dried under vacuum at 45°C for 2h (yield 0.04 g with respect to the ligand, 80%).
- 2- The complex can be prepared with mole ratio 2:1 metal to ligand by using the same metal salt and the ligand, and the same procedure was applied. An olive-green precipitate was formed, however after 10 min a blue precipitate began to form as a second layer over the olive-green precipitate. To avoid forming a mixture of precipitates, the olive-green precipitate was separated by filtration immediately after formation and washed with MeOH several times. The blue precipitate was isolated by filtration after its formation and washed with MeOH. Observing the morphology of olive-green and blue crystals under an optical microscope showed a rhombus and cuboid habit which indicates formation of two different kinds of complexes.

To avoid forming a mixture of blue and olive-green crystals, the 4:1 mole ratio for metal to ligand was adopted to prepare one kind of crystal that is the olive-green crystal of Cu(II):6-MMP (procedure 1).

7.2.3 Synthesis of cobalt (II): 6-methylmercaptapurine $C_{12}H_{22}N_8S_2O_6Co$ (4)

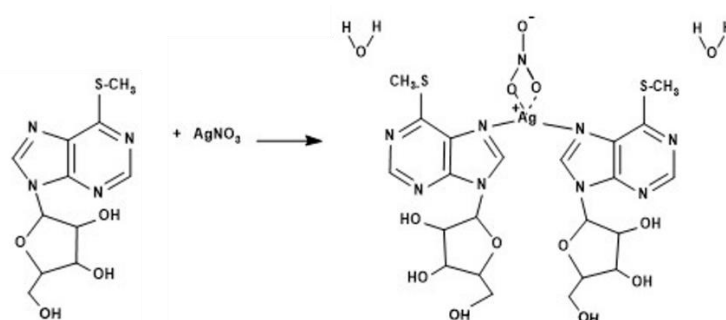
$CoCl_2 \cdot 6H_2O$ (0.0357 g, 0.03 mmol in 0.5 mL H_2O and 2 ml methanol) was added with mixing to a hot solution of 6-MMP (0.05 gm, 0.06 mmol in 10 ml methanol). A pink solution was formed at once. The mixture was heated with stirring for 5 min, and the resulting solution was left to cool at room temperature to crystallize. After one week, pink crystals suitable for X-ray diffraction were formed by slow evaporation.

7.3 Results & Dissociation

7.3.1 Silver:6-methylmercaptapurine riboside $C_{22}H_{28}AgN_9O_{13}S_2$ (1) (Ag:6-MMPR)

7.3.1.1 Synthesis of $C_{22}H_{28}AgN_9O_{13}S_2$ (1)

The reaction of $AgNO_3$ and 6-methylmercaptapurine riboside in mixed solvents of DMSO, MeOH, and H_2O leads to prepare a distorted tetrahedral silver complex. Scheme 7.1 shows the chemical reaction route. FTIR spectroscopy, UV-Vis, elemental analysis, mass spectra, and X-ray diffraction were used to characterize the structure of the complex.



Scheme 7.1 Chemical reaction for synthesis silver:6-methylmercaptapurine riboside (Ag:6-MMPR).

7.3.1.2 FTIR spectroscopy characterization of $C_{22}H_{28}AgN_9O_{13}S_2$ (1)

The stretching mode that belongs to C-S^{35,36} band was found in both the spectra of the ligand (632 cm^{-1}) and the complex (624 cm^{-1}) and this confirms no binding was occurred via S, the small different in the frequency (8 cm^{-1}) can be assigned to the changes in bond force constant at the vibrations that occurs upon coordinating with the metal ion, Fig. 7.4. On the other hand, the new stretch mode at 1296 cm^{-1} in the complex can be assigned to the N-O vibrations of a

nitrate-silver moiety.^{37,38} Perturbation of the nitrate ion spectrum is indicated by the two bands (1296 cm^{-1} and 1381 cm^{-1}) that result from splitting the antisymmetric N-O stretching modes.³⁸⁻⁴⁰ The other new band at 516 cm^{-1} in the complex can be assigned to a symmetric Ag-N stretching bands,³⁷ the Ag-N band has two stretching bands symmetric (usually can be found in 380 cm^{-1}) and asymmetric (between $430\text{--}500\text{ cm}^{-1}$).^{36,41,42} The stretching mode of C=N at 1442 cm^{-1} in the ligand is shifted to higher frequency in the complex (1450 cm^{-1}) which suggests the involvement of metal ion coordination at N7. The band observed (3741 cm^{-1})⁴³⁻⁴⁶ is due to the presence of the free-associated water molecules. The bending^{47,48} mode of H_2O can be seen around at 1660 cm^{-1} .

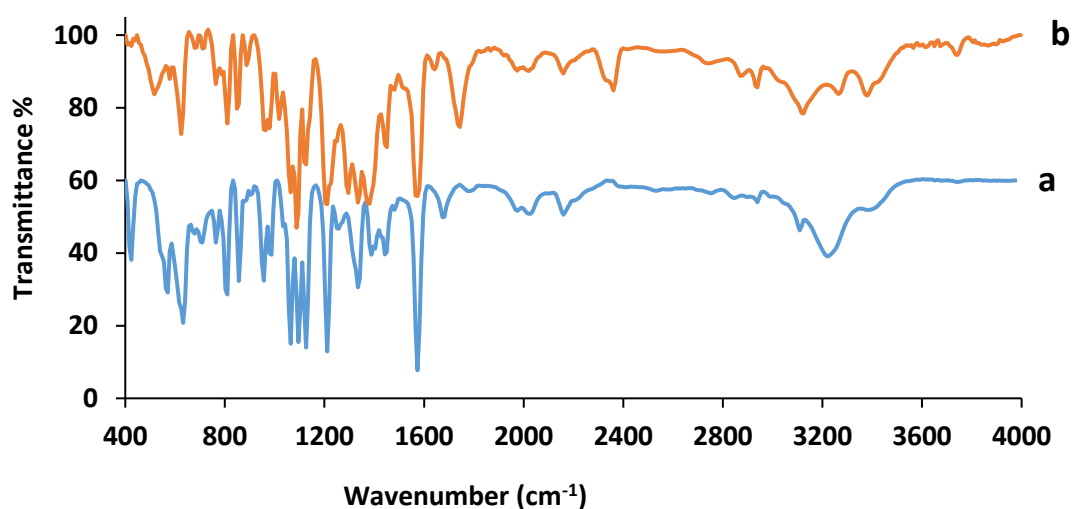


Figure 7.4. Comparison between FTIR spectra of: (a) 6-methylmercaptopurine riboside and (b) Ag:6-MMPR complex.

7.3.1.3 Ultraviolet-Visible (UV-Vis) characterization

The spectrum of the 6-methylmercaptopurine riboside(6-MMPR) nucleoside in methanol in Fig. 7.5 showed a band at 290 nm ^{49,50} attributed to $\pi\text{--}\pi^*$ transitions. A similar band was observed in the complex indicating that only small perturbations of the π system occur as a result of the reaction of Ag(I) with the 6-MMPR.

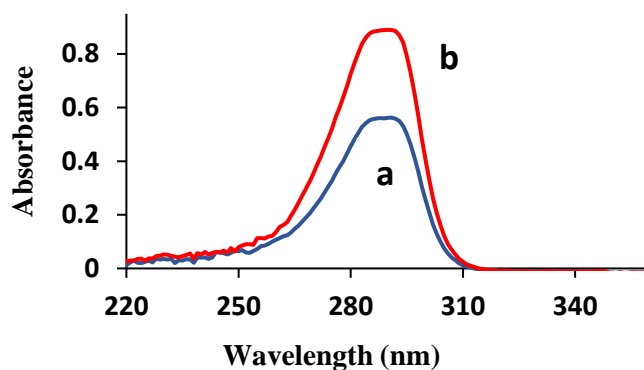


Figure 7.5. Comparison UV-Vis spectra between: a) 6-methylmercaptopurine riboside (6-MMPR), and b) Ag: 6-MMPR in methanol.

7.3.1.4 X-ray diffraction (XRD) characterization for $C_{22}H_{28}AgN_9O_{13}S_2$ (I)

The crystal structure data (obtained by X-ray diffraction) shows that Ag(I) lies on a crystallographic 2-fold rotation axis and the nitrate anion is loosely coordinated as a bidentate ligand to give a discrete molecular complex. These molecules and water molecules are connected by hydrogen bonding. The Ag-N7 distance was 2.153 Å, and Ag-O was 2.627 Å, this data was a good agreement with distorted tetrahedral geometry of Ag(I) complexes.^{51,52} Fig. 7.6 displays the crystal structure of Ag(I):6-MMPR.

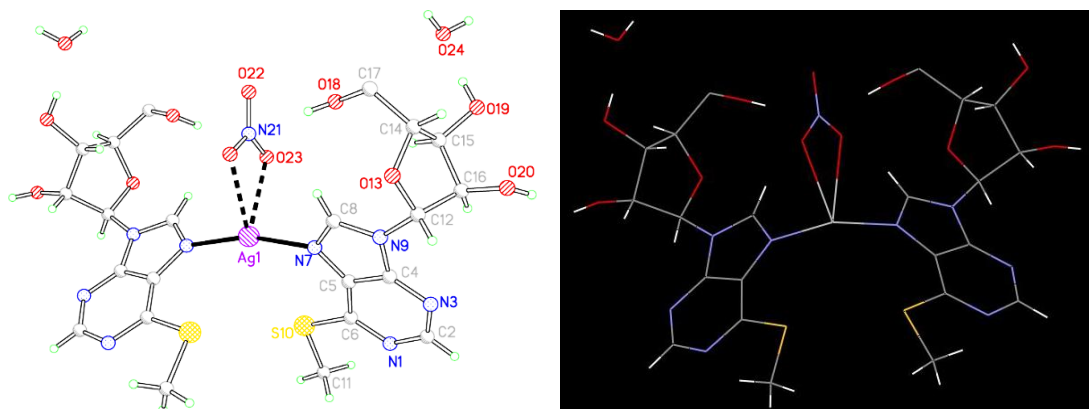


Figure 7.6. Molecular structure of Ag:6-methylmercaptopurine riboside (Ag:6-MMPR).

7.3.1.5 Elemental analysis (C.H.N)

Elemental analysis (C.H.N) for Ag:6-MMPR was used to further confirm the structure, the sample was tested on a Carlo Erba 1108 Elemental Analyser controlled with CE Eager 200 software, run in accordance with the manufacturer's instructions and weighed using a certified Mettler MX5 Microbalance. The C.H.N analysis indicated Ag:6-MMPR complex with formula

$C_{22}H_{28}AgN_9O_{13}S_2$ to have 2:1 ligand-metal stoichiometry, theoretical: C 33.06 %, H 3.50 %, N 15.77%, Found: C 32.96 %, H 3.23 %, N 15.75 %. Table 7.1 presents the data.

Table 7.1. Elemental analysis of Ag:6-Methylmercaptopyruvate riboside.

Element	% Theoretical	% Found
C	33.06	32.96
H	3.50	3.23
N	15.77	15.75

7.3.1.6 Crystal morphology characterization

Optical microscopy was used to examine the morphology of the Ag:6-MMPR crystal formed by coordinating Ag(I) with 6-MMPR. The optical image with scale bar 10 μm showed that the crystals are long, regular, colourless, and ‘ruler shaped’ as shown in Fig. 7.7 (a). Further investigation of the sample was carried out with scanning electron microscopy (SEM); a large scan SEM image (50 μm) displayed with more clearly the arrangement of the crystal as shown in Fig. 7.7(b). It is apparent from these images that the crystals have a highly uniform shape.

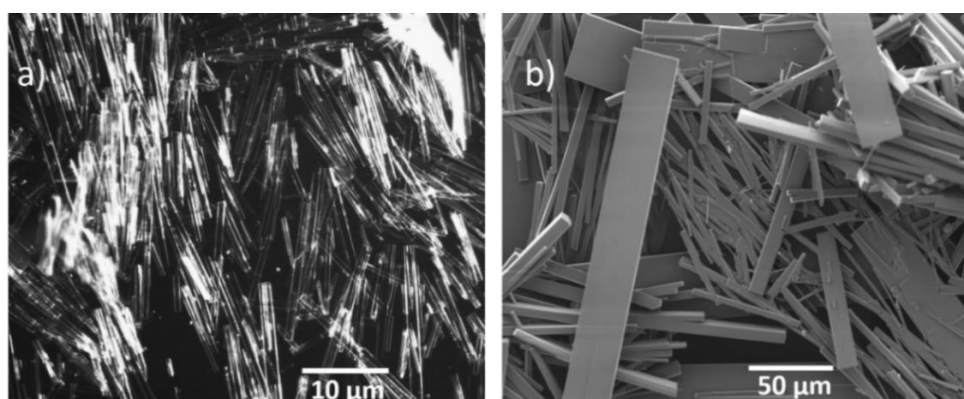


Figure 7.7. Showing: a) optical microscope image of Ag:6-MMPR showing the regular colourless ruler-like crystal, the size of the crystal examined by X-ray diffraction was $0.060 \times 0.020 \times 0.010 \text{ mm}^3$, b) SEM image of Ag:6-MMPR crystal.

7.3.1.7 Mass spectra characterization

ESI-MS (positive mode) was carried out at Sheffield University for Ag(I):6-MMPR with formula $[C_{22}H_{28}AgN_8O_8S_2]$ in acetonitrile revealed m/z : [M] 703.3138, (calculated:704.0151). Fig. 7.8 displays the spectrum.

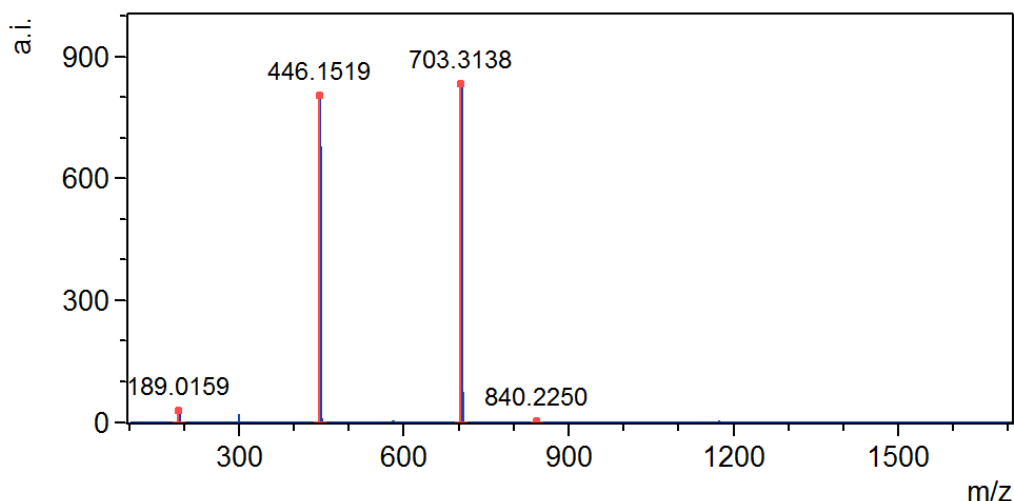
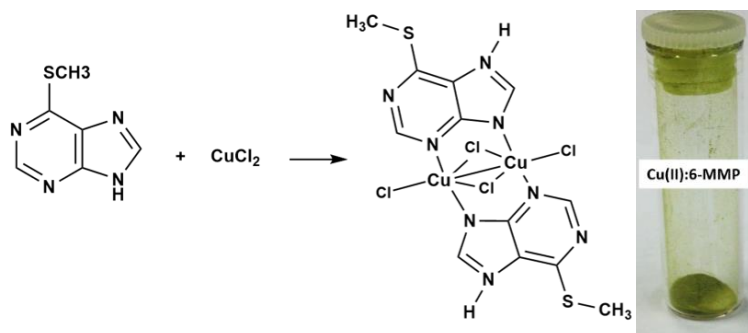


Fig. 7.8. ESI-MS (positive mode) for Ag(I):6-MMPR with formula $[C_{22}H_{28}N_8O_8S_2Ag]$ in acetonitrile.

7.3.2 Copper:6-methylmercaptapurine $C_{12}H_{12}N_8S_2Cl_4Cu_2$ (2)

7.3.2.1 Synthesis of $C_{12}H_{12}N_8S_2Cl_4Cu_2$ (2)

The reaction of 6-methylmercaptapurine with $CuCl_2 \cdot 2H_2O$ in methanol leads to prepare octahedral coordination complex $C_{12}H_{12}N_8S_2Cl_4Cu_2$ (2). In this complex two nucleobases coordinate to two metal ions centres by N3 and N9 atoms in a dimeric mode. Scheme 7.2 shows the route to prepare the olive- green and a photograph of the solid.



Scheme 7.2. Reaction route for synthesis of the olive-green complex of copper:6-methylmercaptapurine (Cu(II):6-MMP) with stoichiometry 2:2 ligand to metal (M_2L_2).

7.3.2.2 FTIR spectroscopy characterization of $C_{12}H_{12}N_8S_2Cl_4Cu_2$ (2)

The two stretching modes that belongs to $N-H^{53}$ at 2800 cm^{-1} and 2993 cm^{-1} in the spectrum of the ligand, Fig. 7.9, were shifted to higher frequency (2970 cm^{-1} and 3093 cm^{-1} , respectively) in the complex. This indicates that N atoms participate in the coordination of the metal.⁵⁴ A new broad band at 3495 cm^{-1} can be seen in the spectrum of the complex and this assigned to the O-H group⁵³ of methanol that was used as solvent. The proton of this group was binding to

N7 atoms at two positions of the dimer leading to form disordered model; this band was not found in the spectrum of the ligand before complexation with Cu ions. Furthermore, the stretching mode that belongs to C=N⁵⁵ at 1550 cm⁻¹ at the ligand was shifted⁵⁶ to 1597 cm⁻¹ after coordination with Cu ions and this can be attributed to take part the N atoms in the complexation. The band at 547 cm⁻¹ in the spectrum of the complex can be assigned to the stretching mode Cu-N.⁵⁶⁻⁵⁹

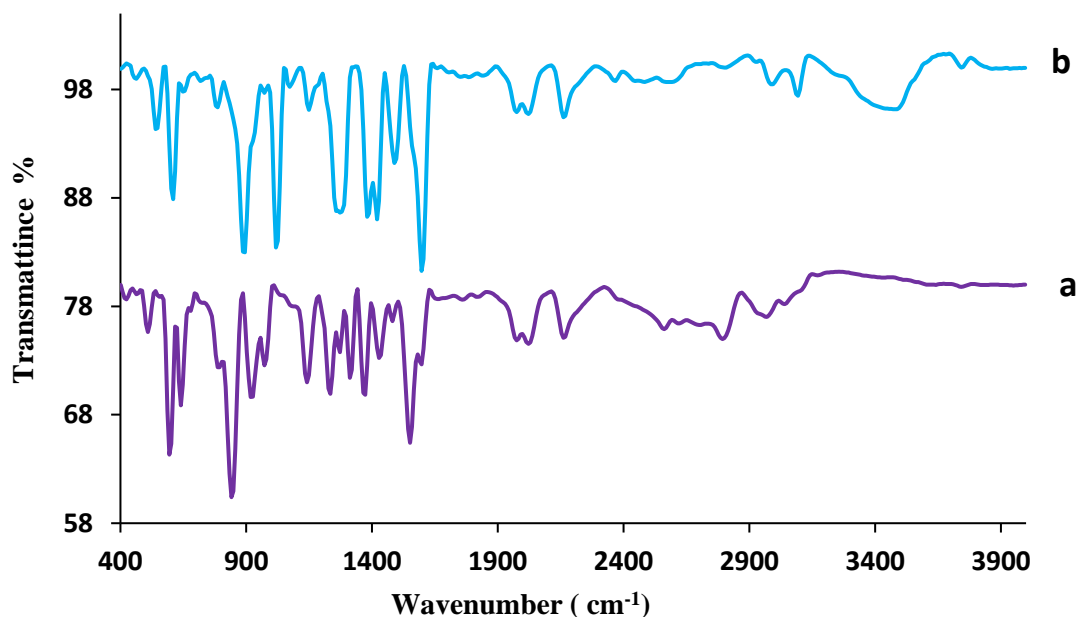


Figure 7.9. Comparison the FTIR spectrum of: (a) 6-methylmercaptopurine (6-MMP) and (b) olive-green Cu(II):6-MMP complex.

It is worthwhile to note here that, in this complex, Cu(II) does not bind to S6 atom that substituted with methyl group and it preferred to bind via N3 and N9 instead. This is in contrast with the Cu(I) tetrahedral complex that was synthesised by Houlton,³³ where the Cu(I) ion was coordinating with (1-(N9-adenine)-3,6-dithiaheptane) via S atoms.

7.3.2.3 Ultraviolet-Visible (UV-Vis) characterization of $C_{12}H_{12}N_8S_2Cl_4Cu_2$ (2)

The absorption spectrum of the ligand 6-methylmercaptopurine (6-MMP) in DMF revealed a single band at 292 nm which can be assigned to $\pi-\pi^*$ transitions. Upon coordinating Cu ions, this band is slightly shifted and a tail at a longer wavelength appears, but there is also a new band at lower energy (435 nm) in the spectrum of olive-green Cu(II):6-methylmercaptopurine (Cu(II):6-MMP) complex in DMF. It is suggested that this band can be assigned to a ligand-to-metal charge transfer (LMCT) transitions.^{60,61} It may also contain Cl \rightarrow Cu transitions,^{28,62}

however LMCT transitions from chloride to copper has been reported to be weak.⁶³ Fig. 7.10 shows the absorption spectra for the ligand and the complex.

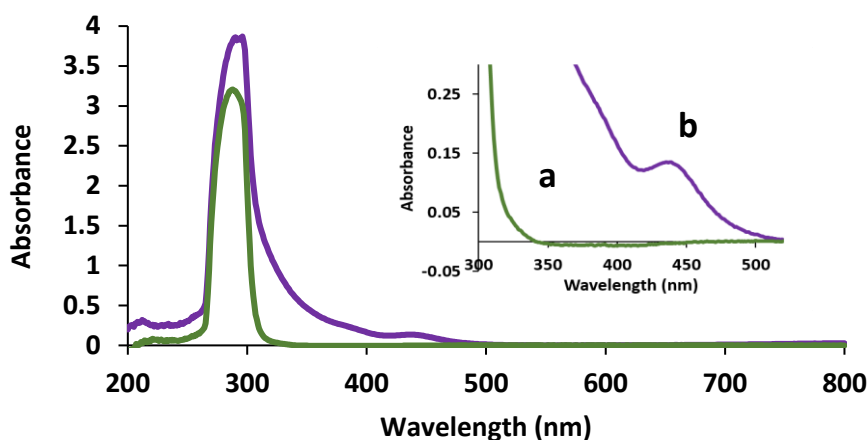


Figure 7.10. Comparison UV-Vis absorption spectrum between: a) 6-methylmercaptopurine (6-MMP), and b) Cu(II): 6-MMP in DMF.

7.3.2.4 X-ray diffraction (XRD) characterization for $C_{12}H_{12}N_8S_2Cl_4Cu_2$ (2)

Investigation of the olive-green crystal of Cu(II):6-MMP by synchrotron radiation revealed that the system of the crystal is triclinic and the compound consists of a dimer of two Cu ions and two ligands. Each ligand is connected to Cu atom via N9 and N3, in addition, each atom of Cu is bound to two chloride ions and there is bridge bond between the two copper atoms. The resulting geometry is a distorted octahedral coordination for both Cu atoms. It is worthwhile to observe here that, deprotonation occurred to N9 after the complexation and the proton transferred to N7. The data revealed that the bond length of Cu-Cu atoms is 2.9124 Å and this agree with the literature.^{26,64-67} Cu-Cl₁ bond distance was 2.36 Å and Cu-Cl₂ was 2.25 Å and these distances were in a good agreement with the literature.^{4,68,69} While Cu-N3 and Cu-N9 distances were 2.00 Å and 1.981 Å, respectively.⁷⁰ Fig. 7.11 presents the crystal structure without (left) and with (right) methanol of solvation.

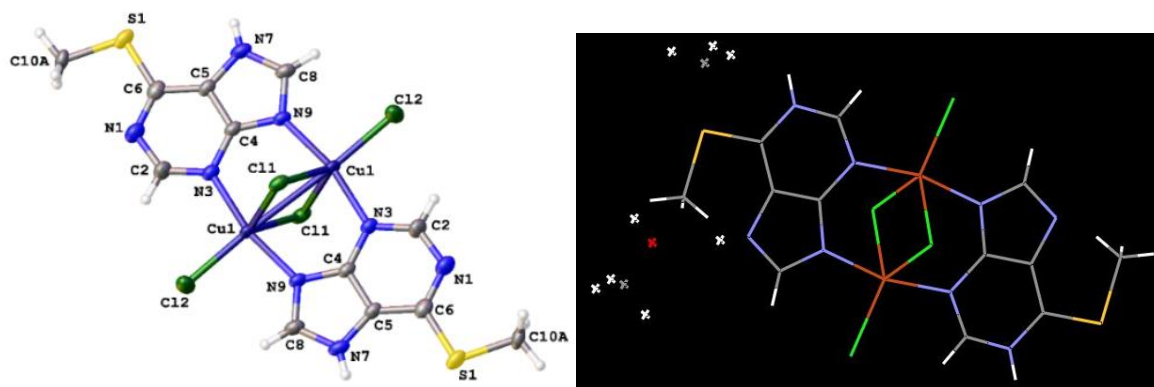


Figure 7.11. Molecular structure of olive Cu(II):6-MMP with (right) and without (left) solvent molecules of methanol.

7.3.2.5 Elemental analysis (C.H.N)

Elemental analysis (C.H.N) for olive Cu(II):6-MMP with formula $C_{12}H_{12}N_8S_2Cl_4Cu_2$ was carried out at the School of Human Sciences, Metropolitan University, London to address further structure characterisation. The data indicated that the complex olive Cu:6-MMP has the expected 2:2 ligand-metal stoichiometry M_2L_2 , theoretical: C 23.97 %, H 2.01 %, N 18.63 %, found: C 23.98 %, H 2.08 %, and N 18.3 %. This data was a good agreement with data from X-ray diffraction. Table 7.2 shows the data.

Table 7.2 Elemental Analysis of olive Cu(II):6-Methylmercaptopyrurine.

Element	% Theoretical	% Found
C	23.97	23.98
H	1.99	2.08
N	18.63	18.3

7.3.2.6 Mass spectra characterization

Matrix-assisted laser desorption and ionization time-of-flight mass spectrometry (MALDI-TOF-MS) with matrix HCCA (α -Cyano-4-hydroxycinnamic acid) that carried out at Sheffield University for the olive-green Cu(II):6-MMP with formula $[C_{12}H_{12}N_8S_2Cl_4Cu_2]$ in acetonitrile revealed m/z (positive mode) data for $[C_{12}H_{12}N_8S_2Cl_4Cu_2 + 2Na + H]^+$ 648.003, (calculated 647.9545), Fig. 7.12 shows the spectrum.

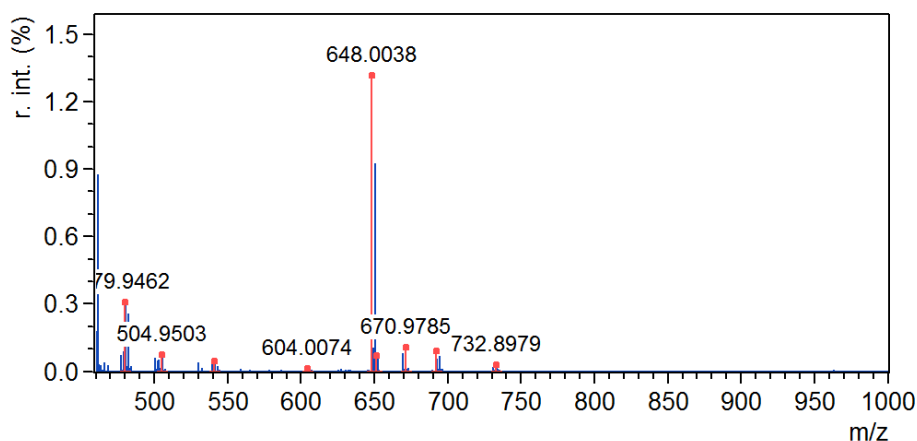


Fig. 7.12. Matrix-assisted laser desorption and ionization time-of-flight mass spectrometry (MALDI-TOF-MS) in acetonitrile carried out with matrix HCCA (α -Cyano-4-hydroxycinnamic acid for the olive-green Cu(II):6-MMP with formula $[\text{C}_{12}\text{H}_{12}\text{N}_8\text{S}_2\text{Cl}_4\text{Cu}_2 + 2\text{Na} + \text{H}]^+$.

7.3.2.7 Crystal morphology characterization

The optical and SEM images that obtained for Cu:6-MMP complexes show two different types of morphology owing to the presence of either chloride or water in the complex. As mentioned in the experimental section for the synthesis of Cu:6-MMP, there are two possibilities to prepare this compound depending on the mole ratio used. First by using 1:2 mole ratio ligand-metal which gives a mixture of blue and olive-green crystals of Cu(II):6-MMP, and second, using 1:4 mole ratio ligand-metal and this method produces only the olive-green compound of Cu(II):6-MMP. Fig. 7.13 displays the optical (a) and SEM image (b) of olive-green Cu(II):6-MMP and blue Cu(II):6-MMP, respectively, one can see with more clearly the difference at the morphology between the two complexes.

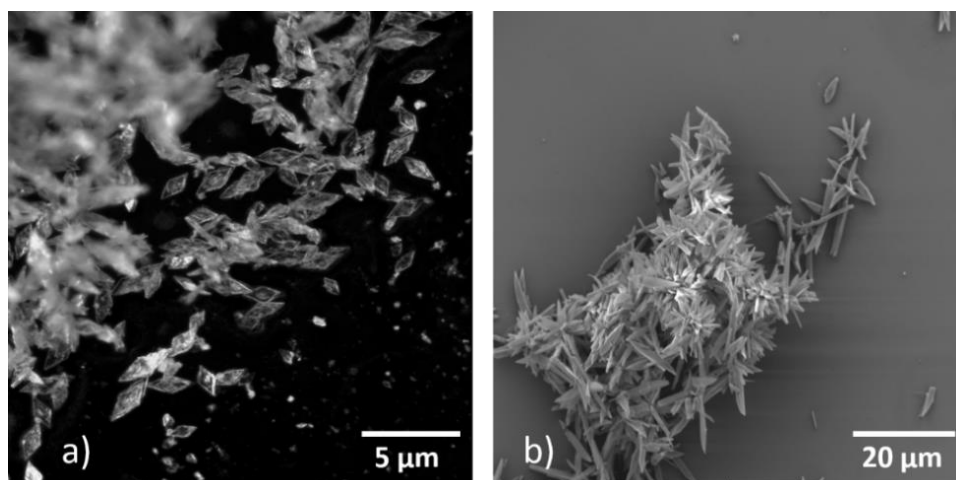
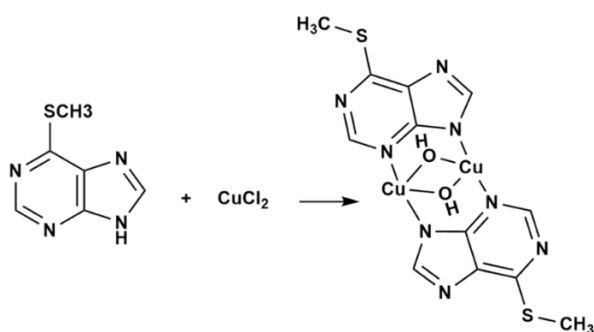


Figure 7.13. Shows: a) fluorescence microscopic images of rhombus crystal structure of olive Cu(II):6-methylmercapto purine, b) SEM image of blue Cu(II):6-methylmercapto purine.

7.3.3 Copper:6-methylmercaptapurine $C_{12}H_{12}Cu_2N_8O_2S_2$ (3)

7.3.3.1 Synthesis of $C_{12}H_{12}Cu_2N_8O_2S_2$ (3)

The reaction of $CuCl_2 \cdot 2H_2O$ with 6-methylmercaptapurine with mole ratio 1:2 ligand to metal afforded a blue Cu(II) complex. The proposed structure for this complex with proposed formula $C_{12}H_{12}Cu_2N_8O_2S_2$ (3) is presented in Scheme 7.3. The two Cu(II) ions are probably coordinated by two hydroxyl groups, this proposal is consistent with the literature precedent for dimeric blue Cu(II) complexes which have a Cu-O-Cu⁷¹⁻⁷⁵ bridge and adopt tetragonal geometry.^{72,73}



Scheme 7.3. Route reaction and proposed structure for synthesis blue Cu(II):6-MMP.

7.3.3.2 FTIR spectroscopy characterization $C_{12}H_{12}Cu_2N_8O_2S_2$ (3)

The spectrum of $Cu_2L_2(OH)_2$ (3) in Fig. 7.14 displays a new band at 3425 cm^{-1} , this band which belongs to the stretching mode of OH group^{56,76,77} was not found in the spectrum of the ligand, and this suggests the presence of OH group in the complex. In addition, the OH bending (in plane) and OH bend (out of plane)⁷⁷⁻⁷⁹ which are in ranges of $1330\text{--}1430\text{ cm}^{-1}$ and $650\text{--}770\text{ cm}^{-1}$, respectively, were found in the complex at frequencies 1396 cm^{-1} and 687 cm^{-1} , respectively, and this also suggests the presence of OH in the complex. The band that can be seen in the ligand at 1550 cm^{-1} which belongs to $C=N$ ⁵⁵ was shifted to higher frequency⁵⁶ (1573 cm^{-1}) as a strong band in the complex and this suggested that Cu ion was binding via N atom. The band at 447 cm^{-1} in the complex can be assigned to the Cu-O bond,^{59,77,80} while the Cu-O band which is related to hydroxy-bridge copper can be observed at 540 cm^{-1} , most copper complexes that has hydroxy bridge displays this band in this frequency.^{77,81} The stretching mode Cu-N⁵⁶⁻⁵⁹ can be seen at 540 cm^{-1} .

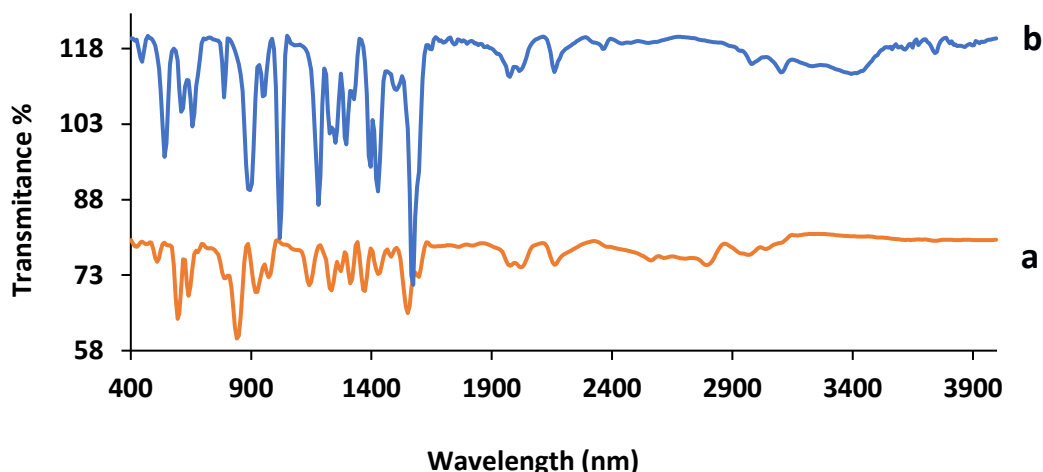


Figure 7.14. Comparison the FTIR spectrum of: (a) 6-methylmercaptapurine (6-MMP) and (b) blue Cu(II):6-MMP complex.

7.3.3.3 Ultraviolet-Visible (UV-Vis) characterization

The optical absorbance spectrum of blue Cu(II):6-MMP in DMF showed formation a new weak band at 628 nm, this band can be assigned to *d-d* absorption which is usually forms at very low energy for Cu(II) complexes.⁸² The *d-d* transitions in this complex are related to geometry of tetragonal of Cu(II) complexes.^{72,73} Fig. 7.15 displays the absorbance spectra of the ligand 6-MMP and the blue Cu(II) complex showing with more clearly the difference at the absorbance between the two compounds.

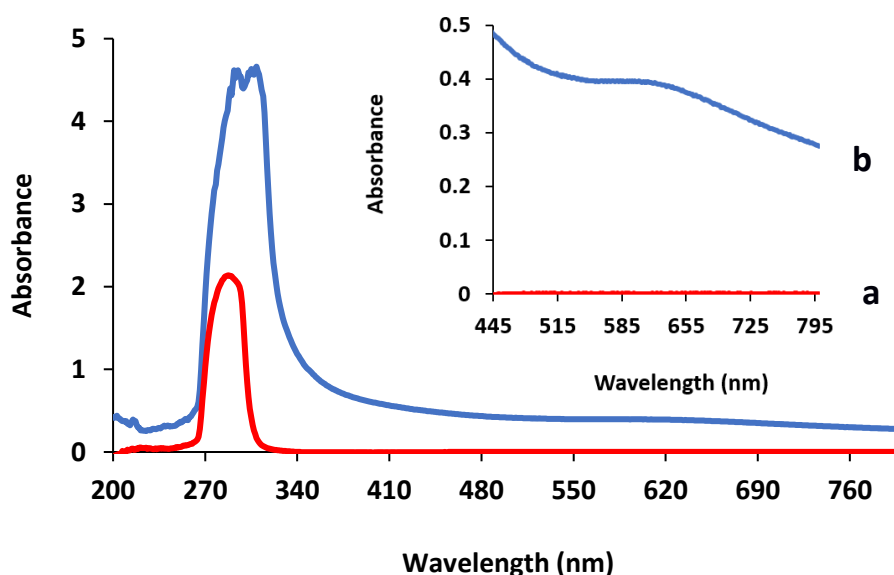


Figure 7.15. Comparison UV-Vis absorption spectrum of: a) 6-methylmercaptapurine (6-MMP), and b) blue copper (II) 6-methylmercaptapurine (Cu(II): 6-MMP) in DMF.

7.3.3.4 Elemental analysis (C.H.N)

The elemental analysis data (C.H.N) for blue Cu(II):6-MMP complex in Table 7.3 below, revealed a good agreement with the theoretical data for the proposed formula $C_{12}H_{12}Cu_2N_8O_2S_2$ (3) (calculated mass: 491.1450), and this suggests that the complex is a dimer with stoichiometry $M_2:L_2$ obtained by coordinating two molecules of the ligand 6-MMP to two Cu(II) atoms via N9 and N3 alongside participation of two ions of hydroxyl coordinated to each atom of copper.

Table 7.3 Elemental Analysis of blue Cu(II): 6-Methylmercaptopyrrole.

Element	% Theoretical	% Found
C	29.31	30.39
H	2.44	2.95
N	22.80	22.76

7.3.3.5 Mass spectroscopy characterization

The ESI-MS (positive mode) for blue Cu(II) complex with proposal formula $C_{12}H_{10}Cu_2N_8S_2$ (3) in acetonitrile displayed m/z $[M + Na + H]^+$ 481.2152, (calculated: 481.1372). Fig. 7.16 shows the spectrum.

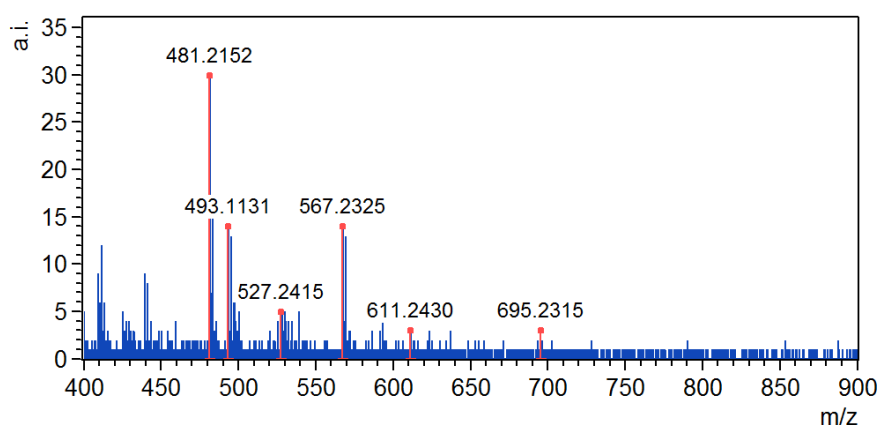
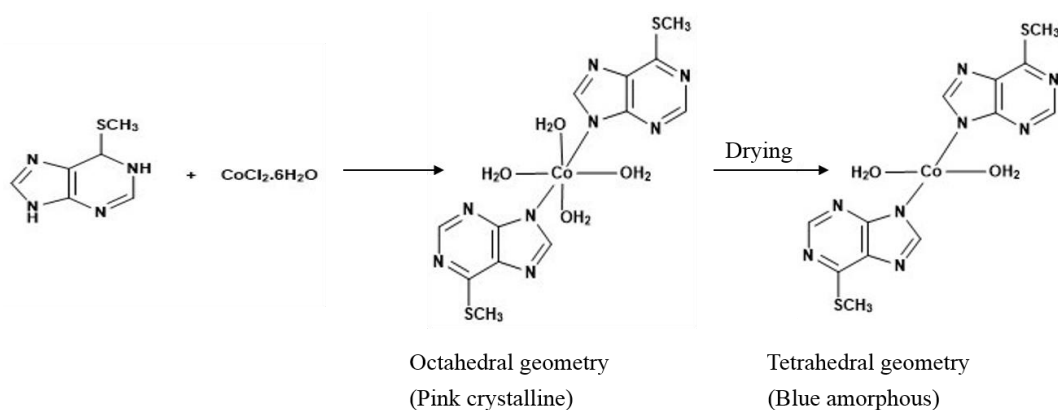


Fig. 7.16. ESI-MS (positive mode) for $[C_{12}H_{10}Cu_2N_8S_2 + Na + H]^+$ in acetonitrile.

7.3.4 Cobalt:6-methylmercaptapurine $C_{12}H_{22}N_8S_2O_6Co$ (4)

7.3.4.1 Synthesis of $C_{12}H_{22}N_8S_2O_6Co$ (4)

The reaction of $CoCl_2 \cdot 6H_2O$ with 6-Methylmercaptapurine in methanol with stoichiometry ligand to metal 2:1 leads to synthesis pink-coloured crystal of octahedral coordination complex of $C_{12}H_{22}N_8S_2O_6Co$ (4). In this complex, two nucleobases coordinate to the $Co(II)$ ion by N9 atoms in a monodentate mode. Drying the pink compound in $60^\circ C$ for 2h in vacuo leads to formation of an amorphous blue compound. The change of the colour and loss of crystallinity upon heating can be assigned to the conversion in the geometry of the pink complex from octahedral to tetrahedral geometry⁸³⁻⁸⁵ with formula $C_{12}H_{14}CoN_8O_2S_2$ (5). Scheme 7.4 displays synthetic route.



Scheme 7.4. Reaction route for synthesis of $Co(II)$:6-MMP complexes with two geometries octahedral (pink, crystalline) and tetrahedral (blue, amorphous).

7.3.4.2 FTIR spectroscopy characterization $C_{12}H_{14}CoN_8O_2S_2$ (5)

FTIR characterization was carried out on the blue $Co(II)$ complex with tetrahedral geometry which resulted from drying the hydrated crystalline pink octahedral complex. The bending mode at 1550 cm^{-1} that belongs to N-H band⁸⁶ in the spectrum of the ligand was shifted to 1612 cm^{-1} in the complex; this suggests that binding was occurred via N atom. On the other hand, this bending^{47,48} mode in the spectrum of complex at 1612 cm^{-1} can also be assigned to the presence of water. New bands can be seen in the spectrum of the complex at 536 cm^{-1} and 416 cm^{-1} , this attributed to the M-N and M-O^{58,59,87} bands, respectively. In addition, a new band was formed at 3441 cm^{-1} and this can be attributed to the stretching⁸⁸ mode of water molecules. Fig. 7.17 presents a comparison of FTIR spectra for the ligand and the Co complex.

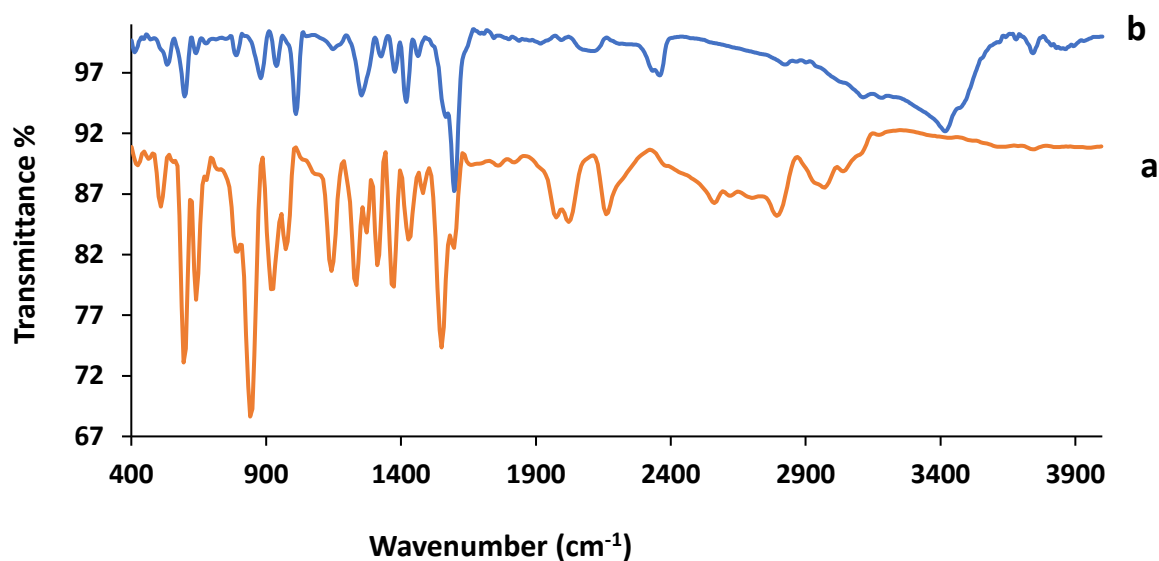


Figure 7.17. Comparison the FTIR spectrum of: (a) 6-methylmercaptapurine (6-MMP) and (b) Co(II):6-MMP complex.

7.3.4.3 Ultraviolet-Visible (UV-Vis) characterization of $C_{12}H_{14}CoN_8O_2S_2$ (5)

According to Cotton,⁸⁹ the pink complex of Co(II) with water molecules has octahedral geometry and has an absorbance maximum around 530 nm, while the blue Co(II) complex has tetrahedral geometry and has an absorbance maximum around 675 nm. Fig. 7.18 presents the spectra of octahedral (A) and tetrahedral (B) for Co(II) complexes reported by Cotton.⁸⁹

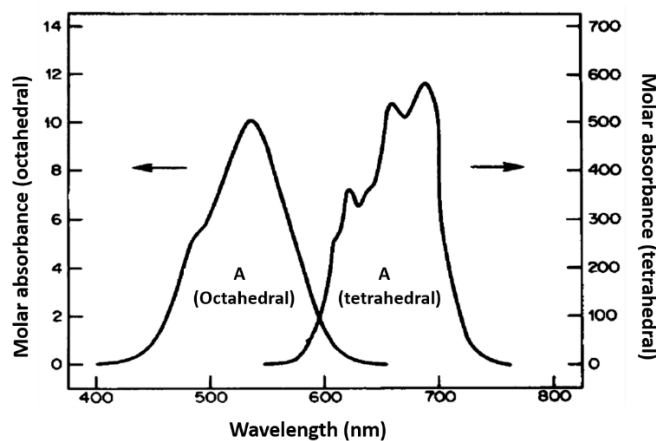


Figure 7.18. UV-Vis spectra for octahedral of $[Co(H_2O)_6]^{+2}$ (A) and tetrahedral of $[CoCl_4]^{-2}$ (B) complexes⁸⁹.

Based on Cotton's observations, the absorption of blue Co:6-MMP which have tetrahedral geometry was measured in methanol and dimethylformamide (DMF).

The spectrum of Co(II) complex in methanol, Fig. 7.19, which produced a pink solution in this solvent, revealed a broad band at 530 nm, this band can be assigned to the formation of ligand metal charge transfer complex (LMCT) or can be assigned to $d-d$ transitions. In addition, this band is usually forms in this area of visible reign for octahedral complexes of Co(II).⁹⁰⁻⁹³ While the spectrum of the ligand displayed a single peak at 290 nm that belongs to $\pi-\pi^*$.

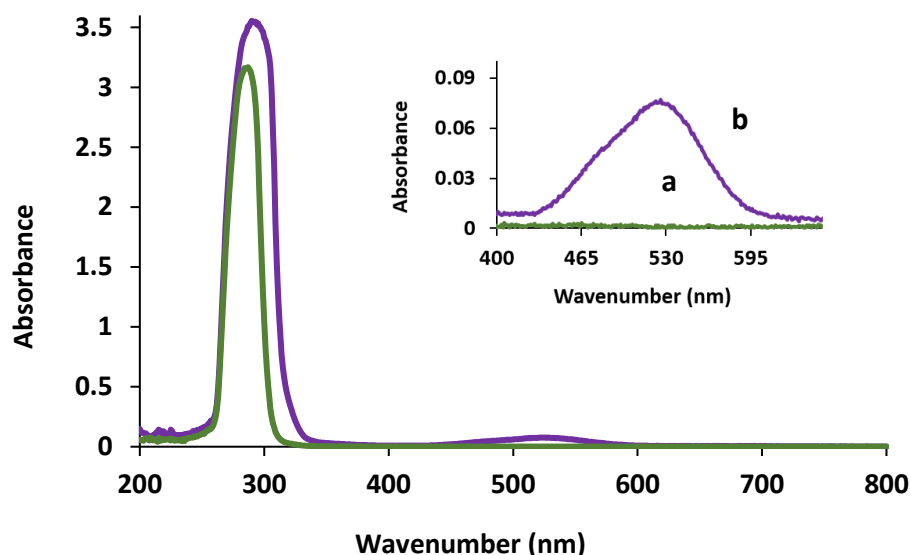


Figure 7.19. UV-Vis absorption spectra of: a) 6-methylmercaptopurine (6-MMP), and b) Co(II): 6-MMP in MeOH.

Measuring the absorption for Co(II) complex in dimethylformamide (DMF), which gave blue colour in this solvent, displayed a peak at 675 nm which is typical of tetrahedral complexes of Co(II).⁹¹⁻⁹⁴

The formation of two different absorption bands for Co complex indicates that the geometry of the complex was changing depending on the solvent. In DMF, where the colour of the complex is blue and the band appears at 675 nm, the complex has tetrahedral geometry, however, changing the solvent to methanol, where the complex has a pink colour and the band displays at 530 nm, suggests conversion of the geometry around the metal centre from tetrahedral to octahedral. The change in the geometry from octahedral to tetrahedral and vice versa upon changing the solvents was widely discussed, and it was found that octahedral species are favoured in methanol and water, while tetrahedral species are favoured in DMF and 4-methyl-2-pentanone.⁹⁵⁻⁹⁸ The characteristics of the complex will change in accordance with the geometry, such as the magnetic and conductance properties.^{89,99} Fig.7.20 displays the absorption spectra for the Co complex in DMF. The ability of the solvent to change the

geometry may be assigned to the porosity features in the complex which helps the solvent to penetrate the complex molecules and make such change. Beauvaais⁹⁵ assigned the vapochromic response to the porosity features in the complex that allows the solvent molecules to enter the solid and obstruct the hydrogen bonded which induces to release water molecules and makes inversion in the geometry from octahedral to tetrahedral without destroy the three-dimension network. In accord to this, the vapochromic response to change the solvent can be find applications as sensor.¹⁰⁰

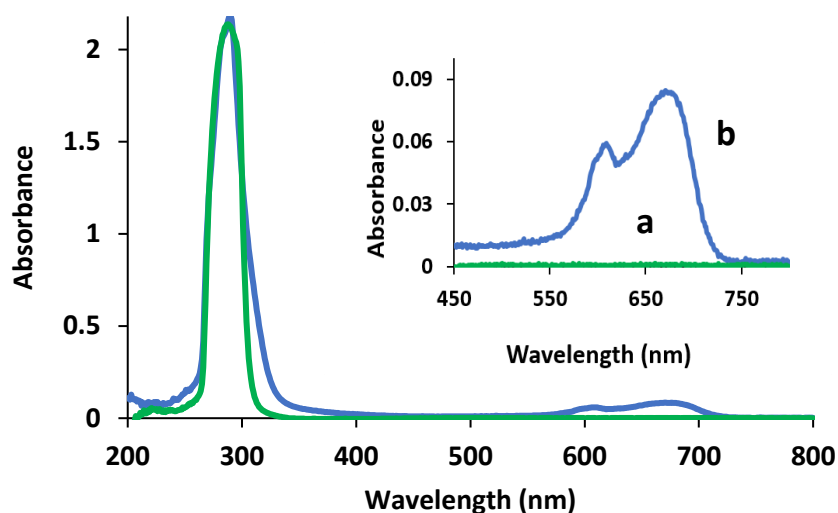


Figure 7.20. UV-Vis absorption spectra of: a) 6-methylmercaptopurine (6-MMP), and b) Co(II): 6-MMP in DMF.

The absorbance intensity of Co complex in methanol (octahedral) was red shifted to lower energy in DMF (tetrahedral) as shown in Fig.7.21 below. In general, the intensities of *d-d* transitions in tetrahedral complexes are higher than that in octahedral complexes and the reason can be attributed to the centre of symmetry which is present in octahedral and lacking in tetrahedral complexes.¹⁰¹ The spectral properties in Fig. 7.21 are consistent with most Co(II) complexes that convert from octahedral to tetrahedral geometry,⁹⁵ as the tetrahedral coordination complex of Co(II) exhibits two typical electronic absorption bands in visible region (611 nm) assigned to transition $^4A_2 \rightarrow ^4T_1(P)$ and in infrared region (675 nm) due to transition $^4A_2 \rightarrow ^4T_1(F)$.^{100,102} The broadening that can be seen in these two bands can be attributed to the spin-orbital coupling and deflection from the typical symmetrical tetrahedral geometry.^{95,103}

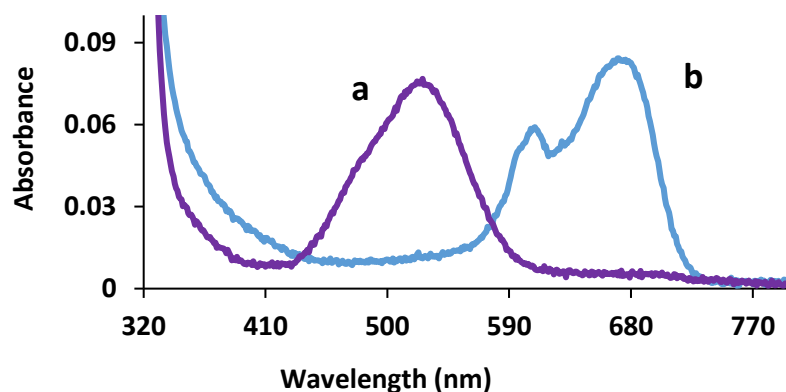


Figure 7.21. The visible spectra for Co complex (4) with geometries octahedral (a) and tetrahedral (b) in MeOH and DMF, respectively.

Based on these observations, the Co:6-MMP complex has two geometries, octahedral in (MeOH) and tetrahedral in (DMF). The colour change in this complex that associated with the kind of the solvent can allow to use this complex in the future as a porous solid material that able to detect volatile organic compounds.^{83,95} On the other hand, nucleobases are attractive compounds to build porous materials with many applications.^{5,104,105} Transition metal ions complexes such as Co complexes were incorporated to prepare porous complexes for example, the complex that synthesis by Gutschke,¹⁰⁶ who found that the colour of the complex was changed from red to blue upon dehydration and he assigned the reason to the change in the coordination number which leads to loss the crystallinity of the complex.

7.3.4.4 X-ray diffraction (XRD) of $C_{12}H_{22}CoN_8O_6S_2$ (4)

X-ray diffraction data for Co(II):6-MMP indicates a monoclinic crystalline system with 3D hydrogen bonding network. The Co (II) metal ion adopts an octahedral geometry, and in this complex, it bonds with two molecules of 6-MMP via N9 and four water molecules to form octahedral geometry. The N3 atoms of the ligands molecules at the crystal involved in hydrogen bonding. The mode of binding Co(II) ion with the molecules of water in this complex is very close to the Co complex that prepared by Verma,¹⁰⁷ who found that the reaction of cobalt ion with modified adenine leads to form octahedral geometry of Co complex where Co (II) ion was binding to four molecules of waters in addition to two oxygen of carboxylic groups at the complex. Zamora¹⁰⁸ prepared a Co complex with modified thymine and uracil, the data showed that Co ion was binding at the complex to four molecular of waters and two oxygen atoms of carboxyl groups. The data of X-ray for Co:6-MMP showed that Co-N distance was 2.12 Å and this consistent with what was found at the literature.^{107,109,110} The distances of Co-

O1&O1¹ and Co-O2&O2¹ at the complex were 2.12 Å and 2.09 Å, respectively, and this matches with the literature.^{46,108,110} Fig. 7.22 displays the structure.

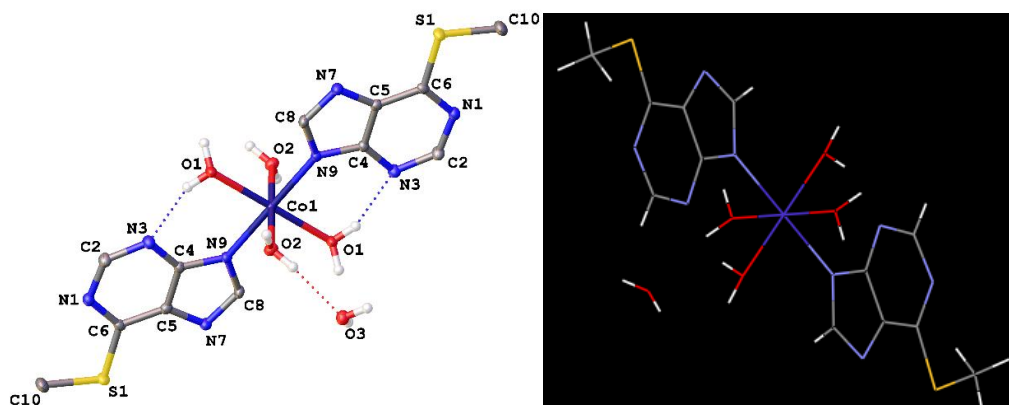


Figure 7.22. Molecular structure of Co(II) complex (4) with (right) and without (left) solvent molecules of water.

7.3.4.5 Mass spectroscopy characterization of $C_{12}H_{14}CoN_8O_2S_2$ (5)

The ESI-MS m/z (positive mode) spectra obtained in Sheffield University for Co(II):6-MMP with formula $C_{12}H_{14}CoN_8O_2S_2$ in acetonitrile $[M + H]^+$ are displayed in Fig. 7.23 (Found: 426.1124, calculated: 426.0096).

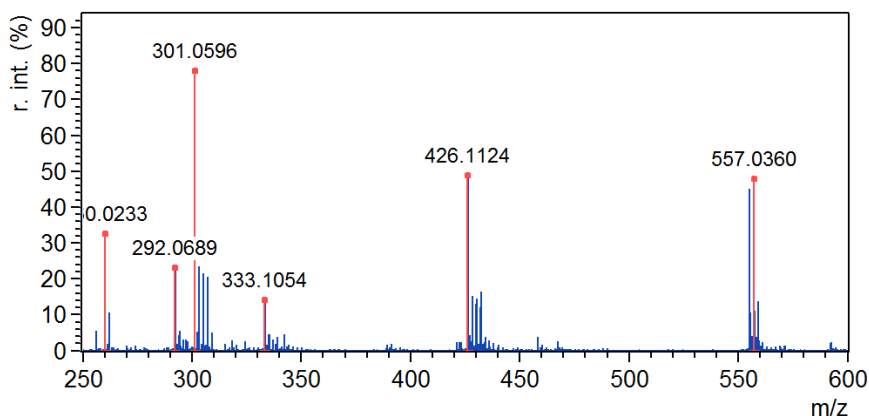


Figure. 7.23. ESI-MS m/z (positive mode) for Co(II):6-MMP with formula $[C_{12}H_{14}CoN_8O_2S_2 + H^+]$ in acetonitrile.

7.4 Conclusion

In summary, new coordination complexes based on Ag-N, Cu-N, and Co-N bonds were formed with 6-methylmercaptapurine riboside and 6-methylmercaptapurine, respectively. The X-ray data for the Ag(I) complex revealed that the distances between the atoms were a good agreement with Ag(I) complexes that have distorted tetrahedral geometry.^{51,52} The molecules in the Ag(I) complex crystal were connected by hydrogen bonding. The X-ray crystal structure

data of the olive Cu:6-MMP complex revealed that the compound is triclinic and the Cu(II) forms a dimeric structure with 6-MMP via N9 and N3. No complex hydrogen bonding network was observed for this complex. The elemental analysis (C.H.N) data for blue Cu(II):6-MMP revealed agreement between the found and the calculated values and this supports the proposed formula, in addition the FTIR displayed stretching and bending (in plane) modes of OH group at 3425 cm⁻¹ and 1396 cm⁻¹, respectively, and this confirms the presence of OH group in the structure of the complex. The X-ray data for the Co(II):6-MMP complex showed that the complex has monoclinic crystalline system with 3D hydrogen bonding network and the Co ion bound two molecules of the ligands via N9.

Table 7.4. Crystal data and structure refinement for Ag:6-MMPR

Identification code	aho150019	
Chemical formula (moiety)	C ₂₂ H ₂₄ AgN ₈ O ₁₀ S ₂ ⁺ ·NO ₃ ⁻ ·2H ₂ O	
Chemical formula (total)	C ₂₂ H ₂₈ AgN ₉ O ₁₃ S ₂	
Formula weight	798.52	
Temperature	100(2) K	
Radiation, wavelength	synchrotron, 0.6889 Å	
Crystal system, space group	orthorhombic, C222 ₁	
Unit cell parameters	a = 4.8791(10) Å	α = 90°
	b = 22.049(5) Å	β = 90°
	c = 28.256(6) Å	γ = 90°
Final R indices [F ₂ >2σ]	R1 = 0.0472, wR2 = 0.1185	
R indices (all data)	R1 = 0.0599, wR2 = 0.1243	

Table 7.5. Bond lengths [Å] and angles [°] for Ag:6-MMPR

Ag1–N7	2.153(5)	Ag1–N7a	2.153(5)
Ag1–O23	2.627(6)	Ag1–O23a	2.627(6)
N1–C2	1.358(9)	N1–C6	1.357(7)
C2–H2	0.950	C2–N3	1.333(9)
N3–C4	1.358(7)	C4–C5	1.390(9)
C4–N9	1.378(8)	C5–C6	1.418(9)
C5–N7	1.394(8)	C6–S10	1.740(7)
N7–C8	1.317(9)	C8–H8	0.950
C8–N9	1.383(8)	N9–C12	1.489(8)
S10–C11	1.816(7)	C11–H11A	0.980
N7–Ag1–N7a	164.0(3)	N7–Ag1–O23	98.2(2)
N7a–Ag1–O23	96.3(2)	N7a–Ag1–O23a	98.2(2)
N7–Ag1–O23a	96.3(2)	O23–Ag1–O23a	48.8(3)
C2–N1–C6	118.8(6)	N1–C2–H2	115.9
N1–C2–N3	128.2(6)	H2–C2–N3	115.9
C2–N3–C4	111.9(6)	N3–C4–C5	126.0(6)
N3–C4–N9	127.2(6)	C5–C4–N9	106.8(5)
C4–C5–C6	117.1(5)	C4–C5–N7	109.3(5)
C6–C5–N7	133.6(6)	N1–C6–C5	117.9(6)
N1–C6–S10	121.9(5)	C5–C6–S10	120.2(4)
Ag1–N7–C5	128.1(4)	Ag1–N7–C8	126.5(4)

C5–N7–C8	105.4(5)	N7–C8–H8	123.6
N7–C8–N9	112.7(5)	H8–C8–N9	123.6
C4–N9–C8	105.9(5)	C4–N9–C12	125.0(5)
C8–N9–C12	129.0(5)	C6–S10–C11	101.9(3)
S10–C11–H11A	109.5	S10–C11–H11B	109.5
S10–C11–H11C	109.5	H11A–C11–H11B	109.5
H11A–C11–H11C	109.5	H11B–C11–H11C	109.5
N9–C12–H12	110.0	N9–C12–O13	108.6(5)
N9–C12–C16	111.2(6)	H12–C12–O13	110.0
H12–C12–C16	110.0	O13–C12–C16	107.0(5)
C12–O13–C14	109.8(5)	O13–C14–H14	109.0
O13–C14–C15	103.7(5)	O13–C14–C17	109.5(5)
H14–C14–C15	109.0	H14–C14–C17	109.0
C15–C14–C17	116.5(6)	C14–C15–H15	109.9
C14–C15–C16	101.8(6)	C14–C15–O19	114.3(5)
H15–C15–C16	109.9	H15–C15–O19	109.9
C16–C15–O19	110.9(5)	C12–C16–C15	100.5(5)
C12–C16–H16	112.3	C12–C16–O20	107.7(7)
C15–C16–H16	112.3	C15–C16–O20	111.1(5)
H16–C16–O20	112.3	C14–C17–O18	112.0(6)
C17–O18–H18	105(4)	C15–O19–H19	109(7)
C16–O20–H20	106(8)	O22–N21–O23	120.6(4)
O22–N21–O23a	120.6(4)	O23–N21–O23a	118.7(8)
Ag1–O23–N21	96.2(5)	H24A–O24–H24B	107(8)

Table 7.6. Hydrogen bonds for Ag:6-MMPR [\AA and $^\circ$].

D–H...A	d(D–H)	d(H...A)	d(D...A)	$\angle(\text{DHA})$
O18–H18...O23b	0.85(4)	2.07(5)	2.895(9)	164(9)
O19–H19...O24	0.86(4)	1.85(5)	2.679(7)	163(10)
O20–H20...N3c	0.83(4)	2.00(5)	2.814(8)	166(11)
O24–H24A...O19d	0.83(4)	2.00(5)	2.770(7)	155(8)
O24–H24B...N1e	0.83(4)	2.12(4)	2.941(8)	168(9)

Table 7.7. Crystal data and structure refinement for Cu(II):6-MMP.

Identification code	aho170021_fa
Empirical formula	$\text{C}_{13.68}\text{H}_{18.7}\text{Cl}_4\text{Cu}_2\text{N}_8\text{O}_{1.68}\text{S}_2$
Formula weight	655.11
Temperature/K	150.0(2)
Crystal system	triclinic
Space group	P-1
$a/\text{\AA}$	7.0847(3)
$b/\text{\AA}$	9.9830(6)
$c/\text{\AA}$	10.0660(4)
$\alpha/^\circ$	63.790(5)
$\beta/^\circ$	70.263(4)
$\gamma/^\circ$	79.811(4)
Final R indexes [$I \geq 2\sigma(I)$]	$R1 = 0.0470$, $wR2 = 0.1233$
Final R indexes [all data]	$R1 = 0.0502$, $wR2 = 0.1262$

Table 7.8. Bond Lengths for Cu(II):6-MMP.

Atom	Atom	Length/Å	Atom	Atom	Length/Å
Cu1	Cu1 ¹	2.9124(12)	N1	C6	1.322(6)
Cu1	Cl1	2.3686(12)	N3	Cu1 ¹	2.000(3)
Cu1	Cl1 ¹	2.5429(12)	N3	C2	1.336(6)
Cu1	Cl2	2.2554(13)	N3	C4	1.361(6)
Cu1	N3 ¹	2.000(3)	N7	C5	1.384(6)
Cu1	N9	1.981(3)	N7	C8	1.368(6)
Cl1	Cu1 ¹	2.5429(12)	N9	C4	1.377(6)
S1	C6	1.737(5)	N9	C8	1.331(6)
S1	C10A	1.809(5)	C4	C5	1.382(6)
S1	C10B	1.833(17)	C5	C6	1.404(6)
N1	C2	1.330(6)	O1	C11	1.385(7)

¹_{1-X,1-Y,-Z}**Table 7.9. Bond Angles for Cu(II):6-MMP.**

Atom	Atom	Atom	Angle/°	Atom	Atom	Atom	Angle/°
Cl1 ¹	Cu1	Cu1 ¹	50.92(3)	C2	N3	Cu1 ¹	125.2(3)
Cl1	Cu1	Cu1 ¹	56.44(3)	C2	N3	C4	112.9(4)
Cl1	Cu1	Cl1 ¹	107.36(4)	C4	N3	Cu1 ¹	121.9(3)
Cl2	Cu1	Cu1 ¹	171.44(6)	C8	N7	C5	106.5(4)
Cl2	Cu1	Cl1	132.04(6)	C4	N9	Cu1	123.3(3)
Cl2	Cu1	Cl1 ¹	120.59(5)	C8	N9	Cu1	131.6(3)
N3 ¹	Cu1	Cu1 ¹	83.78(11)	C8	N9	C4	105.1(3)
N3 ¹	Cu1	Cl1 ¹	85.16(11)	N1	C2	N3	129.2(4)
N3 ¹	Cu1	Cl1	87.55(11)	N3	C4	N9	127.8(4)
N3 ¹	Cu1	Cl2	97.06(11)	N3	C4	C5	121.9(4)
N9	Cu1	Cu1 ¹	83.12(11)	N9	C4	C5	110.3(4)
N9	Cu1	Cl1	86.99(11)	N7	C5	C6	134.2(4)
N9	Cu1	Cl1 ¹	84.94(11)	C4	C5	N7	106.0(4)
N9	Cu1	Cl2	95.58(11)	C4	C5	C6	119.8(4)
N9	Cu1	N3 ¹	166.73(15)	N1	C6	S1	122.2(3)
Cu1	Cl1	Cu1 ¹	72.64(4)	N1	C6	C5	118.1(4)
C6	S1	C10A	102.2(2)	C5	C6	S1	119.6(4)
C6	S1	C10B	94.1(9)	N9	C8	N7	112.2(4)
C6	N1	C2	118.1(4)				

¹_{1-X,1-Y,-Z}**Table 7.10. Hydrogen Bonds for Cu(II):6-MMP.**

D	H	A	d(D-H)/Å	d(H-A)/Å	d(D-A)/Å	D-H-A/°
N7	H7	O1	0.78(7)	1.93(7)	2.707(5)	175(7)

Table 7.11. Crystal data and structure refinement for Co(II):6-MMP.

Identification code	aho170046
Empirical formula	C ₁₂ H ₂₂ CoN ₈ O ₆ S ₂
Formula weight	497.42
Temperature/K	150.0(2)
Crystal system	monoclinic
Space group	P2 ₁ /c
a/Å	9.3913(5)
b/Å	7.7232(3)
c/Å	13.7575(7)
α/°	90
β/°	103.464(5)
γ/°	90
Crystal size/mm ³	0.19 × 0.15 × 0.07

Final R indexes [I >=2σ (I)] R₁ = 0.0298, wR₂ = 0.0609

Final R indexes [all data] R₁ = 0.0401, wR₂ = 0.0657

Table 7.12. Bond Lengths for Co(II):6-MMP.

Atom Atom Length/Å			Atom Atom Length/Å		
Co1	O1	2.1276(14)	N1	C6	1.339(3)
Co1	O1 ¹	2.1276(14)	N3	C2	1.323(3)
Co1	O2 ¹	2.0943(14)	N3	C4	1.347(2)
Co1	O2	2.0943(14)	N7	C5	1.381(3)
Co1	N9 ¹	2.1222(15)	N7	C8	1.343(2)
Co1	N9	2.1222(15)	N9	C4	1.366(2)
S1	C6	1.7455(19)	N9	C8	1.347(2)
S1	C10	1.793(2)	C4	C5	1.402(3)
N1	C2	1.350(2)	C5	C6	1.393(3)

¹2-X,1-Y,1-Z

Table 7.13. Bond Angles for Co(II):6-MMP.

Atom Atom Atom Angle/°				Atom Atom Atom Angle/°			
O1 ¹	Co1	O1	180.0	C2	N3	C4	113.27(16)
O2	Co1	O1	85.57(6)	C8	N7	C5	102.20(15)
O2	Co1	O1 ¹	94.43(6)	C4	N9	Co1	128.94(12)
O2 ¹	Co1	O1 ¹	85.57(6)	C8	N9	Co1	127.75(13)
O2 ¹	Co1	O1	94.43(6)	C8	N9	C4	102.88(15)
O2	Co1	O2 ¹	180.0	N3	C2	N1	128.24(18)
O2	Co1	N9	90.66(6)	N3	C4	N9	127.41(16)
O2	Co1	N9 ¹	89.34(6)	N3	C4	C5	123.74(17)
O2 ¹	Co1	N9 ¹	90.66(6)	N9	C4	C5	108.84(16)
O2 ¹	Co1	N9	89.34(6)	N7	C5	C4	109.01(16)
N9 ¹	Co1	O1	90.93(6)	N7	C5	C6	133.39(17)
N9	Co1	O1	89.07(6)	C6	C5	C4	117.59(17)
N9	Co1	O1 ¹	90.93(6)	N1	C6	S1	121.44(14)
N9 ¹	Co1	O1 ¹	89.07(6)	N1	C6	C5	119.11(17)
N9 ¹	Co1	N9	180.0	C5	C6	S1	119.43(15)

C6	S1	C10	102.16(10)	N7	C8	N9	117.03(17)
C6	N1	C2	117.87(16)				

$$^12\text{-X},1\text{-Y},1\text{-Z}$$

Table 7.14. Hydrogen Bonds for Co(II):6-MMP.

D	H	A	d(D-H)/Å	d(H-A)/Å	d(D-A)/Å	D-H-A/°
O1	H1A	N3 ¹	0.80(3)	1.99(3)	2.748(2)	157(2)
O1	H1B	N7 ²	0.82(2)	2.09(3)	2.909(2)	175(2)
O2	H2A	O3	0.79(3)	1.98(3)	2.772(2)	172(2)
O2	H2B	O3 ³	0.81(2)	1.97(3)	2.768(2)	171(2)
O3	H3A	N1 ⁴	0.79(3)	2.06(3)	2.838(2)	165(2)
O3	H3B	N7 ⁵	0.76(3)	2.11(3)	2.862(2)	169(2)

$$^12\text{-X},1\text{-Y},1\text{-Z}; ^22\text{-X},2\text{-Y},1\text{-Z}; ^32\text{-X},1/2\text{+Y},1/2\text{-Z}; ^41\text{-X},-1/2\text{+Y},1/2\text{-Z}; ^5\text{+X},-1\text{+Y},\text{+Z}$$

References

1. Lapinski, L. & Rostkowskam, H. Infrared spectra of 2-thiocytosine and 5-fluoro-2-thiocytosine; experimental and *ab initio* studies. *Spectrochimica Acta*, **49A**, 551-565 (1993).
2. Flesner, B.K. & Bryan, J.N. 6-Thioguanine and zebularine down-regulate DNMT1 and globally demethylate canine malignant lymphoid cells. *BMC Veterinary Research*, **10**, 290-296 (2014).
3. Elion, G.B. The Purine Path to Chemotherapy. *Science*, **244**, 41-47 (1989).
4. Amo-Ochoa, P., Castillo, O., Guijarro, A., Sanz Miguel, P.J. & Zamora, F. Supramolecular architectures based on 6-purinethione complexes. *Inorganica Chimica Acta*, **417**, 142-147 (2014).
5. Houlton, A., Amo-Ochoa, P., Hribesh, S., Pike, A.R. & Zamora, F. Coordination chemistry of 6-thioguanine derivatives with cobalt: toward formation of electrical conductive one-dimensional coordination polymers. *Inorganic chemistry*, **52**, 5290-5299 (2013).
6. Purohit, C.S. & Verma, S. A Luminescent Silver-Adenine Metallamacrocyclic Quartet. *Journal of the American Chemical Society*, **128**, 400-401 (2006).
7. Jonckheere, D., Hofkens, J., Roeffaers, M.B.J. & De Vos, D.E. Silver-induced reconstruction of an adeninate-based metal-organic framework for encapsulation of luminescent adenine-stabilized silver clusters. *Journal of Materials Chemistry C*, **4**, 4259-4268 (2016).

8. Delgado, S. & Zamora, F. A Conducting Coordination Polymer Based on Assembled Cu₉ Cages. *Inorganic chemistry*, **47**, 9128-9130 (2008).
9. Verma, S. & Kumar, J. The Many Facets of Adenine: Coordination, Crystal Patterns, and Catalysis. *Accounts of Chemical Research*, **43**, 79-91 (2010).
10. Perez-Yanez, S., Aguayo, A.T. & Roman, P. Open-framework copper adeninate compounds with three-dimensional microchannels tailored by aliphatic monocarboxylic acids. *Inorganic chemistry*, **50**, 5330-5332 (2011).
11. DAS, M. & Livingstone, S.E. Metal Chelates as Anti-Cancer Agents. II Cytotoxic Action of Palladium and Platinum Complexes of 6-Mercaptopurine and Thioguanine. *British Journal of Cancer*, **38**, 325-328 (1978).
12. Yamanari, K. & Kaizaki, S. Synthesis and stereochemistry of cobalt(III) complexes containing purine-6- thione and related ligands. *Journal of the Chemical Society, Dalton Transactions*, , 305-309 (1996).
13. Shen, T.Y. & Linn, B.O. Nucleosides. III. Studies on 5-Methylamino-2'-deoxyuridine as a Specific AntiherpesAgent. *Journal of Medicinal Chemistry*, **9**, 366-369 (1966).
14. Ansari, A., Patel, N., Duley, J.A. & Florin, T.H. Low-dose azathioprine or mercaptopurine in combination with allopurinol can bypass many adverse drug reactions in patients with inflammatory bowel disease. *Alimentary Pharmacology & Therapeutics*, **31**, 640-647 (2010).
15. Volonte, C. & Greene, L.A. 6-Methylmercaptopurine Riboside is a Potent and Selective Inhibitor of Nerve Growth Factor-Activated Protein Kinase N. *Journal of Neurochemisrry*, **58**, 700-708 (1992).
16. Presta, M. & Ribatti, D. Purine Analogue 6-Methylmercaptopurine Riboside Inhibits Early and Late Phases of the Angiogenesis Process. *Cancer Research*, **59**, 2417-2424 (1999).
17. Wong, D.R., Engels, L.G.J.B., Verbeek, A.L.M. & Hooymans, P.M. Early prediction of thiopurine-induced hepatotoxicity in inflammatory bowel disease. *Alimentary Pharmacology & Therapeutics*, **45**, 391-402 (2017).
18. Chrzanowska, M. & Fieta, J. Metabolites of mercaptopurine in red blood cells: a relationship between 6-thioguanine nucleotides and 6-methylmercaptopurine metabolite concentrations in children with lymphoblastic leukemia. *European Journal of Pharmaceutical Sciences*, **8**, 329-334 (1999).

19. Sigel, A. & Sigel, R.K.O. The Alkali Metal Ions: Their Role for Life. Aoki, K, and Ning-Hai Hu. Chapter 3. Solid State Structures of Alkali Metal Ion Complexes Formed by Low-Molecular-Weight Ligands of Biological Relevance. **16**(2016).
20. Leonarski, F., D'Ascenzo, L. & Auffinger, P. Binding of metals to purine N7 nitrogen atoms and implications for nucleic acids: A CSD survey. *Inorganica Chimica Acta*, **452**, 82-89 (2016).
21. Lippert, B. Multiplicity of metal ion binding patterns to nucleobases. *Coordination Chemistry Reviews*, **200-202**, 487-516 (2000).
22. Gibson, A.E., Price, C., Clegg, W. & Houlton, A. Inner- and outer-sphere binding of the minor groove site of adenine by alkali metal ions. *Journal of the Chemical Society, Dalton Transactions*, 131-133 (2002).
23. Galindo, M.A., Clegg, W., Harrington, R.W., Moreno Martinez, V. & Houlton, A. Probing metal-ion purine interactions at DNA minor-groove sites. *Inorganic chemistry*, **48**, 10295-10303 (2009).
24. Rajabi, K. & Fridgen, T.D. Structures of Alkali Metal Ion-Adenine Complexes and Hydrated Complexes by IRMPD Spectroscopy and Electronic Structure Calculations. *The Journal of Physical Chemistry A*, **114**, 3449–3456 (2010).
25. Weiss, R. & Venner, H. *Phys. Chem. (Leipzig)*, **345**, 122 (1966).
26. Sletten, E. Crystal Structure of a Dinuclear 2 : 1 Adenine-Copper Complex. *Chemical Communications*, , 1119-1120 (1967).
27. Goodgame, D.M.L. & Price, K.A. Magnetic Exchange in a Copper-Adenine Complex *Nature*, **220**, 783-784 (1968).
28. Trávníček, Z. & Marek, J. Preparation, physicochemical properties and biological activity of copper(II) complexes with 6-(2-chlorobenzylamino)purine (HL₁) or 6-(3-chlorobenzylamino)purine (HL₂). The single-crystal X-ray structure of [Cu(H⁺ L₂)₂Cl₃]Cl.2H₂O. *Journal of Inorganic Biochemistry*, **84**, 23-32 (2001).
29. Bu, X.-H. & Zhang, R.-H. Chiral Noninterpenetrated (10,3)-a Net in the Crystal Structure of Ag(I) and Bisthioether. *Inorganic chemistry*, **41**, 437-439 (2002).
30. Bu, X.-H. & Zhang, R.-H. Adjusting the Frameworks of Silver(I) Complexes with New Pyridyl Thioethers by Varying the Chain Lengths of Ligand Spacers, Solvents, and Counteranions. *Inorganic chemistry*, **42**, 7422-7430 (2003).
31. Sun, J., Wei, Y.-H., Liu, F.-L. & Sun, D. Syntheses, crystal structures and photoluminescent properties of silver(i) and cadmium(ii) coordination polymers

- constructed from flexible hexadentate di-Schiff base ligands. *RSC Advances*, **2**, 10189 (2012).
32. Tjahjanto, R.T. & Beck, J. Synthesis and Characterization of Semiconductive Dichloridobis(thianthrene)gold(1+) Tetrachloridoaurate(1-). *European Journal of Inorganic Chemistry*, **2009**, 2524-2528 (2009).
 33. Galindo, M.A., Clegg, W., Harrington, R.W. & Houlton, A. Self-assembly of a bis(adeninyl)-Cu(i) complex: a cationic nucleobase duplex mimic. *Chemical Communications*, 2833-2835 (2009).
 34. Perea-Cachero, A., Seoane, B., Diosdado, B., Téllez, C. & Coronas, J. Synthesis, structure and characterization of a layered coordination polymer based on Zn(II) and 6-(methylmercapto)purine. *RSC Advances*, **6**, 260-268 (2016).
 35. Rao, C.N. & Kasturi, T.R. Contribution to the Infrared Spectra of Organosulphur Compounds. *Canadian Journal of Chemistry*, **42**, 36-42 (1964).
 36. Fabretti, A.C. & Zanolli, A.F. Copper(I) and silver(I) complexes of 2-amino-1,3,4-thiadiazole and 2-ethylamino-1,3,4-thiadiazole. *Polyhedron*, **2**, 475-477 (1983).
 37. Kubota, M. & Matsubara, I. Complexes of Succinonitrile with Silver(1). A Nitrate-Silver Compound. *Inorganic Chemistry*, **5**, 386-391 (1966).
 38. Goel, R.G. & Pilon, P. Tri-*tert*-butyl phosphine Complexes of Silver(1). Preparation, Characterization, and Spectral Studies *Inorganic Chemistry*, **17**, 2876-2879 (1978).
 39. Senel, E. & Harrisonb, W.T. A New One-Dimensional Coordination Polymer of Silver(I) with Bridging 2-(2-Aminoethyl)pyridine and Nitrate Ligands: $[\text{Ag}_2(\mu\text{-NO}_3)_2(\mu\text{-aepy})_2]_n$. *Z. Naturforsch.* **60b**, 659-662 (2005).
 40. Li, M.-X. & Zhu, S.-R. Metal-Organic Frameworks Constructed from 2,4,6-Tris(4-pyridyl)-1,3,5-triazine. *Inorganic chemistry*, **47**, 4481-4489 (2008).
 41. Morzyk-Ociepa, B. & Michalska, D. Vibrational spectra of 1-methyluracilate complex with silver(I) and theoretical studies of the 1-MeU anion. *Spectrochimica Acta Part A: Molecular and Biomolecular Spectroscopy*, **59**, 1247-1254 (2003).
 42. Geddes, A.L. & Bottger, G.L. The Infrared Spectra of Silver-Ammine Complexes. *Inorganic Chemistry*, **8**, 802-807 (1969).
 43. Mitev, P.D., Eriksson, A., Boily, J.F. & Hermansson, K. Vibrational models for a crystal with 36 water molecules in the unit cell: IR spectra from experiment and calculation. *Physical Chemistry Chemical Physics*, **17**, 10520-10531 (2015).

44. Cheng, F., Cheng, H., Wang, X. & Miller, J. FTIR analysis of water structure and its influence on the flotation of arcanite (K_2SO_4) and epsomite ($MgSO_4 \cdot 7H_2O$). *International Journal of Mineral Processing*, **122**, 36-42 (2013).
45. Lepodise, L.M., Horvat, J. & Lewis, R.A. Collective librations of water molecules in the crystal lattice of rubidium bromide: experiment and simulation. *Physical Chemistry Chemical Physics*, **15**, 20252-20261 (2013).
46. Munno, G., Armentano, D., Anastassopoulou, J. & Theophanides, T. New supramolecular complexes of manganese(II) and cobalt(II) with nucleic bases. Crystal structures of $[M(H_2O)_6(1-Mecyt)_6][ClO_4]_2 \cdot H_2O$, $[Co(1-Mecyt)_4][ClO_4]_2$ and $[M(H_2O)_4(cyt)_2][ClO_4]_2 \cdot 2cyt \cdot 2H_2O$ [$M = Co^{II}$ or Mn^{II} cyt = cytosine; 1-Mecyt = 1-methylcytosine]. *Journal of the Chemical Society, Dalton Transactions*, , 1625-1629 (2000).
47. Rey, R. & Hynes, J.T. Pathways for H_2O Bend Vibrational Relaxation in Liquid Water. *The Journal of Physical Chemistry A*, **113**, 8949–8962 (2009).
48. Elioff, M.S. & Mullin, A.S. Vibrational Energy Gain in the ν_2 Bending Mode of Water via Collisions with Hot Pyrazine ($E_{vib} = 37900 \text{ cm}^{-1}$): Insights into the Dynamics of Energy Flow. *The Journal of Physical Chemistry A*, **104**, 10304-10311 (2000).
49. Zimmerman, T.P. & Elion, G.B. Identification of 6-Methylmercaptapurine Ribonucleoside 5'-Diphosphate and 5'-Triphosphate as Metabolites of 6-Mercaptapurine in Man. *Cancer Research*, **34**, 221-224 (1974).
50. Dervieux, T. & Boulieu, R. Identification of 6-methylmercaptapurine derivative formed during acid hydrolysis of thiopurine nucleotides in erythrocytes, using liquid chromatography–mass spectrometry, infrared spectroscopy, and nuclear magnetic. *Clinical Chemistry*, **44**, 2511-2515 (1998).
51. Bu, X.-H. & Zhang, R.-H. Adjusting the Frameworks of Silver(I) Complexes with New Pyridyl Thioethers by Varying the Chain Lengths of Ligand Spacers, Solvents, and Counteranions *Inorganic Chemistry*, **42**, 7422-7430 (2003).
52. Qureshi, N., Yufit, D.S., Howard, J.A. & Steed, J.W. Ion-Pair Binding by Mixed N,S-Donor 2-Ureidopyridine Ligands. *Dalton Transactions*, , 5708-5714 (2009).
53. Rajabi, K. & Fridgen, T.D. Structures of Alkali Metal Ion-Adenine Complexes and Hydrated Complexes by IRMPD Spectroscopy and Electronic Structure Calculations. *The Journal of Physical Chemistry A*, **114**, 3449–3456 (2010).

54. Novotna, R., Travnicek, Z. & Herchel, R. SOD-Mimic Cu(II) Dimeric Complexes Involving Kinetin and Its Derivative: Preparation and Characterization. *Bioinorganic Chemistry and Applications*, **2012**, 704329-704335 (2012).
55. Masuda, S. & Tasumi, M. Infrared Intensities of the C=C and C=N Stretching Modes of Conjugated Schiff Bases. A Study Based on *ab Initio* Molecular Orbital Calculations. *The Journal of Physical Chemistry*, **100**, 15335-15339 (1996).
56. Rey, N.A. & Pereira-Maia, E.C. Two Different Modes for Copper(II) Ion Coordination to Quinine-Type Ligands. *Journal of the Brazilian Chemical Society*, **17**, 497-504 (2006).
57. Tachikawa, H. & Hamabayashi, T. Metal–ligand interactions of the Cu–NO complex at the ground and low-lying excited states: an *ab initio* MO study. *Electronic journal of theoretical chemistry*, **2**, 263–267 (1997).
58. Ahmed, R.M., Yousif, E.I. & Al-Jeboori, M.J. Co(II) and Cd(II) complexes derived from heterocyclic Schiff-Bases: synthesis, structural characterisation, and biological activity. *The Scientific World Journal*, **2013**, 754868-754873 (2013).
59. Anitha, C., Sheela, C.D., Tharmaraj, P. & Hema, V.V. Synthesis, Spectroscopic Characterization, and Biological Activities of Metal Complexes of 4-((4-Chlorophenyl)diazenyl)-2-((*p*-tolylimino)methyl)phenol. *Journal of Chemistry*, **2013**, 724163-724174 (2013).
60. Karlin, K.D. & Zubieta, J. Models for Met-Hemocyanin Derivatives: Structural and Spectroscopic Comparisons of Analogous Phenolate and X (X = OH⁻, OMe⁻, N₃⁻, Cl⁻, OAc⁻, OBz⁻) Doubly Bridged Dinuclear Copper (II) Complexes *Inorganic Chemistry*, **26**, 1271-1280 (1987).
61. Karlin, K.D. & Zubieta, J. Copper-Mediated Hydroxylation of an Arene: Model System for the Action of Copper Monooxygenases. Structures of a Binuclear Cu(I) Complex and Its Oxygenated Product. *Journal of the American Chemical Society*, **106**, 2121-2128 (1984).
62. Ainscough, E.W. & Waters, J.M. Antitumour copper(II) salicylaldehyde benzoylhydrazone (H₂sb) complexes: physicochemical properties and the single-crystal X-ray structures of [{Cu(H₂sb) (CCl₃CO₂)₂}₂] and [{Cu(Hsb) (ClO₄)(C₂H₅OH)}₂] and the related salicylaldehyde acetylhydrazone (H₂sa) complex, [Cu(Hsa)Cl(H₂O)].H₂O. *Inorganica Chimica Acta*, **267**, 27-38 (1998).

63. Meinders, H.C. & Challa, G. The role of μ -hydroxo-ligands in the catalytic properties of binuclear copper-tertiary amine complexes. *Journal of Molecular Catalysis*, **5**, 225-233 (1979).
64. Amo-Ochoa, P., Verma, S., Kumar, J. & Zamora, F. Semiconductive and magnetic one-dimensional coordination polymers of Cu(II) with modified nucleobases. *Inorganic chemistry*, **52**, 11428-11437 (2013).
65. Zhang, X., Cheng, J.-K., Zhang, M.-J. & Yao, Y.-G. A new luminescent Cu(I) complex stabilized by Cu \cdots Cu interactions. *Inorganic Chemistry Communications*, **20**, 101-104 (2012).
66. Saxena, A., Dugan, E.C., Liaw, J., Dembo, M.D. & Pike, R.D. Copper(I) complexes of heterocyclic thiourea ligands. *Polyhedron*, **28**, 4017-4031 (2009).
67. Johnson, K. & Steed, J.W. Effects of non-molecular forces on molecular structure in tris(thiourea)-copper(I). *Journal of the Chemical Society, Dalton Transactions*, , 2601-2602 (1998).
68. Dubler, E. & Gyr, E. New Metal Complexes of the Antitumor Drug 6-Mercaptopurine. Syntheses and X-ray Structural Characterizations of Dichloro(6-mercaptopurinium)copper(I), Dichlorotetrakis(6-mercaptopurine)cadmium(II), and Bis (6-mercaptopurinato)cadmium (II) Dihydrate. *Inorganic chemistry*, **27**, 1466-1473 (1988).
69. Nagapradeep, N., Venkatesh, V., Tripathi, S.K. & Verma, S. Guanine-copper coordination polymers: crystal analysis and application as thin film precursors. *Dalton Transactions*, **43**, 1744-1752 (2014).
70. Abdel-Rahman, L.H. & Mahmoud, R.M. Synthesis and characterization of ternary L-histidine complexes. Crystal structure of (2,2'-dipyridyl)-(L-histidinato-N,N',O)copper(II) perchlorate 1.5 hydrate. *Journal of Chemical Crystallography*, **24**, 567-571 (1994).
71. Striegler, S. & Pickens, J.B. Discrimination of chiral copper(ii) complexes upon binding of galactonoamidine ligands. *Dalton Transactions*, **45**, 15203-15210 (2016).
72. Gyurcsik, B. & Nagy, L. Equilibrium and solution structural study of the proton, copper(II), nickel(II) and zinc(II) complexes of 1-(2-aminoethylamino)-1-deoxy-Dgalactitol. *Journal of the Chemical Society, Dalton Transactions*, , 2125–2130 (1997).
73. Lesniak, W. & Pecoraro, V.L. Solution Chemistry of Copper(II)-Gentamicin Complexes: Relevance to Metal-Related Aminoglycoside Toxicity. *Inorganic chemistry* **42**, 1420-1429 (2003).

74. Crawford, V.H. & Hatfield, W.E. Relationship between the Singlet-Triplet Splitting and the Cu-O-Cu Bridge Angle in Hydroxo-Bridged Copper Dimers. *Inorganic Chemistry*, **15**, 2107-2110 (1976).
75. Lindgren, T. & Sillanpaa, R. Synthesis, Characterization, Crystal Structures and Magnetic Exchange in Dinuclear Copper Complexes with 3-Amino-1 -propanol as Terminal and Bridging Ligand. *Inorganica Chimica Acta*, **171**, 95-102 (1990).
76. Nagata, Y., Hsieh, C.S., Backus, E.H. & Bonn, M. Water Bending Mode at the Water-Vapor Interface Probed by Sum-Frequency Generation Spectroscopy: A Combined Molecular Dynamics Simulation and Experimental Study. *The Journal of Physical Chemistry Letters*, **4**, 1872-1877 (2013).
77. Ferraro, J.R. & Walker, W.R. Infrared Spectra of Hydroxy-Bridged Copper(II) Compounds. *Inorganic Chemistry*, **4**, 1382-1186 (1965).
78. Smith, B.C. Infrared Spectral Interpretation: A Systematic Approach. CRC Press, USA. (1999).
79. Jr, S.V. Analytical Techniques and Methods for Biomass. Ferrer, A & Ríos, J. Chapter 3. Analyses of Biomass Fibers by XRD, FT-IR, and NIR, p 66. Springer International Publishing Switzerland. (2016).
80. Helios, K., Wysokiński, R., Pietraszko, A. & Michalska, D. Vibrational spectra and reinvestigation of the crystal structure of a polymeric copper(II)–orotate complex, $[\text{Cu}(\mu\text{-HOr})(\text{H}_2\text{O})_2]_n$: The performance of new DFT methods, M06 and M05-2X, in theoretical studies. *Vibrational Spectroscopy*, **55**, 207-215 (2011).
81. Mcwhinnie, W.R. Magnetic Susceptibilities and Far Infra-Red Spectra of some Hydroxo-and Alkoxo-Bridged Copper (II) Complexes. *Journal of Inorganic and Nuclear Chemistry*, **27**, 1063-1070 (1965).
82. Perlepes, S.P. & Christou, G. Dinuclear Copper(II) Complexes with the New $[\text{Cu}_2(\mu\text{-OR})(\mu\text{-OAc})_2]^+(\text{R}=\text{Alkyl})$ Core: Preparation and Characterization of $[\text{Cu}_2(\text{Or})(\text{OAc})_2(\text{Bpy})_2]^+(\text{R}=\text{Me, Et, Pr}^n)$ Salts. *Polyhedron*, **14**, 1073-1081 (1995).
83. Burneo, I., Fontrodona, X., Imaz, I. & Maspoch, D. Two New Adenine-Based Co(II) Coordination Polymers: Synthesis, Crystal Structure, Coordination Modes, and Reversible Hydrochromic Behavior. *Crystal Growth & Design*, **15**, 3182-3189 (2015).
84. Uemura, K. & Mizutani, T. Novel Flexible Frameworks of Porous Cobalt(II) Coordination Polymers That Show Selective Guest Adsorption Based on the Switching of Hydrogen-Bond Pairs of Amide Groups. *Chemistry A European Journal*, **8**, 3587-3600 (2002).

85. Chen, Q., Song, H.B., Hu, T.L. & Bu, X.H. A Controllable Gate Effect in Cobalt(II) Organic Frameworks by Reversible Structure Transformations. *Angewandte Chemie International Edition*, **52**, 11550-11553 (2013).
86. Baranska, M. Optical Spectroscopy and Computational Methods in Biology and Medicine. Springer Dordrecht Heidelberg New York London. (2014).
87. Singh, J. & Singh, P. Synthesis and Structural Properties of Copper(II), Nickel(II) and Cobalt(II) Complexes with 2,4-Furyliminobenzylacetophenone. *International Scholarly Research Network (ISRN) Physical Chemistry*, **2012**, 1-6 (2012).
88. Kolesov, B.A. & Geiger, C.A. Behavior of H₂O Molecules in the Channels of Natrolite and Scolecite: a Raman And IR Spectroscopic Investigation of Hydrous Microporous Silicates. *American Mineralogist*, **91**, 1039-1048 (2006).
89. Cotton, F.A. & Wilkinson, G. Advanced Inorganic Chemistry A Comprehensive Text. Fourth edition. John Wiley & Sons. USA. (1980).
90. Roberts, G.L. & Field, F.H. The Absorption Spectra of Certain Nickel(II) and Cobalt (II) Complex Ions. *Journal of the American Chemical Society*, **72**, 4232–4235 (1950).
91. Zsigrai, I., J & Nagy, L. Electronic Spectra and Stability of Cobalt Halide Complexes in Molten Calcium Nitrate Tetrahydrate. *Verlag der Zeitschrift für Naturforschung Tübingen*, **59a**, 602-608 (2004).
92. Vraneš, M., Gadžurić, S.B. & Zsigrai, I.J. Cobalt Halide Complex Formation in Aqueous Calcium Nitrate–Ammonium Nitrate Melts. II. Cobalt(II) Bromide. *Journal of Molecular Liquids*, **145**, 14-18 (2009).
93. Vraneš, M., Gadžurić, S.B., Zsigrai, I.J. & Dožić, S. Absorption Spectra of Cobalt(II) Chloride and Nitrate Complexes in Aqueous Calcium Nitrate–Ammonium Nitrate Melts: The Influence of Solvent Composition. *Journal of Molecular Liquids*, **152**, 34-38 (2010).
94. Buffagnai, S. & Dunn, T.M. The Xpectra of Inorganic Complexes in Non-aqueous Solvents. Part 1. Chlorocobaltate Ion and Cobalt Chloride. *Journal of the Chemical Society*, , 5105-5114 (1961).
95. Beauvais, L.G. & Long, J.R. Cyano-Bridged Re₆Q₈ (Q = S, Se) Cluster-Cobalt(II) Framework Materials: Versatile Solid Chemical Sensors. *Journal of the American Chemical Society*, **122**, 2763-2772 (2000).
96. Brubakerjr, C.H. & Jhonson, C.E. The Spectra of Solutions of Cobalt(II) Thiocyanate Complexes in 4-Methyl-2-pentanone. *Journal of the American Chemical Society*, **80**, 5037-5040 (1958).

97. Silber, H.B. & Murguia, M.A. Spectrophotometric Investigations of the Octahedral-Tetrahedral Equilibria in Cobalt (II)-Thiocyanate Systems in Aqueous Methanol. *Inorganic Chemistry*, **24**, 3794-3802 (1985).
98. Ishiguro, S. & Ozutsumi, K. Thermodynamics and Structure of Isothiocyanato Complexes of Manganese(II), Cobalt(II), and Nickel(II) Ions in N,N-Dimethylformamide. *Inorganic Chemistry*, **29**, 1117-1123 (1990).
99. McCourt, É., Manyar, H.G., Hawelek, L. & Paluch, M. Temperature- and Pressure-Induced Structural Changes of Cobalt(II) in a Phosphonium-Based Ionic Liquid. *The Journal of Physical Chemistry C*, **120**, 10156-10161 (2016).
100. Aizawa, S. & Funahashi, S. Octahedral-Tetrahedral Equilibrium and Solvent Exchange of Cobalt(II) Ions in Primary Alkylamines. *Inorganic Chemistry*, **41**, 4555-4559 (2002).
101. Qye, H.A. & Gruen, D.M. Octahedral Absorption Spectra of the Divalent 3d Metal Ions in Molten Aluminum Chloride. *Inorganic Chemistry*, **3**, 836-841 (1964).
102. Garrett, B.B. & Quagliano, J.V. Electronic Spectra of Pseudotetrahedral Cobalt (II) and Nickel (II) Complexes of C_{3v} Symmetry. *Journal of the American Chemical Society*, **92**, 489-493 (1970).
103. Lever, A.B.P. *Inorganic Electronic Spectroscopy*, Elsevier: Amsterdam, . (1968).
104. Amo-Ochoa, P. & Zamora, F. Coordination polymers with nucleobases: From structural aspects to potential applications. *Coordination Chemistry Reviews*, **276**, 34-58 (2014).
105. Thomas, J. SupraMOFs: Supramolecular Porous Materials Assembled From Metal–Nucleobase Discrete Entities. Thesis, University of the Basque Country. (2015).
106. Gutschke, S.O.H. & Wood, P.T. Rational Design of Open-Framework Coordination Solids-Synthesis and Structure of $[Co_5(OH)_2\{1,2,4,5-(O_2C)_4C_6H_2\}_2(H_2O)_4] \cdot xH_2O$. *European Journal of Inorganic Chemistry*, , 2739-2741 (2001).
107. Mishra, A.K., Kumar, J., Khanna, S. & Verma, S. Crystallographic Signatures of Cobalt Coordination with Modified Adenine Nucleobase Containing Carboxyl Group Pendants. *Crystal Growth & Design*, **11**, 1623-1630 (2011).
108. Hassanein, K., Zamora, F., Castillo, O. & Amo-Ochoa, P. Supramolecular interactions in Cobalt(II)–nucleobases complexes: A methyl matter. *Inorganica Chimica Acta*, **452**, 251-257 (2016).
109. Bennington, M.S., Feltham, H.L., Buxton, Z.J., White, N.G. & Brooker, S. Tuneable Reversible Redox of Cobalt(III) Carbazole Complexes. *Dalton Transactions*, **46**, 4696-4710 (2017).

110. Nfor, E.N., Keenan, L.L., Dzesse, C.N.T. & Offiong, O.E. A Novel Mixed Ligand Dinuclear Complex of Cobalt (II): Synthesis, Characterization and Magnetic Studies. *Crystal Structure Theory and Applications*, **03**, 22-29 (2014).

Chapter 8. Synthesis and Properties of a Au(I): 2-Thiocyto sine Complex

Abstract

In this work, a gold(I):2-thiocyto sine (Au:2-TC) complex was prepared and characterised with powder X-ray diffraction, FTIR, UV-Vis, elemental analysis (C.H.N), NMR, mass spectra, fluorescence spectroscopy, and fluorescence microscopy. Elemental analysis revealed that the complex has 1:2 metal-ligand stoichiometry. The complex was observed to be photosensitive in solution but not in solid state. The crystals were needle-like, similar to Ag-2TC, but after oxidation with $I_2(g)$ showed evidence of electronic conductivity similar to Au:6-TGR (chapter three).

8.1 Introduction

Photochemical properties of thio nucleobases¹ have been exploited in photo-chemotherapy, *e.g.* skin cancer treatment², and some thio nucleobases have demonstrated potential in photodynamic therapy towards different kinds of cancers.³ In particular, 2-thiocyto sine(2-TC) possess numerous medical applications owing to its bioactivity as an antibacterial,⁴ anticancer,⁵ antiviral,⁶ and anti-cytotoxic agent.⁷ Common gold thiolate complexes which are light sensitive include myochrysine (sodium aurothiomalate) and auranofin.^{8,9} Myochrysine is photostable in the solid state but in aqueous it is light sensitive.⁸ Auranofin is light sensitive in solution but not in colloidal form⁸. There are a few reports of compounds that include Au(I), 2-TC, and phosphine thiolates such as gold ferrocenyl amide phosphine thiolate derivative¹⁰ and aminophosphine gold(I) thiolate.⁴ Gold reactions with nucleobases were found such as the reaction reported by Lippert¹¹ between $KAuCl_4$ and 1,3-dimethyl uracil which exhibited metal binding via C5; oxidation of the dimer leads to produce a complex of di(1,3-dimethyl uracil-C5, C5') with gold. The same reaction was carried out later by the same researchers¹² and by using *trans*- $K[Au(CN)_2Cl_2]$, $K[Au(CN)_2Cl(1,3\text{-dimethyluracil-C5})]$ was isolated and characterized by X-ray diffraction. Au:2-TC was prepared in this work as part of a study of metal thiolate complexes because of the interesting structure formed by Au:6-TGR (chapter three in the thesis). Moreover, the most known and important complex for gold (I) in aqueous solutions¹³ is $Au(CN)_2^-$, and preparing gold(I):2-TC in aqueous medium in this work will acquire this compound a special importance in similar manner to $Au(CN)_2^-$.

Au(I) can bind to sulfur atoms in the ligands and forms complexes with either thiol forms ($-S-Au$) or thione forms ($=S-Au$). For example the reaction of 2-thiocyto sine with bis

(phosphine) gold complexes lead to the corresponding phosphine gold (I) thiolate complexes,¹⁴ as shown in Fig. 8.1.

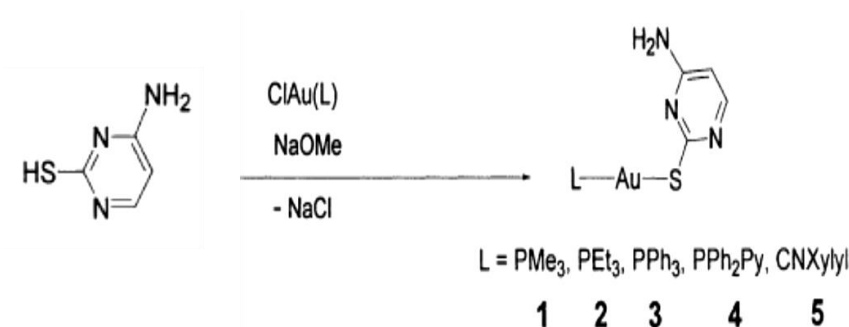


Figure 8.1. Synthesis phosphine Au(I) thiolate complexes.¹⁴

In the gold ferrocenyl amide phosphine thiolate complex prepared by Goitia¹⁰ and aminophosphine gold(I) thiolate complex synthesised by Fillat,⁴ the Au(I) was bound via the S atom with the ligand in thiol form, as shown in Figs. 8.2 & 8.3, respectively.

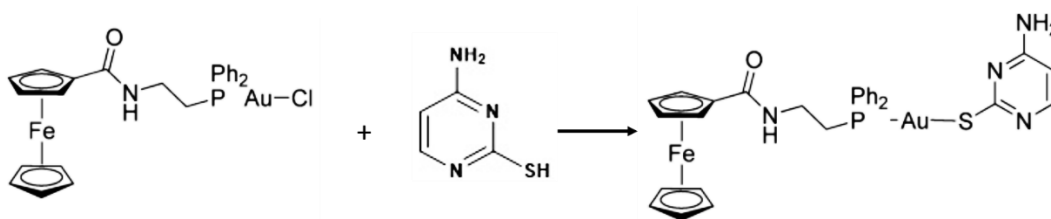


Figure 8.2. Au(I) phosphine thiolate complex that prepared by the reaction of 2-thiocytosine with gold chloride derivative of ferrocenyl-amine phosphine of in the presence of K_2CO_3 and CH_2Cl_2 .¹⁰

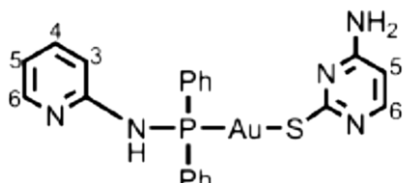


Figure 8.3. Au(I) thiolate complex that produce from the reaction of (aminophosphane)gold(I) chloride and 2-thiocytosine in the presence of triethylamine.⁴

An Au(I) complex with the thione form was prepared by Jones¹⁵ by reaction of Au(I) with bis(ethylenethiourea). Fig. 8.4 displays the unit cell of the complex. In this complex, the O atom of a water molecule forms a bridge to connect two molecules of the ligand, while Au(I) bound to with two S atoms in a linear geometry.

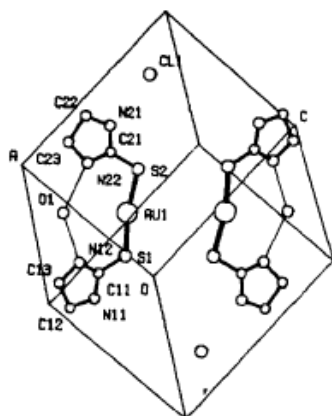


Figure 8.4. Unit cell for Au(I):bis(ethylenethiourea) thionate complex.¹⁵

The analogous complexes of auranofin, thionate (triethylphosphine) gold (I) were synthesised by Isab,¹⁶ to give another example of a gold (I) complex in thione form, Fig. 8.5.

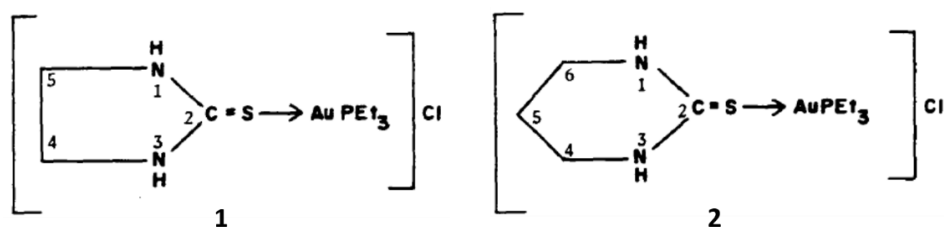


Figure 8.5. Au(I) thionate complexes: 1) Imidazolidine-2-thionato(triethylphosphine)gold(I) chloride, 2) 1,3-Diazinane-2-thionato(triethylphosphine)gold(I) chloride.¹⁶

In addition, a gold (I) complex of bis(N-propyl-1,3-imidazolidine-2-thione) in Fig. 8.6, which was prepared by Hussain,¹⁷ is also an example of a gold (I) thionate complex.

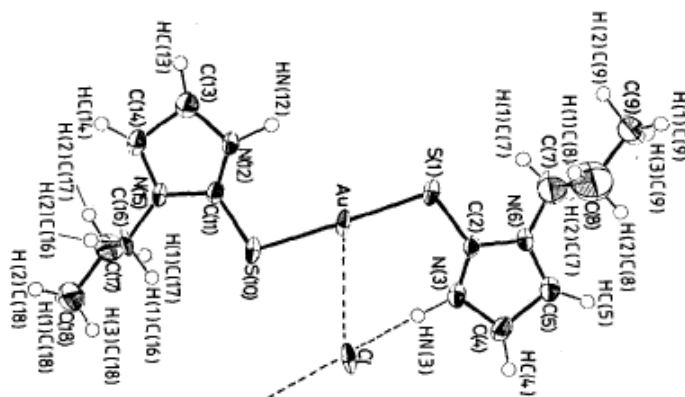


Figure 8.6. Au (I) complex of bis(N-propyl-1,3-imidazolidine-2-thione).¹⁷

Cationic Au(III) tetrakis –(methimazole) was synthesised as a hydrated square planar complex with thione form by Lynch¹⁸. The complex was prepared in methanol with mole ratio 1:4 of metal to ligand. Fig. 8.7 displays the chemical structure of the complex.

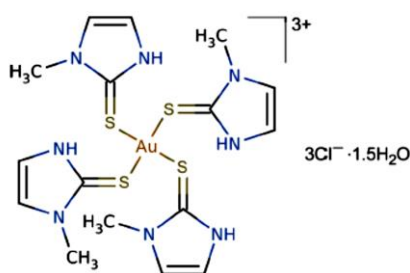


Figure 8.7. Chemical structure of Au(III) tetrakis –(methimazole).¹⁸

The cationic complex, [bis(1-(2,6-xylyl)-2-imidazolidinethione)Au(I)]Cl, was synthesised by Quillian,¹⁹ by the reaction of HAuCl₄ with the thionic ligand 1-(2,6-xylyl)-2-imidazolidine in methanol. A pale-yellow crystal was produced and characterised by X-ray diffraction. In this complex, the Au(III) ion was reduced to Au(I) during the reaction. Fig. 8.8 displays the reaction route.

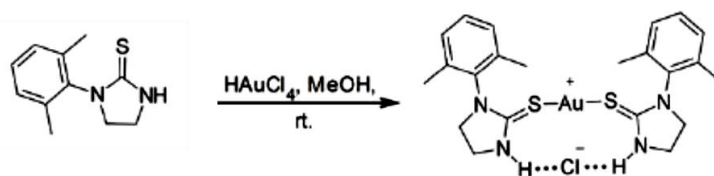


Figure 8.8. Route for synthesis of cationic[bis(1-(2,6-xylyl)-2-imidazolidinethione)Au(I)]Cl.¹⁹

Gold complexes, Fig. 8.9, with thione form were also synthesised using ligand *N*-methylbenzothiazole-2-thione (mbtt),²⁰ X-ray diffraction was used to characterise the structure of the complexes.

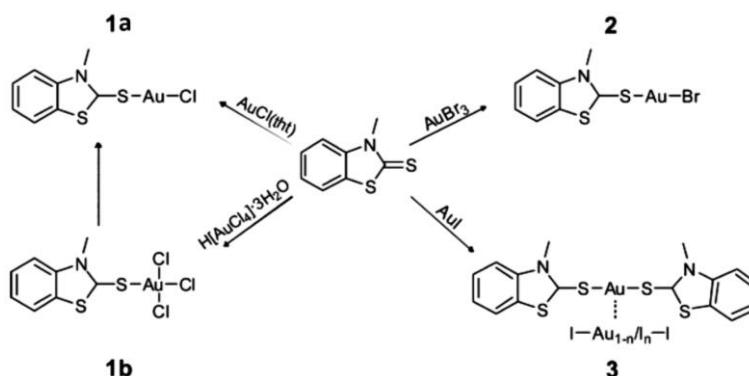


Figure 8.9. Route for synthesis of gold complexes using the ligand *N*-methylbenzothiazole-2-thione (mbtt).²⁰

8.2 Experimental

8.2.1 Synthesis of Au(I) 2-thiocytosine complex

The complex of gold (I): 2-thiocytosine (Au:2-TC) was prepared with a mole ratio 1:1 of L:M. $\text{HAuCl}_4 \cdot 3\text{H}_2\text{O}$ (130 mg, 0.33 mmol in 400 μL MeOH and 1.6 ml H_2O), was reduced with two equivalents of thiodiglycol (50 μL), and then added to a warm solution of 2-thiocytosine (42 mg, 0.33 mmol in 8 ml of 1 N HCl, after dissolving, 8 ml of hot H_2O was added). After leaving the solution 10 min in the dark, a pale precipitate formed. Inspection of the precipitate under an optical microscope showed the presence of small crystals. The solution was left for a further 2 h then filtered or left overnight in the dark. After Buchner filtration, the crystals were washed with water and dried for 2h at 50°C and kept in the dark, (yield with respect to the ligand was 0.033 gm, $\sim 80\%$).

8.3 Results & Discussion

8.3.1 Proposed structure

The oxidation states of gold range from +1 to +5, however the most common are (+1) and (+3) with electronic configuration of $5d^{10} 6s^0 6p^0$ and $5d^8 6s^0 6p^0$, respectively. Complexes of Au(I) have a linear geometry while Au(III) complexes are often to be square planar.¹⁸ 2-Thiocytosine, which is present as the thiol form in solid state^{5,21} and as the thione form in water,⁵ was reacted with Au(I) ions in acidic medium to form a crystalline compound of Au(I):2-TC with a metal to ligand stoichiometry of 1:2. The reaction was very rapid and easy to prepare; Fig. 8.10 displays the reaction route to prepare the complex. The linear geometry with coordination state (2) is common in Au(I) complexes.²²⁻²⁷ Electroneutrality is maintained with chloride as counterion; this consistent with several literatures for gold complexes in which Au(I) was bonded to the ligand via thione-S.¹⁵⁻¹⁷

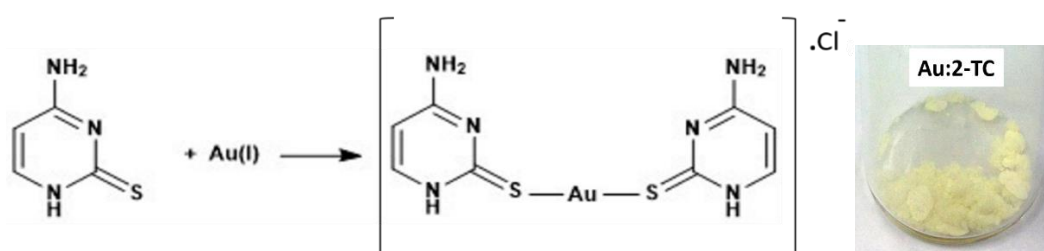
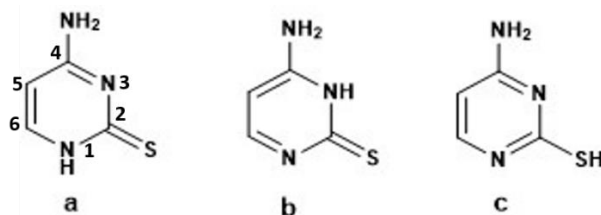


Figure 8.10. Chemical reaction route for synthesis Au:2-TC complex with simplified proposed structure and photograph of the product Au:2-TC.

Gold (I) complexes⁹ with strong reducing ligands (azide, iodide, and thiolate) show ligand to metal charge transfer (LMCT) transitions at long wavelength and this may be accompanied with metal centred transitions (MC). Upon reaction with 2-TC a pale yellow crystalline compound was formed with high percentage (% 80), 2-TC pyrimidine nucleobase exhibits several tautomers,⁵ the common forms are thione (a & b) and thiol (c) as shown in Scheme 8.1. In the solid state the thiol form is dominant rather than the thione,^{5,21} while in water the order of stability is $a \sim b > c$.⁵



Scheme 8.1. Tautomers of 2-TC in thione (a & b) and thiol (c) forms.

In addition, the crystal structure of ligand 2-thiocytosine (2-TC) showed two non-equivalent molecules linked by two kinds of hydrogen bonding: N-H....N and N-H....S, the difference between the molecules was found in the length of the C4-C5 double bond.²⁸

8.3.2 Fourier transform infrared spectroscopy (FTIR) characterisation

The weak band at 2696 cm^{-1} in the 2-TC spectrum, Fig. 8.11 (a) or (b), which is assigned to the stretching mode S-H²⁹ was not found in the spectrum of Au:2-TC, in addition, a new sharp peak at 1219 cm^{-1} which can be assigned to C=S stretching mode was found in the complex indicates that the complex is in thione form, and this change in the form comes from dissolving the ligand in water prior to bind with Au(I). The two bands at 925 cm^{-1} and 856 cm^{-1} which belong to bending mode S-H²¹ were found in the ligand indicates that the ligand was in the thiol form; both of these bands were disappeared in the Au:2-TC spectrum. This is additional evidence for the thione form of the complex and suggests that the binding of Au(I) occurred via S. The N-H^{21,30,31} in-plane bending mode in the ligand can be observed at 1627 cm^{-1} ; this band was shifted to 1639 cm^{-1} in the complex. The stretching mode of symmetric N-H³⁰ which was found at 3317 cm^{-1} in the ligand was shifted in the Au:2-TC complex, but to lower frequency (3155 cm^{-1}) as a result of intermolecular hydrogen bonding. The band at 1296 cm^{-1} in the ligand that is related to a stretching mode²⁹ N1-C2 was also shifted to 1327 cm^{-1} in the complex which suggests coordination of Au(I) to S atom at C2. The bending mode of NH₂ at 1627 cm^{-1} was also slightly shifted to lower frequency (1639 cm^{-1}). Over-all the FTIR spectra

of the ligand and the complex Au:2-TC are broadly in agreement with the proposed structure of Fig. 8.10.

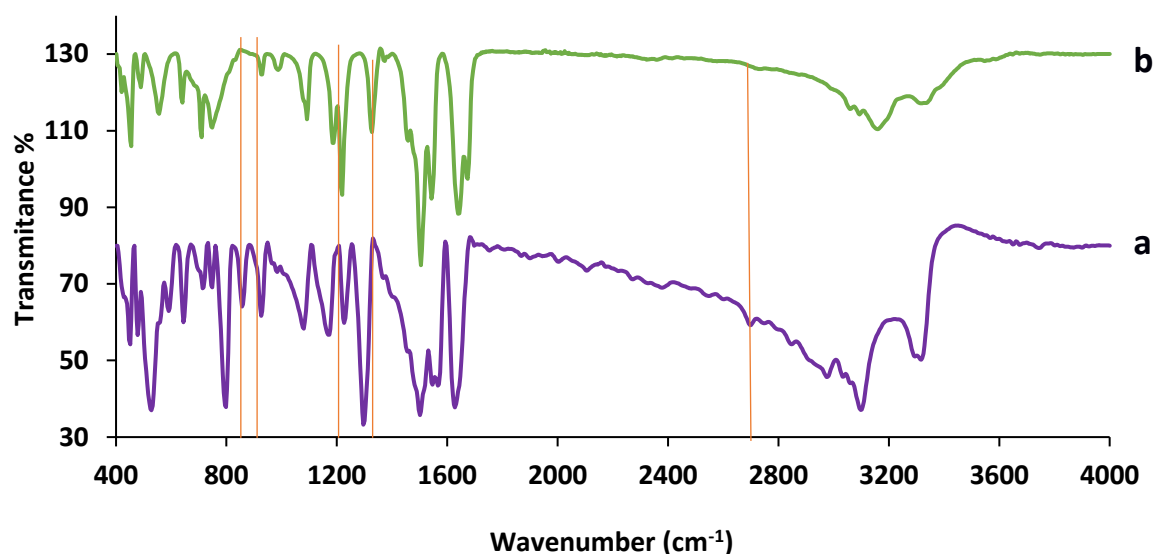


Figure 8.11. FTIR spectra of: (a) 2-thiocytosine (2-TC) and (b) gold (I):2-thiocytosine (Au:2-TC).

8.3.3 UV-Vis Absorption spectroscopy

The spectrum of 2-thiocytosine (2-TC) in Fig. 8.12 shows two peaks at 245 nm and 281 nm which belong to π - π^* .³² After complexation with Au(I), the peak at 245 nm disappeared from the spectrum of the Au:2-TC complex, and a new peak at 402 nm was formed. This longer wavelength band in the spectrum of Au:2-TC recorded in MeOH is attributed to a ligand-metal charge transfer transitions (LMCT).^{22,33}

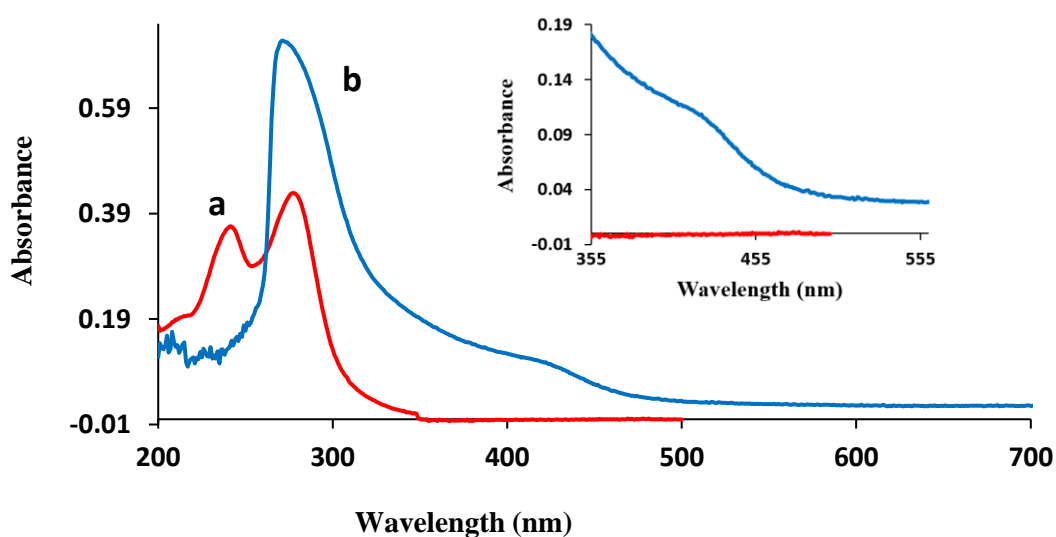


Figure 8.12. UV-Vis absorption spectra in MeOH for: (a) 2-thiocytosine (2-TC), red line, and (b) gold (I):2-thiocytosine (Au:2-TC), blue line.

8.3.4 Fluorescence spectroscopy of Au:2-TC

A fluorescence spectrum of Au:2-TC in methanol in Fig. 8.13 was carried out with excitation light of wavelength $\lambda = 405$ nm corresponding to the absorption feature in the Au:2-TC spectrum of Fig. 8.12. A broad peak can be seen in the spectrum covering the region from 495 nm to 753 nm and centred at 622 nm. This peak can be assigned to lowest energy of the triplet excited state which leads to $p\pi(S) \rightarrow p\sigma(Au)$ charge transfer transitions (LMCT) in Au complexes. In addition, aerophilic interactions may contributed via metal centred transitions $d\sigma^*(Au) \rightarrow p\sigma(Au)$.^{22,33-35}

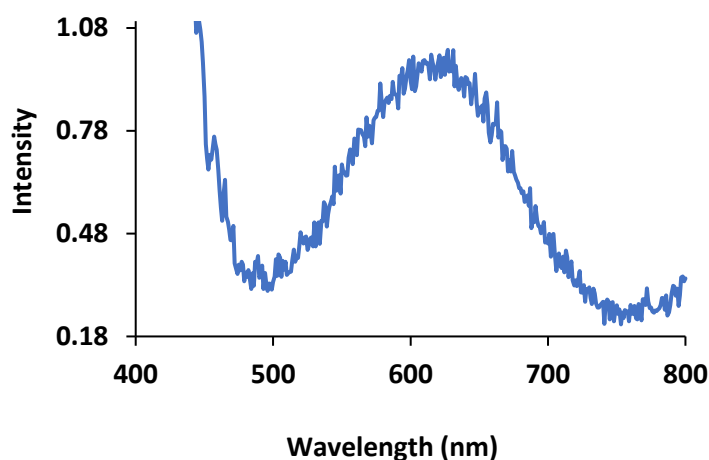


Figure 8.13. Fluorescence spectrum of gold (I):2-thiocytosine(Au:2-TC) in methanol with an excitation wavelength of 405 nm.

The fluorescence spectrum of 2-thiocytosine(2-TC) ligand in Fig. 8.14 was also recorded with an excitation wavelength of 242 nm; it shows a broad peak from 280 nm to 427 nm and centred at 342 nm. The peaks related to second order scattering can also be seen in the spectrum of the ligand. No emission is observed corresponding to that shown in Fig. 8.13 under 405 nm excitation, in keeping with the assignment to transitions involving Au.

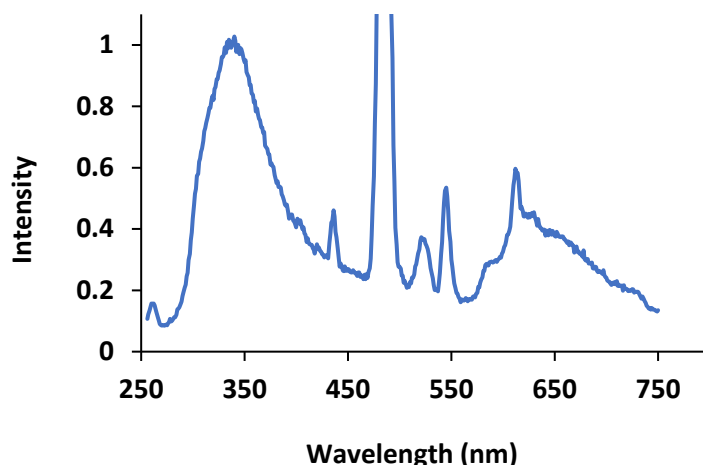


Figure 8.14. Fluorescence spectrum of 2-thiocytosine(2-TC) in DMSO with excitation 242 nm.

8.3.5 Elemental analysis (C.H.N)

Elemental analysis (C.H.N) was obtained from the service at the School of Human Sciences, London Metropolitan University. For Au:2-thiocytosine complex with proposed formula $C_8H_{10}N_6S_2Au.Cl.2H_2O$, the theoretical values were: %C 18.37, %H 2.67, and %N 16.07, Found: %C 18.16, % H 2.04, and % N 15.53. Table 8.1 displays the data. According to the elemental analysis data, Au(I) binds two molecules of 2-TC and the proposed structure of Fig. 8.10 is consistent with the literature on Au(I) chemistry which indicates the linear two coordination of Au(I) complexes predominates.^{22,36,37}

Table 8.1. Elemental analysis of Au:2-thiocytosine.

Element	% Theoretical	% Found
C	18.37	18.16
H	2.67	2.04
N	16.07	15.53

8.3.6 Mass spectra

Mass spectra was carried out at Sheffield University with Matrix-assisted laser desorption and ionization time-of-flight mass spectrometry (MALDI-TOF-MS) for Au:2-TC in acetonitrile, m/z (positive mode) for $C_8H_{10}N_6S_2Au$ found: 451.0245, (calculated: 451.0078), the data revealed metal to ligand of M:L₂ stoichiometry and this confirms the linear geometry for Au:2-TC, Fig. 8.15. displays the spectrum.

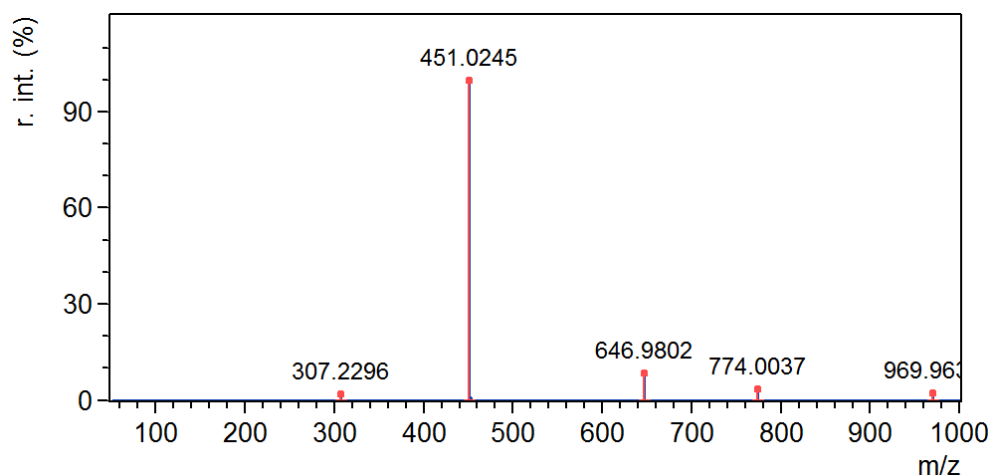


Figure 8.15. Matrix-assisted laser desorption and ionization time-of-flight mass spectrometry (MALDI-TOF-MS) mass spectrum for Au:2-TC in acetonitrile.

8.3.7 ^1H and ^{13}C NMR of Au(I):2-TC complex

A comparison of the ^1H NMR spectra of the ligand 2-TC and Au:2-TC complex in DMSO- d_6 (500 MHz, 25 °C) displays shifts in the positions of several signals, as shown in Fig. 8.16. H1, which was sharp in the ligand (s, 11.96 ppm), is shifted downfield by 1.26 ppm in the complex (s, 13.22 ppm). The broadening of the -NH peak (H1) in the complex can be assigned to the inductive effect of the metal binding at S which makes H1 at the nearby N atom more acidic,³⁸ and since the internal NH (which has acidity in rang 5-11pKa)¹⁹ is strongly acid-dependent³⁹ and the chemical shift is pH-dependent,⁴⁰ this leads to form a broadened downfield H1 signal. In addition, all other peaks at the ligand include doublet H6 (d, 7.39 & 7.35 ppm, $J = 7.0$ Hz), doublet H5 (d, 5.93 & 5.91 ppm, $J = 7.0$ Hz), and NH_2 (s, 7.54 & 7.4 ppm, 2H) were shifted downfield also in the complex: H6 (d, 7.76, 7.75 ppm, $J = 7.1$ Hz), H5 (d, 6.35, 6.33 ppm, $J = 7.1$ Hz), and NH_2 (s, 8.50, 8.38 ppm) and this can be assigned to the decrease of electronic density⁴¹ in the ligand upon binding with Au(I) ion.

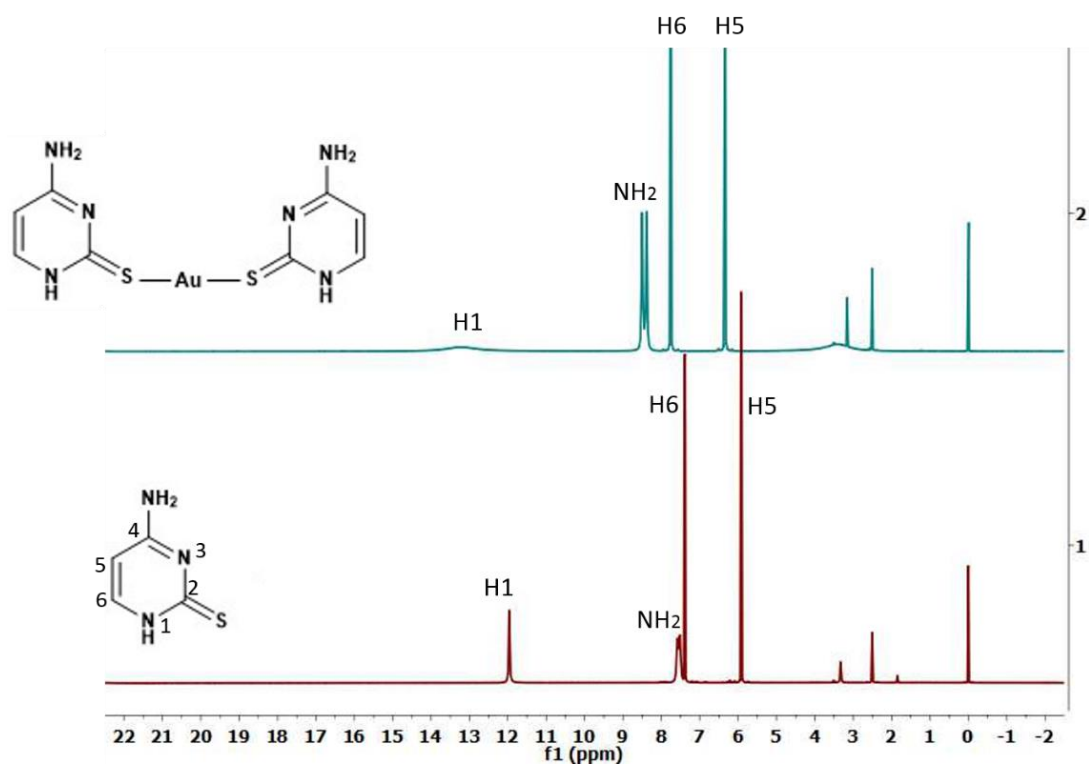


Figure 8.16. ^1H NMR of 2-TC and Au(I):2-TC at $\text{DMSO-}d_6$ in 500 MHz.

The peak assigned to NH_2 splits into two peaks and this can be attributed to the non-equivalence of the NH bonds (the difference is around 0.05 \AA between the N-H bonds in solid 2-TC),²⁸ Fig. 8.17 shows small area of Fig. 8.16 to display with more clearly the splitting in the peak of NH_2 that assigned to non-equivalent NH bonds, in addition, to show the very small splitting in the doublet peaks of H6 and H5.

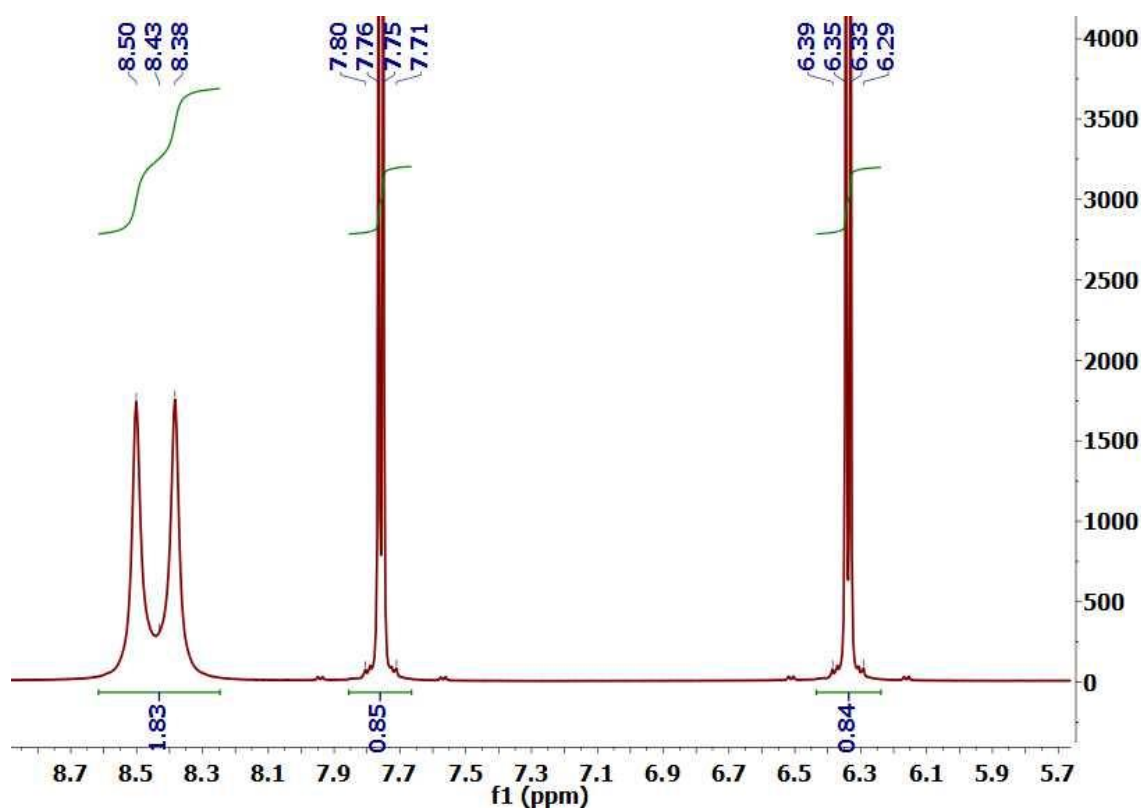


Figure 8.17. Region 8.7-5.7 ppm of Figure 8.13 displaying details of the ^1H NMR of Au(I):2-TC at DMSO- d_6 in 500 MHz to show the doublets H6 and H5, the splitting of NH_2 , and the corresponding integrals.

Fig. 8.18 presents a comparison of the ^{13}C NMR spectra between the ligand 2-TC and the Au:2-TC complex in DMSO- d_6 (500 MHz, 25 °C). The spectrum of the ligand displayed four signals at 180.43(C2), 162.95(C4), 142.92(C6), 96.88(C5) ppm. Notably, all peaks for C atoms in the Au:2-TC complex were not strongly shifted except C2 which was shifted upfield (171.90 ppm) and this can be attributed to the resonances in the complex that occurred upon coordination with Au(I) which reduced the shielding for C=S carbon in the complex as a result of forming two coordinate species and this supports thione-S bonding to Au(I) ion.¹⁷ C5 was slightly shifted downfield in the complex (100.53 ppm) due to increase the character of double bond of thione group C=S.⁴²

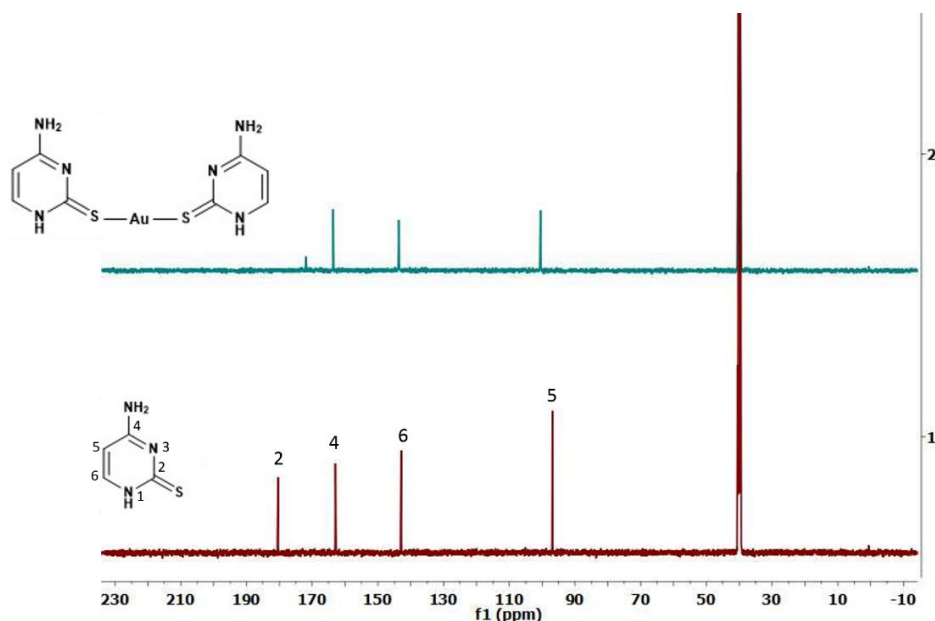


Figure 8.18. ^{13}C NMR of 2-TC and Au(I):2-TC at DMSO- d_6 in 500 MHz.

8.3.8 Powder X-ray diffraction (XRD) of Au:2-TC

Sharp Bragg peaks were found in the X-ray diffraction pattern for Au:2-TC as shown in Fig. 8. 19 indicating that the sample was microcrystalline. This is very different to the case of Au:6-TGR discussed in chapter 3 which shows only very broad bands and appears amorphous. A few peaks in the pattern correspond to distances $d=2\pi/Q$ of 0.281 and 0.264 nm which are consistent with Au-Au interactions and $d = 0.247$ nm is consistent with Au-S bond length.¹¹^{43,44} Table 8.2, is presents the data.

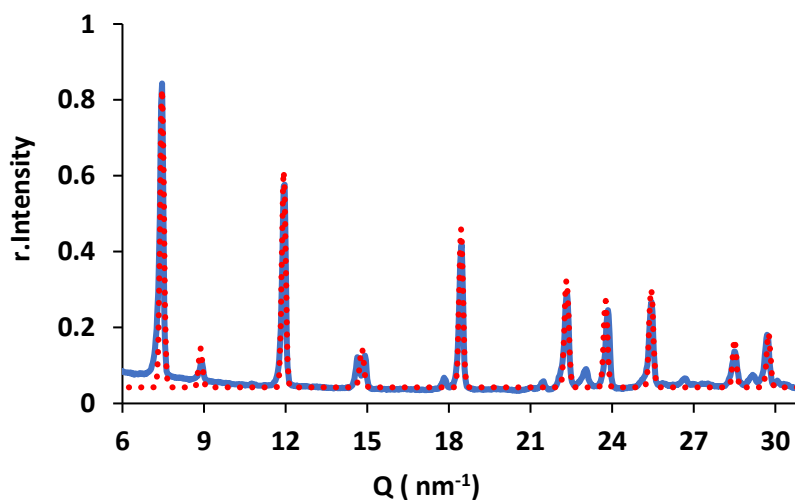


Figure 8. 19. XRD pattern for Au:2-TC. The blue line is the experimental diffraction data and the red dotted line is the theoretical fit.

Table 8.2. Distances extracted from the analysis of the XRD data for Au:2-TC.

Distance /nm	Suggested Assignment
0.281	Au-Au
0.264	Au-Au
0.247	Au-S

8.3.9 Conductivity of Au(I):2-thiocyto sine

In chapter 3, Au:6-thioguanosine was shown to produce a novel conductive coordination polymer upon oxidative doping. The Au:2-TC was also found to display similar behaviour upon treatment with iodine vapour. This is also significant for a more detailed interpretation of the structure of Au:2-TC, because it suggests extended Au/S interactions not depicted in the simple proposal of Fig. 8.10.

To fabricate electronic devices for electrical characterisation of Au:2-thiocyto sine microcrystalline, platinum microband electrodes (MBEs) were used, which were made up of Si/SiO₂ substrates. On the top of the SiO₂ layer there were four platinum electrodes are patterned with height 200 nm and 10 μ m width with 10 μ m spaces between them. The surfaces of the MBEs were electrically insulated except for a 2 x 2 mm² area for depositing the sample. Devices were fabricated by depo casting the Au:2-TC solution onto the Platinum MBEs. A drop (~1 μ l) of Au:2-thiocyto sine solution that contained the microcrystalline of Au:2-TC was casted onto the uninsulated area on the platinum microband electrodes (MBE). The drop was dried at 45 °C under vacuum to produce a dry layer of the Au:2-TC on and between the Pt-electrodes. The dried Au:2-TC on platinum MBEs was exposed to iodine vapour for 1h by heating 0.1 g of iodine to 45 °C in a sealed flask. Current-voltage curves were collected before and after oxidation.

8.3.9.1 Two-terminal I–V characteristics of the Au:2-TC complex

A two terminal I–V technique with a probing station (Cascade Microtech) and a B1500A semiconductor analyser (Agilent) was used to assess the conductance of Au(I):2-TC before and after oxidation with I₂. The I–V characterisation was carried out under a dry nitrogen atmosphere at room temperature. The data in Fig. 8.20 presents the variation the current with applied potential at room temperature, the voltage was swept from -2 to 2 V in 0.2 V steps with a measurement time of 100 ms at each step constant rate (100 m s /0.2 V). As also observed

for Au:6-thioguanosine, the complex is insulating prior to oxidation, but after oxidation, an ohmic I-V curve was obtained.

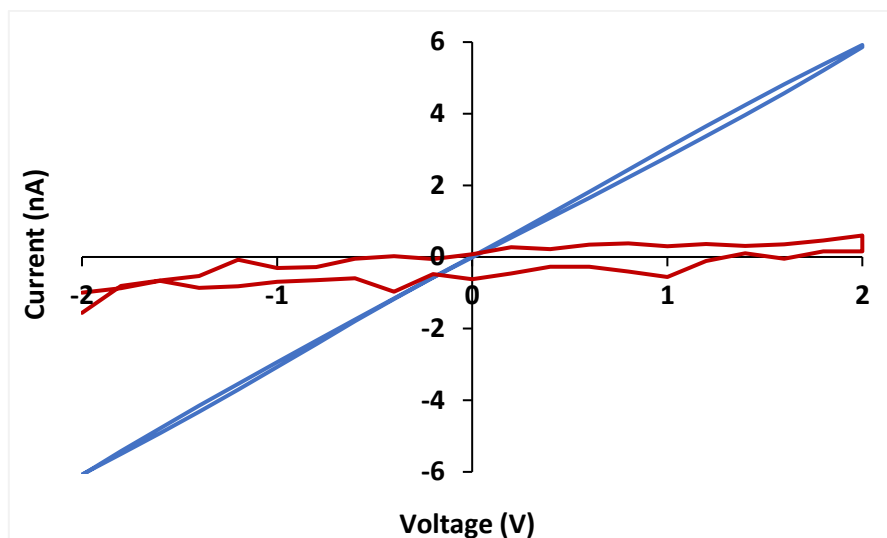


Figure 8. 20. Showing current varies with potential before (red line) and after (blue line) oxidation with I_2 at room temperature taken over a constant rate $100 \text{ m s} / 0.2 \text{ V}$.

The observed change in conductance suggests, by comparison with chapter 3, that conductivity in Au:thionucleobases complexes may be common. It is interesting that the microcrystalline Au:2-TC shows conductance comparable to that of polymer Au:6-thioguanosine despite the clear differences in the morphology of the two materials.

8.3.10 Morphology of solid Au(I):2-TC

The presence of two kinds potential of hydrogen bonding (N-H....N and N-H....S) in the chemical structure of the molecular of 2-TC gives a rise to festinating structures for the complexes of this pyrimidine nucleobase with metal ions. Fig. 8.21 shows optical (right) and fluorescence (left) images for Au:2-TC. In the images, long needle-like crystals were formed. The material is definitely microcrystalline from the XRD data, but the crystals have a large aspect ratio and in this respect have some similarity to the long polymeric fibres of Ag:2-thiocytosine.

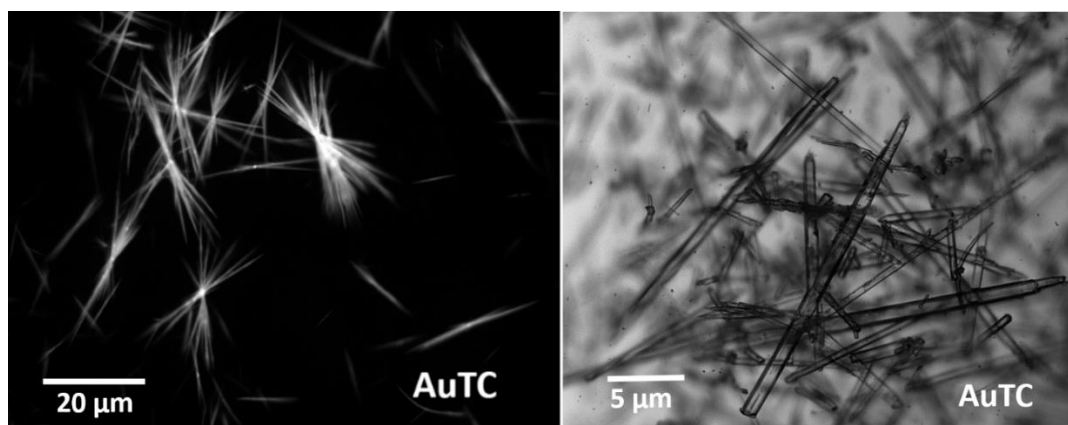


Figure 8. 21. Optical (right) and fluorescence (left) images showing the morphology and the size of Au:2-TC crystal. The left image displaying the fluorescence of the compound.

As mentioned in Chapter 6 the reaction of Ag(I) with 2-TC forms a polymer which is converted with time into bundles. Upon comparing the initial structure of the optical images for Ag(I):2-TC with that for Au(I):2-TC, an interesting similarity was found. Both compounds have very similar morphology, but the XRD data show Ag(I) compound is an amorphous polymer and the Au(I) is crystalline. Fig. 8.22 displays the comparison between Au and Ag:2-TC complexes.

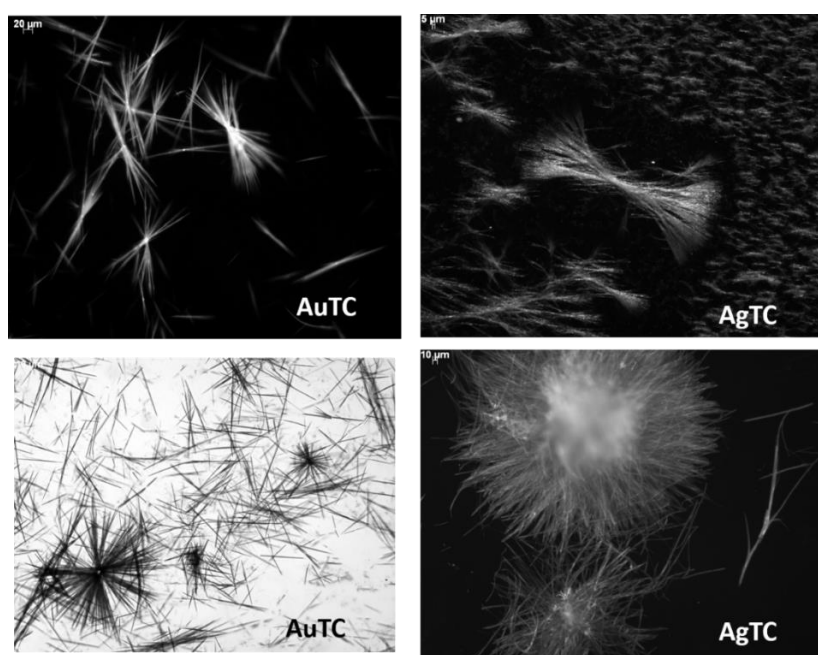


Figure 8. 22. Comparison the morphology between Au & Ag:2-TC complexes display the similarity at the morphology between the two complexes and this reflects orientation the metals ions (Au/Ag) to bind with the same binding site (S atom) at the two complexes.

8.4 Conclusion

A new gold (I) complex with 2-thiocytosine (2-TC) was synthesised and characterized. FTIR characterization has shown that Au(I) ion binds via S atom, and the elemental analysis (C.H.N) suggested that the complex of Au:2-TC has 2:1 ligand to metal stoichiometry. This suggests a linear coordination for Au(I) in the complex. The data of x-ray diffraction showed sharp Bragg peaks indicating that the complex was microcrystalline, unlike the coordination polymers observed for other thionucleobases and the distances $d=2\pi/Q$ of 0.34, 0.264, and 0.247 nm can be tentatively assigned to Au...Au, Au-S. The complex displayed fluorescence properties similar to other gold complexes. The crystal structure of 2-TC molecular has two non-equivalent molecules which are linked by two types of hydrogen bonds N-H...N and N-H...S. The existence of two molecules at the crystal structure of 2-TC gives a rise to form interesting architecture for the 2-TC and the compounds that are prepared upon coordination 2-TC with metal ions such as Au(I). According to the importance 2-TC as a ligand at medicine field and the role of gold at different importing medicine, the complex of Au:2-TC is expected to have a promising application in the pharmaceutical field.

References

1. Pollum, M., Jockusch, S. & Crespo-Hernandez, C.E. Increase in the photoreactivity of uracil derivatives by doubling thionation. *Physical Chemistry Chemical Physics*, **17**, 27851-27861 (2015).
2. Attard, N.R. & Karran, P. UVA photosensitization of thiopurines and skin cancer in organ transplant recipients. *Photochemical & Photobiological Sciences*, **11**, 62-68 (2012).
3. Gemenetzidis, E., Shavorskaya, O., Xu, Y.Z. & Trigiante, G. Topical 4-thiothymidine is a viable photosensitizer for the photodynamic therapy of skin malignancies. *Journal of Dermatological Treatment*, **24**, 209-214 (2013).
4. Fillat, M.F., Ortego, L. & Villacampa, M.D. Synthesis, Structure and Bactericide Activity of (Aminophosphane)gold(I) Thiolate Complexes. *European Journal of Inorganic Chemistry*, **2011**, 1487-1495 (2011).
5. Vetter, C., Wagner, C., Paschke, R. & Steinborn, D. Synthesis, characterization, and cytotoxicity of trimethylplatinum(IV) complexes with 2-thiocytosine and 1-methyl-2-thiocytosine ligands. *Inorganica Chimica Acta*, **362**, 189-195 (2009).

6. Shigeta, S. & Saneyoshi, M. Anti-herpesvirus activities and cytotoxicities of 2-thiopyrimidine nucleoside analogues *in vitro*. *Antiviral Chemistry & Chemotherapy*, **10**, 195-209 (1999).
7. Lozzio, C.B. & Wigler, P.W. Cytotoxic effects of thiopyrimidines. *Journal of Cellular Physiology*, **78**, 25-31 (1971).
8. Kunkely, H. & Vogler, A. Excited State Properties of Myochrysin and Auranofin. *Verlag der Zeitschrift für Naturforschung*, **51b**, 1086- 1071 (1996).
9. Vogler, A. & Kunkely, H. Photoreactivity of gold complexes. *Coordination Chemistry Reviews*, **219-221**, 489-507 (2001).
10. Goitia, H., Nieto, Y., Laguna, A. & Gimeno, M.C. Antitumoral Gold and Silver Complexes with Ferrocenyl-Amide Phosphines. *Organometallics*, **32**, 6069-6078 (2013).
11. Zamora, F. & Lippert, B. 5,5'-Diuracilyl Species from Uracil and $[\text{AuCl}_4]^-$: Nucleobase Dimerization Brought about by a Metal. *Angewandte Chemie International Edition*, **38**, 2274-2275 (1999).
12. Zamora, F. & Lippert, B. Au^{III} binding to C5 of the model nucleobase 1,3-dimethyluracil (1,3-DimeU): Preparation and X-ray crystal structures of *trans*- $\text{K}[\text{Au}(\text{CN})_2 \text{Cl}(1,3\text{-DimeU})]$ and of two derivatives. *Journal of Organometallic Chemistry*, **552**, 127-134 (1998).
13. Cotton, F.A. & Wilkinson, G. *Advanced Inorganic Chemistry A Comprehensive Text*. Fourth edition. John Wiley & Sons. USA. (1980).
14. Wilton-Ely, J.D. & Schmidbaur, H. Hydrogen-bonded networks: (phosphine)gold(I) 4-amino-2-pyrimidine-thiolates. *Journal of Organometallic Chemistry*, **643-644**, 313-323 (2002).
15. Jones, P.G. & Sheldrick, G.M. Bis(ethylenethiourea)gold(I) Chloride Hydrate . *Acta Crystallographica Section B*, **32**, 3321-3322 (1976).
16. Isab, A.A. & Shaw, C.R. Synthesis of Thionato (Triethylphosphine) Gold(I) Complexes: Analogues of “Auranofin,” an Antiarthritic Drug. *Journal of Inorganic Biochemistry*, **38**, 95-100 (1990).
17. Hussain, M.S. & Isab, A.A. Bis(N-propyl-1,3-imidazolidine-2-thione)gold(I) Chloride: Crystal and Molecular Structure. *Transition Metal Chemistry*, **10**, 178-181 (1985).
18. Lynch, W.E., Padgett, C.W., Quillian, B. & Haddock, J. A square-planar hydrated cationic tetrakis(methimazole)gold(III) complex. *Acta Crystallographica Section C Structural Chemistry*, **71**, 298-300 (2015).

19. Quillian, B. & Schanz, H.-J. Bis(1-(2,6-Xylyl)-2-Imidazolidinethione Gold(I) and Copper(I) Halides: Synthesis, Characterization and Structure. *Structural Chemistry & Crystallography Communication*, **1**, 1:5 (2015).
20. Koskinen, L., Kalenius, E., Hirva, P. & Haukka, M. Role of C–H···Au and Auophilic Supramolecular Interactions in Gold–Thione Complexes. *Crystal Growth & Design*, **14**, 1989-1997 (2014).
21. Lapinski, L., Nowak, M.J. & Rostkowskam, H. Infrared spectra of 2-thiocytosine and 5-fluoro-2-thiocytosine; experimental and *ab initio* studies. *Spectrochimica Acta*, **49A**, 551-565 (1993).
22. Barbieri, A., Accorsi, G. & Armaroli, N. Luminescent complexes beyond the platinum group: the d¹⁰ avenue. *Chemical Communications*, 2185-2193 (2008).
23. White-Morris, R.L. & Balch, A.L. Auophilic Interactions in Cationic Gold Complexes with Two Isocyanide Ligands. Polymorphic Yellow and Colorless Forms of [(Cyclohexyl Isocyanide)₂Au^I](PF₆) with Distinct Luminescence. *Journal of the American Chemical Society*, **125**, 1033-1040 (2003).
24. White-Morris, R.L. & Balch, A.L. Remarkable Variations in the Luminescence of Frozen Solutions of [Au{C(NHMe)₂}₂](PF₆), 0.5(Acetone). Structural and Spectroscopic Studies of the Effects of Anions and Solvents on Gold(I) Carbene Complexes. *Journal of the American Chemical Society*, **124**, 2327-2336 (2002).
25. White-Morris, R.L. & Balch, A.L. New Insights into the Effects of Self-Association of the Cation [Au{C(NHMe)₂}₂]⁺ on Its Solid State Structure and Luminescence. *Inorganic Chemistry*, **41**, 2313-2315 (2002).
26. Moro, A.J., Rome, B., Lima, J.C. & Rodriguez, L. A coumarin based gold(I)-alkynyl complex: a new class of supramolecular hydrogelators. *Organic & Biomolecular Chemistry*, **13**, 2026-2033 (2015).
27. Vergara, E., *et al.* Antiproliferative Activity of Gold(I) Alkyne Complexes Containing Water-Soluble Phosphane Ligands. *Organometallics*, **29**, 2596-2603 (2010).
28. Furberg, S. & Jensen, L. Crystal Structure of Thiocytosine. *Acta Crystallographica Section B*, **26**, 1260-1268 (1970).
29. Kwiatkowski, J. & Leszczyn´ski, J. Molecular Structure and Vibrational IR Spectra of Cytosine and Its Thio and Seleno Analogues by Density Functional Theory and Conventional *ab Initio* Calculations. *Journal of Physical Chemistry*, **100**, 941-953 (1996).
30. Yadav, L. Organic Spectroscopy. Springer-Science+Business Media, B. V. (2005).

31. Nowak, M. & Lapinski, L. Infrared experimental and *ab initio* quantum mechanical studies of 2-mercaptopyrimidine tautomers. *Spectrochimica Acta*, **47A**, 339-353 (1991).
32. Loofbourow, J.R. & Sinsheimer, R.L. Ultraviolet Absorption Spectra at Reduced Temperatures: II. Pyrimidines and Purines. *Journal of Biological Chemistry*, **187**, 313-324 (1950).
33. Fernandez, E.J., Laguna, A., Lopez-de-Luzuriaga, J.M., Monge, M. & Sanchez-Forcada, E. Different phosphorescent excited states of tetra- and octanuclear dendritic-like phosphine gold(I) thiolate complexes: photophysical and theoretical studies. *Dalton Transactions*, **40**, 3287-3294 (2011).
34. Forward, J.M. & Staples, R.J. Luminescence Studies of Gold(1) Thiolate Complexes. *Inorganic chemistry*, **34**, 6330-6336 (1995).
35. Balzani, V. & Campagna, S. Photochemistry and Photophysics of Coordination Compounds I. Topics in Current Chemistry. Springer-Verlag Berlin Heidelberg. **280**, 117 (2007).
36. Laguna, A. Modern Supramolecular Gold Chemistry: Gold-Metal Interactions and Applications. Gimeno, M .C. Chapter 1. The Chemistry of Gold. WILEY-VCH Verlag GmbH & Co. KGaA, Weinheim. 1-64 (2008).
37. Yang, W. & Li, T. From Achiral Molecular Compnents to Chiral Supermolecules and Supercoil Self-Assembly. *Chemistry A European Journal*, **5**, 1144-1149 (1999).
38. Harkins, T., R & Freiser, H. Adenine-Metal Complexes. *Journal of the American Chemical Society*, **80**, 1132-1135 (1957).
39. Walter, R.I. & Linschitz, H. A Proton NMR Study of the Reactions with Acid of meso-Tetraphenylporphyrins with Various Numbers of 4-Dimethylamino Groups. *Journal of Physical Chemistry*, **97**, 13308-13312 (1993).
40. Platzer, G., Okon, M. & McIntosh, L.P. pH-dependent random coil ¹H, ¹³C, and ¹⁵N chemical shifts of the ionizable amino acids: a guide for protein pKa measurements. *Journal of Biomolecular NMR*, **60**, 109-129 (2014).
41. Bennington, M.S., Feltham, H.L., Buxton, Z.J., White, N.G. & Brooker, S. Tuneable Reversible Redox of Cobalt(III) Carbazole Complexes. *Dalton Transactions*, **46**, 4696-4710 (2017).
42. Akhtar, M., Isab, A., Hussain, M. & Al-Arfaj, A. Synthesis of thionato(trimethylphosphine)gold(I) complexes. *Transition Metal Chemistry*, **21**, 553-555 (1996).

43. Mansour, M.A. & Eisenberg, R. Linear Chain Au(I) Dimer Compounds as Environmental Sensors: A Luminescent Switch for the Detection of Volatile Organic Compounds. *Journal of the American Chemical Society*, **120**, 1329-1330 (1998).
44. Bau, R. Crystal Structure of the Antiarthritic Drug Gold Thiomalate (Myochrysine): A Double-Helical Geometry in the Solid State. *Journal of the American Chemical Society*, **120**, 9380-9381 (1998).

Chapter 9. Conclusion

This chapter includes two parts: the first part displays the data for silver:6-mercaptapurine riboside hydrogel (Ag:6-MPR). The second part presents some general conclusions from all the complexes in this thesis.

9.1 Silver 6-mercaptapurine riboside (Ag:6-MPR)

9.1.1 Experimental

This gel was prepared by reaction AgNO₃ solution (11.95 mg, 0.07 mmol in 40 μ L MeOH, 160 μ L H₂O) to the warm solution of 6-mercaptapurine riboside (20 mg, 0.07 mmol in 400 μ L NaOH (0.1N), 200 μ L MeOH, and 200 μ L H₂O) after mixing the two solutions, 1 ml of yellow gel was formed. Fig. 9.1.1 displays the reaction route.

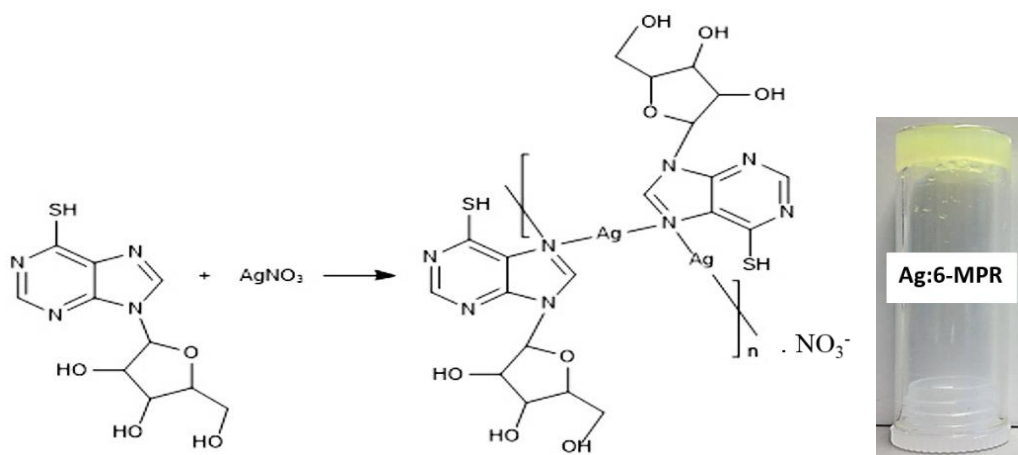


Figure. 9.1.1. Reaction route for Ag(I):6-mercaptapurine riboside hydrogel.

9.1.2 Results & Dissociation

9.1.2.1 Fourier Transform Infrared Spectroscopy (FTIR) characterisation of Ag:6-MPR hydrogel

Fig. 9.1.2 shows the FTIR spectra of 6-mercaptapurine riboside (6-MPR), and Ag:6-MPR hydrogel. The band at 1203 cm⁻¹ which is related to the stretching mode C=S in the nucleoside 6-MPR does not change at the complex and that confirms that S6 atom does not participate in the binding with Ag(I), while the bands in the nucleoside at 1589 cm⁻¹ and 1473 cm⁻¹ which in particular belongs to the stretching mode of C=C and C=N were shifted to 1573 cm⁻¹ and 1597

cm^{-1} , respectively suggesting that the binding of Ag ion to the 6-MPR nucleoside was occurred via N7.

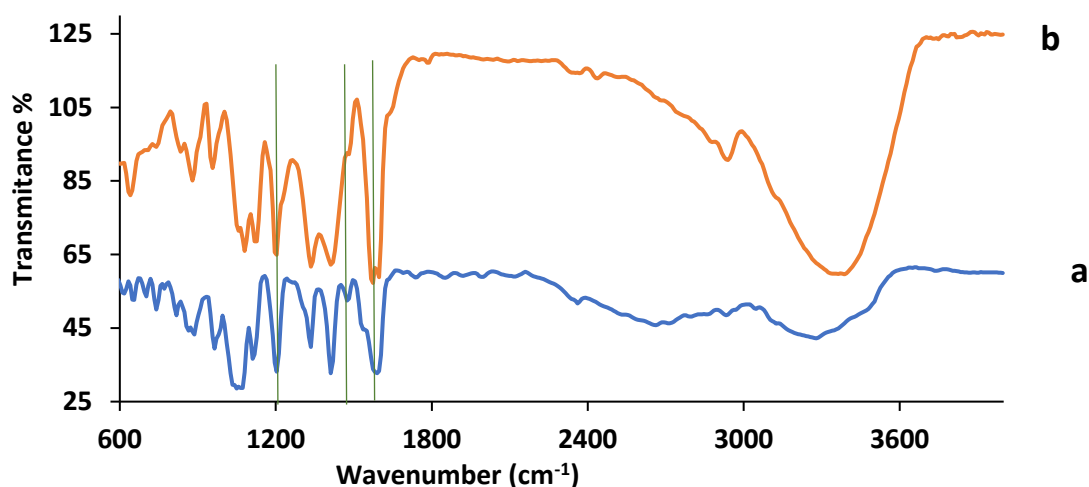


Figure 9.1.2. FTIR spectra compression between: (a) 6-mercaptopurine riboside (6-MPR) and (b) Ag:6-MPR gel.

9.1.2.2 UV-Vis Absorption Spectroscopy

The absorption spectrum of 6-mercaptopurine riboside (6-MPR) in pH 12 and pH 2 gave peaks at 310 nm and 324 nm as a result of the thiol and thione forms, respectively. The formation of thiol form in pH 12 was probably combined with deprotonation of N1-H, Fig. 9.1.3.

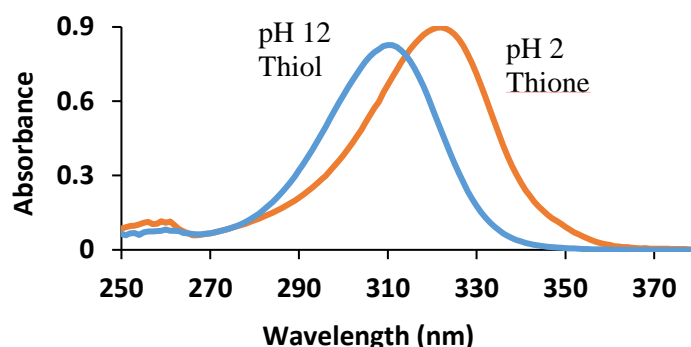


Figure 9.1.3. UV-Vis absorbance spectra of 6-mercaptopurine riboside(6-MPR) at pH 12 and pH 2 show thiol and thione forms, respectively.

The basic solution of the 6-mercaptopurine riboside in pH 12 displays a band at 312 nm and this suggests that the solution is in thiol form. While the absorption spectrum of Ag:6-MPR hydrogel which was prepared in pH (12) showed a new band at 335 nm, as shown in Fig. 9.1.4.

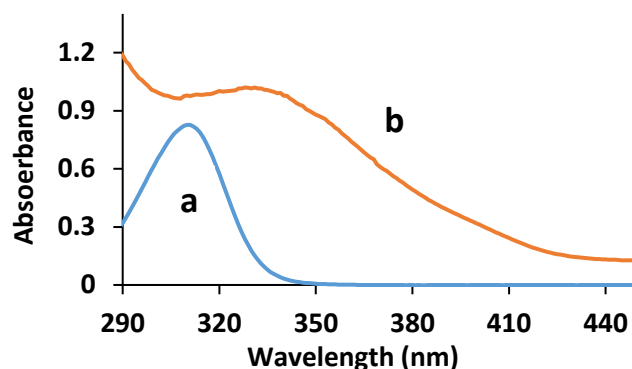


Figure 9.1.4. Comparison between: (a) the spectrum of 6-Mercaptopurine riboside (6-MPR) in pH 12 and the spectrum of 1:1 Ag:6-MPR (b) gel.

9.1.2.3 Fluorescence Spectrum of Ag: 6-Mercaptopurine riboside (Ag:6-MPR)

Ag(I):6-MPR hydrogel shows a weak fluorescence fluorescence in the region between 498 to 640 nm. Fig. 9.1.5

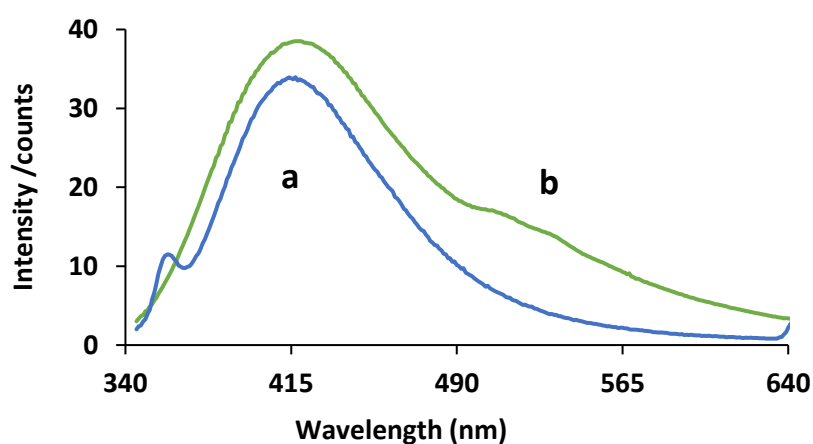


Figure 9.1.5. of, Ag:6-MPR gels, the excitation was 310 nm and 332 nm for 6-MPR, Ag:6-MPR, respectively.

9.1.2.4 Circular Dichroism (CD) studies

Fig. 9.1.6 presents the CD spectra of the ligand (6-MPR) and the gel Ag(I):6-MPR. The spectrum of the ligand displayed two peaks at 203 nm and 330 nm. While the spectrum of the gel showed new peaks at 252 nm and 400 nm along with a substantial increase in the intensity suggests that the gel has fibres with a helical structure.

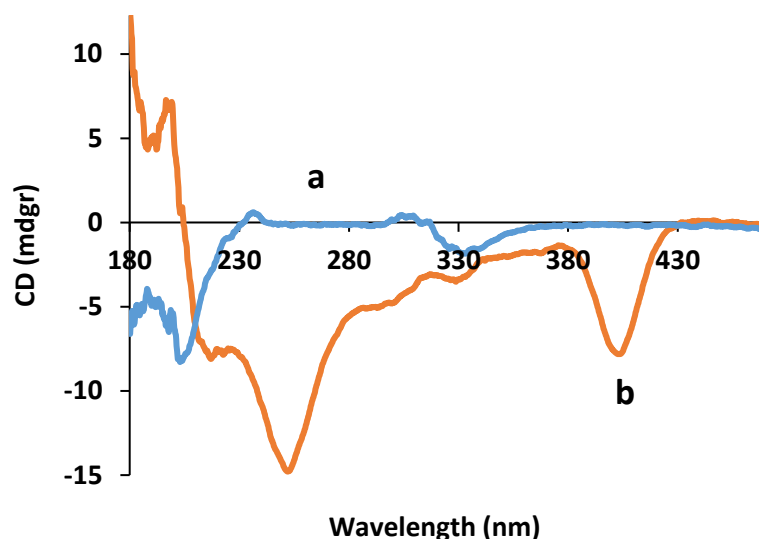


Figure 9.1.6. Displays the CD spectra for: (a) the ligand (6-MPR) and (b) the Ag (I):6-MPR hydrogel.

9.1.2.5 Powder X-Ray Diffraction

The data of XRD for Ag:6-MPR shows amorphous scattering. Analysis of this data distances for Ag-N and Ag-Ag at 0.228 nm and 0.318 nm, respectively. This supports the proposed structure in Fig. 9.1.7 that Ag(I) bounds to N7 in the gel.

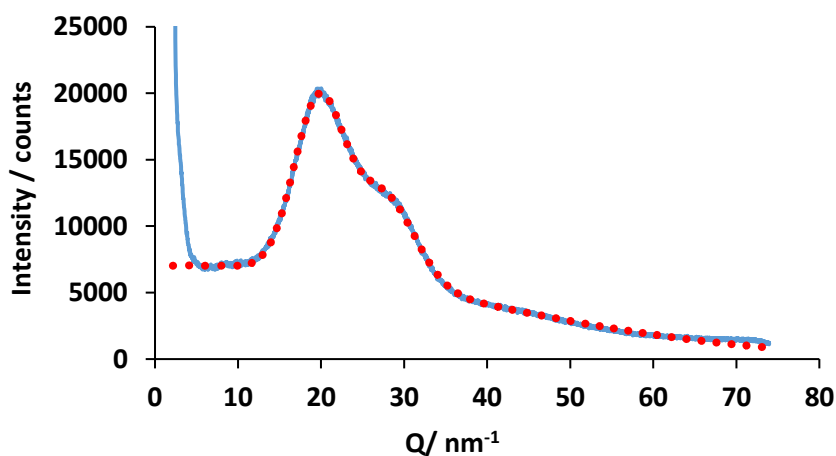


Figure 9.1.7. XRD pattern for Ag:6-MPR hydrogel. The blue line is the experimental diffraction data and the red dotted line is the theoretical fit.

Table 9.1.1. Distance extracted from the analysis of the XRD data for Ag:6-MPR gel.

Distance /nm	Suggested Assignment
0.318	Ag-Ag
0.228	Ag-N

9.1.2.6 Atomic Force Microscopy (AFM)

To probe the morphology and the size of the fibres in the gels, surface topography imaging was carried out using tapping mode AFM by depositing 2 μL of Ag:6-MPR, gel into a silicon wafer. All AFM images showed long fibres, Fig. 9.1.8. The statistical analysis was carried out to show the height and the size (diameter) distribution of the fibres in the gel, as shown in Fig. 9.1.9.

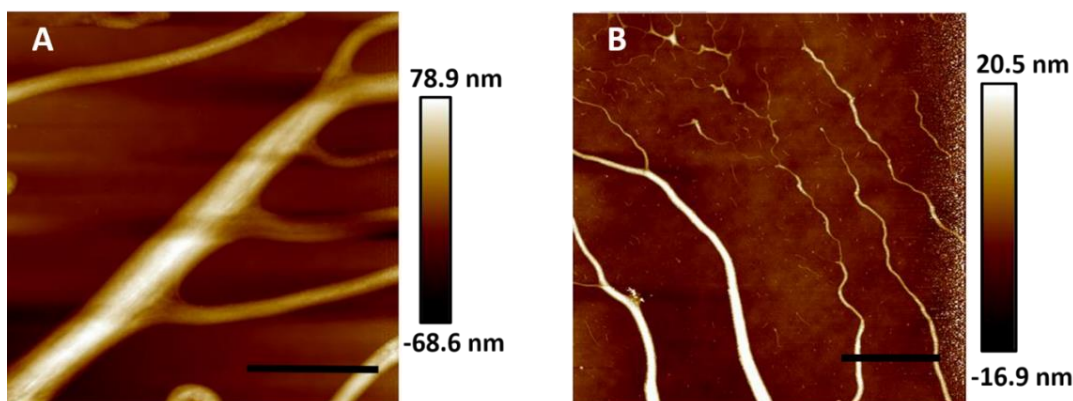


Figure 9.1.8. Tapping mode AFM height image of Ag:6-MPR. The scale bar in both A & B was 5 μm and the grayscale are 78.9 nm & 20.5 nm, respectively.

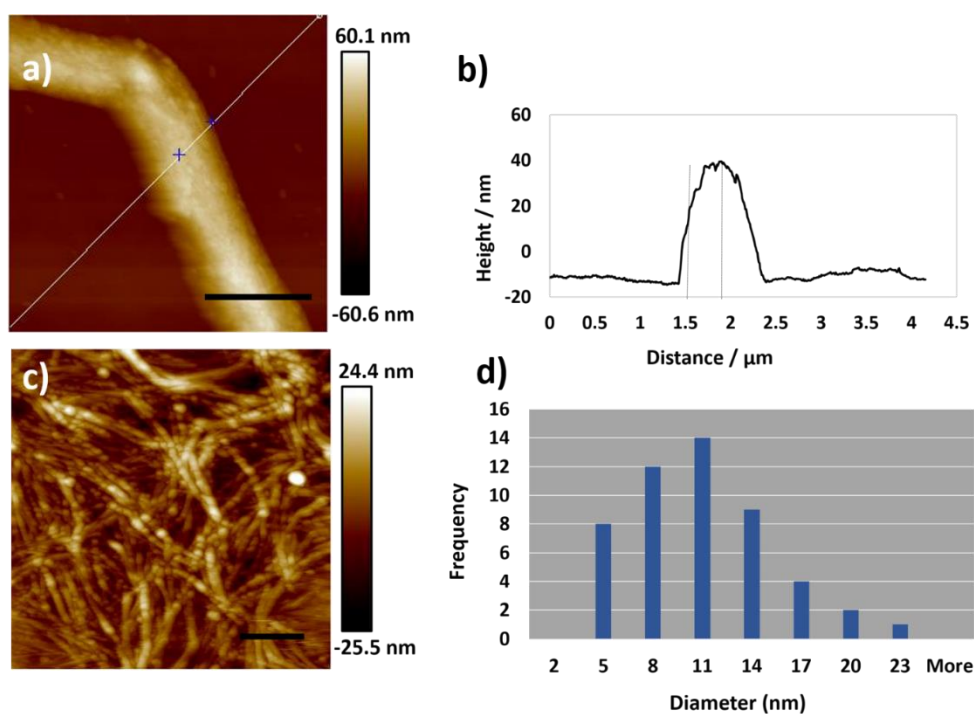


Figure 9.1.9. Tapping mode AFM image of 1:1 Ag-6-mercaptopurine riboside gel prepared with 0.1 N NaOH and drop cast onto a silicon wafer. The scale bars are 4 μm & 1 μm and the height (grayscale) are 60.1 nm & 24.4 nm in (a) and (c) respectively. (b) The cross section of (a) shows the height of the fibrous ~ 40 nm. (d) Histogram of the size (diameter) distribution of the Ag:6-MPR fibres. Image (c) was imaging from the end of one of the rough fibre which displays that was formed from gathering several small fibres.

9.1.2.7 Transmission Electron Microscopy (TEM)

TEM images in Fig. 9.1.10 showed long, uniform, and branched fibres. Most TEM images for other kinds of the gels that prepared in the thesis showed entangle networks, however, Ag(I):6-MPR gel is different in its morphology and this may be assigned to the binding site which is suggested to be by N7.

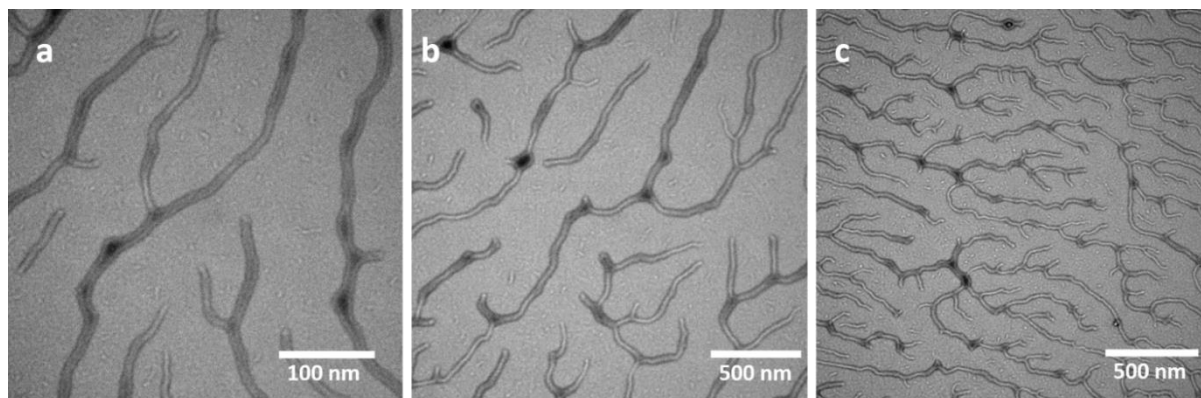


Figure 9.1.10. TEM of 1: 1 Ag- 6-mercapto purine riboside (Ag:6-MPR), the scale bar was 100 nm and 500 nm at (a), (b)& (c), while the magnification was 64000x, 34000x, and 25000x, respectively.

9.2 Conclusions

The work in this thesis has focused on studies of the reaction of metal ions (Au, Ag, Cu, and Co) with thio nucleobases and thio nucleosides as ligands to prepare coordination complexes. Most previous studies of similar systems concentrated on natural nitrogen bases or their alkylated derivatives rather than the thio bases.

In this thesis, different thionucleobase and thionucleoside based hydrogels and discrete structures were formed by coordinating with range of metal ions (Au, Cu, Ag, *etc*). The compounds were investigated with different spectroscopies and microscopies aiming to address their chemical structures and morphologies. Metal-nucleobases complexes have attracted great interest for many years in order to understand the biological roles of these compounds; in particular they form a good model to understand the interaction between metal ions and DNA (*e.g.* cis -platin). However, coordination between metal ions and nucleobases also allows the preparation of different kinds of materials: simple complexes (discrete entities), coordination polymers, and more complex architectures (supramolecules).

The reaction of 6-thioguanosine with coinage metal ions (Au, chapter 3), (Cu & Ag, chapter 4) lead to the formation of hydrogels comprising networks of an Au, Cu, Ag:6-TGR coordination polymers. Different spectroscopic techniques were used to characterize the chemical structures

such as FTIR, UV-Vis, XPS, XRD, and fluorescent spectroscopy. While AFM, TEM, and fluorescent microscope were used to characterize the morphology. The Au:6-TGR coordination polymer itself showed interesting luminescence and, upon oxidative doping, it became electronically conductive. In chapter 5, 2'-deoxy-6-thioguanosine was prepared and characterized with different techniques and used to prepare hydrogels with coinage metal ions. It shows the ability to form hydrogels despite a lack of hydroxyl group (2'OH) from the sugar structure. In chapter 6, thionucleobases also exhibit ability to form hydrogels despite the absence of sugar group in their structures. Also in chapter 6, 2-thiocytosine formed a polymer with Ag(I), the compound was very stable in solid state and has microcrystalline structure, however, leaving the complex in the solution lead to loss of the microcrystallinity and formation of a black hydrogel. Chapter 7, showed the formation of three complexes (Ag:6-MMPR, Cu:6-MMP, and Co:6-MMP) as discrete structures. The structures of these complexes were characterized by X-ray diffraction. In chapter 8, the reaction of Au(I) with 2-thiocytosine formed a stable complex in the solid state with a microcrystalline structure.